Inaugural dissertation

for

obtaining the doctoral degree

of the

Combined Faculty of Mathematics, Engineering and Natural Sciences

of the

Ruprecht - Karls - University

Heidelberg

Presented by

M.Sc. Yannik Voß

Born in Siegen, Germany

Oral examination: 11.12.2023

The role of phase separation in centrin interactions during *Plasmodium falciparum* schizogony

Referees: Prof. Dr. Michael Lanzer
Prof. Dr. Friedrich Frischknecht

Summary

Extensive proliferation of the malaria-causing parasite *Plasmodium falciparum* inside red blood cells is essential for its pathogenesis and survival strategy. Here *Plasmodium spp.* proliferate asexually via schizogony, an atypical form of cell division, wherein the parasite undergoes multiple rounds of asynchronous nuclear division in a shared cytoplasm. The *Plasmodium* centrosome, the centriolar plaque, is a critical regulator in this process that nucleates mitotic spindle microtubules and limits proliferation as it needs to duplicate before each nuclear division. However, little is known about the molecular and physiochemical composition of this protein-dense and amorphous organelle.

Within this thesis, I investigated the localization, dynamics, and biochemical interactions of the four *Plasmodium* centrins, PfCen1-4, a family of highly conserved centrosomal proteins. I demonstrated that all four localize to the centriolar plaque at the onset schizogony and defined a coordinated disassembly event during its final stages. To study their localization in more detail, I adapted live-cell Stimulated Emission Depletion Microscopy (STED) to *Plasmodium* for the first time, which revealed a highly dynamic rearrangement of PfCen1-Halo within the centriolar plaque. Investigating the underlying interactions of the Ca^{2+}-binding centrins via microscopy-assisted *in vitro* assays revealed that specifically PfCen1 and PfCen3 can undergo Ca^{2+}-dependent liquid-liquid phase separation, individually or as joint condensates. By testing a phylogenetically diverse panel of eukaryotic centrins, including human centrin 2, I further demonstrated that phase separation capability is an evolutionarily conserved feature. *In vitro* mutagenesis revealed a critical dependence on the N-terminus, wherein the presence of an intrinsically disordered region is predictive of phase separation capability. As the protein density and absence of structural features within the centriolar plaque could be well explained by it being a proteinaceous liquid, I investigated whether centrin dynamics and localization might be driven by phase separation *in vivo*. As one of the defining features of phase separation is its dependency on a critical concentration, I developed pFIO, a new DiCre/loxP based inducible overexpression system for *P. falciparum*. This allowed me to exert better control over intracellular PfCen1 levels, where increasing concentration correlated with formation of artificial non-centrosomal assemblies and premature recruitment to the centriolar plaque. Loss of Ca^{2+}-binding capability also abolished both *in vitro* phase separation and *in vivo* assembly. However, machine-learning assisted analysis of PfCen1 distribution in a large dataset of live cells revealed an inconsistent cellular concentration during assembly, arguing against a concentration threshold as a key trigger for localization. Centrosomal and artificial PfCen1-GFP assemblies also showed little turnover, suggesting a more solid state, but could still be dissolved and had no affinity to aggregate stains. This might point towards a gradual hardening process.

This work represents the first study of liquid-liquid phase separation in *Plasmodium* and pioneered useful toolsets for its subsequent research. It further provides important context for future studies on centrins across the eukaryotic spectrum and has potential implications for the material state and assembly mechanism of the centriolar plaque.

Zusammenfassung

Die beträchtliche Vermehrung des Malariaerregers *Plasmodium falciparum* in roten Blutkörperchen ist von entscheidender Bedeutung für seine Pathogenese und Überlebensstrategie. Hier vermehren sich *Plasmodium* Spezies asexuell durch Schizogonie, eine untypische Form der Zellteilung, bei welcher der Parasite mehrere Runden asynchroner Kernteilung in einem gemeinsamen Zytoplasma durchläuft. Das Zentrosom von *Plasmodium*, die zentrioläre Plaque, ist ein entscheidender Regulator in diesem Prozess, welcher Mikrotubuli der mitotischen Spindel nukleiert und die Proliferation limitiert, da sie sich vor jeder Kernteilung verdoppeln muss. Über die molekulare und physiochemische Zusammensetzung dieses proteindichten und amorphen Organells ist jedoch nur wenig bekannt.

Im Rahmen dieser Dissertation untersuchte ich die Lokalisierung, Dynamik, und biochemischen Wechselwirkungen der vier *Plasmodium* Centrine, PfCen1-4, einer Familie hochgradig konservierten zentrosomaler Proteine. Ich demonstrierte, dass alle vier zu Beginn der Schizogonie an der zentriolären Plaque lokalisieren und definierte ein koordiniertes Disassemblierungs Event in der Endphase. Um ihre Lokalisierung genauer zu untersuchen habe ich zum ersten Mal Stimulated Emission Depletion Microscopy (STED) für lebende Zellen in *Plasmodium* adaptiert, was eine hochdynamische Umstrukturierung von PfCen1-Halo innerhalb der zentriolären Plaque aufdeckte. Die Untersuchung der zugrundeliegenden Interaktionen der Ca^{2+}-bindenden Centrine mittels Mikroskopie-gestützter *in vitro* Tests ergab, dass spezifisch PfCen1 und PfCen3 eine Ca^{2+}-abhängige flüssig-flüssig Entmischung durchlaufen können, einzeln oder als gemeinsame Kondensate. Anhand einer phylogenetisch vielfältigen Auswahl eukaryotischer Centrine, einschließlich von humanem Centrin 2, zeigte ich außerdem, dass die Fähigkeit zur Entmischung ein evolutionär konserviertes Merkmal ist. *In vitro* Mutagenese ergab eine kritische Abhängigkeit vom N-Terminus, wobei das Vorhandensein einer intrinsisch ungeordneten Region mit der Fähigkeit zur Entmischung korreliert. Da die Proteindichte und Abwesenheit von Strukturen innerhalb der zentriolären Plaque sich gut dadurch erklären ließen, dass es sich um eine proteinöse Flüssigkeit handelt, untersuchte ich, ob die Centrin Dynamik und Lokalisation *in vivo* durch Entmischung getrieben sein könnte. Da eines der entscheidenden Merkmale von Entmischung ihre Abhängigkeit von einer kritischen Konzentration ist, entwickelte ich pFIO, ein neues DiCre/loxP-basiertes, induzierbares Überexpressionssystem für *P. falciparum*. Dies ermöglichte mir eine bessere Kontrolle über die intrazellulären PfCen1-Level, wobei steigende Konzentration mit der Bildung artifizieller, nicht-zentrosomaler Verbindungen und einer verfrühten Rekrutierung an die zentriolären Plaque korrelierte. Verlust der Ca^{2+}-Bindungsfähigkeit verhinderte sowohl *in vitro* Entmischung wie auch *in vivo* Assemblierung. Eine durch maschinelles Lernen unterstütze Analyse der PfCen1 Verteilung in einem großen Datensatz lebender Zellen zeigte jedoch eine inkonsistente zelluläre Konzentration während der Assemblierung, was gegen eine Konzentrationsschwelle als zentraler Auslöser für Lokalisierung spricht. Zentrosomale und artifizielle PfCen1-GFP Verbindungen zeigten ebenfalls einen geringen Austausch

mit der Umgebung, was auf einen solideren Zustand hindeutet, konnten jedoch aufgelöst werden und hatten keine Affinität zu Aggregat-Färbemitteln. Dies könnte auf einen graduellen Verhärtungsprozess hindeuten.

Diese Arbeit ist die erste Studie von flüssig-flüssig-Entmischung in *Plasmodium* und kreierte nützliche Instrumente für die weitere Erforschung. Darüber hinaus schafft sie wichtigen Kontext für künftige Centrin Studien im gesamten eukaryotischen Spektrum und hat potenzielle Implikationen für den Materialzustand und Assemblierungs-Mechanismus der zentriolären Plaque.

Table of Contents

Summary V
Zusammenfassung VII
Table of Contents X
List of Abbreviations XII
1 Introduction 1
1.1 Malaria 1
1.2 The elaborate *Plasmodium* lifecycle 2
1.3 Intraerythrocytic schizogony 4
1.4 The centriolar plaque 5
1.5 The centrin protein family 8
1.6 Liquid-liquid phase separation 11
1.7 Thesis Aims 14
2 Results 15
2.1 PfCen1-4 localization and dynamics 15
2.1.1 PfCen1-4-GFP localize to the CP's outer core during schizogony 15
2.1.2 PfCen1 undergoes dynamic rearrangement at the centriolar plaque 18
2.1.3 Duplication of centrin foci is microtubule independent 19
2.2 Characterizing centrin assembly and the role of structural elements 21
2.2.1 PfCen1 and PfCen3 undergo Ca^{2+}-dependent LLPS *in vitro* 22
2.2.2 Centrin LLPS is an evolutionarily conserved feature 28
2.2.3 N-terminal IDRs predict centrin LLPS capabilities 30
2.2.4 PfCen3 N-terminal phosphorylation prevents LLPS but not CP localization 33
2.2.5 PfCen1 and PfCen3 interact through condensation 35
2.3 In *vivo* dynamics of PfCen1 are influenced by its concentration 39
2.3.1 pFIO – An inducible overexpression system for *P. falciparum* 39
2.3.2 PfCen1-GFP overexpression induces premature formation of non-centrosomal foci 43
2.3.3 PfCen1-GFP foci formation and disassembly are regulated independently of cellular concentration 50
2.4 Determinants of centrin accumulation 54
2.4.1 Structural mutations abrogating LLPS *in vitro* impact *in vivo* foci formation 54
2.4.2 PfCen1-GFP does not respond to intracellular Ca^{2+}-level modulation 56
2.5 Investigating the material state of centrin foci 57
2.5.1 FRAP shows no exchange of PfCen1-GFP between foci and dilute fraction 57
2.5.2 Centrin foci are not stained by a protein aggregation dye 61
2.5.3 1,6-Hexanediole dissolves PfCen1 foci 63
3 Discussion 65
3.1 Methodological advancements 65
3.1.1 pFIO – An inducible overexpression system for *P. falciparum* 65
3.1.2 Establishing live-cell STED in *P. falciparum* 71

3.2 Implications for *Plasmodium* and centrin biology 72

3.2.1 Centrosomal localization of PfCen1-4 72
3.2.2 Independence of centriolar plaque duplication from spindle formation 74
3.2.3 Centrin *in vitro* LLPS capability is evolutionarily conserved 75
3.2.4 Structures driving homotypic and heterotypic centrin interactions 79
3.2.5 Assembly and disassembly of PfCen1 foci *in vivo* 86
3.2.6 The material state of foci 91
3.2.7 Implications for centrosomal structures 94

3.3 Conclusion 96

4 Methods 99

4.1 Cloning of plasmids 99

4.1.1 Cloning strategy 99
4.1.2 Generation of dsDNA fragments 101
4.1.3 Purification of dsDNA fragments 103
4.1.4 Plasmid assembly 104
4.1.5 Plasmid selection and purification 105

4.2 *P. falciparum* strain culturing and generation 106

4.2.1 *P. falciparum* blood culturing and synchronization 106
4.2.2 Freezing & thawing of *P. falciparum* cell lines 106
4.2.3 pFIO DiCre induction 106
4.2.4 *P. falciparum* transfection 107

4.3 *P. falciparum* population analysis 108

4.3.1 Western Blot 108
4.3.2 GFP quantification via flow cytometry 109

4.4 Microscopy 110

4.4.1 Seeding of iRBCs on imaging dishes 110
4.4.2 Confocal microscopy for IFAs 111
4.4.3 Confocal time-lapse microscopy 112
4.4.4 STED microscopy 116

4.5 Recombinant protein biochemistry 116

4.5.1 Recombinant Protein expression and purification 116
4.5.2 Coomassie SDS-PAGE 118
4.5.3 Mass spectrometry analysis 118
4.5.4 Circular dichroism spectroscopy 118
4.5.5 Generation of Antibodies 119
4.5.6 Quantification of Centrin LLPS dynamics via turbidity assay 119
4.5.7 IDR likelihood analysis via IUPRED 119

4.6 List of materials 120

5 List of References 133

6 Acknowledgements 146

7 Supplements 150

List of Abbreviations

3D	Three-dimensional
6His	6 histidine
A (nucleobase)	Adenine
A (amino acid)	Alanine
AA	Amino acid
AKiT7	Apicomplexan kinetochore protein 7
ALS	Amyotrophic lateral sclerosis
Amp	Ampicillin
ANS	8-anilino-naphthalene-1-sulfonic acid
Ark1	Aurora-related kinase 1
ArtiG	ArtiGranule
aTc	Anhydrotetracycline
AU	Arbitrary units
bp	Base pair
BSA	Bovine serum albumin
C (nucleobase)	Cytosine
c	concentration
CD	Circular dichroism
Cdc31	Cell division control protein 31
cDNA	Complementary DNA
Cen	Centrin
CenH3	Centromere-specific histone H3
CP	Centriolar plaque
Cr	*Chlamydomonas reinhardtii*
CRISPR	Clustered regularly interspaced short palindromic repeats
CRK4	Cdc2-related protein kinase 4
cRPMI	Complete RPMI
c_{sat}	Saturation concentration
D (amino acid)	Aspartate
ddH_2O	Deionized distilled water
DIC	Differential interference contrast
DiCre	Dimerizable Cre recombinase
DMSO	Dimethyl sulfoxide
DNA	Deoxyribonucleic acid
DNA-FISH	DNA fluorescence in situ hybridization
DOZI	Development of zygote inhibited
dsDNA	Double stranded deoxyribonucleic acid
E (amino acid)	Glutamate
ECCA	Extra-centrosomal centrin accumulations
E. coli	Escherichia coli
EDTA	Ethylenediaminetetraacetic acid
EFh	EF-hand
eGFP	Enhanced green fluorescent protein
EGTA	Ethylene glycol-bis(β-aminoethyl ether)-N,N,N′,N′-tetraacetic acid
Eo	*Euplotes octocarinatus*
F (amino acid)	Phenylalanine
F (primer)	Forward primer
Fig	Figure
Fiji	Fiji is just ImageJ

FKBP	FK506 binding protein
FRAP	Fluorescence recovery after photobleaching
FSC	Forward scatter
FUS	Fused in sarcoma
G (nucleobase)	Guanine
G (amino acid)	Glycine
G	Gibbs free energy
g (unit)	Gram
G1	Gap 1 phase
gDNA	Genomic Deoxyribonucleic acid
GDV1	Gametocyte development 1
GFP	Green fluorescent protein
glmS	Glucosamine-6-phosphate activated ribozyme
γ-TuRC	γ-Tubulin ring complex
H	Enthalpy
h (unit)	Hour
hDHFR	Human dihydrofolate reductase
HEPES	4-(2-hydroxyethyl)-1-piperazineethanesulfonic acid
Hoechst	Hoechst 33342
hpi	Hours post infection
Hs	*Homo sapiens*/human
HyD	Hybrid detectors
I_0	Post-bleaching intensity
I_i	Pre-bleaching intensity
IDR	Intrinsically disordered region
IFA	Immunofluorescence complex
IMC	Inner membrane complex
I_p	Recovery plateau intensity
IPTG	Isopropyl ß-D-1-thiogalactopyranoside
iRBC	Infected red blood cells
iRPMI	Incomplete RPMI
Kan	Kanamycin
Kb	Kilobase
kDa (unit)	Kilodaltons
L (amino acid)	Leucine
l (unit)	Liter
LC-MS	Liquid chromatography–mass spectrometry
LLPS	Liquid-liquid phase separation
loxP	Locus of X-over P1
M (amino acid)	Methionine
M (unit)	molar
m (unit)	Meter
m (unit prefix)	Milli
µ (unit prefix)	Micro
MACS	Magnetic-activated cell sorting
Mad1	Mitotic arrest deficient 1
MaP	Max-Planck (Institute)
MCS	Multiple cloning site
Met (amino acid)	Methionine
min (unit)	Minute(s)
M_F	Mobile fraction

mGFP	Monomeric green fluorescent protein
mRNA	Messenger RNA
MTOC	Microtubule-organizing center
n (unit prefix)	Nano
NA	Numerical aperture
NF54	Nijmegen *falciparum* strain 54
Ni-NTA	Nickel nitrilotriacetic acid
NLS	Nuclear localization sequence
NMR	Nuclear Magnetic Resonance
NPM1	Nucleophosmin 1
OD	Optical density
o/n	overnight
ORF	Open reading frame
PAGE	Polyacrylamide gel electrophoresis
Pb	*Plasmodium berghei*
PBS	Phosphate-buffered saline
PCM	Pericentriolar material
PCNA1	Proliferating cell nuclear antigen
PCR	Polymerase chain reaction
PEG	Polyethylene glycol
Pf	*Plasmodium falciparum*
PFA	Paraformaldehyde
pFIO	*Plasmodium falciparum* inducible overexpression
φ	Volume fraction
POI	Protein of interest
PTM	Post-translational modification
PV	Parasitophorous vacuole
R (primer)	Reverse primer
RAP	Rapamycin
RBC	Red blood cell
RescueSTED	Reduction of state transition cycles STED
RNA	Ribonucleic acid
RPMI	Roswell Park Memorial Institute
RT	Room temperate
S (amino acid)	Serine
S	Entropy
s (unit)	Second(s)
Sc	Saccharomyces cerevisiae
SDS	Sodium dodecyl sulphate
SEC	Size-exclusion chromatography
SIM	Structured illumination microscopy
SiR	Silicon rhodamine
SLI	Selection-linked integration
Slp	Sfi1-like protein
SOC	Super optimal medium with catabolic repressor
SPB	Spindle pole body
SSC	Side scatter
ssDNA	Single stranded deoxyribonucleic acid
STED	Stimulated emission depletion
T (nucleobase)	Thymidine
T (amino acid)	Threonine

T	Temperature
T2A	Thosea asigna virus 2A
TAE	Tris-acetate-EDTA
Tb	*Trypanosoma brucei*
TE	Tris-EDTA
TetR	Tet repressor
TEV	Tobacco etch virus
Tg	*Toxoplasma gondii*
TPM	Transcripts per million
TRIS	Tris(hydroxymethyl)aminomethane
TSS	Transcription start site
U-ExM	Ultrastructure expansion microscopy
uRBC	Uninfected red blood cell
UTR	Untranslated region
UV	Ultraviolet
V (unit)	Volt
v/v	Volume per volume
W (unit)	Watt
WB	Western Blot
WHO	World Health Organisation
WR	WR99210
WT	Wild type
V (unit)	Volt
v_m	Molecular volume
w/v	Weight per volume
XPC	Xeroderma pigmentosum group C
Y (amino acid)	Tyrosine
YFP	Yellow fluorescent protein

1 Introduction

1.1 Malaria

Throughout the history of mankind, probably no other disease has had such a profound humanitarian, societal, and evolutionary impact as malaria [1]. Already affecting humanity from the dawn of its earliest civilizations [2]–[4], to this day the World Health Organisation (WHO) estimated 247 million new cases and 619,000 deaths annually (2021) [5]. It is endemic in 84 countries across Africa, Latin America, as well as South- and South-East Asia, placing half the world population at risk of infection [5]. The disease causes a major economic burden on affected areas [6]–[8] and has often left an evolutionary legacy of protective, yet debilitating genetic diseases, such as sickle-cell anaemia or thalassemia [1], [9].

Originally named “mal’ aria”, compacted Italian for “bad air”, after its presumed cause, the actual causative agents of the disease are mosquito-borne unicellular parasites of the genus *Plasmodium* [2], [10]. These protozoans belong to the phylum of *Apicomplexa*, which also includes the toxoplasmosis pathogen *Toxoplasma gondii*. Over 200 *Plasmodium* species have been described to date, successfully infecting a broad range of vertebrates from mammals, birds, to reptiles [11]. Five of these species are known to cause human malaria: *P. falciparum*, *P. malariae*, *P. vivax*, *P. ovale*, and, more recently the zoonotic *P. knowlesi* [12]. Out of the five human infecting species *P. falciparum* is both the most prevalent and deadliest, causing over 95% of cases and deaths, predominantly in Africa [5].

While global malaria eradication programs have achieved successful elimination of malaria in several endemic countries, progress has stagnated in recent years, with case numbers being on the rise again after two decades [5]. A central element of these campaigns is vector control via distribution of insecticide-treated mosquito nets. Besides disruptions during the COVID-19 pandemic, the effectiveness of these measures is threatened by the increasing emergence of insecticide resistance in vector populations across 78 countries [5]. Simultaneously there are growing concerns about the long-term efficacy of artemisinin-based combination therapies, the current frontline treatment against malaria. PfKelch13 mutations causing delayed parasite clearance and even cases of recrudescence are prevalent around Thailand and have also emerged in African countries as well [5], [13]. Meanwhile, the first approved malaria vaccine RTS,S/AS01 only showed a low protection efficacy of 26% and 36% in infants and children respectively after 3 doses and a booster [14]. However, more recently the R21 vaccine achieved 75% efficacy with 3 dose plus booster regimen in a phase III clinical trial, which has already prompted its licensing in three African countries [15]. Even so, significant challenges remain, highlighting the need for fundamental research to uncover new targets for treatments. Beyond its importance for medical progress, researching the divergent biology of the parasite in itself offers fascinating insights into unique biological solutions developed by an early-branching eukaryote.

1.2 The elaborate *Plasmodium* lifecycle

The life cycle of *Plasmodium* is dependent on alternating infections of the vertebrate host and female *Anopheles* mosquitos [16]. Throughout this cycle across two different organisms and multiple tissues, the parasite is faced with multiple bottlenecks, in which a small founding population of parasites must expand extensively to ensure successful transmission. Herein they display a remarkable plasticity in terms of morphology of the different life cycle stages, as well as their replication speed and progeny number (Fig. 1).

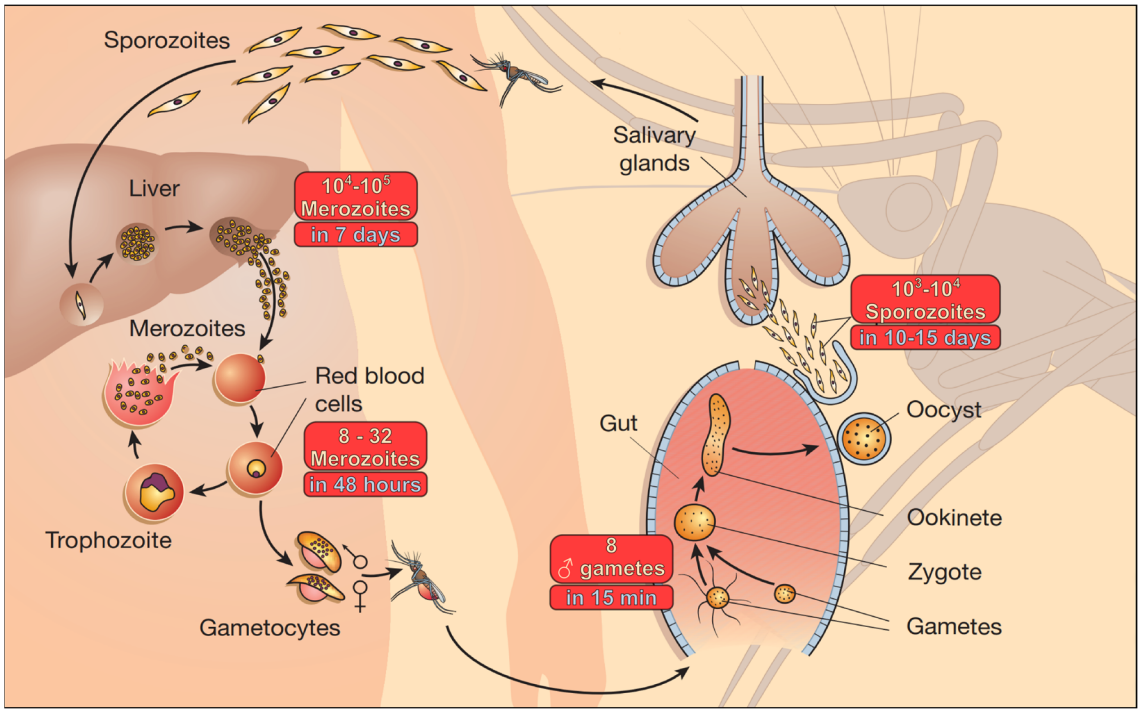


Figure 1 Life cycle of *Plasmodium falciparum*. An overview of the *P. falciparum* life cycle across human (left) and mosquito host (right). Approximate timeframes and progeny numbers are indicated. Modified from Wirth (2002) [17].

Using the example of *P. falciparum* the human host is infected when an infected *Anopheles* mosquito takes a blood meal. During this process the mosquito injects saliva containing motile parasite stages called sporozoites residing in the salivary glands into the dermis via its proboscis [18], [19]. These extracellular parasites then actively glide through the skin in search of a blood vessel to penetrate for transport to the liver [18]. Here they transmigrate through the cells of the sinusoidal barrier, comprised of endothelial and Kupffer cells, and a few underlying hepatocytes before settling inside one [16], [18], [20]. This intracellular stage resides inside a host-membrane derived compartment called the parasitophorous vacuole (PV) to undergo hepatocytic schizogony, the parasite's mode of replication, forming up to 90,000 daughter cells over ~6.5 days [21]. These merozoites are then released into the bloodstream in vesicles called merosomes to commence the asexual cycle of erythrocyte/red blood cell (RBC) infection [21], [22]. Herein merozoites invade erythrocytes to undergo erythrocytic schizogony, giving rise to 8-32 daughter merozoites, which are then released by lysis of the host cell to rapidly invade new erythrocytes and repeat the cycle every 48 h [23]–[26]. Merozoites invade the host cell using a hallmark structure of apicomplexans, the apical complex,

wherein they secrete proteins onto the target membrane from rhoptries and micronemes. These then form a tight junction between host and parasite, through which the merozoite pulls itself into an invaginating membrane entering the cell and forming a PV from the RBC membrane in the process [27]. Directly after invasion ,the merozoite transforms into the ring stage and starts to remodel the erythrocyte by exporting parasite proteins into its lumen to establish membrane-bound organelles and introduce new nutrient channels into the host cell membrane [28]–[30]. This serves the uptake of hemoglobin from the host cell, which is digested to attain amino acids that support growth during the following trophozoite stage [31]. This digestive process releases heme as a toxic by-product which is detoxified into crystalline hemozoin, which is stored in the parasite's digestive vacuole. This visually distinguishes the ring stages from trophozoites. Furthermore, the parasite establishes small protrusions called knobs on the erythrocyte surface, which adhere to host receptors at the endothelium to sequester infected RBCs (iRBCs) and prevent their clearance in the spleen [16]. The parasite then develops into a schizont where DNA replication, nuclear division, and daughter cell formation take place, which is described in detail in 1.3 [32]. As this asexual cycle is solely reliant on erythrocytes as host cells, it can be continuously maintained in blood cell cultures [33]. Importantly, the blood cycle is the sole cause of pathogenesis and therefore of high clinical relevance [16]. The exponential growth of the parasite population elucidates the characteristic rhythmic febrile response pattern of malaria due to the synchronized release of merozoites and digestive vacuole contents [16], [34], [35]. In severe cases patients develop anaemia as a result of RBC lysis compromising oxygen transport, while microvascular obstruction caused by the parasite's cytoadhesion can contribute to brain swelling leading to coma and death [16], [36], [37]. Accordingly, parasite biomass is a major predictor for disease outcome, accentuating the link between parasite proliferation and pathogenesis [38].

During each asexual cycle, the offspring of a small number of schizonts (<1%) instead differentiate into non-proliferative male and female gametocytes after invasion of the next erythrocyte [39], [40]. Sexual conversion rate increases with parasite density is dependent on a number of factors including host nutrient levels [40]. After sexual commitment, gametocytogenesis occurs sequestered in the bone marrow, where parasites develop through five morphologically distinct stages over ~15 days (I-V) [41]. Fully matured stage V gametocytes then re-enter the blood stream where they can be taken up by a mosquito during a bloodmeal.

Once ingested by the female *Anopheles* mosquito, the drop in temperature and presence of xanthurenic acid in the midgut environment induces rapid gametocyte activation [42]. In male gametocytes, this triggers 3 rapid rounds of DNA replication within 15 min followed by a single nuclear division, leading to the formation of 8 motile haploid microgametes [42]–[44]. These are released from the gametocyte and host RBC via a process called exflagellation. Meanwhile, the female gametocytes transform into a macrogamete while releasing mRNAs important for the zygote from the translational repressor DOZI [42], [45]. The male microgamete subsequently fertilizes the female macrogamete, forming a zygote by undergoing nuclear fusion [42]. The zygote then differentiates into a tetraploid, motile ookinete by undergoing meiotic DNA-replication

[46]. The ookinete then crosses the monolayer midgut epithelium by invading and traversing an epithelial cell to form an oocysts between epithelium and basal lamina [42]. Within, extensive DNA replication and nuclear division give rise to hundreds of mononucleated, haploid sporozoites over the course of 1-2 weeks [47]. These motile sporozoites are then released into the circulating haemolymph, eventually reaching and invading the salivary glands [18]. Here they mature into their infectious forms awaiting the next bloodmeal to infect the next human host, thus closing the cycle [48].

1.3 Intraerythrocytic schizogony

The goal of *Plasmodium's* exponential proliferation in the blood is to generate a high enough parasite density to enable efficient uptake of gametocytes by mosquitos. Schizogony is therefore not only relevant for pathogenesis, but also an existential part of the parasite's continued survival. Besides its important role during the infection it is also a highly atypical and fascinating form of cell division that differs fundamentally from model organisms [32], [49]. Over the course of schizogony, the initially mononucleated parasite forms a multinucleated cell (coenocyte), through multiple rounds of DNA-replication and closed nuclear division, wherein the nuclear envelope remains intact throughout [50]. At the end of schizogony, daughter merozoites are formed through a single cytokinetic segmentation event before egress via PV and host cell lysis [32], [49].

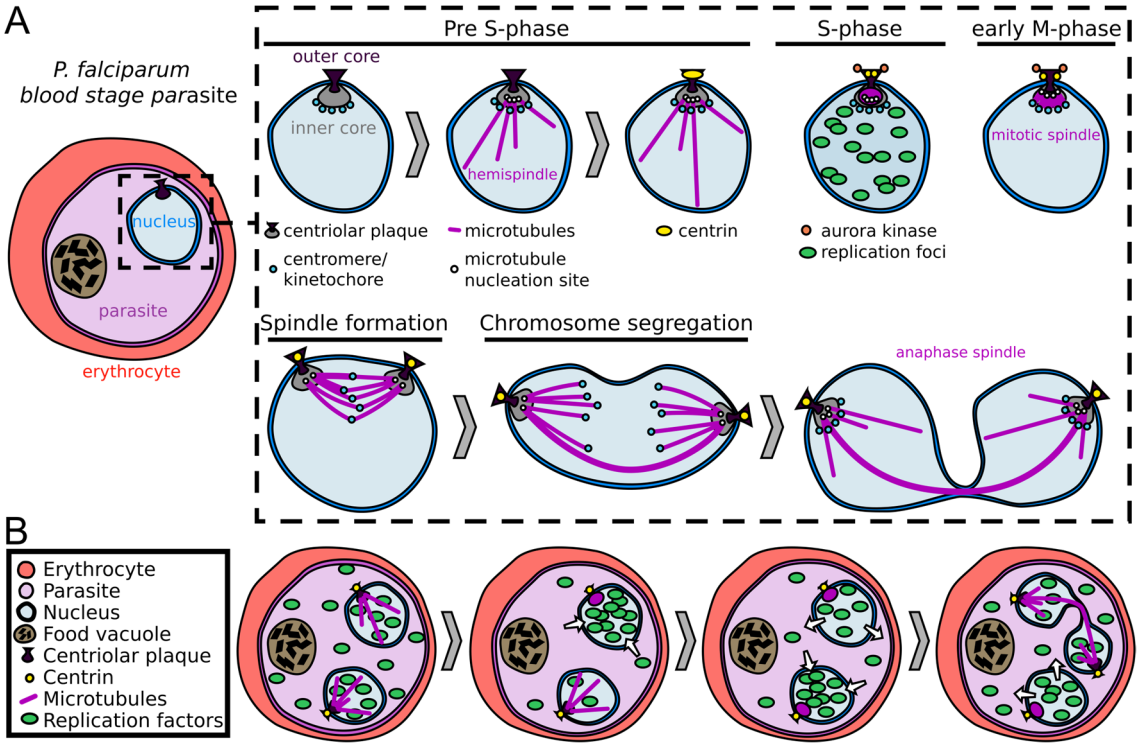


Figure 2 Intraerythrocytic schizogony. (A) A detailed overview of CP and spindle morphology during the 1st (closed) nuclear division of schizogony indicating the different nuclear stages. S-phase onset is marked by hemispindle collapse and influx of replication factors into the nucleus, where they form replication foci. **(B)** During schizogony multiple nuclei replicate asynchronously in a shared cytoplasm, resulting in nuclei with different stages of the mitotic cycle. Modified from Voß, Klaus, *et al.* (2023) [32]

While the transition from ring to schizont stage is clearly marked by the emergence of the hemozoin pigment at ~ 24 hours post infection (hpi) of the RBC [29], the transition to the schizont stage and thus schizogony is less obvious. Within the context of this work the onset of schizogony is defined as the initiation of DNA-replication during S-phase, which occurs 30-32 hpi and is dependent on the cell cycle kinase CRK4 [32], [51]. The first currently known harbinger of S-phase onset is the formation of intranuclear microtubules at the centriolar plaque (CP), the *Plasmodium* centrosome, which is embedded in the nuclear envelope (more details in 1.4) (Fig. 2A) [32], [52]. This so called hemispindle is highly dynamic, with its branches varying in both length (0.5-2 µm) and number (2-11) [52]. While its function remains unknown, it collapses into an early mitotic spindle at the onset of S-phase, coinciding with an influx of DNA-replication factors and emergence of replication foci in the nucleus [50], [53]. In accordance with a duplication of vertebrate centrosomes at the G1/S transition, the CP then duplicates and separates while staying associated with the nuclear envelope [32], [52], [54], [55]. The now bipolar mitotic spindle is connected to the chromosome's kinetochores and persists for approximately 150 min [32], [56]. Afterwards, the chromosomes, which remain uncondensed, are segregated via extension of a large microtubule bundle forming the anaphase spindle [32], [52]. Nuclear division is then completed by karyofission and severing of the interpolar spindle microtubules, leaving two daughter nuclei with one CP and hemispindle each [32], [52], [57]. From here on, the nuclei repeat this cycle of DNA replication and nuclear division until segmentation, where nuclei are encapsulated together with the apical complex and organelles by an invagination of the parasite membrane [32], [58]. During segmentation no intranuclear spindles are present, instead subpellicular microtubules form from the apical end of the developing merozoite [32]. The spindle stages and CP duplication can therefore serve as indicators of the status of each nucleus [32], [50].

Importantly, the cycles of nuclei are independent from one another and asynchronous in their replication cycles, despite their close proximity in a shared cytoplasmic volume [50] (Fig. 2B). This nuclear autonomy implies a regulation of replication on the level of each individual nucleus, rather than a global control. As such, the centriolar plaque has been proposed as a regulatory "pacemaker", as it is closely associated with each individual nucleus with its duplication being a limiting factor for nuclear division [49].

1.4 The centriolar plaque

Centrosomes are the microtubule organizing center (MTOC) of the mitotic spindle. They are membrane-less organelles that can also act as signalling hubs and regulators for the cell cycle progression that integrate multiple mitotic kinases [59]. For example, they are essential for initiation of G1/S transition in mammals and regulate entry into M-phase in yeast [59], [60]. Despite centrosomes' consistent role as MTOCs during mitosis, eukaryotic lineages have evolved vastly different centrosomal structures.

In metazoans centrosomes consist of a pair of barrel-shaped centrioles at their center, which consists of microtubule triplets arranged in a 9-fold symmetry around a central

cartwheel structure [61]. They recruit a surrounding sphere of pericentriolar material (PCM), which appears to act as a scaffold for the recruitment of more dynamic client proteins [54], [62]. These are capable of concentrating tubulin and nucleating microtubules by recruiting, amongst others, γ-tubulin and the γ-TuRC complex [63]. Centrioles duplicate via *de novo* assembly of daughter centrioles perpendicular to the cartwheel of the mother centriole during S-phase. The original centriole pair subsequently segregates while expanding its PCM ~30 fold [62].

Meanwhile the functionally equivalent organelle of *Saccharomyces cerevisiae*, the spindle pole body (SPB), consists of multiple highly organized plaque layers that are partially embedded into the nuclear envelope [55], [64]. While the central plaque anchors the SPB to the membrane, the outer and inner plaques nucleate cytoplasmic (astral) microtubules and nuclear spindles respectively [65]. A PCM like structure has thus far only been observed in *S. pombe* [66]. Duplication is mediated by a bridge structure consisting of parallel bundles of the elongated α-helical protein Sfi1, attached on one side to the central plaque and tethered to the nuclear envelope [55], [67]. The initial half-bridge extends to a full bridge during late mitosis through antiparallel dimerization of Sfi1 molecules and forms a SPB precursor satellite *de novo* during the G1 phase, which develops into a mature SPB before separation of the two SPBs at the start of S-phase [55], [67].

In stark contrast, the centriolar plaque of *Plasmodium* does not contain any apparent organized structures (Fig. 3A) [43], [52], [56], [68]. Instead it consists of a very protein-dense inner and outer nuclear core, which are connected through the nuclear envelope by an unknown pore structure (Fig. 3) [52]. The rounded inner core is ~350 nm x 250 nm in size and functions as the nucleation site of intranuclear microtubules [52]. Furthermore, it displaces the chromatin, creating a DNA-free region below the CP with centromeres resting at the interface [32], [52]. Meanwhile, the shape of the protein-dense area of the outer core often assumes an inverted cone or branched shape that also appears to change throughout the nuclear cycle (Fig. 3B, C)[68]. The function of the outer core is less clear, but an increasing number of studies point towards a potential role in merozoite formation and positioning of organelles therein [32], [69]. Early studies noted that rhoptries and the apical complex as well as the inner membrane complex (IMC), a network of flattened vesicles structurally stabilizing the merozoite membrane, form in direct proximity to the outer CP core [32], [70]. A recent study furthermore suggested that the outer core tethers the nucleus to the apical structures [69]. This conclusion stemmed from a disruption of kinetochores leading to both disengagement of the outer core from the nucleus and a disassociation of the nucleus from the apical complex. The same study also postulated that the subpellicular microtubules are nucleated by the outer CP core. Surprisingly, interference with its function via depletion of Sfi1-like protein (PfSlp) also led to aberrant intranuclear spindle structures [71]. In this line, a regulatory function of the CP is further supported by the transient localization of mitotic Aurora-related kinase 1 (PfArk1) to the outer core during S-phase, which appears to also have a critical role in spindle formation [72], [73]. Finally, DNA-replication foci first appear close to the CP, before spreading

throughout the nucleus from there, indicating a role of the centrosome as a signal emitter [53].

While the dynamics of the spindle microtubule reorganization during the nuclear cycle are, at this point, well characterized the progression of the CP morphologies is less well understood. The first direct evidence of the CP's existence during the asexual cycle is the assembly of the hemispindle at its inner core prior to S-phase onset [32], [52], [53]. However, the clustering of centromere histone CenH3 in a single focus at the nuclear periphery during early trophozoites suggests the presence of a form of intranuclear core from a significantly earlier timepoint [74]. This is supported by a recently published pseudo-timeline of the CP, that suggests the presence of the inner core already at an indeterminate time prior to S-phase where the protein-dense mass of the outer core is still absent (Fig. 3C) [68]. The authors then postulate a *de novo* recruitment of the outer core closer to S-phase, which first assumes a cone-shape then gradually splits during CP duplication at the onset of S-phase [68]. While up until this point it has not been clear whether CPs duplicate via fission or *de novo* assembly, this observation would support a fission model. However, for confirmation time-resolved data of a duplication event of a single CP will be required. In either case, it remains unknown which structures generate the forces driving CP duplication and its subsequent segregation.

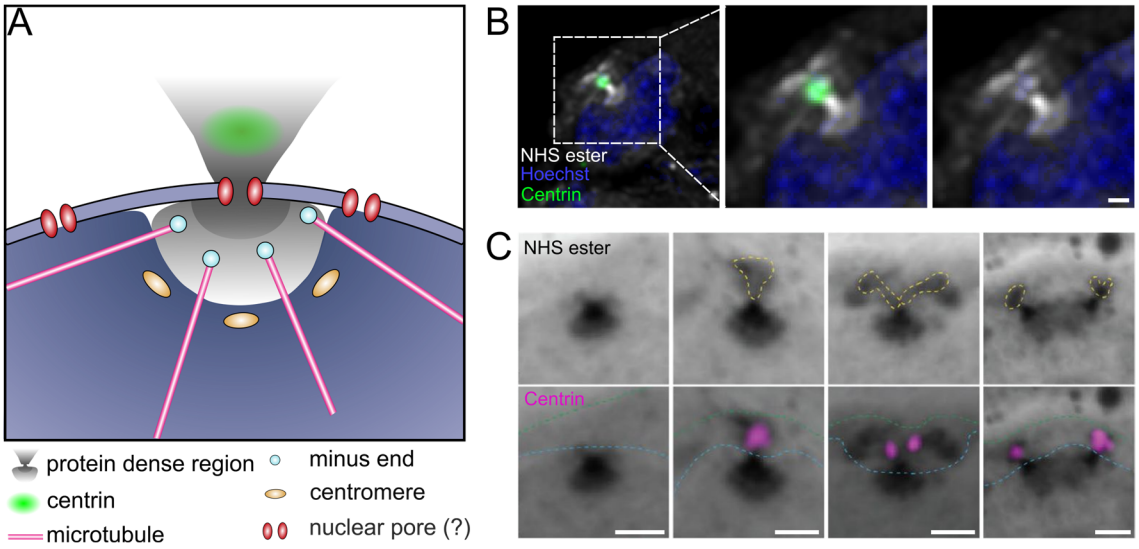


Figure 3 Centriolar plaque organisation. (A) Current model of the centriolar plaque during the hemispindle stage. **(B)** Deconvolved confocal U-ExM image of a *P. falciparum* CP during schizogony labelled for protein density (NHS ester, greys), DNA (Hoechst, blue), and centrin (green, antibody). Nature of the hypothesized nuclear pore structure is unclear. (A, B) from Simon *et al.* (2021) [52]. **(C)** Proposed progression of CP assembly and duplication. U-ExM images of different *P. falciparum* CPs during schizogony labelled for protein density (NHS ester, greys), and centrin (magenta, antibody). Yellow line, cytoplasmic CP extension; blue line, nuclear envelope. Maximum intensity projection. Modified from Liffner *et al.* (2023) [68]. All scalebars 1 µm (after expansion, typical expansion factor is 4.5x).

An important marker for the stages of CP development is centrin 3 (Cen3) [70]. It localizes to the outer core as a single focus after hemispindle assembly, but prior to S-phase, and duplicates alongside it [52]. It was the first identified protein of the *Plasmodium* centrosome in 2008 and remained as such until recently [70]. In fact, while over 200 centrosomal proteins have been identified in humans and the composition of

SPB is very well characterized the vast majority of CP components remain virtually unknown [49], [64]. While a recent gene-by-gene screen of chromosome 3 detected a few new inner core proteins of unknown function [75], most classical centrosome components (e.g. polo-like kinases) have no known conserved homologues in *Plasmodium*. Besides γ-tubulin, which localizes to the inner core [43], centrin is one of the few exceptions and was the only known protein of the outer CP core of *P. falciparum* prior to this work.

The seemingly dynamic and amorphous structure of the CP without any evident structures raises many interesting questions about its composition and organization. As one of the very few known components, the study of its centrins could provide a gateway into a deeper understanding of this divergent centrosome.

1.5 The centrin protein family

Centrins were first described as a major component (63% of protein mass) of the calcium-responsive striated flagellar root of the green algae *Tetraselmis striata* [76]. Soon after they were detected at the basal bodies of *Chlamydomonas reinhardtii* and have since been recognized as a universal component of centrosomes across eukaryotes [77], [78]. As such, all investigated eukaryotic organisms encode at least one centrin [79].

Centrin structure

Centrins are a highly conserved family of small (~20 kDa) structural proteins. Their 'dumbbell' structure consists of two pairs of Ca^{2+}-binding EF-hand (EFh) domains as well as a highly variable N-terminus (Fig. 4, S4) [70]. While the N-terminus appears to be disordered and can typically not be resolved via nuclear magnetic resonance spectroscopy (NMR) or X-ray crystallography, the EFh domains adopt a conserved conformation [80]–[83]. EFh domains consists of a helix-loop-helix structure, which can chelate a Ca^{2+} ion within the flexible loop via 7 coordinating groups (mostly acidic D or E sidechains) in a pentagonal bipyramidal fashion [84]. In case of human centrin 2 (HsCen2) or calmodulin, Ca^{2+}-binding induces a conformational transition from a closed to an open state to facilitate interaction with binding partners (compare N- and C-terminal EFh domains in Fig. 4A) [84]–[86]. With dissociation constants ranging from 10^{-4}-10^{-9} M not all EFh domains are 'active' at physiological Ca^{2+} concentrations [84]. While certain amino acids (AA) of the EFh loop, such as aspartate at position 1 or glycine at position 7, are critical for Ca^{+2}-binding capability, the overall affinity is a complex interplay of increasing entropy from the release of bound water molecules and binding enthalpy balancing attraction of the coordinating ligands to Ca^{2+} with mutual repulsion [84]. As such, the activity of an individual EFh domain can only be determined to a limited degree from its AA sequence. Additionally, EFh domains are selective and binding of Ca^{2+} is typically strongly favoured over Mg^{2+}, discriminated via differences in ionic radius and ligand geometry (pentagonal bipyramidal for Ca^{2+}, octagonal for Mg^{2+}) [84].

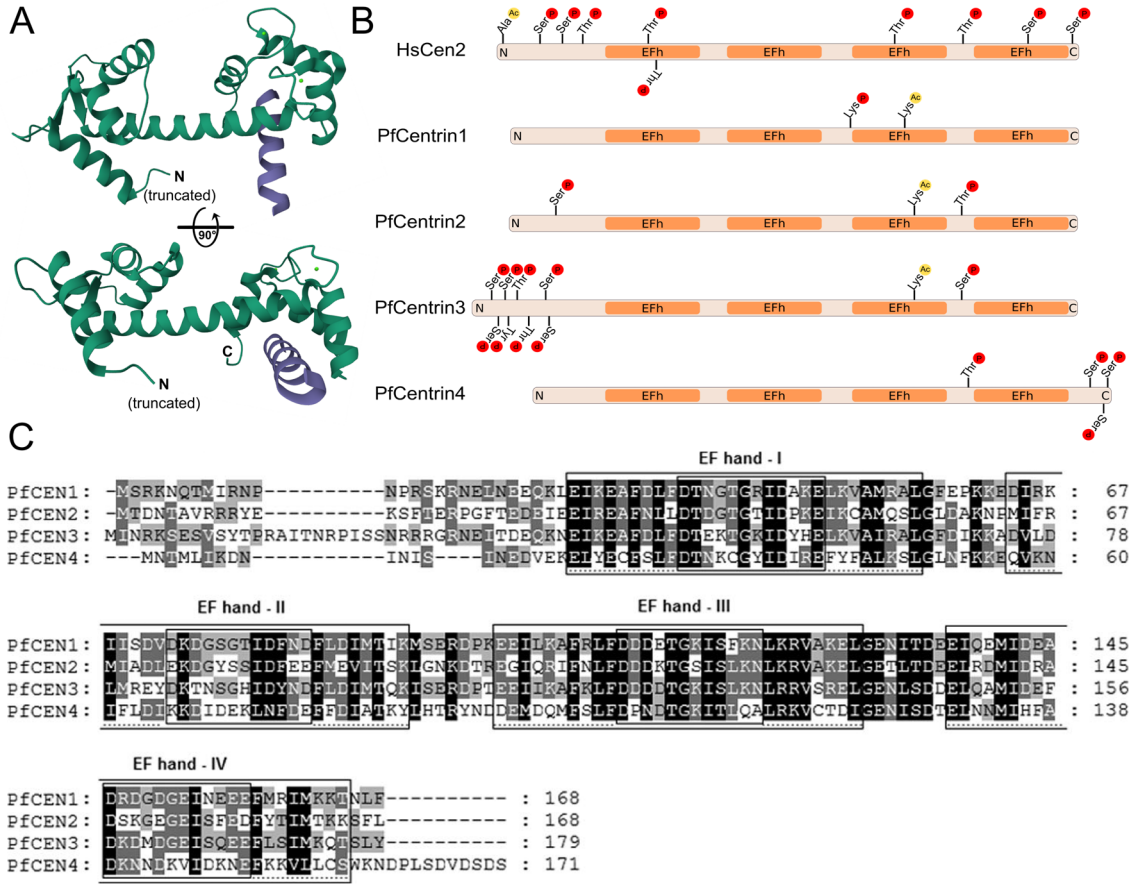


Figure 4 Structure of centrins. (A) X-ray diffraction structure of HsCen2 (green) complexed with an XPC-derived peptide (purple). EFh III and IV (right side) chelate 2 Ca^{2+} ions (green spheres) and are in an open conformation. First 23 N-terminus (N) are missing since they could not be resolved. Structure derived from Thompson *et al.* (2006) [86]. **(B)** Proportional sizes of HsCen2 and PfCen1-4 structural domains. Documented post translational modifications (red P, phosphorylation; yellow Ac, acetylation) are indicated [51], [87]–[96]. Modified from *Voß et al.* (2023) [79]. **(C)** Primary sequence alignment of PfCen1-4. Boxed sequence indicates the central EFh binding loop sequence with dotted line marking the EFh α-helical domains. Shading indicates residue similarity ≥80%. From Mahajan *et al.* (2008) [70].

Localization and function

In human centrosomes HsCen2 localizes along the inner walls of the core region and to the distal opening of the centrioles [97], [98]. Here it is recruited at the onset of daughter centriole assembly during S-phase [98]. At the distal tip, it is important for the interdependent recruitment of human Sfi1 (HsSfi1) [98]. Contrary to earlier reports, HsCen2 depletion did not affect centriole duplication, but had lasting effects on their integrity [98], [99]. A role in *de novo* centriole assembly is nonetheless supported by HsCen2 stabilization or overexpression leading to centriole overproduction [100], [101]. The centrin homologue of *S. cerevisiae*, ScCdc31, is essential for SPB duplication where it localizes to the (half-) bridge by interacting with binding motif repeats along the extended α-helix of ScSfi1 [67], [102]. These interactions stabilize the half bridge by promoting lateral interaction between parallel ScSfi1 molecules as well as the elongated structure of the protein itself [67], [103], [104]. ScCdc31 binding is furthermore essential for recruitment of daughter SPB components [67]. In *Plasmodium's* (relatively) close relative *Toxoplasma gondii* centrin 1-3 (TgCen1-3) localize to the centrosome as well, although TgCen2 additionally associates with the basal complex, apical preconoidal ring, and peripheral annuli [105], [106]. A knockdown of TgCen2 led to a hierarchical

depletion from these organelles, with the centrosomal pool proving most persistent [105]. Besides an invasion defect the parasites also displayed abnormal replication. While centrosome duplication was not affected, they were not segregated, leading to inconsistent centrosome and nuclei numbers in across daughter cells [105]. *Trypanosoma brucei* centrin 2 (TbCen2) localizes to the basal body, with conflicting reports whether it is involved in duplication or segregation of the organelle [107], [108].

Besides their role in centrosome biology, other functions of centrin have been observed as well [78]. Depletion of human centrin led to defects in nucleotide excision repair, which is consistent with HsCen2 binding to xeroderma pigmentosum group C (XPC) (Fig. 4A), which detects DNA damage such as that caused by UV light [78], [86], [109], [110]. Accordingly, induction of DNA damage caused a sequestration of centrin in the nucleus [111]. In yeast, Cdc31 also binds the XPC orthologue Rad4p and has an additional role in protein degradation [78], [112]. It also binds to Sac3 as an element of the TREX-2 complex, which is part of the mRNA export machinery. Yeast centrin therefore appears to have a role in mRNA export as well as the association of the complex with nuclear pores, both of which are affected by Cdc31 mutations [113], [114].

Plasmodium centrins

P. falciparum, like all other *Plasmodium* species, encodes four centrins, centrin1-4 (PfCen1-4) (Fig. 4B, C). While PfCen1 and PfCen3 are part of two evolutionarily conserved centrin clade that include, amongst others, HsCen2 and HsCen3 respectively, PfCen2 and PfCen4 are the result of an Alveolata-specific expansion [70]. The purpose of this expansion and need for four different centrins is not clear, as their functions remain unknown. A genome-wide knockout-screen suggests essential functions for all four during the asexual blood cycle, implying that they are not functionally redundant [115]. Here transcript levels also suggest a similar expression timing during mid-trophozoite to schizont stage [116]. Importantly an earlier study into the *Plasmodium* centrins identified a centrosomal localization of PfCen3 based on antibodies, but was not able to determine the position of the other three [70].

Centrin self-assembly

Intriguingly, a recurring characteristic of different recombinant centrins across a multitude of organisms is their ability to self-assemble *in vitro* in response to Ca^{2+}. This has been observed for HsCen2, HsCen1, TgCen1, and centrin from *Euplotes octocarinatus* (EoCen) [117]–[121]. Despite detailed studies into the biochemistry of their interactions, the nature of the resulting structures remains unknown and have never been observed directly. As a result an interaction of the four *Plasmodium* centrin as suggested by pulldown study of centrin 4 in *Plasmodium berghei* (PbCen4) (a rodent model malaria parasite) and a reported interaction between PfCen3 and PfCen1 is highly intriguing, as it implies a potential role of centrin self-assembly *in vivo* [71], [122].

Investigation of the localization and potential interactions of the four *Plasmodium* centrins could provide leads to understand their different roles within the parasite.

1.6 Liquid-liquid phase separation

A critical challenge for cells is the special organisation of biochemical reactions and interactions, for which the solution was compartmentalization via organelles [123]. In many classical organelles like mitochondria, the necessary boundary separating the internal reaction space from its surroundings is provided via a lipid membrane. However, there are also many examples of organelles that are not delineated by a membrane, like the nucleolus, Cajal bodies, or the centrosome [123], [124]. How these membraneless organelles concentrate macromolecules as a separate compartment without a physical barrier while still maintaining internal and external diffusion has been a longstanding question [124], [125]. In 2009, a study on P granules introduced a radical new paradigm based on the observation that these organelles behaved like liquids within the cell [126]. They fused, deformed ('dripped/wetted') in response to physical contact, and showed rapid internal mixing. This led to the proposition that membraneless organelles could be proteinaceous liquid condensates that form via liquid-liquid phase separation (LLPS). This phenomenon, often exemplified by oil droplets in water, has long been known in polymer or colloidal chemistry, but had not gathered much attention in biology except by structural biologist as an undesired side effect of protein crystallization [125], [127].

Molecular assemblies, including proteins, can transition between different states, such as solids or liquids. Assembly into solids or liquids in a complex mixture with two or more components occurs if the separation into two or more phases constitutes a reduction of free energy of the system [123], [128]. While entropy drives the system towards a mixed state with a uniform concentration (Fig. 5Ai), this is counteracted if interactions between like-neighbours are favoured, interactions between unlike-neighbours (e.g. hydrophilic vs hydrophobic) are disfavoured (Fig. 5Aii) [123], [128]. In this scenario the chemical potential of the mixed state is increased and demixing of the components (e.g. water and proteins) into two different phases becomes energetically favourable as it minimizes unfavourable interactions. In other words, phase separated molecules have a higher affinity towards themselves than their solvent, in which they exceeded their solubility. This results in an enriched dense phase and a depleted dilute phase, which are separated by a phase boundary [123]. Molecules can still diffuse between the two phases without equalizing the concentrations, as long as the chemical potential between them, i.e. the tendency to change the number of a molecule within a local region, remains in equilibrium [123]. As a result, adding more molecules to the dilute phase will be compensated by diffusion into the dense phase to re-establish equal chemical potentials. Which material state the dense phase assumes is dependent on interaction parameters between molecules. A liquid state is favoured by long-ranged multivalent interactions with weak to moderate binding energy [123]. Indeed many proteins were shown to form liquid droplets *in vitro*, which can be promoted by further increasing their valency [129]. It has further been proposed that the range of interactions can be enhanced by structural flexibility of the protein, e.g. through disordered regions [123]. Accordingly membraneless organelles are typically enriched with multivalent and disordered proteins [125], [130].

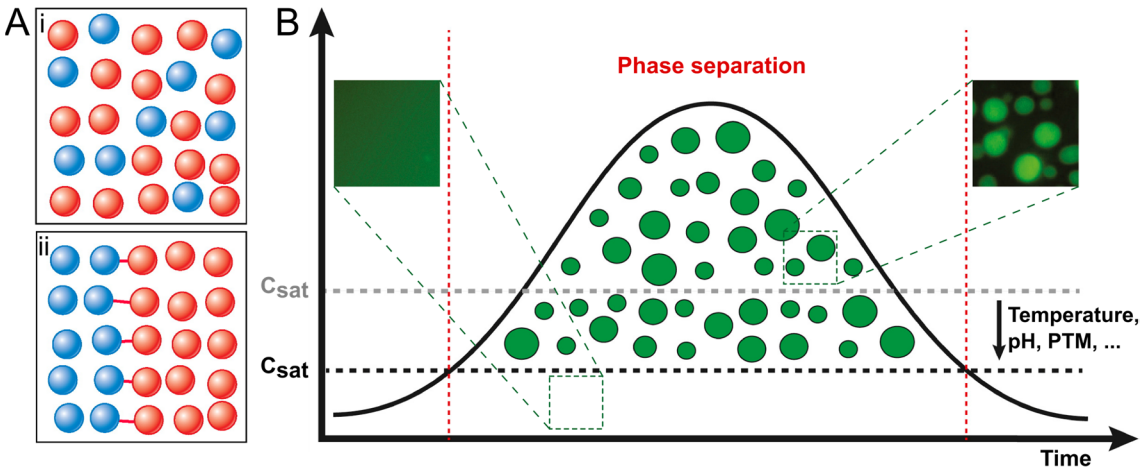


Figure 5 Principles of liquid-liquid phase separation. (A) Examples of two solutions with different molecules (blue and red) in an entropically driven mixed state (i), and a demixed state (ii) driven by the minimization of disfavoured bonds (red lines). Modified from Hyman (2014) [123]. **(B)** A protein (here FUS) above a critical concentration threshold c_{sat} condensates into liquid droplets, the dense phase, with a surrounding dilute phase. The process is reversible and dropping below c_{sat} dissolves the droplets. The c_{sat} is not static and depends on a variety of external and protein internal parameters. Modified from Alberti (2017) [131].

Importantly, assembly and disassembly of protein droplets via LLPS is critically dependent on concentration (Fig. 5B) [131]. As such, the dense phase will arise once the concentration of a protein has saturated a given solvent and exceeded its solubility threshold, the critical concentration or saturation concentration (c_{sat}) [128], [131]. This critical concentration is dependent on a number of environmental factors (including temperature, pH, presence of small molecules, molecular crowding, etc.), but also protein intrinsic factors such as conformational changes or post-translational modifications (PTMs) [131]. To control the assembly of condensates, cells can theoretically either modulate the protein concentration, the protein's solubility, it's affinity to interaction partners, or its valency [131]. For example, LLPs of many RNA-binding proteins, such as FUS (fused in sarcoma), is strongly promoted by RNA, who's linear sequence likely provides multivalent binding [132], [133]. Furthermore, the cell can theoretically employ nucleation sites, which locally decrease the c_{sat} or enrich proteins at a specific site, which can also help determine the number and localization of condensates [123], [131].

It has been proposed that condensates could fulfil various aspects of compartmentalization. They can create an environment which enriches certain molecules (enzymes, substrates) to, for example, optimize reaction kinetics while excluding others (e.g. proteases) according to their respective solubility. For example, the disordered FG-repeats within the inner cavity of nuclear pore complexes have been interpreted as a selective phase barrier, in which nuclear import factors can "dissolve" [125]. Due to the constant concentration ratio between dense and dilute phase, they could also act as buffers against fluctuations of sensitive cellular concentrations [128].

In this paradigm membraneless organelles are often thought of as complex coacervates consisting of tens to hundreds of components [128]. One model describes them as an assembly of phase separating, multivalent "scaffolds" that are essential for condensate formation and subsequently recruit dynamic "clients" [124], [128]. These scaffolds often

consist of binding domains (“stickers”) interspersed with flexible linkers (“spacers”) [133], [134]. While liquids, as opposed to solids, have no shape memory and thus lack elasticity, they tend to assume a spherical shape. This is the result of surface tension wherein a sphere offers the minimal surface area for a given volume [62], [63]. This is reflected in the often rounded shape of membraneless organelles. Studies on several membraneless organelles furthermore reported that they appeared to have a complex, multilayered internal organisation consisting of multiple phases. Examples include a solid core within stress granules surrounded by a dynamic layer, or an additional internal liquid phase within the already supposedly liquid nucleolus [133], [135], [136]. Condensates can also transition from a liquid to solid and intermediate states over time, referred to as maturation, aging, or hardening. Many disordered proteins such as FUS or α-Synuclein can mature from a liquid into a more viscous gel-like state and even form amyloid fibres, with a proposed involvement in neurodegenerative diseases like Amyotrophic Lateral Sclerosis (ALS) or Parkinson’s [128], [137]–[139]. While aggregation into fibrils is likely promoted by the high local concentration, gel-like states are thought to arise as a result of saturated binding surfaces (“valency exhaustion”) leading to a kinetically trapped, “vitrified” systems [62], [128], [134].

These concepts are exemplified by the centrosome. In 2017, Woodruff *et al.* declared the centrosome to be a “selective condensate” based on their observation that a select number of recombinant centrosomal proteins could form liquid droplets that accumulated and nucleated tubulin [140]. SPD-5, a *C. elegans* PCM protein, herein acted as the phase separating scaffold that self-assembled into droplets which recruited other client factors such as polo-like kinase 1. Interestingly, while initially liquid, these droplets hardened over time and became less dynamic. The authors later proposed that this behaviour could settle the longstanding conflict between centrosomes displaying both characteristics of liquids and solids [62]. According to their model the PCM forms as a liquid nucleated by the centrioles in an autocatalytic fashion, explaining its spherical shape [141]. However, a purely liquid state was contradicted by the lack of internal rearrangement during metaphase, PCMs persisting during extraction and dilution, as well as the resistance it needs to provide against forces exerted by the mitotic spindle [62]. Within their model, these contrary states were reconciled by proposing a maturation of the initially liquid PCM into a “kinetically arrested condensate” with cell cycle progression, akin to the hardening observed *in vitro*.

While LLPS has never been studied in *Plasmodium*, the emerging concept of the centrosome as a liquid condensate is particularly interesting in light of the amorphous and protein-dense structure of the centriolar plaque.

1.7 Thesis Aims

The centriolar plaque is a key player in the unusual division of the malaria parasite. However, despite recent advancements, the organisation underlying its highly atypical structure as well as its composition remain mostly unknown. Prior to this work, PfCen3, as a member of a family of highly conserved centrosomal proteins, was one of the very few known components and the only known element of the CP's outer core. I therefore aimed to study centrins as a gateway to a better understanding of the CP's biology. A central lead was the documented interaction of *Plasmodium* centrins with each other. This suggests a collective localization at the CP and could imply a role of the well documented Ca^{2+}-dependent self-assembly in recruitment.

On this foundation I pursued the following aims within this thesis:

1.) Determine the yet unknown localization of PfCen1, PfCen2, and PfCen4. Thereby I hope to determine whether these centrins could be involved in other non-centrosomal processes explaining their non-redundancy. Knowledge of their localization would further help clarify whether the documented interactions could occur in a centrosomal context.

2.) Study the precise localization and dynamics of centrins within the CP via super resolution microscopy. This serves to elucidate the organisation of the CP throughout the nuclear cycle in more detail and determine the existence of potential sub-compartments as well as morphological transitions of the outer core.

3.) Study the homotypic and heterotypic assembly mechanisms of recombinant centrins. Investigating the structural biochemistry underlying their interactions *in vitro* can provide context to their reported *in vivo* interactions. It could furthermore clarify functional differences between them to help explain why *Plasmodium* species encode four separate centrins.

4.) Evaluate my findings in the context of LLPS *in vitro* and *in vivo*. The phase separation paradigm could offer an intriguing perspective on the CP's structure. The biochemistry of centrins as well as their mode of localization to the CP and their dynamics within could provide insights into its applicability.

2 Results

[The results of this work have been partially published (Voß et al. 2023 [79]) and elements of figures that were adapted from this publication are indicated in the respective figure description. Data generated in collaboration with others is likewise indicated, with their contributions being additionally highlighted and contextualized at the end of each relevant sub-chapter.]

2.1 PfCen1-4 localization and dynamics

Centrins are canonical centrosomal proteins across a broad range of eukaryotic organism. However, in several eukaryotes encoding multiple centrins, other localizations, like the apical annuli and nuclear periphery in *Toxoplasma gondii*, have been described as well [105]. Furthermore, the localization of centrins within the diverse eukaryotic centrosomal structures varies drastically. *Plasmodium* species encode four centrins and while PfCen3 [70] and PbCen4 [122] have previously been described to localize to the CP, the localization of PfCen1, PfCen2, and PfCen4 were inconclusive. As a first step towards understanding *Plasmodium* centrin biology, I therefore aimed to determine the precise localization of PfCen1-4 and study their dynamics in asexual stages.

2.1.1 PfCen1-4-GFP localize to the CP's outer core during schizogony

A previous study that aimed to localize PfCen1-4 employed an immuno-staining using antibodies raised individually against the four proteins [70]. The caveat of this approach is the potential unspecificity of antibodies, both regarding other proteins, but especially between the four centrins themselves, which share a high degree of sequence similarity outside of their short N-terminus (Fig. S4). Furthermore, antibodies do not allow for the study of protein dynamics within living cells. To be able to unambiguously differentiate between the four centrins and study their dynamics *in vivo*, Nicolas Lichti, under my supervision, generated *P. falciparum* NF54 lines episomally expressing GFP tagged versions of PfCen1-4 (PF3D7_0107000, PF3D7_1446600, PF3D7_1027700, PF3D7_1105500) from the pARL expression vector. Endogenous tagging with GFP had previously been successfully employed by a study for PbCen4, which also showed that the centrin 1-3 genes were highly refractory [122]. This is consistent with my own unsuccessful attempts of C-terminal tagging for the endogenous PfCen1-4 loci using the selection-linked integration (SLI) system [142]. I therefore instead chose an episomal expression system over endogenous tagging. Of note, GFP signal in these generated cell lines was often quite weak and only present in a subset of cells, which further decreased over time, despite continued selection drug pressure. This indicates that even episomal expression of tagged centrins infers a fitness cost to parasites.

During the initial phases of asexual replication, the ring and trophozoite stage, PfCen1-4-GFP appeared evenly dispersed throughout the cell without discernible site-specific accumulations. As shown using the example of PfCen1-GFP during live-cell imaging,

part of the signal then began to coalesce into a single focus during transition into the schizont stage (Fig. 6A). This focus later duplicated, while the dispersed cellular signal remained. A separate study using these strains as well as immunostainings of WT parasites performed by Dr. Caroline Simon confirmed the formation of the first focus shortly before the onset of schizogony as marked by the collapse of the nuclear hemispindle [52]. Using immune-fluorescence assays (IFAs) I observed PfCen1-4-GFP foci exclusively in cells undergoing nuclear division (indicated by the presence of nuclear microtubules), which were absent in later segmenters, suggesting that they are formed for schizogony and dissolved again before egress (also see 2.3.2). Immuno-fluorescence staining against GFP demonstrated that these foci are located at the centrosomes as marked by the poles of intranuclear hemi- and mitotic spindles, showing that PfCen1-4-GFP can all localize to the CP (Fig. 6B). Other rare and inconsistent foci localizations (Fig. 6B, arrows) were likely overexpression artifacts as further discussed in 2.3.2. Centrin signals did not overlap with spindle origins or the DNA-free region that mark the inner core of the CP, instead suggesting a localization within the outer core.

To further investigate if the centrins inhabit distinct subregions or form specific sub-diffraction structures within this part of the CP, which only appear as a round focus using conventional confocal microscopy (~200 nm resolution), I performed STED microscopy. The additional resolution (~40 nm) revealed a variety of centrin shapes that ranged from round to elongated, sometimes consisting of multiple sub-foci (Fig. 6B). Importantly, these shapes differed not only between PfCen1-4, but also between each individual centrosome with no clear consistency or pattern. This raised the hypothesis that centrin localization within the outer CP core is in constant flux.

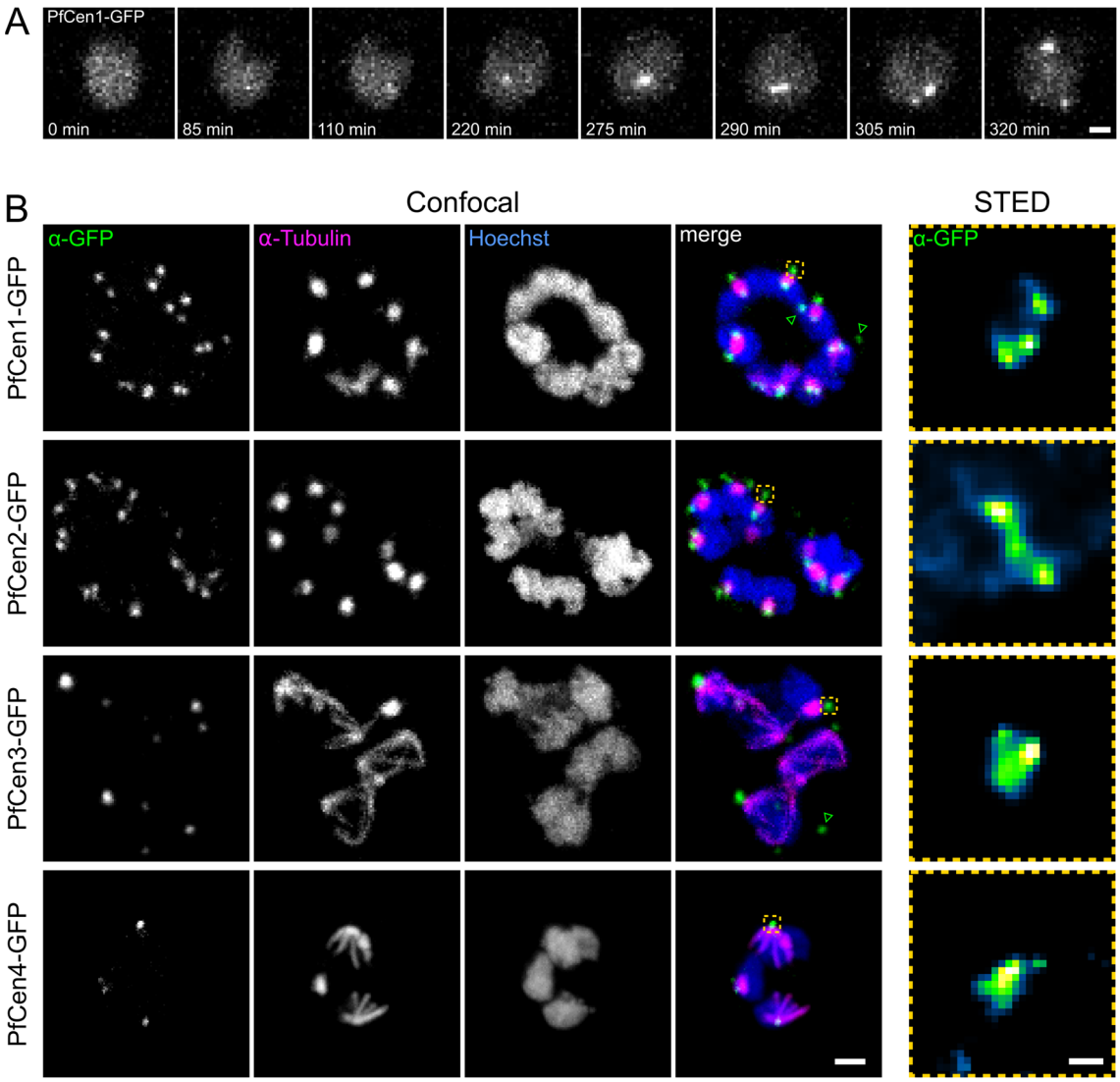


Figure 6 Localization of PfCen1-4. (A) Select timepoints from confocal live-cell imaging of an NF54_pARL-PfCen1 cell at the onset of schizogony showing assembly of PfCen1-GFP (grey) into a focus and subsequent duplication. Scalebar 1 µm. **(B)** Representative IFAs of NF54 Schizonts expressing the indicated centrin with a GFP tag from a pARL vector. Individual confocal channels of GFP (green), tubulin (magenta), and DNA staining (hoechst, blue), as well as a merge, are shown on the left. Green arrows indicate non-CP foci. Images are maximum intensity Z-projections. Cytoplasmic α-GFP signal trimmed for clarity. Deconvolved STED microscopy images of select α-GFP foci marked by a dashed yellow square are shown on the right. Scalebar confocal 1 µm, STED 100 nm. (B) Modified from Voß *et al.* (2023) [79]. Strains generated by Nicolas Lichti (under my supervision) and Dr.Caroline Simon.

In conclusion, PfCen1-4 partially accumulate from a disperse cytoplasmic signal into foci in the outer CP at the onset of schizogony, which dissolve again before segmentation. Within the outer CP special organization of centrins is highly variable and potentially dynamic.

[pARL_PfCen3-GFP was kindly provided by the lab of Dr. Tim Gillberger, located at the BNITM, Hamburg. The parasite strain was generated by Dr. Caroline Simon. pARL_PfCen1-2-4-GFP and respective strains were generated by Nicolas Lichti during his Bachelor Thesis in 2019 under my supervision.]

2.1.2 PfCen1 undergoes dynamic rearrangement at the centriolar plaque

While inconsistent sub-diffraction localization patterns within fixed cells can be explained by dynamic rearrangement, adequate testing of this hypothesis requires super resolution live-cell microscopy. Towards this end I established live STED in *P. falciparum*. As STED microscopy employs high laser intensities, classical protein fluorophore tags are not photostable enough, instead requiring labelling with synthetic fluorophores. This was achieved for live cells by tagging PfCen1 with Halo, a self-labelling enzyme of 35 kDa that can covalently bind synthetic ligands, such as cell permeable STED-capable dyes, via a chloroalkane linker (Fig. 7A) [143]. I chose PfCen1 since PfCen1-GFP had shown the best expression properties out of the four NF54_pARL-Cen1-4-GFP strains, reasoning that this might also be true for a different tag. An NF54 line expressing PfCen1-Halo (with a 14 AA linker) from a pARL vector was generated by Johanna Bauer. For fluorescent labelling I employed ligand called MaP-SiR-Halo, consisting of chloroalkane linker coupled to a silicone-rhodamine (SiR) based dye [144]. Rhodamine exists in an equilibrium between a cell-permeable spirocyclic and a fluorescent zwitterion form. Binding to its target, in this case Halo via a synthetic chloroalkane ligand, stabilizes the zwitterion making the dyes fluorogenic (Fig. 7A) [144]. This fluorogenic property drastically reduces background fluorescence so imaging can be performed in the presence of the dye in the medium. This eliminates the need for an additional washing step and allows for continued labelling of newly expressed PfCen1-Halo. I used SPY505-DNA, a live-cell DNA dy,e to determine the relative position of centrin to the nucleus throughout imaging. Labelling of PfCen1-Halo was successful and showed the same localization to the CP as PfCen1-GFP, evidenced by the centrin signal being consistently located next to the DNA-free region (Fig. 7B).

Acquiring live-cell STED movies in 1-30 s intervals followed by deconvolution showed a rapid rearrangement of PfCen1-Halo within the CP (Fig. 7C). Across 21 evaluable foci this was predominantly expressed as a round shape “wobbling” or an elongated signal seemingly contracting and expanding along an axis tangential to the nucleus. These are respectively expressed in a consistent aspect ratio of ~1 or as an oscillating aspect ratio (Fig. 7D). Due to the lack of a live-cell compatible equivalent of an NHS-ester staining of the protein outer CP core, the relative localization and movement within the CP could not be assessed precisely. However, based on the DNA signal, the relative position of PfCen1-Halo to the nucleus stayed constant, at least during the observed timeframes. Imaging was typically limited to 5-10 timepoints before the signal was bleached, or the centrosome/nucleus had drifted out of frame. Nonetheless, even over these short periods it became clear that PfCen1 is not integrated into a static structure at the centrosome and instead rearranges in a fluid-like manner.

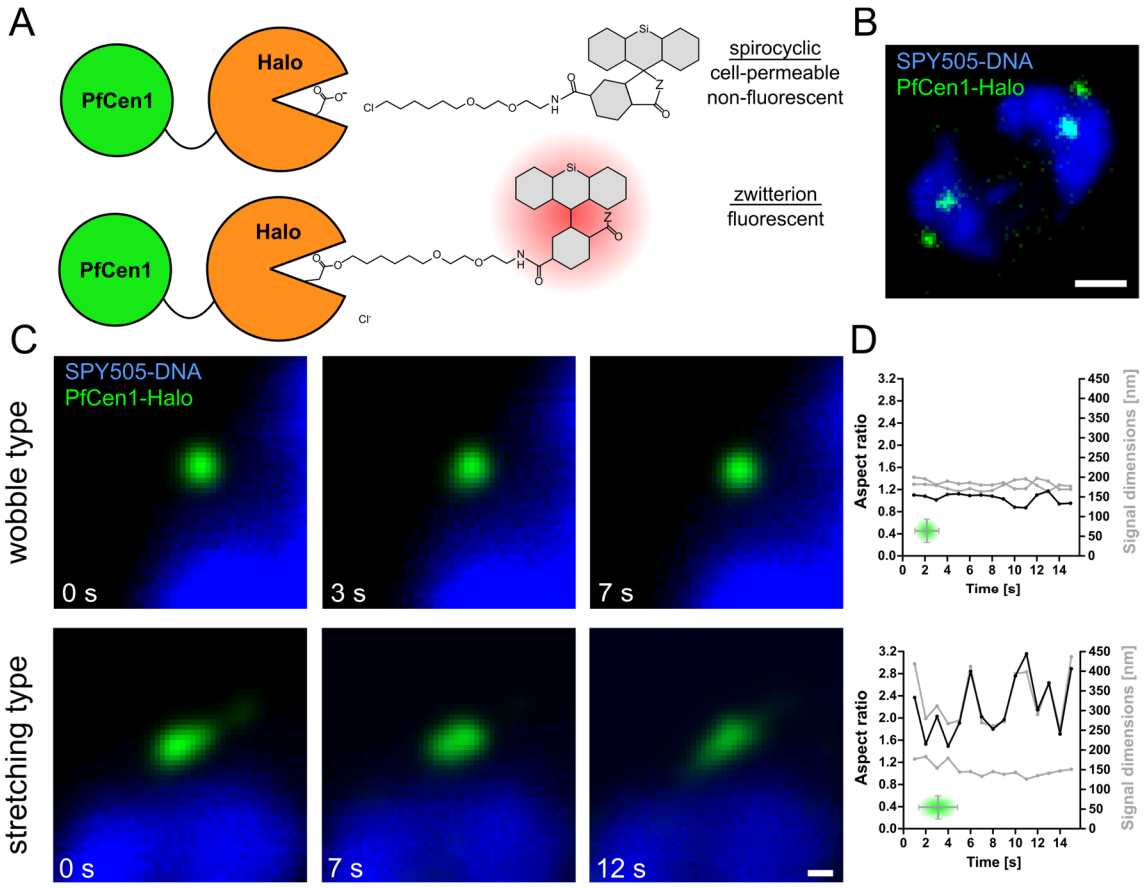


Figure 7 Centrosomal PfCen1-Halo dynamics. (A) Illustration of the autocatalytic labelling of the Halo tag with a silicone rhodamine dye in its spirocyclic and zwitterion form. **(B)** Representative confocal image live-cell image of an NF54 Schizonts expressing PfCen1-Halo from a pARL vector stained with SPY505-DNA (blue) and MaP-SiR-Halo (green). Image is a maximum intensity Z-projections. Scalebar 1 um. **(C)** STED time-lapse imaging of a PfCen1-Halo focus at the CP labelled with Map-SiR-Halo (green, deconvolved, bleach corrected) and DNA labelled with SPY505-DNA (blue) in NF54_pARL_PfCen1-Halo parasites. Representative images of the observed stretching and wobbling shape are shown. Images acquired in 1 s intervals. Scalebar 100 nm. **(D)** Width, height (grey lines, right axis) and resulting aspect ratio (black line, left axis) of shapes shown in (C) over time. Graphic in bottom left illustrates the aspect ratio concept. (C-D) modified from Voß *et al.* (2023) [79]. Strain generated by Johanna Bauer. Analysis in (D) performed by Dr. Julien Guizetti.

[Johanna Bauer cloned pARL_PfCen1-Halo and generated the respective NF54 strain during her Bachelor thesis in 2020 under the supervision of Dr. Caroline Simon. MaP-SiR-Halo was kindly provided by Dr. Nicolas Lardon from the lab of Dr. Kai Johnson located at the MPI for medical research, Heidelberg. Aspect ratio measurements of PfCen1-Halo foci were performed by Dr. Julien Guizetti.]

2.1.3 Duplication of centrin foci is microtubule independent

Live-cell imaging shows that PfCen1-GFP foci are duplicated and subsequently segregated alongside the CP to form the opposing spindle poles of the mitotic spindle (Fig. 2A, 6A). While it remains unclear whether CPs duplicate through fission or *de novo* assembly, the segregation requires an internal or external force. In mammals and yeast this force is generated by motor proteins along microtubules [145]–[148]. While no microtubules have been detected in the outer CP core, it is plausible that the separation

force is generated through the interaction of the spindles originating from the inner cores of the duplicated daughter CPs during transition from a monopolar to a bipolar spindle (Fig. 2A). To test whether separation of duplicated centrin foci is driven indirectly by the forming mitotic spindles I observed their dynamics through live-cell imaging in the presence of the microtubule polymerization inhibitor Oryzalin.

The drug's capacity to prevent microtubule formation in *P. falciparum* at 20 µM has been documented [149], which I confirmed independently via immuno-staining of treated cells NF54 WT cells against tubulin (data not shown). In the 3D7_DiCre cell line I employed in this assay PfCen1-GFP was expressed from an inducible expression vector pFIO_hsp70p_Cen1-GFP I developed, which will be introduced in detail in chapter 2.3.1. I chose this strain over NF54_pARL_PfCen1-GFP due to its superior expression qualities. I used the DNA marker 5-SiR-Hoechst to follow nuclear division. To confirm absence of spindles, I labelled the microtubules with SPY555-Tubulin. While readily detectable in the DMSO control, no spindles were present within the Oryzalin treated cells over the course of live-cell imaging (Fig 8A). Despite the lack of microtubules, I observed duplication and separation of DNA-adjacent PfCen1-GFP foci (Fig. 8A, arrows). Although I was not able to assess whether these foci represent fully intact CP, the results demonstrate that their separation is not fundamentally dependent on external forces generated by the spindles. There were, however, severe defects in nuclear division as evidenced by the presence of a large, amorphous DNA signal, probably representing a single large nucleus. This was likely a result of nuclear fission being unsuccessful in the absence of an anaphase spindle. This further resulted in nuclei with more than 2 centrin foci, suggesting that successful nuclear fission is not controlled for during the regulation of CP duplication.

This continued progression through schizogony in spite of major perturbations was interesting. In many other eukaryotes mitosis is strictly controlled through a series of checkpoints capable of inducing a cell cycle arrest if a problem arises that could lead to erroneous cell division. One prominent example is the spindle assembly checkpoint, which prevents chromosome segregation until all kinetochores are attached to a mitotic spindle [150]. To assess whether the absence of spindles or the resulting down-stream defects in nuclear division triggered a cell cycle arrest in the parasite, I compared the increase in DNA levels over one erythrocytic cycle of Oryzalin treated cells to a DMSO control. I generated a tightly synchronized (± 1 h) culture of 3D7_DiCre_pFIO_hsp70p_PfCen1-GFP, which I subjected to DMSO or Oryzalin treatment from the ring stage onward (14 hpi), long before the first microtubules are formed. I then assessed cellular DNA content of the parasites every 4 h using a previously established flow cytometry based assay, which employs the dye SYBR Green after elimination of RNA through RNase treatment to remove background signal [51]. I first detected an increase of DNA levels in the control around 30 hpi (Fig. 8B), which is in line with previously reported timings of DNA replication onset [32], [51]. Average DNA content then peaked at 42 hpi after which it decreased again due to egress and reinvasion of daughter cells, as evidenced by the simultaneous increase in parasitemia. The oryzalin treated cells' DNA levels increased at a similar rate, albeit with a small delay of

approximately 2 h, demonstrating that the parasite does not induce a complete cell cycle arrest in response to the absence of microtubules. The parasitemia also remained constant, showing that the parasites failed to distribute their DNA into daughter merozoites, a process also heavily reliant on microtubules [32].

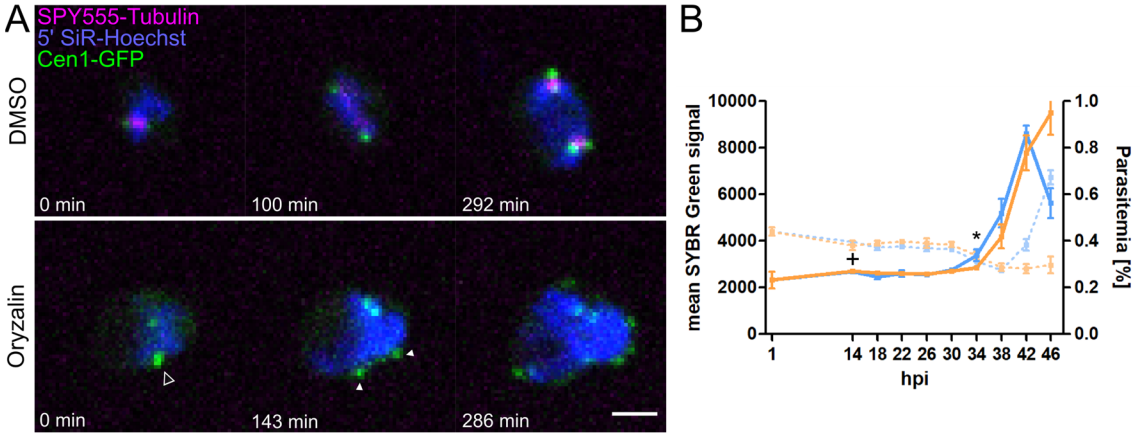


Figure 8 Influence of microtubule disruption on schizogony. (A) Live-cell imaging of induced 3D7-DiCre_pFIO_hsp70p_PfCen1-GFP schizonts treated with 20 µM Oryzalin or 0.02% DMSO as a control. Tubulin was stained with SPY555-Tubulin (deconvolved) and DNA with 5'Sir-Hoechst. Arrows indicate separation of a PfCen1-GFP focus (black, large) into two daughter foci (white, small). Maximum intensity Z-projections; Scalebar 2 µm. **(B)** Mean DNA signal (solid line) and parasitemia (dashed line) of tightly synchronized parasite populations treated with 20 µM Oryzalin or 0.02% DMSO at 14 hpi (+) as measured via flow cytometry using SYBR Green as a DNA marker. *, P=0.025; Two-tailed t-test. Error bars indicate standard deviation of technical replicates, n=3, 1000 iRBCs each.

Together these results show that *Plasmodium* does not require microtubules for the duplication and separation of PfCen1-GFP foci in the outer CP. Continued duplication as well as DNA replication further suggest that the regulation of these processes is independent of spindle formation, kinetochore attachment, or nuclear division. This further suggests the absence of relevant cell cycle checkpoints monitoring the successful completion of these events.

2.2 Characterizing centrin assembly and the role of structural elements

Centrins are structural proteins that can bind Ca^{2+} ions through their EFh domains. The resulting conformational changes have been described to mediate reversible self-interaction for a variety of centrins, including HsCen2 [117], [118], [120]. Pulldown studies further suggested an interaction between the four *Plasmodium* centrins *in vivo* [71], [122]. While some biochemical properties of these interactions have been studied, no clear model of the resulting centrin complexes has emerged. Based on the previously discovered liquid-like rearrangement of PfCen1 (Fig. 7C) and the high protein density of its environment within the CP, I hypothesized that centrin interaction could be mediated through LLPS. I therefore analysed if, and under which conditions, their interactions form liquid condensates, and which structural features are involved.

2.2.1 PfCen1 and PfCen3 undergo Ca^{2+}-dependent LLPS *in vitro*

To assess the principal ability of PfCen1-4 to undergo LLPS in a controlled *in vitro* environment I first sought to replicate the self-interaction of HsCen2, which had previously been studied using an absorption photometry based turbidity assay [117]. Towards this end I expressed recombinant PfCen1-4 in *E. coli* and also included HsCen2 as a positive control. A C-terminal 6His-tag was added for purification via Ni-NTA column. For the expression of for PfCen1-6His, PfCen2-6His and HsCen2-6His, I employed the pET-28 expression vector in conjunction with the BL21 (De3) *E. coli* strain with the help of Nicolas Lichti. In this vector a single glycine was included between the centrin and 6His tag as cloning limitations did not allow for a complete removal of any linker (4.1.1). However, PfCen3-6His and PfCen4-6His could not be produced in soluble form using the same system, only as aggregated inclusion bodies. Instead, I expressed them using the pZE13d-C expression vector in conjunction with the W3110-Z1 *E. coli* strain [151].With this system no additional amino acid needed to be included between the centrin and 6His tag. While the proteins still formed inclusion bodies, about 50% remained soluble and could be purified.

To determine the purity of the purified proteins and whether they were expressed in their entirety, I performed SDS-PAGE with Coomassie staining (Fig. S1A). No significant impurities were detected, however PfCen2&4-6His appeared lower on the gel than their predicted molecular weight and potential degradation bands were visible in case of PfCen3-6His and HsCen2-6His. For clarity, mass spectrometry analysis was performed on these native protein solutions by the CFMP core facility at the ZMBH Heidelberg. The results confirmed that molecular the weight of the major peaks corresponded to the respective full-length centrin, with the minor caveat that PfCen1&2-6His and some of PfCen3-6His were missing their N-terminal methionine (which is often cleaved in *E. coli* [152]) (Fig. S1B). The additional band seen with PfCen3-6His is likely the result of a degradation, corresponding to an N-terminal deletion of 14 amino acids. In case of HsCen2-6His, the additional bands correspond to truncated versions of the protein starting at methionine at position 72 and 84, which are likely the result of alternative start codons. While purification of the full-length protein would have been feasible by placing the 6His-tag at the N-terminus, which is absent in the shortened proteins, I decided against this as the high variability in length and sequence of the N-termini between centrins suggested that an N-terminal 6His-tag had a higher likelihood of altering the proteins' behaviour than a tag at the much shorter C-terminus. I therefore proceeded with the purified protein solutions as they were. As protein concentration is a critical factor in LLPS, I measured the concentrations of the purified solutions using two different methods. First, I chose the colorimetric Pierce 660 nm assay as it primarily reacts with histidine, lysin, and arginine, as well as to a lesser extend tryptophane, tyrosine, and phenylalanine, whose ratios are similar across the expressed centrins to ensure comparability. My second approach was measurement of the absorption at 280 nm primarily resulting from tyrosine and tryptophane. With the exception of PfCen1-6His, where 280 nm absorption could not be employed as it any lacks tyrosine and tryptophane, both methods yielded similar concentrations (data not shown).

Tourbez *et al.* [117] observed that a solution of recombinant HsCen2 in 50 mM BisTris (pH 7.1), 20 mM KCl, and a baseline concentration of any divalent cation (1-2 mM) turns turbid (measured as $OD_{450\ nm}$) when heated to 37°C in the presence of Ca^{2+}. They hypothesized that this indicates the centrin forming large polymers. I modified this assay by removing KCl, as monovalent cations are a known inhibitor of LLPS [153], and increasing the Ca^{2+} concentration to fulfil both roles as the baseline divalent cation and EFh domain ligand. Furthermore, as opposed to using the temperature as a variable to trigger turbidity, I kept it constant at 37°C and instead supplemented Ca^{2+} (or other substances) during the measurement to study its effect on the centrins. Unless stated otherwise I used a standardized protein concentration of 30 µM (~600 µg/ml centrin) for consistent comparison between different centrins. Utilizing this assay, I was able to replicate the results of Tourbez *et al.* for HsCen2-6His. A previously clear solution at a standard centrin concentration of 30 µM showed a rapid increase in turbidity, which I quantified by absorption at 450 nm upon addition of $CaCl_2$ (Fig. 9). I observed the same results for PfCen1-6His and PfCen3-6His. PfCen2-6His and PfCen4-6His, on the other hand, had a much weaker reaction, even at higher concentrations. Different from Tourbez *et al*. turbidity of the HsCen2 solution could not be reversed by a decrease in temperature. However, the addition of a 5-fold molar excess of EDTA (relative to $CaCl_2$) to chelate Ca^{2+} ions and act as a competitor to the centrins' EFh domains rapidly reversed turbidity almost completely in case of HsCen2-6His and PfCen1-6His. Turbidity returned if I subsequently added more Ca^{2+} beyond EDTA concentration (data not shown). In case of PfCen2-6His and PfCen3-6His, turbidity was only partially reversible. The buffer alone showed no reaction to either Ca^{2+} or EDTA.

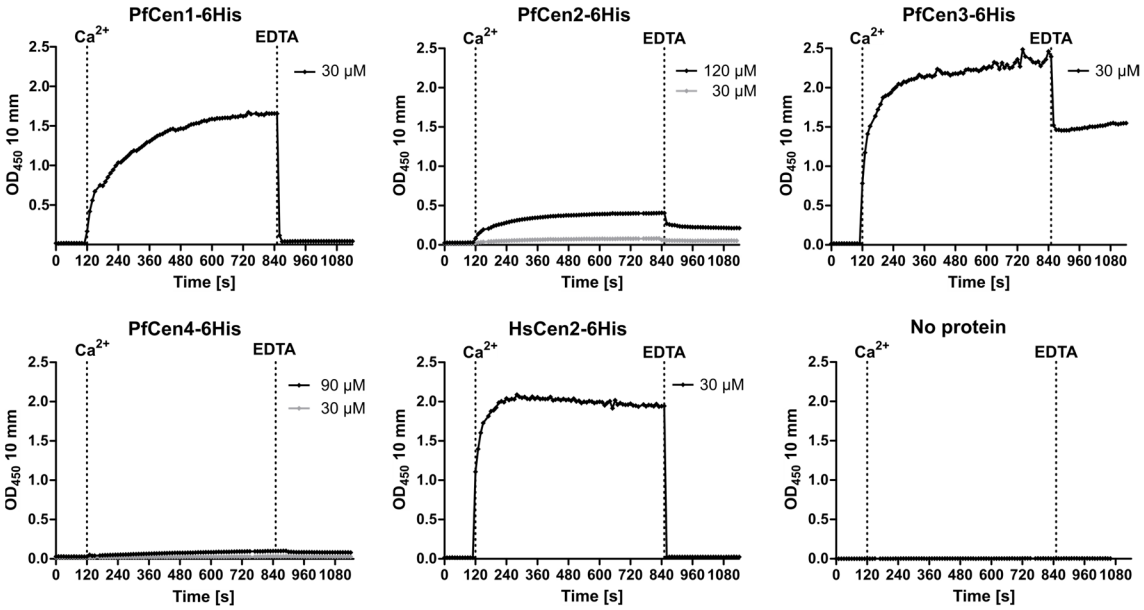


Figure 9 Reaction of recombinant centrins to Ca^{2+}. Turbidity assays of recombinant PfCen1-4-6His and HsCen2-6His at 37°C in 50 mM BisTris (pH 7.1). Buffer control (no protein) shown. Turbidity was quantified as light adsorption at 450 nm. Ca^{2+}, $CaCl_2$ addition to 2 mM; EDTA, EDTA addition to 10 mM. Modified from Voß *et al.* (2023) [79].

I then observed this reaction more directly under the microscope, which revealed for the first time, that the turbidity of HsCen2-6His, PfCen1-6His, and PfCen3-6His stems from the rapid formation of liquid protein droplets through LLPS upon Ca^{2+} addition (Fig.

10A). The liquid state of these droplets was evident through their occasional fusion, as well as the droplets "wetting" on the bottom surface of the well upon settling. I herein employed a higher protein concentration, which leads to the formation of more condensate, to increase droplet density and facilitate observation of fusion events. However, droplets also formed at the previously used concentration of 30 µM (Fig. 10B). Here I further stained the droplets with the fluorescent dye Atto550-NTA, which interacts with 6His tags, demonstrating that the droplets are indeed composed of recombinant 6His-tagged centrins.

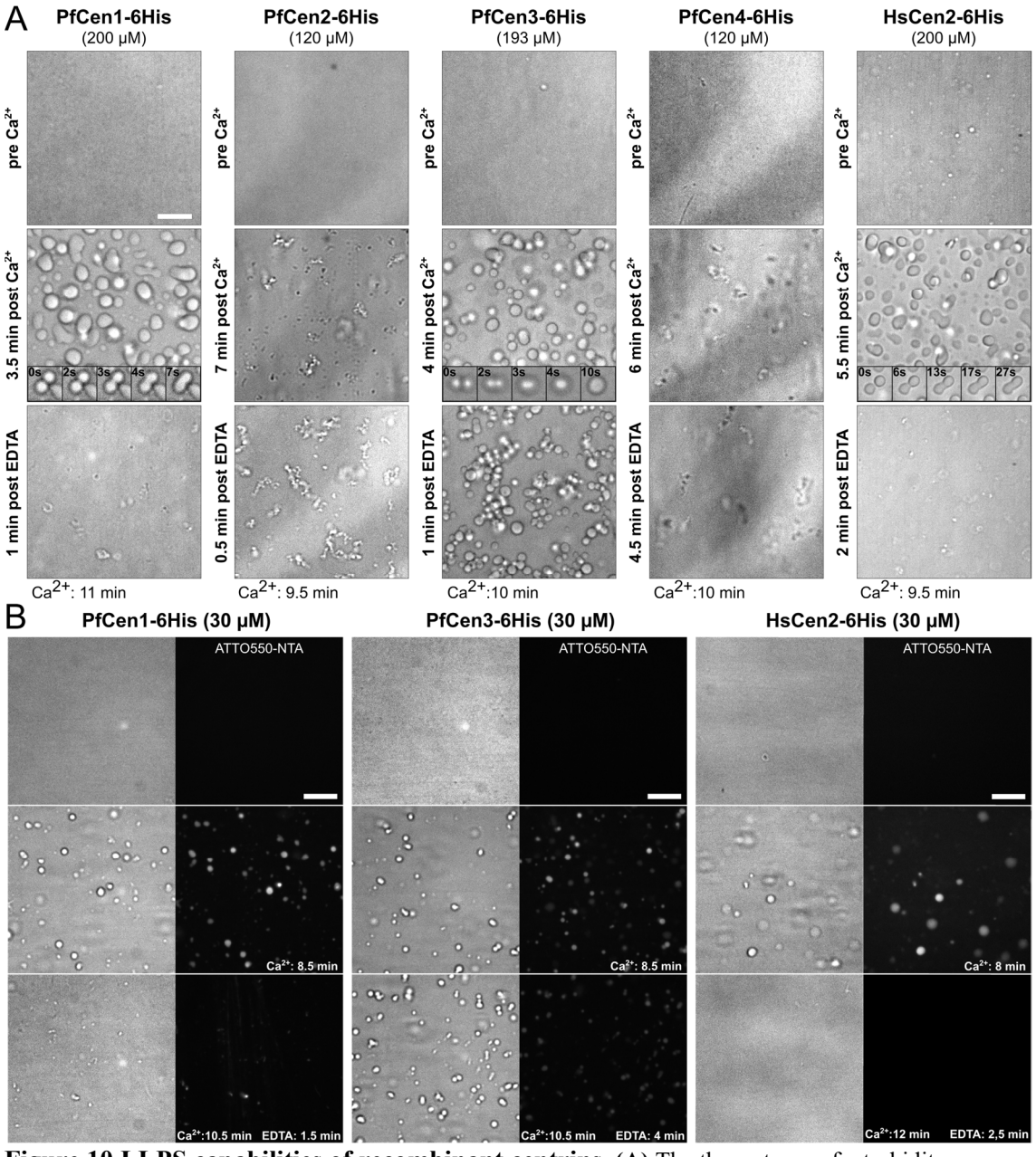


Figure 10 LLPS capabilities of recombinant centrins. (A) The three stages of a turbidity assay as in Fig. 9 observed by bright-field microscopy. Inlays show droplet fusion events where observed. Approximate elapsed time after Ca^{2+} and EDTA addition is indicated. Higher protein concentrations were used to increase droplet density. Scalebars 10 µm**. (B)** Performed as in (A) but proteins at 30 µM were additionally labelled fluorescently using 300 nM NTA-ATTO-550 for confocal imaging of the droplets. Scalebars 10 µm. Modified from Voß *et al.* (2023) [79].

PfCen2-6His meanwhile showed no droplets, but instead displayed elongated structures of different sizes and shapes. These were irreversible after EDTA addition and thus considered likely aggregates. In contrast HsCen2-6His and PfCen1-6His droplets disappeared completely and merely left behind minor aggregates. Interestingly, a fraction of PfCen3 droplets remained after EDTA addition and retained their shape but were no longer liquid as evidenced by their close proximity without undergoing fusion and lack of surface wetting. Their presence explains the partial turbidity remaining after Ca^{2+} depletion (Fig. 9). This is reminiscent of the phenomenon of maturation, describing the potential of some liquid condensates to harden into highly viscous gel-like or solid states over time [139], [153]. My further investigations revealed that condensation is initially reversible, with an irreversible fraction first arising between 2 and 7 min post Ca^{2+} addition (Fig. 11A). PfCen1-6His turbidity on the other hand, remained fully EDTA-reversible even 3 h after Ca^{2+} addition.

LLPS occurs only once a protein solution reaches a critical concentration, or c_{sat}, which depends on a combination of various parameters like temperature, pH, the presence/absence of certain compounds, or conformation of the protein itself (Fig. 5B). In the case of PfCen1 and PfCen3, addition of Ca^{2+} triggering LLPS indicates that its presence alters the previously higher c_{sat} of the centrins below the given concentration, likely by binding to the EFh domains. However, even in the presence of Ca^{2+} a critical concentration threshold remains, which I determined through testing of the response of various centrin concentrations to Ca^{2+}. This threshold appears to lie between 10 and 15 µM for both PfCen1-6His and PfCen3-6His under my experimental parameters, as no LLPS could be triggered for either at 10 µM anymore for either (Fig. 11B). In general, LLPS is favoured through molecular crowding, such as within the protein-dense cytoplasm. This is also the case for PfCen3-6His, where the addition of 8% polyethylene glycol (PEG), a commonly used crowding agent [154], decreased the c_{sat} threshold below 10 µM (Fig. 11B). As a result, turbidity, i.e. condensates, was also increased compared to the same centrin concentrations without PEG

The favourable effect of Ca^{2+} on centrin LLPS can be explained by the specific interaction with the EFh domains inducing conformational changes that promote centrin interactions [85], [117]. To test whether Ca^{2+} triggers centrin LLPS through either specific interactions or an unspecific effect I performed another set of turbidity assays using Mg^{2+} as an alternative divalent cation. EFh domains generally have a strong selectivity for Ca^{2+} over Mg^{2+}, and therefore the latter would not be expected to specifically bind to centrin in a comparable capacity [84]. Indeed, under the same conditions PfCen1-6His showed almost no turbidity in response to Mg^{2+}, while PfCen3-6His and HsCen2-6His only showed a mild reaction (Fig. 11C). In these cases, the reaction to the subsequent Ca^{+2} addition was much stronger. PfCen4-6His continued to show no reaction to either cation. Meanwhile, PfCen2-6His had a similarly strong reaction to Mg^{2+} as to Ca^{2+}, indicating that the previously observed aggregation is unspecific. I furthermore generated a mutant of PfCen1 with inactive EFh-domains. Mutation of an aspartate, present at position 1 of all functional EFh domains, to alanine is known to render them incapable of binding Ca^{2+} without obvious changes in protein conformation [155], [156]. Towards this end, I

introduced this mutation into all four EFh domains of PfCen1 (positions 37, 73, 110, and 146), as it is unknown which are active in the WT protein. Circular dichroism (CD) spectroscopy showed no evidence of an impact of these mutations on the conformation of the protein (Fig. S2). As opposed to the WT the mutant, dubbed EFh-dead-PfCen1-6His, indeed showed no LLPS in response to Ca^{2+} (Fig. 11D). This result further supports that Ca^{2+} triggering LLPS in PfCen1 involves binding to one or more of its EFh domains.

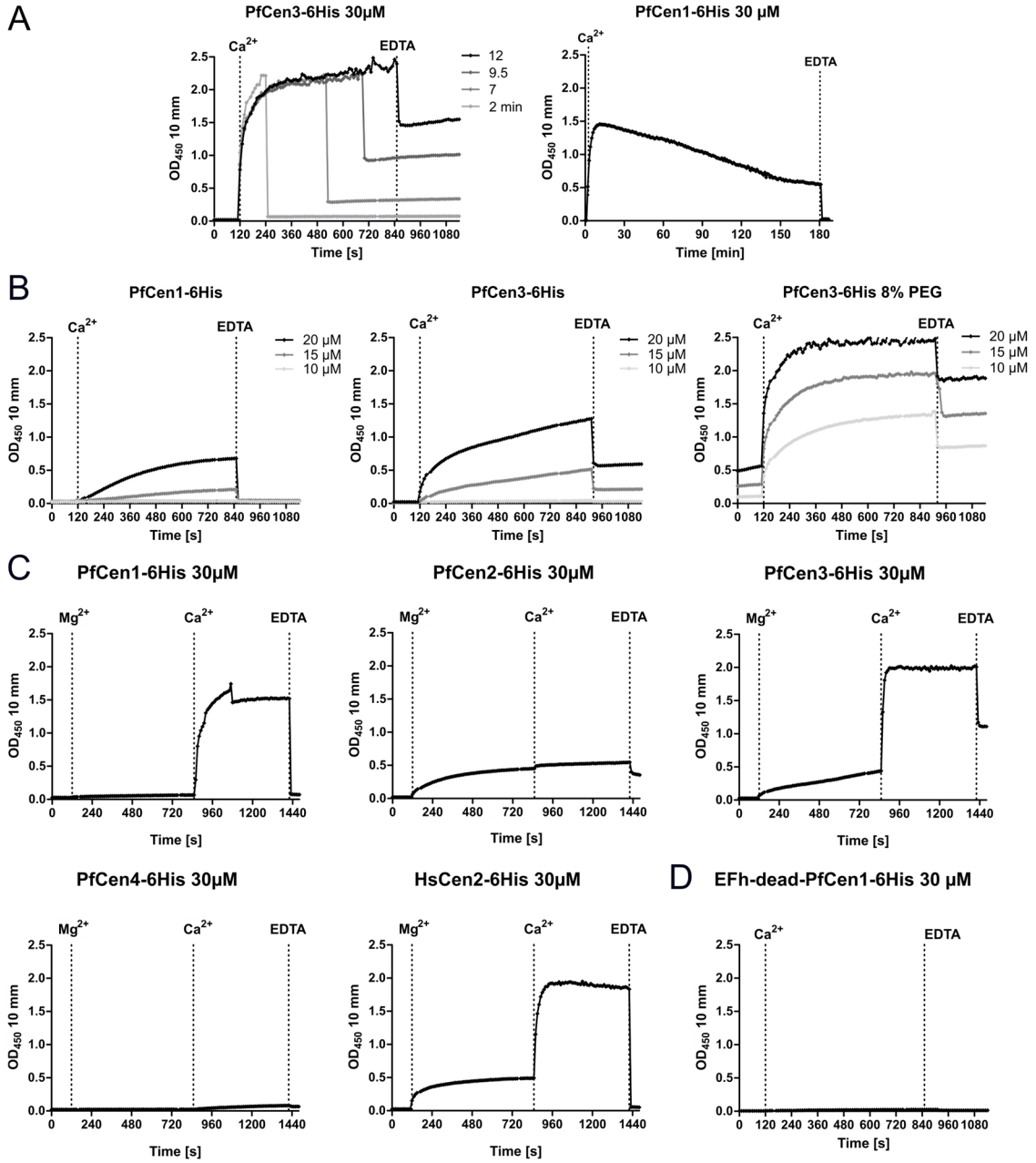


Figure 11 Properties of centrin LLPS. (A-D) Turbidity assays of recombinant centrins at indicated concentrations at 37°C in 50 mM BisTris (pH 7.1). Turbidity was quantified as light adsorption at 450 nm. Ca^{2+}, $CaCl_2$ addition to 2 mM; Mg^{2+}, $MgCl_2$ addition to 2 mM, EDTA, EDTA addition to 10 mM. **(A)** EDTA-reversibility of PfCen3-6His at different timepoints after Ca^{2+} addition and PfCen1-6His after 3 h. Decrease in turbidity over time in case of PfCen1-6His likely stems from droplets settling to the bottom of the test volume below the light beam. (**B)** Measurements of PfCen1-6His and PfCen3-6His turbidity at different protein concentrations with or without 8% (w/v) PEG to determine the critical concentration/c_{sat} for LLPS under the experimental parameters. **(C)** Sequential addition of Mg^{2+} and Ca^{2+} to PfCen1-4-6His and HsCen2-6His to determine the reactions' specificity for Ca^{2+} compared to other divalent cations. **D.)** Turbidity assay of non-Ca^{2+}-binding mutant EFh-dead-PfCen1-6His. Scalebars 10 µm**.** Modified from Voß *et al.* (2023) [79].

In all these experiments I employed 6His-tagged proteins due to the ease and reliability with which they can be purified. However, to rule out a potential effect of even this small C-terminal 6 AA tag (7 AA, G + 6His, in case of PfCen1/2-6His and HsCen2-6His, see Table 18) on the centrins' LLPS behaviour, I later implemented a pipeline to produce these proteins without tag. Herein I produced PfCen1-4 with an N-terminal 6His-TEV sequence, which could be cleaved off using the TEV-protease, leaving only an N-terminal glycine. I expressed the proteins using the modified pZE13d-TEV vector with W3110-Z1 *E. coli* line. Analysis via SDS-PAGE and Coomassie-staining showed sufficient purity after TEV-treatment and removal (Fig. S1C), with the protein band sizes being in agreement with those of PfCen1-4-6His. I did not include HsCen2 as a previous study had already demonstrated turbidity for the unaltered protein [117]. These 6His-tag free centrins, for the most part, confirmed the results obtained with their tagged counterparts qualitatively, with slight differences in their kinetics (Fig. S3A). PfCen1 and PfCen3 continued to form liquid droplets, which for the latter matured into a more solid, EDTA-irreversible state (Fig. S3B). PfCen4 also continued to show no reaction. Only PfCen2 displayed fundamentally different behaviour compared to PfCen2-6His as it no longer formed the elongated structures in response to Ca^{2+} even at 300 µM (Fig. S3A). This suggests that these had been an artifact caused by the 6His tag, in line with the previously noted lack of Ca^{2+} specificity. However, the C-terminal 6His-tag did not appear to fundamentally alter LLPS behaviour of centrins.

Taken together, I showed that PfCen1, PfCen3, and HsCen2, but not PfCen2 and PfCen4, can undergo Ca^{2+}-dependent, and specific, LLPS *in vitro*. In addition, PfCen3 droplets appear to mature into a gel-like or solid state over time.

[The PfCen1-6His, PfCen2-6His, and HsCen2-6His expression vectors were cloned by Nicolas Lichti during his Bachelor Thesis in 2019 under my supervision. He additionally helped with the optimization of expression parameters. Mass spectrometry was performed by the CFMP core facility at the ZMBH, Heidelberg. CD Spectroscopy was performed by the Protein Expression and Purification Core Facility at EMBL Heidelberg, which also provided consultation for the design of the N-terminal 6His-TEV tag design.]

2.2.2 Centrin LLPS is an evolutionarily conserved feature

Centrin orthologues are ubiquitous across eukaryotes with LLPS not being exclusive to those of *Plasmodium*, as demonstrated by HsCen2-6His. To further investigate whether the presence of phase separating centrins in these two distant species is representative of a wider evolutionary conservation of this feature, I investigated additional centrins from distinct phylogenetic branches of the *Eukarya*: ScCdc31 from *Saccharomyces cerevisiae*, TbCen2 (aka TbCenA) from *Trypanosoma brucei*, and ScCen from *Chlamydomonas reinhardtii* (Fig. 12).

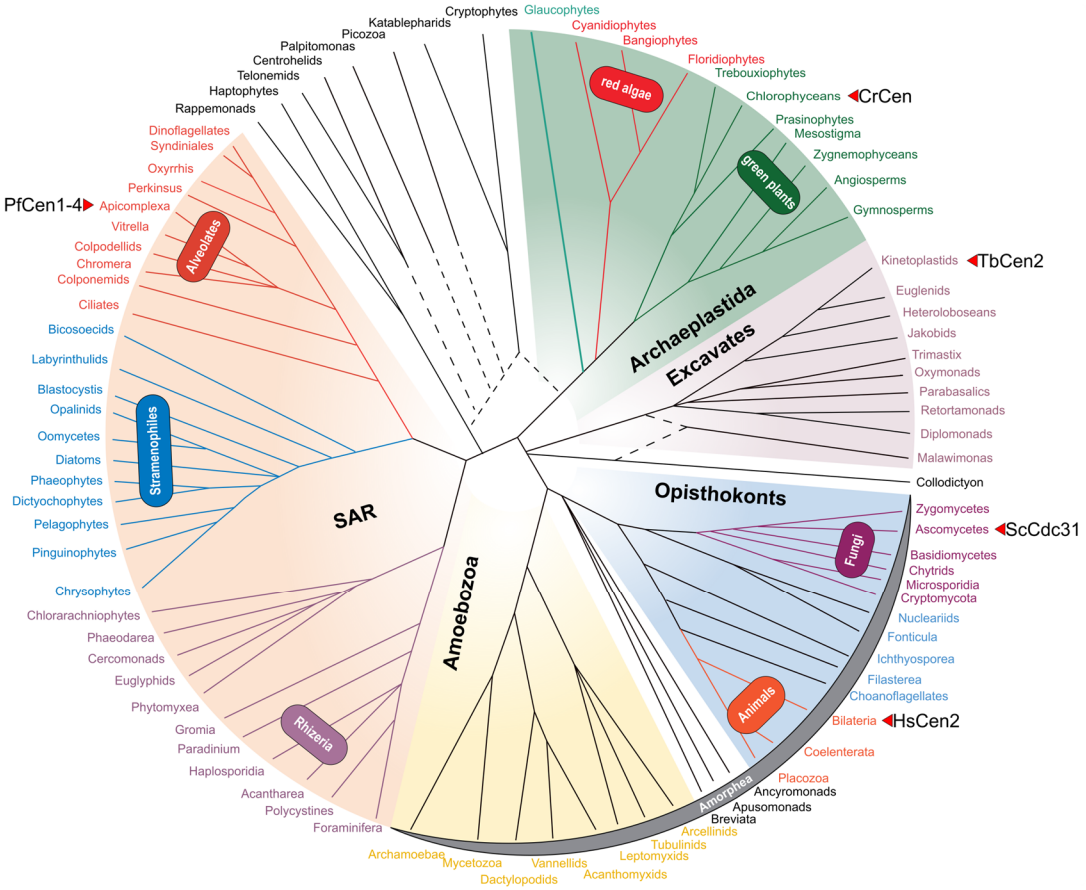


Figure 12 Phylogenetic relation of investigated centrins' origin species. Phylogenetic tree of *Eukarya* illustrating the relation of the species from which *Plasmodium falciparum* centrin 1-4, *Chlamydomonas reinhardtii* centrin, *Trypanosoma brucei* centrin 2, *Saccharomyces cerevisiae* Cdc31, and *Homo sapiens* centrin 2 originate. The position of these respective centrin's origin species is indicated by red arrows. Graphic recreated from Burki (2014) [157].

As, for example, PfCen1-6His before (see 2.2.1) I produced ScCdc31-6His, TbCen2-6His, and CrCen-6His using the pET-28 expression vector in conjunction with BL21 (De3) cells, and purified via Ni-NTA. The proteins did not show significant amounts of aggregation in inclusion bodies and SDS-PAGE analysis showed that the band sizes corresponded within tolerance to the full-length proteins (Fig. S1C), with only minor secondary bands in case of ScCdc31-6His.

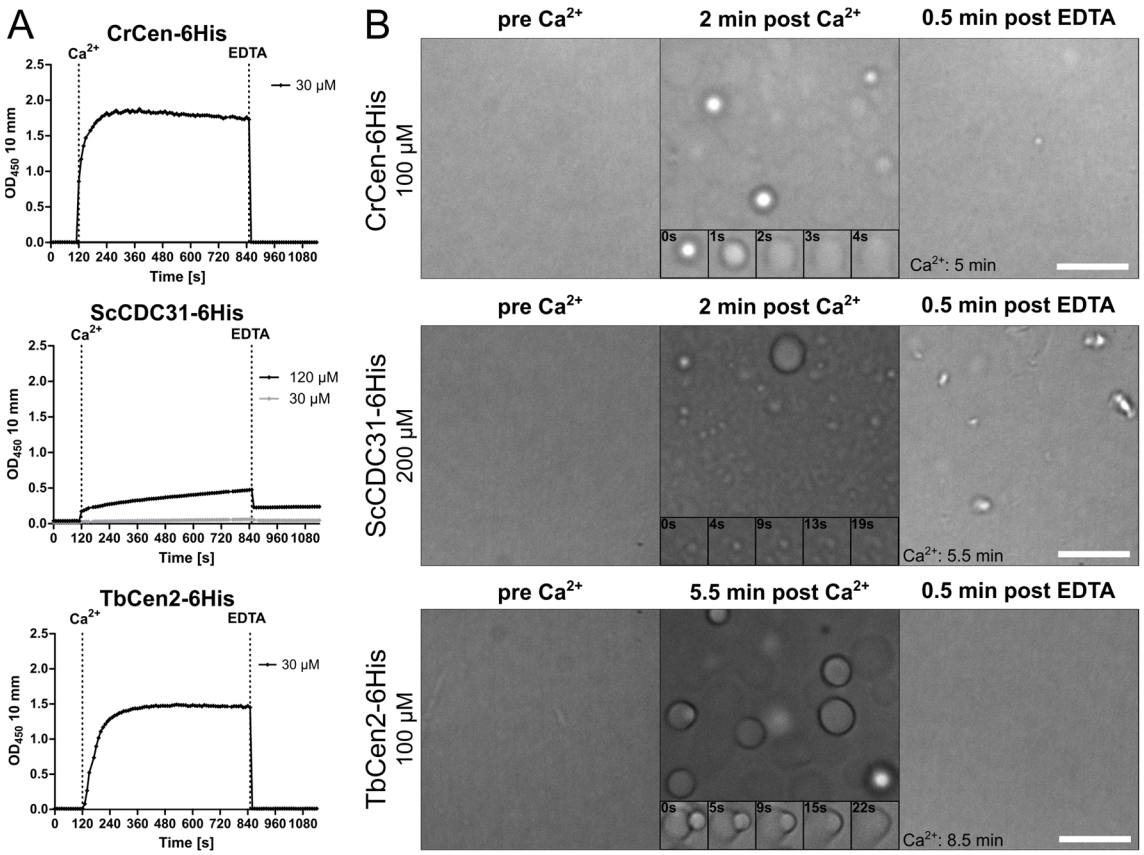


Figure 13 *In vitro* LLPS capability of evolutionary diverse centrins. (A) Turbidity assays of recombinant CrCen-6His, ScCdc31-6His, and TbCen2-6His at 37°C in 50 mM BisTris (pH 7.1). Turbidity was quantified as light adsorption at 450 nm. Ca^{2+}, $CaCl_2$ addition to 2 mM; EDTA, EDTA addition to 10 mM. **(B)** The three stages of the turbidity assay as in (A) observed by bright-field microscopy. Inlays show droplet fusion or wetting events. Approximate elapsed time after Ca^{2+} and EDTA addition is indicated. Higher protein concentrations were used to increase droplet density. Scalebars 10 µm**.** Modified from Voß *et al.* (2023) [79].

Employing turbidity assays, I observed that TbCen2-6His and CrCen-6His at 30 µM displayed a similar behaviour as PfCen1 did, with a rapid increase in fully EDTA-reversible turbidity triggered by Ca^{2+} (Fig. 13A). ScCdc31-6His only showed a response to Ca^{2+} at a higher concentration of 120 µM and turbidity was only partially reversible. Closer investigation into the nature of the turbidity via microscopy revealed that all three centrins formed droplets demonstrating liquid behaviour such as fusion and wetting (Fig. 13B). The EDTA-irreversible fraction of ScCdc31-6His was revealed to be non-uniform aggregates, unlike the uniformly round solidified droplets formed by PfCen3 (Fig. 10B).

In conclusion, I demonstrated that centrins with the ability to undergo LLPS can be found in species from five divergent eukaryotic branches, suggesting this is an evolutionarily conserved feature of centrin biology.

2.2.3 N-terminal IDRs predict centrin LLPS capabilities

Centrins have high structural similarity but nonetheless show contrasting LLPS behaviour, with PfCen1 and PfCen3 being capable of phase separation while PfCen2 and PfCen4 are not. I therefore investigated the limited differences between the phase separating and non-phase separating centrins to determine which structural features enable centrin LLPS.

I previously showed that the ability to bind Ca^{2+} is important for PfCen1 condensation (Fig. 11D). Similarly, the different LLPS capabilities between centrins could be the result of varying Ca^{2+}-binding properties. While most centrins possess four EFh-domains, these have different Ca^{2+}-binding constants or can even be completely inactive, properties that can only be inferred to a limited degree from their sequence [84]. In case of HsCen2, EFh domain IV and to a lesser extent III can each bind Ca^{2+} [85]. For PfCen1-4 the principal ability of all four to bind (radioactive) Ca^{2+} has been reported, but the number and distribution of the active domains is unknown [70]. These studies are typically conducted using calorimetric assays or NMR spectroscopy. As I did not have access to these toolsets, investigation would have required an extensive range of mutations to render the four *Plasmodium* centrins' EFh-domains inactive in various combinations.

I instead focused on the N-termini as these are a highly variable element in the otherwise fairly conserved structure of centrins (Fig. S4). Previously resolved 3D structures of HsCen2 and other centrins notably excluded the N-terminus [80]–[83], suggesting that it is unstructured. I therefore screened the sequences of the eight investigated centrins with the IUPred3 algorithm [158], which predicts a likelihood of intrinsically disordered regions (IDRs). These elements do not adopt a stable conformation and are known predictors of phase separating proteins [130]. Indeed, the results consistently revealed a higher peak likelihood of IDRs present within the N-termini of five phase separating centrins, PfCen1 (85.3%), PfCen3 (75.6%), HsCen2 (85.8%), TbCen2 (92.4%), and CrCen (62.8%) than the two non-phase separating ones, PfCen2 (49.7%) and PfCen4 (16.5%) (Fig. 14). The ability of a centrin to undergo LLPS and the likely presence of an N-terminal IDR is therefore correlated. The precise IDR likelihood peaks were 85.3%, 75.6%, and 85.8% respectively. Interestingly, the peak IDR likelihoods for PfCen2 and PfCen4 N-termini were only 49.7% and 16.5%. ScCdc31 (61.1%) was an intermediate case that was in principle capable of phase separation, but at a much higher critical concentration than the other phase separating centrins.

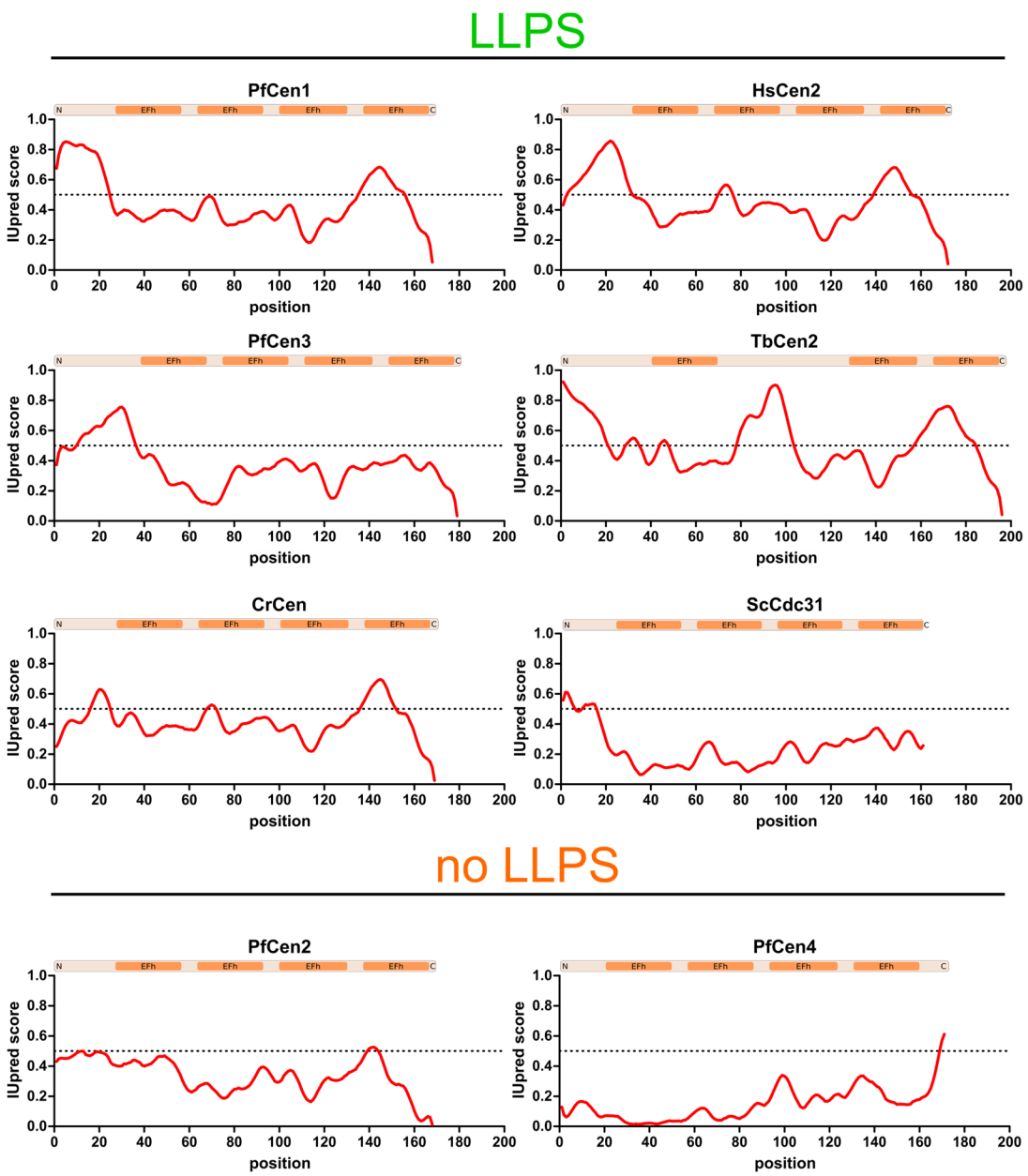


Figure 14 Relation between IDRs and LLPS capability of centrins. IUPred3 IDR likelihood scores [158] throughout different centrins divided in an LLPS-capable and LLPS non-capable group based on previous *in vitro* testing (see 2.21 and 2.2.2). Amino acid positions in the graphs are matched to graphics (to scale) indicating the position of N/C-Terminus and EFh domains. Modified from Voß *et al.* (2023) [79].

Indeed, the importance of the N-terminus for the LLPS of HsCen2 has previously been documented indirectly, as a deletion mutant of the 25 N-terminal amino acids no longer showed a turbidity reaction to Ca^{2+} [117]. Focusing on PfCen1 as the closest to HsCen2 [70]in terms of sequence and LLPS behaviour, Marina Iocca, under my supervision, investigated if the same was true for a Δ19-PfCen1-6His mutant. I chose the length of the deletion as such that the structured elements of the N-terminus (Alphafold [159] structures rated "confident" and above, Q8I272) were left in place to not disturb the protein conformation. The recombinant mutant only showed limited and EDTA-irreversible turbidity in response to Ca^{2+}, which microscopy revealed as aggregates (Fig. 15). Therefore, the N-terminus of PfCen1 appears to be essential for its ability to undergo LLPS.

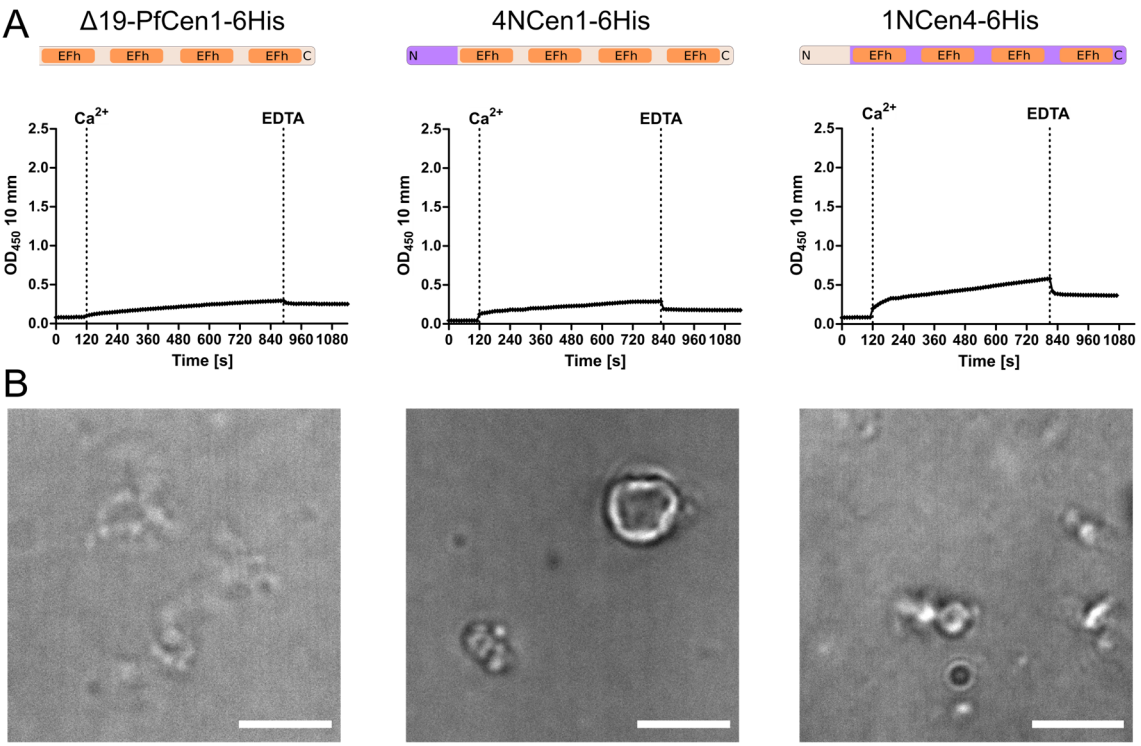


Figure 15 The influence of the N-terminus on centrin LLPS. (A) Turbidity assays of recombinant Δ19-PfCen1-6His, 4NCen1-6His, and 1NCen4-6His at 37°C in 50 mM BisTris (pH 7.1). Graphics illustrate N-terminal alterations in the deletion mutant and chimeras. Not to scale. Turbidity was quantified as light adsorption at 450 nm. Ca^{2+}, $CaCl_2$ addition to 2 mM; EDTA, EDTA addition to 10 mM. **(B)** Turbidity as in (A) post Ca^{2+} addition observed by bright-field microscopy in presence of 300 nM NTA-Atto-550 (not shown). 30 µM were used for Δ19-PfCen1-6His and 4NCen1-6His, 50 µM for 1NCen4-6His. Scalebars 10 µm**.** (A) modified from Voß *et al.* (2023) [79]. Turbidity assays were performed by Marina Iocca under my supervision. Images were acquired jointly.

Under my supervision, Marina Iocca then tested whether the PfCen1 N-terminus is not only essential but also sufficient to enable centrins to undergo LLPS, by swapping N-termini of PfCen1 and PfCen4. PfCen4 was chosen as it only shows a minimal reaction to Ca^{2+} and thus provides the ideal contrast to the phase separating PfCen1. For both proteins the cutoff for the N-terminus was set 9 amino acids before EFh I, based on homology and consistency with the previous Δ19-PfCen1-6His mutant (Fig. 4C, S4). The recombinant 4N-PfCen1-6His mutant, where the first 19 amino acids were replaced with the first 12 of PfCen4, showed a similar lack of Ca^{2+} response as Δ19-PfCen1-6His, both in terms of turbidity kinetics and aggregate-like morphology under the microscope (Fig. 15). This demonstrates that the critical function of the PfCen1 N-terminus for LLPS can not be rescued by the substitution with the N-terminus from the non-phase separating PfCen4. The recombinant 1N-PfCen4-6His mutant, where the first 12 amino acids were replaced with the first 19 of PfCen1, showed a much stronger turbidity response to Ca^{2+} than WT PfCen4 had at the same concentration. Although weaker than the LLPS response of PfCen1, it showed partial reversibility. However, no droplets, only aggregates, could be detected under the microscope. Of note, I had previously observed a higher propensity of this chimera to aggregate during expression and purification upon buffer exchange. This could perhaps indicate a general instability of the artificial protein, which would then trigger aggregation in response to changes in buffer parameters, such as Ca^{2+}-addition. While it is notable that the PfCen1 N-terminus drastically alters the response of the previously inert PfCen4, it does not enable LLPS.

In conclusion the N-terminus of PfCen1 is essential for LLPS, perhaps due to the presence of an IDR, but not sufficient to convey LLPS to other centrins.

[The experiments within this section were partially prepared and performed by Marina Iocca in the context of a lab rotation in 2020/2021 under my direct supervision. This included the cloning of the Δ19-PfCen1-6His, 4N-PfCen1-6His, and 1N-PfCen1-6His expression vectors, as well as the expression and purification of the proteins.]

2.2.4 PfCen3 N-terminal phosphorylation prevents LLPS but not CP localization

Besides the presence of an IDR, the N-terminus of PfCen3 is also notable due to the large concentration of documented phosphorylation sites (8 within 17 amino acids) (Fig. 4B, 16A). These were reported in previously published phosphoproteomes, with some phosphorylations appearing more consistently than others [51], [87]–[91]. Besides a potential influence on conformation, the 8 additional phosphate groups would invert the charge of the N-terminus (position 1-30, Fig. 4C, S4) from +6.4 to -6.5 (calculated with Prot Pi, see Table 14). This is notable as previous studies not only pointed to a positive charge of the N-terminus as a recurring feature across different centrins, but showed that electrostatic interactions are critical in self-interaction and turbidity formation of HsCen2 and TgCen1 [117], [120]. It is therefore conceivable that the charge of the N-terminus is important for centrin interactions and thus LLPS. To investigate the effect of these phosphorylations on LLPS as a potential posttranslational regulatory mechanism I generated recombinant phosphomimetic mutants of PfCen3.

Phosphomimetic mutations substitute the phosphorylatable serine, threonine, or tyrosine into a negatively charged aspartate or glutamate to mimic the -2 charge of a phosphate group. However, this is only an approximation as aspartate and glutamate sidechains can only carry a -1 charge. As a result, introducing a phosphomimetic mutation at all 8 positions only decreases the N-terminus charge to -1.6 at pH 7.1, instead of the charge of -6.5 that actual phosphorylations would achieve. A second factor to consider was the influence on the N-terminus structure of PfCen3, or the lack thereof, as it likely consists of an IDR. Mutations altering the unstructured conformation could therefore conceivably alter LLPS behaviour independent of the charge. To minimize such unwanted side effects, I exchanged serine (S) and threonine (T) to aspartate (D) and tyrosine (Y) to glutamate (E), as the length of their sidechains resemble the original amino acid closest. However, the aromatic ring of tyrosine cannot be accurately represented. Re-evaluating the influence of these phosphomimetic mutants on the N-terminal IDR likelihood revealed minor changes in the profile, which largely stemmed from the Y11 mutation (Fig. 16A). Therefore, I generated two mutants, one where all three amino acids were mutated, dubbed PfCen3-SYT, and one where I left Y11 intact, only mutating serines and threonins, dubbed PfCen3-ST (N-terminus charge -0.6 at pH 7.1). Previous mass spectrometry of PfCen3-6His suggested that no additional PTMs were added to the recombinant protein by *E. coli* (Fig. S1B).

My investigation of the recombinant PfCen3-SYT-6His and PfCen3-ST-6His response to Ca^{2+} by turbidity assay showed that the introduction of phosphomimetic mutations completely abrogated LLPS at the standard (30 µM) and even 4-fold increased concentration (Fig. 16B) While PfCen3-ST-6His showed almost no response, PfCen3-SYT-6His generated a noticeable amount of turbidity at higher concentration, which was, however, almost completely EDTA-irreversible. These results support the hypothesis that N-terminal hyperphosphorylation could serve as a mechanism to rapidly control centrin phase separation *in vivo*. In this light, it was interesting to determine the effect of these phosphomimetic mutations on the localization of the protein, as this could provide an indication whether LLPS is involved in the recruitment of PfCen3 to the centrosome. Towards this aim, Marina Iocca, under my supervision, generated *P. falciparum* lines expressing GFP-tagged PfCen3-SYT/ST from the pARL vector system. IFAs revealed a localization as (mostly) centrosomal foci for both mutants that was consistent with WT PfCen3-GFP (Fig. 16C), with live-cell imaging further confirming that these foci also arose from a disperse cellular background and duplicated successfully.

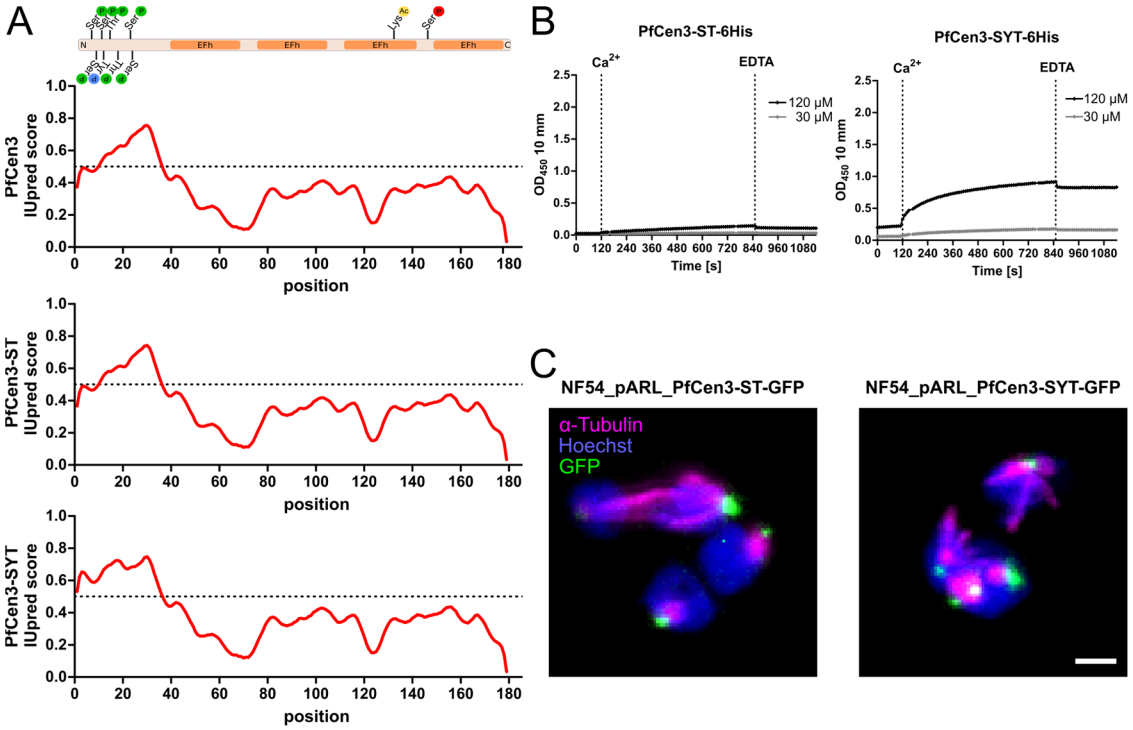


Figure 16 The influence of the phosphomimetic mutation on PfCen3 LLPS and localization. **(A)** Graphic (to scale) shows documented phosphorylations of PfCen3 (see Fig. 4B), which were mimicked for both the PfCen3-ST and PfCen3-SYT mutants (green), or only the PfCen3-SYT mutant (blue). Influence of phosphomimetic mutations on IDR likelihood is shown as IUpred3 scores [158]. **(B)** Turbidity assays of recombinant PfCen3 phosphomutants at 37°C in 50 mM BisTris (pH 7.1). Turbidity was quantified as light adsorption at 450 nm. Ca^{2+}, $CaCl_2$ addition to 2 mM; EDTA, EDTA addition to 10 mM. **(C)** Representative IFA confocal images of NF54 Schizonts expressing the indicated PfCen3 phosphomutant with a GFP tag from a pARL vector. Merge of GFP (green), tubulin (magenta), DNA staining (hoechst, blue). (A) graphic modified from Voß *et al.* (2023) [79]. Cytoplasmic GFP signal trimmed for clarity. Images are maximum intensity Z-projections. Scalebar 1 um. Strains and IFA for (C) were generated by Marina Iocca under my supervision. Images were acquired jointly.

In conclusion, phosphomimetic mutations of the PfCen3 N-terminus abrogate LLPS of recombinant proteins *in vitro*, but do not prevent foci formation and CP localization *in vivo*.

[pARL_PfCen3-ST-GFP and pARl_PfCen3-SYT-GFP as well as the respective P. falciparum lines were generated by Marina Iocca in the context of a lab rotation in 2020/2021 under my direct supervision. She also prepared the IFAs of these lines under my supervision, which were then imaged by myself.]

2.2.5 PfCen1 and PfCen3 interact through condensation

A previous pulldown study of PfCen1-GFP indicated an interaction with PfCen3 in *P. falciparum*, which is further supported between an apparent interaction of PbCen1-4 evidenced by a similar pulldown in *P. berghei* [71], [122]. As LLPS plays a role in the self-interaction of centrins I investigated whether it could further play a role in these interaction between the *Plasmodium* centrins observed *in vivo*. As a first step I studied if recombinant centrins can contribute to a common critical concentration threshold, which would indicate an LLPS promoting interaction.

I approached this question by combining PfCen1-6His, PfCen2-6His, and PfCen3-6His at concentrations that are sub-critical individually to observe if the different centrins can cooperate and overcome the critical concentration collectively. An important factor to consider is molecular crowding, which I previously established as a major contributor to LLPS in case of PfCen3-6His (Fig. 11B). Therefore, to determine any specific LLPS-promoting interactions between different centrins, protein density must be kept consistent. As protein and PEG concentrations cannot be easily equated, I instead used bovine serum albumin (BSA) to achieve consistent protein concentrations between the tested centrin solutions. Consistent with the c_{sat} I previously determined for PfCen1-6His and PfCen3-6His (Fig. 11B), neither PfCen1-6His, PfCen2-6His, nor PfCen3-6His showed any reaction to Ca^{2+} at 10 µM when supplemented to 30 µM total protein with BSA (Fig. 17A). However, when combining 10 µM of these three proteins to the same total protein concentration of 30 µM Ca^{2+} triggered a clear increase in turbidity with a peak OD_{450} of 0.657. This indicated that different centrins can indeed contribute to a common critical concentration threshold, supporting a direct interaction between the different centrins beyond an unspecific molecular crowding effect. Addition of 10 µM PfCen4-6His, on the other hand, did not contribute to turbidity, instead decreasing the peak OD_{450} to 0.505 (Fig. 17B). A more detailed investigation combining 10 µM each of two centrins at a time (total protein concentration 20 µM) revealed that an interaction of PfCen1-6His and PfCen3-6His with a peak OD_{450} of 0.601 is the predominant driver of the additive assembly (Fig. 17C). Combinations of PfCen2-6His with PfCen1-6His or PfCen3-6His only showed a minor reaction to Ca^{2+} addition. Interestingly, the turbidity kinetics of the mixed centrin solutions show combined features of the individual centrins, like the partial EDTA-irreversibility (~15%) of the PfCen1 + PfCen3 mixture, which is lower than the irreversible fraction of PfCen3-6His (~64%), but above the complete reversibility of PfCen1-6His.

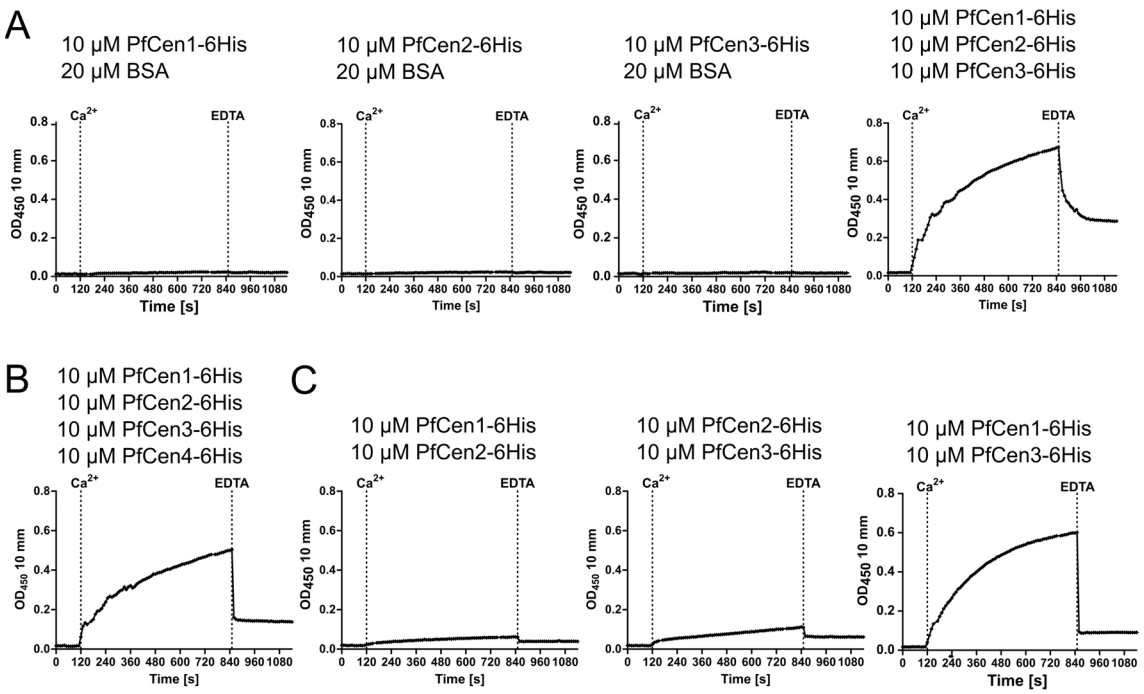


Figure 17 Centrin interactions contributing to joint concentration thresholds. Turbidity assays of recombinant PfCen1-4-6His individually and in combination to determine interactions between different centrins. 37°C in 50 mM BisTris (pH 7.1). Turbidity was quantified as light adsorption at 450 nm. Ca^{2+}, $CaCl_2$ addition to 2 mM; EDTA, EDTA addition to 10 mM. **(A)** Turbidity assay of recombinant PfCen1-3-6His at subcritical concentrations independently or in combination. BSA is used to standardize total protein concentration to 20 µM. **(B)** Combination of all four centrins to determine the additional influence of PfCen4-6His **(C)** Combinations of two different centrins at individually subcritical concentrations. Partially adapted from Voß *et al.* (2023) [79].

To be able to determine via microscopy whether this common contribution towards LLPS of PfCen1-6His and PfCen3-6His was the result of the formation of joint condensates, the two centrins had to be visually distinguishable. My initial attempts to pre-label one centrin but not the other with Atto550-NTA were unsuccessful, as the dye dissociated and re-distributed between the centrins too quickly upon mixing. I instead recombinantly expressed and purified a C-terminally GFP tagged version of PfCen1. The tag did not disrupt the capability of PfCen1-GFP-6His to undergo LLPS, as evidenced by an immediate increase in turbidity upon Ca^{2+} addition and full EDTA reversibility (Fig. 18A). I further confirmed droplet formation via microscopy, which showed a diffuse background GFP signal coalescing into droplets with a strong and homogeneous fluorescence (Fig. 18B). Interestingly the tag instead seemingly decreased the critical LLPS concentration compared to PfCen1-6His as evidenced by stronger turbidity even at lower concentrations (20 µM vs 30 µM, see Fig. 9). With the LLPS capability of PfCen1-GFP-6His established, I investigated if it and PfCen3-6His would form joint or separate droplets. To be certain of the presence of the non-fluorescent PfCen3-6His in such joint condensates, I observed whether PfCen1-GFP-6His could integrate into pre-formed PfCen3-6His droplets. I did not use recombinant PfCen3-mCherry-6His as its LLPS capabilities were severely impaired by the tag (data not shown). Instead, I mixed PfCen3-6His first with Ca^{2+} until droplets were visible under the microscope after which I added PfCen1-GFP-6His (without prior Ca^{2+}) to the solution. Tracking of the same PfCen3-6His droplets over time showed a rapid accumulation of GFP signal in these droplets seconds after PfCen1-GFP-6His addition, indicating the mixture of the two centrins in the same

condensates (Fig. 18C). EDTA addition caused PfCen1-GFP-6His to rapidly drain from the joint condensates, while a vaguely droplet shaped solid structure remained, which is presumably composed of PfCen3-6His (Fig. 18D).

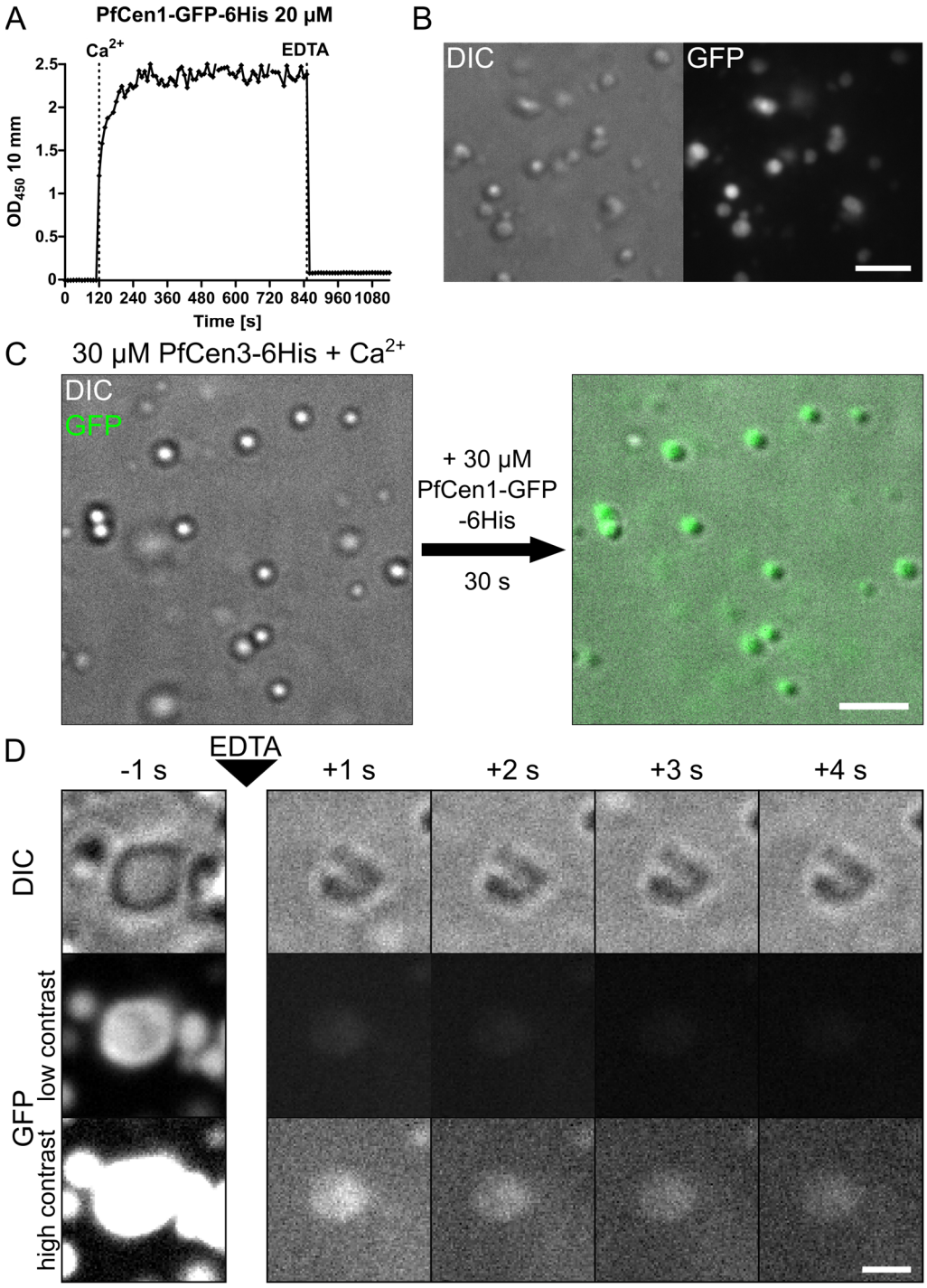


Figure 18 Heterotypic interaction of PfCen1 and PfCen3. (A) Turbidity assays of recombinant PfCen1-GFP-6His at 37°C in 50 mM BisTris (pH 7.1). Turbidity was quantified as light adsorption at 450 nm. Ca^{2+}, $CaCl_2$ addition to 2 mM; EDTA, EDTA addition to 10 mM. **(B)** Turbidity of PfCen1-GFP as in A post Ca^{2+} addition observed by bright-field (DIC) and confocal fluorescence microscopy using the GFP tag. Differences in droplet intensity are due to variation in position relative to the focal plane. Scale bar 5 µm. **(C)** Bright-field (grey scale) and confocal fluorescence imaging (green) before and 30 s after addition of 30 µM PfCen1-GFP-6His to pre-formed PfCen3-6His droplets. Ca^{2+} addition to 2 mM had occurred prior to imaging. Scale bar 10 µm. **(D)** PfCen3-6His droplets incorporating PfCen1-GFP-6His before and after EDTA addition to observe effect on centrin interaction. High contrast of GFP signal shown for better visibility in changes post EDTA addition. Scale bar 2 µm. (A, C) modified from Voß *et al.* (2023) [79].

My previous findings from the investigation of PfCen1/4 chimera (see 2.2.3) and PfCen3 N-terminal phosphorylation (see 2.2.4) suggested an importance of the N-terminus for centrin LLPS. I further wanted to investigate whether it is also involved in the cross-interaction between PfCen1 and PfCen3 by testing whether the PfCen3 N-terminus can substitute for the PfCen1 N-terminus and vice versa. I therefore created two chimeras with switched N-termini, 1NCen3-6His, and 3NCen1-6His. Once again, I set the cutoff for the N-terminus 9 AA before EFh I, based on homology (Fig. 4C, S4) and consistency with the previous Δ19-PfCen1-6His mutant as well as 4NCen1-6His and 1NCen4-6His chimeras Fig. 15). The proteins were expressed using the pZE13d-C W3110-Z1 system and purified via their His-Tag using Ni-NTA (Fig. S1C). Of note, 1NCen3-6His formed a sizable amount of inclusion bodies, as PfCen3 had before.

Investigation of the chimera independently via turbidity assay showed that both were capable of undergoing Ca^{2+}-dependent LLPS as confirmed via microscopy (Fig. 19A, B). However, the required c_{sat} (>30 µM) were noticeably higher than that of the WT proteins. Interestingly the EDTA irreversible fraction typical for PfCen3 was present for 1NCen3-6His, but not 3NCen1-6His, suggesting maturation is a trait conferred by the PfCen3 C-terminus.

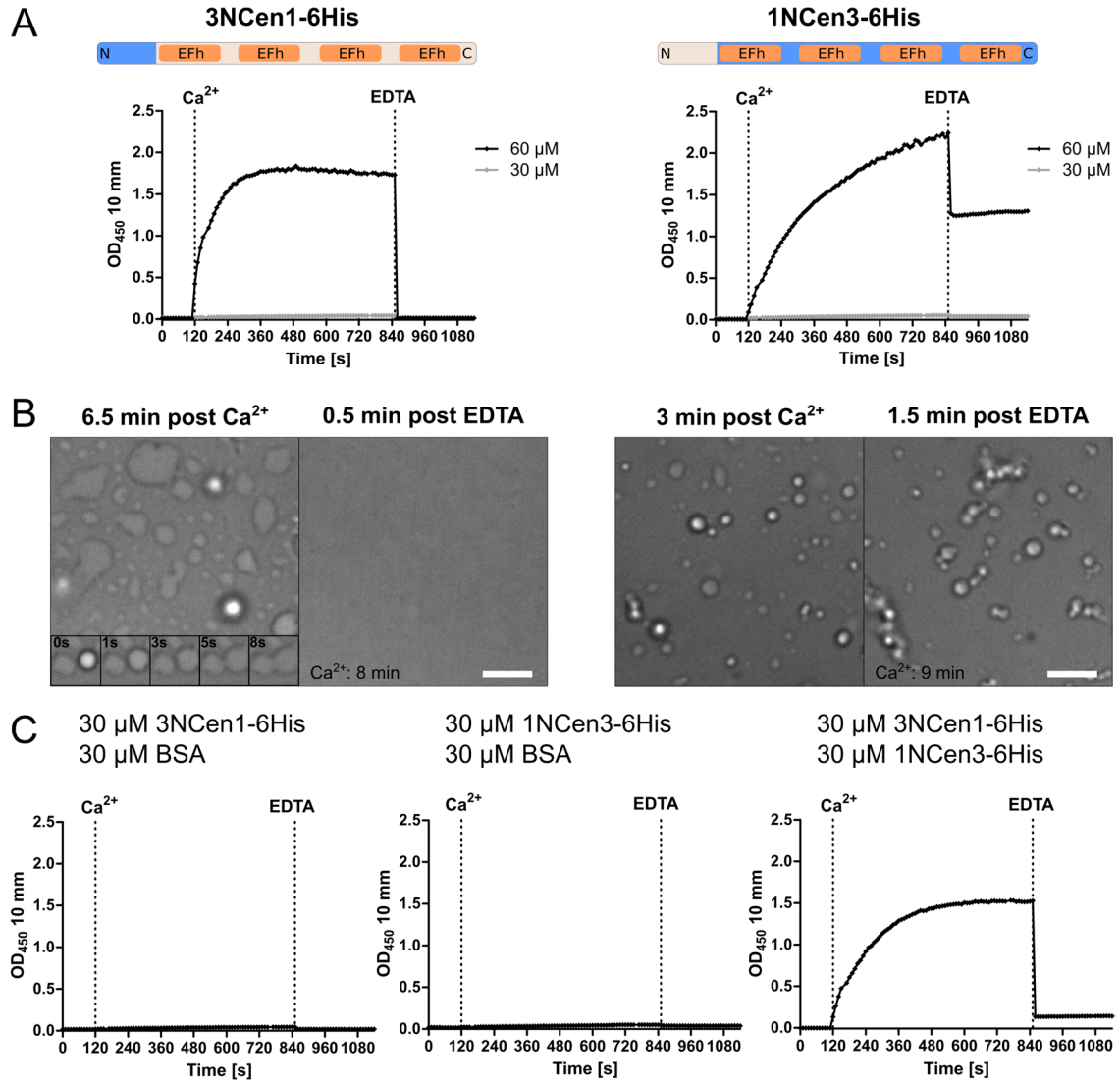


Figure 19 LLPS and interaction of PfCen1-PfCen3 chimeras. (A) Turbidity assays of recombinant 3NCen1-6His and 1NCen3-6His at 37°C in 50 mM BisTris (pH 7.1). Graphics (not to scale) illustrate N-terminal alterations in the chimeras. Turbidity was quantified as light adsorption at 450 nm. Ca^{2+}, $CaCl_2$ addition to 2 mM; EDTA, EDTA addition to 10 mM. **(B)** Turbidity assay as in (A) observed by bright-field microscopy. Inlays show droplet fusion or wetting events. Approximate elapsed time after Ca^{2+} and EDTA addition is indicated. Higher protein concentration of 100 µM were used to increase droplet density. Scalebars 10 µm**. (C)** Turbidity assay of the two chimeras at subcritical concentrations independently or in combination. BSA was used to standardize total protein concentration to 60 µM.

Repeating the previous intermixing experiment (Fig. 17) showed that while 30 µM of 3NCen1-6His or 1NCen3-6His independently did not undergo LLPS even in the presence of 30 µM BSA, a mixture of 30 µM of both chimeras did (Fig. 19C). The irreversible fraction of the mixture (9%) was lower than that of 1NCen3-6His alone (55%), but higher than the complete reversibility of 3NCen1-6His alone. These findings demonstrate that similar to the interaction between PfCen1 and PfCen3, the two chimeras can interact as well.

Taken together these results demonstrate that PfCen1 and PfCen3 interact by forming joint condensates and contribute to a common critical concentration. My results further suggest an involvement of the N-terminus in this interaction, with different models being discussed in 3.2.4.

2.3 In *vivo* dynamics of PfCen1 are influenced by its concentration

After I established the ability of PfCen1 and PfCen3 to undergo Ca^{2+}-dependent LLPS under minimal *in vitro* conditions, the next step was to evaluate if this is also relevant in the much more complex context of the parasite *in vivo*. The PCM of centrosomes has previously been hypothesized to assemble as a liquid condensate [62], [140]. If centrin LLPS were to play a role in living cells, this could not only help explain how centrins can localize to a broad range of diverse centrosomes in different eukaryotic organism, but also have important implications for the material state and duplication of the centriolar plaque. If the CP constituted a condensate this would offer a comprehensive explanation for its protein density, absence of solid structures, and apparent dynamic rearrangement of centrins within its confines.

LLPS had not been previously investigated in *Plasmodium* species and thus required the implementation of new experimental approaches and tools. I herein focused on the strong dependency of condensation on a critical concentration threshold and studied how centrin expression levels influence their localization and foci formation dynamics.

2.3.1 pFIO – An inducible overexpression system for *P. falciparum*

Observation of centrin behaviour at different intracellular concentrations requires the ability to modulate expression. Unfortunately, knockdown of centrins was not an option as centrin genes are notoriously refractory, which is also true in other *Plasmodium* species [122]. Specifically, I was unable to integrate the glmS ribozyme [160] 3’ of the open reading frames (ORF) using the SLI system [142]. As this system relies on C-terminal

tagging of endogenous centrin with a resistance gene for selection of successful single crossover integration, the likely cause for failure was the general intolerance of centrins to tagging. However, a knockdown by integration of a 3' glmS sequence or integrating loxP sites for an inducible DiCre-based knockout via CRISPR without altering the PfCen3 ORF were not successful either.

As a result, I opted for the opposite approach of artificially increasing centrin levels. This required a robust overexpression system that can express the protein of interest (POI) at high levels consistently. Unfortunately, expression of PfCen1-4 with the pARL vector system demonstrated that the parasite severely reduces or completely silences expression of centrin over time. This resulted in only a fraction of cells expressing centrin at low levels despite continued drug selection (Fig. 20F). While the expression levels of vectors can normally be modulated by implementing expression cassettes with weaker or stronger promoters, the parasite appears to throttle expression down to a minimal level regardless of 5' untranslated region (UTR). While the exact mechanism remains speculative, I hypothesized that silencing only occurs once the protein of interest is expressed, as pARL silencing is directly dependent on the expressed protein. pARL_PfPCNA1-GFP, for example, leads to high expression levels in most cells [50]. This suggests the expression cassette is not a target of silencing by default but rather selective pressure against expressing cells. It is also unlikely that the ORFs of the centrins would be a default target, as they employ the same sequence as the endogenous genes (without introns). Therefore, the parasite would only have cause for silencing the expression cassette once POI overexpression incurs a fitness cost.

Due to the nature of *P. falciparum* transfections, the period from electroporation and first expression of the POI until an analysable population has arisen after selection can last multiple weeks. This affords the parasite a broad window of opportunity to establish silencing before the POI can be observed. I speculated that minimizing the time from first expression to observation would significantly reduce silencing, thus improving expression levels. I achieved this by designing a DiCre/loxP based inducible expression vector called pFIO, which is short for ***P****. **f**alciparum* **i**nducible **o**verexpression (Fig. 20A). The plasmid consists of a strong promoter placed in front of two ORFs. By default, only the first ORF encoding hDHFR, a resistance gene for the selection drug WR, tagged with mCherry is expressed, as the stop codon and 3'UTR prevent translation and transcription of the second ORF encoding the POI. Silencing of the expression cassette is prevented as resistance and therefore parasite survival is directly tied to its active state. When transfected into a *P. falciparum* strain constitutively expressing the split DiCre recombinase [161], the addition of the drug Rapamycin (RAP) induces formation of the active Cre recombinase, which then recombines out the first ORF and 3'UTR as they are flanked by loxP sites. This places the second ORF in front of the promoter, thus inducing its expression. The DiCre/loxP system is renowned for its efficiency with RAP incubation times as low as 30 min inducing recombination near of plasmids in *P. falciparum* or *P. berghei* with very little leak activity [161]–[163]. Failed induction would be indicated by the mCherry-tag of the first ORF. I designed the system with two promoters of different strengths for comparing varying expression levels and therefore protein concentrations.

The first was a truncated *Pfhsp70* (PF3D7_0818900) 5'UTR sequence which performed best in previous comparative study between different *P. falciparum* promoters [164]. The second was a *Pfhsp86* (PF3D7_0708400) 5'UTR. Transcript levels are in the 99.6 percentile for both 0-32 hpi with a peak at 24 hpi followed by a drop off during schizogony (Fig. 20B). This expression pattern is ideal for the study of proteins during schizont stage (~ 29 hpi onward) due to the delay between transcription and translation. While transcriptomic studies suggest an almost 2-fold higher expression of the *hsp70* [165], transcription start sites (TSS) mapping suggest stronger activity of the *hsp86* promoter [166], (Fig. 20C). Of note the primary TSS is located 41 bp before the previously published hsp70 promoter sequence I employed, which might reduce its strength.

I transfected both versions, pFIO_hsp70p and pFIO_hsp86p, encoding PfCen1-GFP in their second ORF, into *P. falciparum* 3D7_DiCre. After WR selection for plasmid presence via the first ORF, I induced the second ORF in a synchronized schizont culture with 100 nM RAP (in DMSO) for 4 h. While other studies employing the DiCre system for knockouts in *P. falciparum* typically induce the recombinase during the ring stage [161], I reasoned that earlier induction would increase maximum protein levels by providing more time for transcription and translation. A negative effect on the schizogony of the induction cycle was unlikely due to the delay between induction and protein production. This was confirmed by my preliminary tests where induction during the previous schizont stage out-performed the ring stage induction in terms of expression levels (data not shown). WR selection was discontinued after RAP treatment, as the resistance gene should no longer be active.

I then benchmarked the two plasmids to determine relative expression strength, induction efficiency, and leakiness. Towards this end I performed flow cytometric analysis of GFP levels in schizont cultures that had been induced or treated with DMSO as a control 2 days prior in the previous cycle. I differentiated iRBCs from uninfected RBCs (uRBCs) using the infra-red DNA stain SYTO61, as (human) erythrocytes don't contain DNA on their own. The DMSO control of both plasmids revealed only minimal leak expression of PfCen1-GFP in a small subpopulation (Fig. 20D). In contrast, RAP induction led to a measurable GFP signal in ~55% of schizont the population for both promoters. However, the median expression from the hsp86 promoter was ~3 times stronger compared to the hsp70 promoter (Fig. 20E).

Potential reasons for an incomplete induction far below the documented efficiency of the DiCre recombinase in *Plasmodium* (endogenous and episomal [161], [163]) are discussed in 3.1.1. However, it was noted that even the PfCen1-GFP expressing population remained at least partially WR resistant, indicating that the system can behave differently *in vivo* than intended.

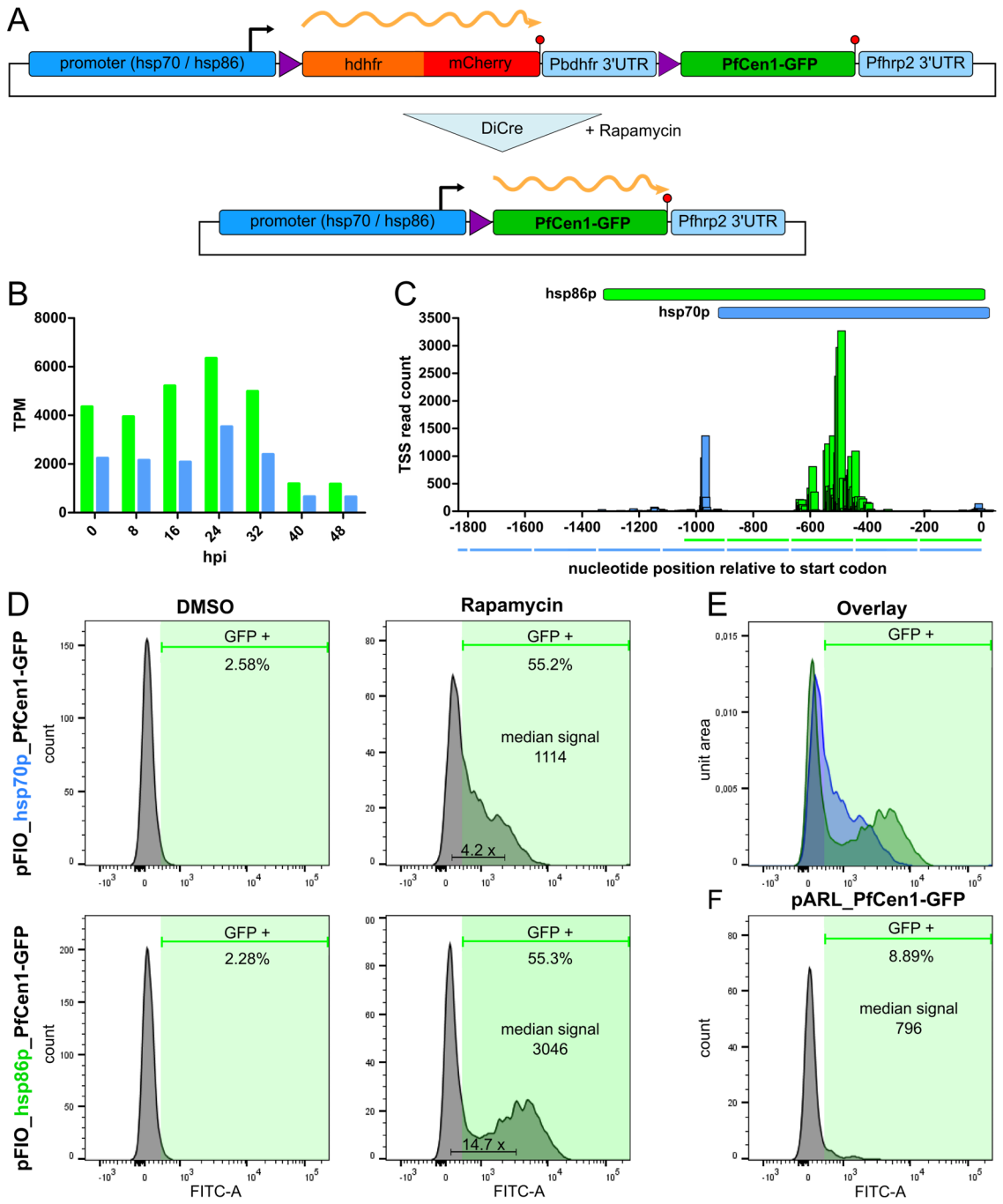


Figure 20 The pFIO inducible overexpression system. (A) Schematic illustrating the principle of the pFIO plasmid system intended for transfection into *P. falciparum* strains expressing DiCre recombinase. The episomal plasmid contains two ORFs behind a strong hsp70 or hso86 promoter. The first is floxed by two loxP sites (purple arrow) and contains an hdhfr resistance gene that conveys resistance to WR for selection, which additionally prevents silencing of the expression cassette. Upon induction of DiCre via the drug RAP, the first ORF is recombined out and the second one is expressed. mRNA in yellow; red pins represent stop codons. **(B)** Transcript levels of the endogenous hsp70 (blue) and hsp86 gene (green) during the asexual blood cycle as determined via RNA-sequencing [165]. **(C)** Published positions and frequency of TSSs as determined via RNA-sequencing [166] in the endogenous hsp70 and hsp86 promoter region relative to the respective start codon (at 0). Filled bars at the top shows the sequence present in the pFIO plasmids, dashed line below graph indicates the annotated 5' UTR of mRNAs transcribed from the endogenous genes [167]. **(D)** Flow cytometry analysis of 3D7-DiCre_hsp70p_PfCen1-GFP and 3D7-DiCre_hsp86p_PfCen1-GFP cell lines to determine frequency and intensity of PfCen1-GFP expression 48 h post induction with RAP or control treatment with DMSO. Cells were gated for multinucleated parasites as determined using the DNA stain SYTO61. Share of the GFP positive (GFP +) population, median signal intensity of the GFP + population, and ratio between median intensity of GFP positive to GFP negative population are shown. **(E)** Overlay of induced populations from (D). **(F)** Same as in (D), but with the previously employed NF54_pARL_PfCen1-GFP strain. (A,D, F) modified from Voß *et al.* (2023) [79].

I further performed tests to assess whether expression levels could be further increased by raising the WR concentration up to 10-fold (25 nM) to select for higher hDHFR-mCherry expression. This would either be the result of a more active expression cassette or more plasmid copies, which in turn should also increase expression of the second ORF. While selection of 3D7-DiCre_pFIO_hsp86p_PfCen1-GFP with 25 nM WR did indeed result in a ~30% relative increase in the GFP-positive population compared to 2.5 nM, the median expression level was not increased noticeably (data not shown). Given the negative impact on parasite growth, this practice was therefore not implemented, as a larger expressor population provides little benefit for single-cell based microscopy studies (see 2.3.2/2.3.3).

In conclusion, the two pFIO versions can express PfCen1-GFP without significant leakiness at far higher levels and consistency than pARL. Importantly, different expression levels can be achieved with these two promoters, thus allowing the study of PfCen1 behaviour at different concentrations.

[Nicolas Lichti is credited for the discovery that GFP positive parasites can remain WR resistant after pFIO induction. He conceived and performed the experiment while working on his Master Thesis under my supervision in 2022.]

2.3.2 PfCen1-GFP overexpression induces premature formation of non-centrosomal foci

To assess the validity of my hypothesis that centrins accumulate in centrosomal foci through LLPS, it was critical to test their ability to phase separate *in vivo*. Due to the strong dependency of LLPS on concentration it was therefore important to investigate how altered centrin levels influenced their dynamics in the parasite. I herein focused on PfCen1 over PfCen3 as a *Plasmodium* centrin that had demonstrated the principal ability to phase separate *in vitro*, since the irreversible fraction of PfCen3 was a potential confounding factor for assessing liquid-like dynamics *in vivo*. Meanwhile, the turbidity of PfCen1 was nigh completely reversible with very little aggregation. I had also already been the most prevalent subject of my *in vitro* studies and was thus the best understood out of the *P. falciparum* centrins.

As knockdowns were unavailable, overexpression from episomal plasmids remained the most feasible option, which was possible due to pFIO. As described in 2.3.1 I was able to generate parasite populations overexpressing PfCen1-GFP at different median concentrations using the 3D7-DiCre pFIO_hsp70p_Cen1-GFP and pFIO_hsp86p_Cen1-GFP cell lines (Fig. 20D). I employed GFP-tagged PfCen1 instead of the WT PfCen1 as the pFIO system does not induce expression in the entire population. The addition of the GFP-tag allows for identification of the cells where overexpression is successful and further assess the expression level directly via GFP intensity. The tag furthermore enabled me to study the dynamics of PfCen1 under overexpression conditions in live cells. I previously confirmed that the GFP tag did not interfere with the ability of PfCen1 to undergo LLPS *in vitro* (Fig. 18A, B).

Like the previous weaker expression from pARL, both pFIO cell lines strongly overexpressing PfCen1-GFP showed a uniform cellular signal as well as distinct foci arising over time (Fig. 6B, 21A). However, under overexpression conditions these foci are often located outside the CP's outer core, as evidenced by their considerable distance from the mitotic spindle and the nucleus (Fig. 21 A, B). I therefore dubbed these foci **E**xtra-**C**entrosomal **C**entrin **A**ccumulations (ECCAs). To assess whether these could be PfCen1-GFP droplets formed by LLPS, I quantified their frequency in the weaker pFIO_hsp70p and stronger expressing pFIO_hsp86p populations to determine if it correlated with the intracellular PfCen1-GFP concentration. I focused on early schizonts, defined as cells with 1-5 nuclei and at least one intranuclear spindle, as centrin foci under normal conditions are only present from the onset of schizogony (approximated by mitotic spindle formation/hemispindle collapse) and disappear in late schizonts prior to segmentation (see 2.1.1). While I performed the IFAs using fixed cells, I did either not stain GFP at all or only with labelled primary nanobodies (GFP-booster), to prevent the misidentification of artifacts introduced by inevitable unspecific primary + secondary antibody staining as foci. I quantified foci over a large sample size of cells, which revealed a direct correlation between ECCA frequency and PfCen1-GFP concentration, both on the level of pFIO_hsp70p vs pFIO_hsp86p populations and individual cells (Fig. 21 C, D). While in the weaker expressing pFIO_hsp70p population 48% of GFP-positive early schizonts contained ECCAs in a 0.29:1 ratio to centrosomal foci, 97% of early schizonts in the stronger expressing pFIO_hsp86p population contained ECCAs in a 1.24:1 ratio to centrosomal foci (Fig. 21C). In both populations this ratio was positively correlated with GFP signal density/concentration on the level of individual cells, indicating that an increase in cellular PfCen1-GFP concentration also increases ECCA frequency (Fig. 21D).

As previously noted (2.1.1), parasites expressing centrins from the pARL system also rarely displayed non-centrosomal centrin foci (Fig. 6B, arrows). In light of the correlation between protein concentration and ECCA frequency, these rare events can likely be attributed to the weak overexpression from the pARL plasmid.

While mitotic spindles would often harbour an adjacent centrosomal PfCen1-GFP focus also under strong overexpression conditions, many CPs lacked such foci in the presence of ECCAs (Fig. 21A, B). Live-cell imaging revealed that ECCAs frequently, but not always, originated as centrosomal foci that separated from the CP and adjacent spindle after accumulating an unusually large amount of PfCen1-GFP (Fig. 21E). Of note, this was accompanied by a strong increase in mobility throughout the cell, which was a consistent feature of ECCAs. Centrosomal foci on the other hand were largely stationary, likely resulting from the CP being tethered to the nuclear envelope. This characteristic allowed for the differentiation of ECCAs and centrosomal foci even before spindles were detectable.

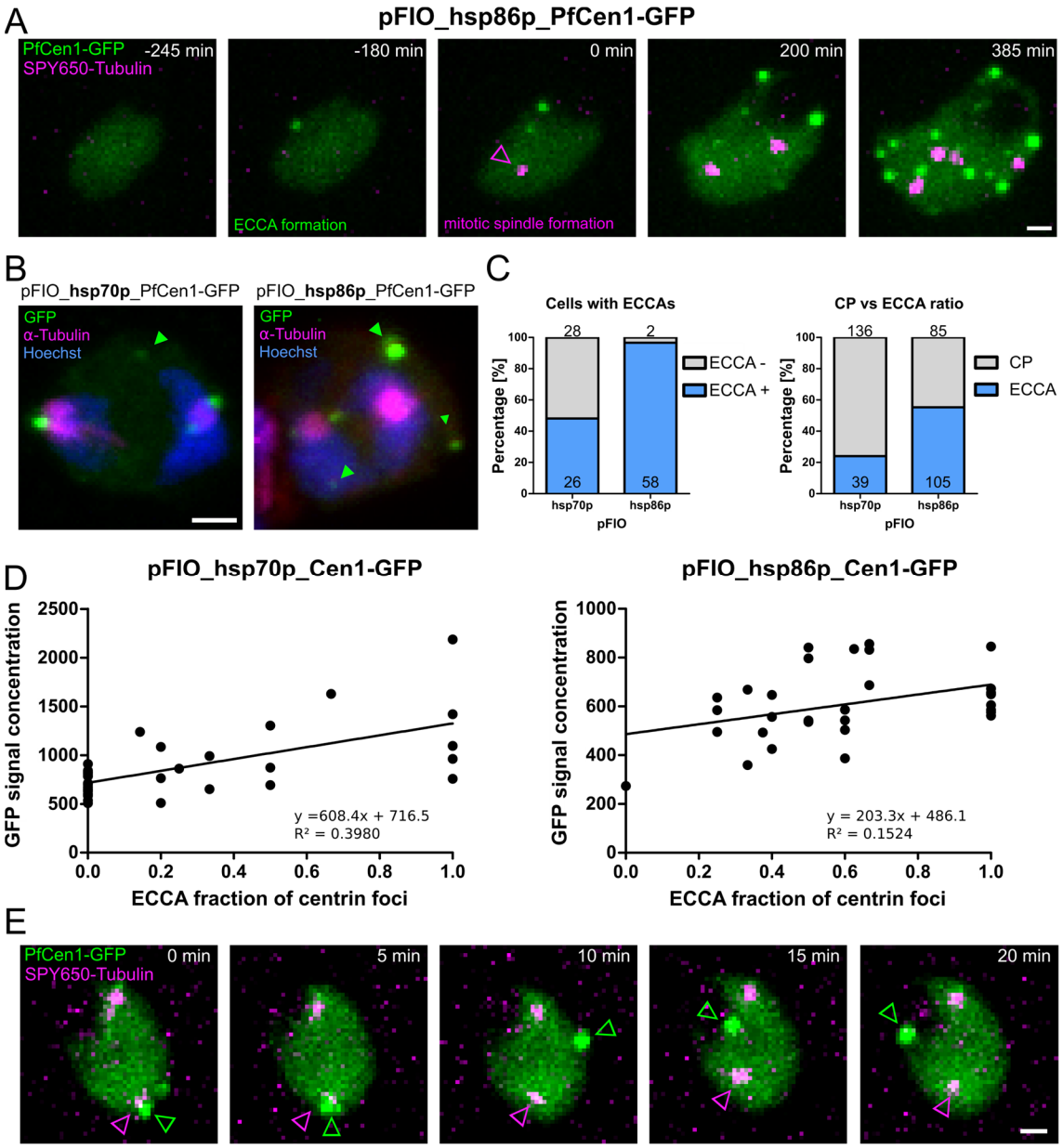


Figure 21 Effect of PfCen1-GFP overexpression on foci localization. (A) Confocal live-cell imaging of an induced 3D7-DiCre_pFIO_hsp86p_PfCen1-GFP parasite from late trophozoite stage through schizogony. Microtubules were stained with SPY650-Tubulin (magenta). Time relative to appearance of first mitotic spindle (magenta arrow) is indicated. Scale bar 1 µm. **(B)** Confocal IFA images of schizonts from induced 3D7-DiCre_pFIO_hsp70p or _hsp86p_PfCen1-GFP cell lines stained against tubulin (magenta) and DNA (Hoechst, blue), with PfCen1-GFP left unstained (green). Cells are representative examples of cell populations quantified in C and D. Images are maximum intensity projections. Scale bar 1 µm. **(C)** Quantification of the share of ECCA positive cells and ratio of ECCAs to CP foci in IFAs (examples in (B)) of induced 3D7-DiCre_pFIO_hsp70p_ or _hsp86p_PfCen1-GFP cell lines. All cells were GFP positive schizonts with 1-5 nuclei and at least 1 intranuclear spindle. Inlays show number of events in the respective sub-population. **(D)** Relationship between cellular GFP signal density/concentration and ECCA to CP foci ratio. Intensities are not comparable between cell lines, as the acquisition parameters had to be adjusted due to the weaker expression from pFIO_hsp70p_PfCen1-GFP. **(E)** Time-lapse confocal imaging of a 3D7-DiCre_pFIO_hsp86p_PfCen1-GFP schizont where a CP focus (green arrow) detaches from an intranuclear spindle (purple arrow) and turns into an ECCA. Maximum intensity projection. Scale bar 1 µm. (A-B, D-E) modified from Voß *et al.* (2023) [79].

I also observed the formation of ECCAs independent of a CP either before or after their locations were clearly identifiable by the presence of a spindle. I identified CP foci formed before the hemispindle was detectable by their lower mobility in combination with a spindle later forming at their location. While the first focus in cells with moderate PfCen1-GFP overexpression still mostly formed at the CP, first foci in cells with high overexpression were predominantly ECCAs (Fig. 22A). This can be interpreted as the need of the CP for foci formation decreasing with increasing concentration.

I further studied how concentration influenced the timing of foci formation. After induction of pFIO cellular PfCen1-GFP levels increase over time (Fig. 24A). If foci formation is driven by LLPS, it would be dependent on a critical concentration threshold. Cells strongly overexpressing PfCen1-GFP would therefore overcome this threshold sooner than weaker expressing ones, leading to earlier appearance of foci. Under weak pARL_PfCen1-GFP expression conditions the first centrin focus is usually detected between 40 min prior or post collapse of the first hemispindle into a mitotic spindle. This hemispindle collapse has been shown to coincide with the onset of S-phase [52], [53]. Conveniently, the collapse of the elongated hemispindle into a much more compact mitotic spindle and the associated increase of local tubulin concentration is easily detectable in live-cell movies by a strong increase of SPY640-tubulin signal at the spindle. As the onset of S-phase is a central regulatory event within the cell cycle, especially in regards to cell division, I chose it as a normalization for the parasite stage. I therefore performed time-lapse imaging on two large populations of trophozoites expressing PfCen1-GFP from pFIO_hsp70p or pFIO_hsp86p with 5 min temporal resolution and catalogued the appearance of the first foci (Fig. 22A). As the experiment relies on two cell populations exhibiting different median PfCen1-GFP expression levels as observed before, I chose the cells randomly without regard to GFP signal intensity. I further differentiated whether the first focus was centrosomal or an ECCA based on vicinity to a spindle, if already present, and mobility. Overall, in cells with strong PfCen1-GFP expression from pFIO_hsp86p, foci formed significantly earlier than in cells with weaker pFIO_hsp70p expression, at an average of 173 min and 17 min prior to hemispindle collapse. This trend was true for both ECCAs (180 min vs 98 min prior to hemispindle collapse), and for centrosomal foci (145 min prior vs 1 min after hemispindle collapse), demonstrating that PfCen1-GFP foci formation timing in at the CP and outside is influenced by overexpression levels and thus concentration. Interestingly, in the pFIO_hsp70p population ECCAs formed significantly earlier than centrosomal foci. Regardless of the effects on foci formation, neither overexpression level affected mitosis itself, as the average duration of the mitotic spindle from hemispindle collapse to anaphase was not significantly different at an average of 130 min (pFIO_hsp86p) and 119 min (pFIO_hsp70p) (Fig. 22B) and is in line with published timeframes [52].

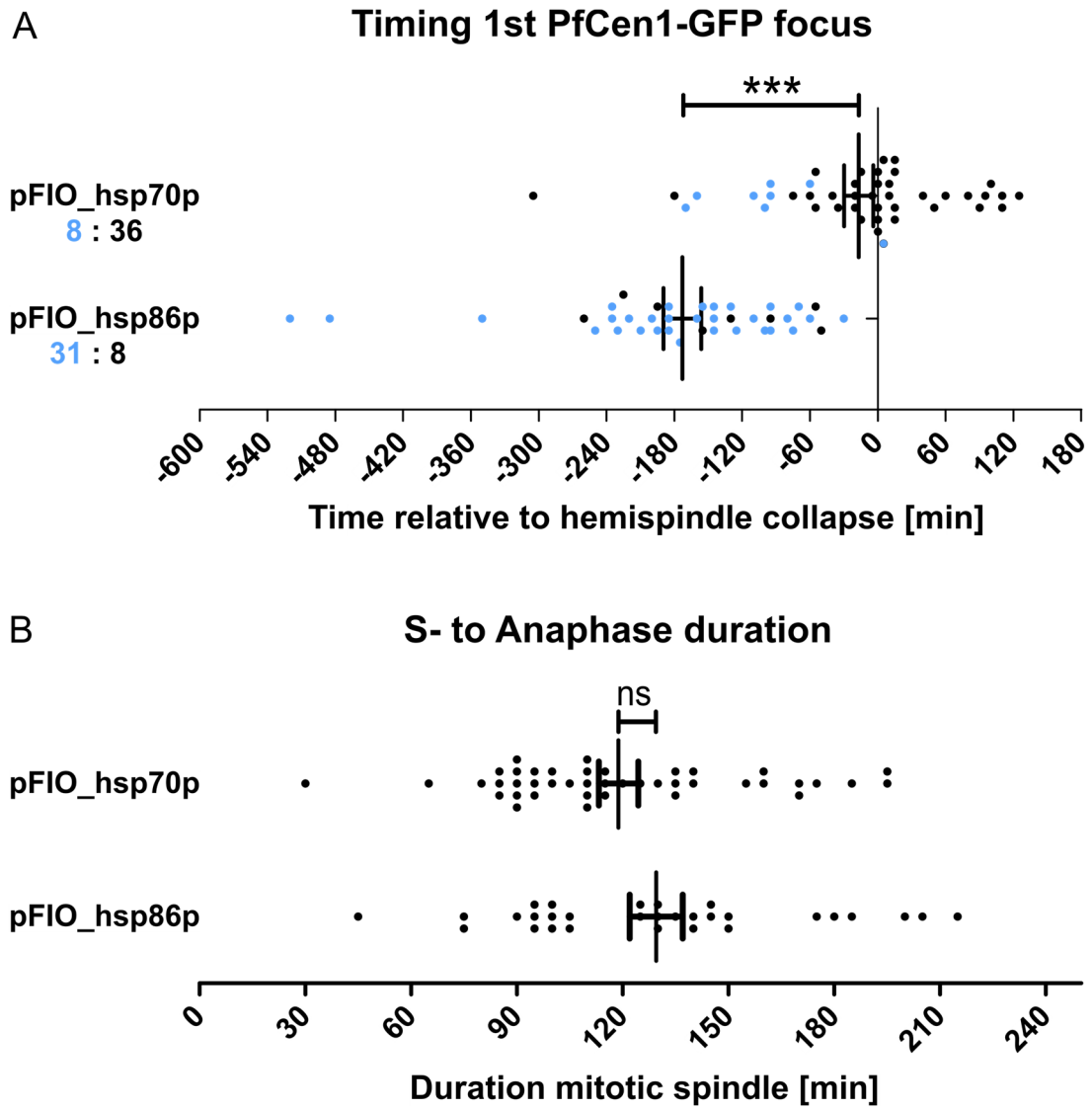


Figure 22 Effect of PfCen1-GFP overexpression on foci formation timing. (A) Formation of the first CP focus (black) and ECCA (blue) relative to the collapse of the hemispindle into the first mitotic spindle as visualized by live-cell imaging of 45 3D7-DiCre_pFIO_hsp70p_ and 46 _hsp86p_PfCen1-GFP parasites. Microtubules were stained with SPY650-Tubulin. Numbers of ECCAs and CP foci are provided on the left. **(B)** Duration of the first mitotic spindle as measured by the time from hemispindle collapse to anaphase spindle formation in 42 3D7-DiCre_pFIO_hsp70p_ and 30 _hsp86p_PfCen1-GFP parasites. **(A, B)** Standard error of the mean is shown. ***, P<0.0001; ns, not significant Two-tailed t-test. (A) modified from Voß *et al.* (2023) [79].

Prompted by the previously noted (2.2.5) decrease in c_{sat} for PfCen1-GFP-6His compared to PfCen1-6His observed in turbidity assays (Fig. 18A), I investigated whether ECCA formation might be an artifact facilitated by the GFP tag, or if they also arise from overexpression of native PfCen1. For this purpose, I devised a version of pFIO where the 2nd ORF contained the T2A skip-peptide, leading to a separation into two polypeptides during translation [168], [169]. In this later version of pFIO I also removed mCherry from the 1st ORF as prior experience had shown a limited usefulness. This plasmid, pFIO_hsp86p_~~mCherry~~_GFP-T2A-PfCen1, leads to the expression of GFP-T2A and PfCen1 upon induction, with only a proline from the skip peptide sequence remaining at the N-terminus of PfCen1 (Fig. 23A). The presence of GFP-T2A allowed for the identification of successfully induced parasites while overexpressing PfCen1 in a

virtually native state. It further enabled me to evaluate overexpression levels and leakiness via flow cytometry. To allow for comparison between datasets from different acquisition sessions I normalized the median expression intensity of the GFP-positive population to the peak of the GFP-negative fraction. Flow cytometric analysis revealed a normalized median GFP signal of 7.4x in the parasites used for this experiment (Fig. 23B), which is below that of 3D7-DiCre_pFIO_hsp86p_Cen1-GFP (Fig. 20D) with 14.7x. However, as 3D7-DiCre_pFIO_hsp70p_Cen1-GFP still consistently produced ECCAs (Fig. 21C) even at even lower normalized median expression of 4.2x (Fig. 20D), I considered these levels sufficient to produce ECCAs in this experiment. As confirmed via Western blot (WB) skipping efficiency was 96%, as seen by the GFP stained band being mostly present at the size expected from GFP-T2A, with only a minor amount detectable at the size of GFP-T2A-Cen1 (Fig. 23C). Concomitantly centrosomal foci did not contain any or only minimal amounts of GFP signal (Fig. 23D). In addition, PfCen1 overexpression was also evident from a strong increase in disperse background signal when performing immunofluorescence staining against centrin.

As centrin foci now no longer incorporated GFP, PfCen1 needed to be stained with a polyclonal rat antibody specifically raised on my behalf by Davids Biotechnology GmbH against PfCen1-6His (Fig. S5). However, while a GFP signal unambiguously indicates the presence of the POI (background fluorescence and tag cleavage not withstanding), antibodies always introduce a degree of unspecificity. This antibody in particular, while recognizing centrosomal foci, also showed foci all over the cell in uninduced parasite to a much higher degree than what was ever observed for PfCen1-GFP in the NF54_pARL-PfCen1-GFP lines (Fig. 23D, 6B). A WB also showed a strong unspecific affinity towards PfCen3-6His (Fig. S5). To compensate for false positive signal arising from unspecific binding, I quantified non-centrosomal foci in both uninduced and induced populations, wherein I only considered foci with a peak signal equal or higher to that of the weakest centrosomal focus. I did this to reduce false-positive quantification of foci resulting from unspecific binding, under the assumption that the specific signals were stronger than the unspecific ones. It should be noted that due to these different sets of criteria this quantification can not be directly compared to those performed on the pFIO_PfCen1-GFP cell lines (Fig. 21C). I quantified centrosomal and non-centrosomal foci across two populations of 49 GFP-positive induced and 53 (GFP negative) uninduced cells. Compared to the uninduced cells, the induced population showed an increased number in non-centrosomal foci (Fig. 23E). This was expressed both in the higher share of cells carrying non-centrosomal foci (78% vs 51%), and especially the 2.9-fold higher ratio of non-centrosomal to centrosomal foci (0.69:1 vs 0.24:1). Overexpression of (GFP-T2A-)PfCen1 therefore led to the formation of non-centrosomal foci that exceeded the false-positive signals resulting from antibody unspecificity.

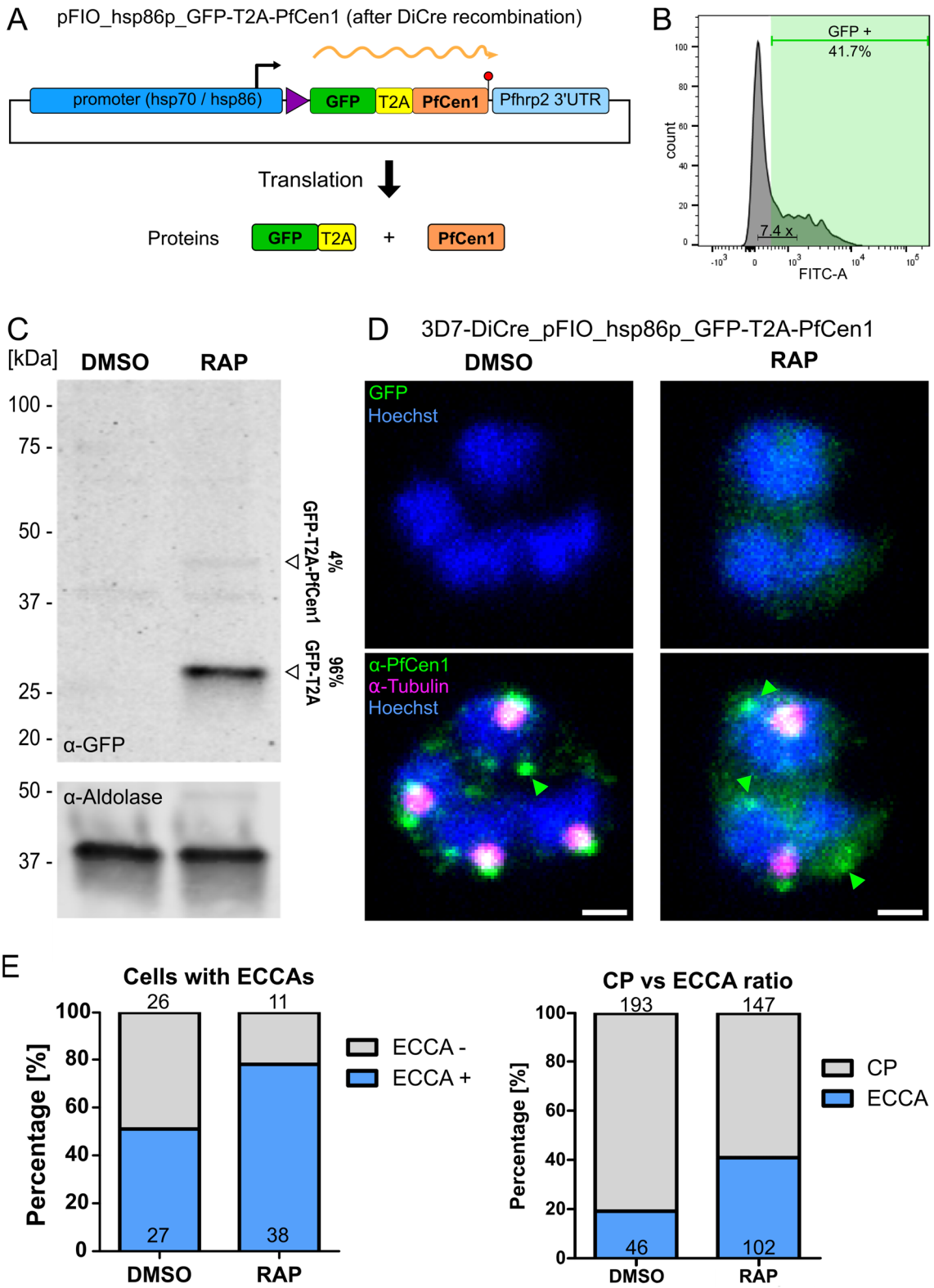


Figure 23 Overexpression of tag-free PfCen1. (A) Schematic of pFIO_hsp86p_GFP-T2A-PfCen1 after recombination showing the products of translation after skipping by the T2A skip-peptide. **(B)** Flow cytometry analysis of 3D7-DiCre_hsp86p_GFP-T2A-PfCen1 48 h post induction with RAP. Cells were gated for multinucleated parasites as determined using the DNA stain SYTO61. Share of the GFP positive (GFP +) population and ratio between median intensity of GFP positive to GFP negative population are shown. **(C)** WB against GFP in induced RAP or uninduced DMSO treated 3D7-DiCre_hsp86p_GFP-T2A-PfCen1 population samples. Staining against aldolase (bottom) was used as a loading control. Bands representing unskipped GFP-T2A-PfCen1 (48.41 kDa) and skipped GFP-T2A (28.86 kDa), as well as their relative share in total signal, are shown. **(D)** Representative confocal IFA images of GFP (top green) negative (uninduced, DMSO control) and GFP positive (induced, RAP) 3D7-DiCre_ pFIO_hsp86p_GFP-

T2A-PfCen1 cells stained against DNA (Hoechst, blue), tubulin (magenta) and PfCen1 (bottom green). To compensate for unspecific binding introduced by the anti-PfCen1 antibody non-centrosomal foci were only counted as ECCAs (green arrow) when the maximal signal matched or exceeded that of the weakest centrosomal focus. All images are maximum intensity projections. Scale bar 1 µm. **(E)** Quantification of the share of ECCA positive cells and ratio of ECCAs to CP foci in GFP positive induced and GFP negative uninduced 3D7-DiCre_ pFIO_hsp86p_GFP-T2A-PfCen1 cells. All cells were GFP positive schizonts with 1-5 nuclei and at least 1 mitotic spindle. Inlays show number of events in the respective sub-population. (A, C, E) modified from Voß *et al.* (2023) [79].

In conclusion, the cellular PfCen1-GFP concentration profoundly impacts the dynamics of foci formation *in vivo*. I demonstrated that a high cellular concentration enables PfCen1-GFP to form foci independent of the centrosome, with its preference as assembly site decreasing with increasing concentration. However, foci formation still occurs preferentially (but not exclusively) at the CP, which can subsequently become supersaturated with PfCen1-GFP and detach to form an ECCA. The timing of centrin accumulation in ECCAs but also at the centrosome being affected by expression levels supports a concentration threshold dependent mode of assembly, such as phase separation.

[The polyclonal rat anti-PfCen1-6His antibody was commissioned from Davids Biotechnology GmbH using antigen produced by myself.]

2.3.3 PfCen1-GFP foci formation and disassembly are regulated independently of cellular concentration

After establishing that PfCen1-GFP foci formation dynamics are affected by concentration, which could be an indication of an involvement of phase separation in the assembly process, I went on to characterize the relationship between PfCen1-GFP concentration and foci emergence over time.

A consistent observation across all cell lines expressing PfCen1-GFP was that despite the protein coalescing into centrosomal foci and/or ECCAs, a disperse background signal remains throughout schizogony (Fig. 6A, 21A). Furthermore, upon induction of pFIO, the levels of PfCen1-GFP increase over time towards schizogony (Fig. 24A), with transcript levels suggesting a similar dynamic for endogenous centrin. I therefore hypothesized that a steadily increasing intracellular concentration would eventually reach c_{sat} and thereby act as the trigger for foci formation at the onset of schizogony. In single component systems, this dynamic is expressed as the dilute fraction reaching a plateau marking the c_{sat}, upon which additionally expressed centrin past this point condenses into the dense/foci fraction [170]. From this point onwards, the concentration of both fractions remains constant. This hypothesis would be in line with overexpression causing premature foci formation (Fig. 22A).

To determine whether this is in line with PfCen1-GFP dynamics in the cell, I quantified GFP signal within both foci and dilute fraction (cytoplasm and karyoplasm) as well as their volume across a large number of time-lapse microscopy movies of 3D7-DiCre_pFIO_hsp86p_PfCen1-GFP cells. From these values the PfCen1-GFP

concentration of the dilute fraction could be derived. Due to the quantity of cells and timepoints, this necessitated an automated analysis pipeline capable of distinguishing between foci and disperse/dilute signal. This was accomplished in collaboration with Dr. Severina Klaus by training the machine-learning software ILASTIK on cells with manually annotated foci (see 4.4.3 for details). In total, I analysed 33 movies of 3D7-DiCre_pFIO_hsp86P_PfCen1-GFP cells starting before the appearance of first foci and S-phase onset. I had previously used same population to determine the timing of first foci formation (Fig. 22A) and again normalized it to the timing of S-phase onset marked by the collapse of the first hemispindle into a mitotic spindle. As not all cells survived until egress and acquisition was started at different periods before S-phase onset, the n-value varies between timepoints. The analysis made no distinction between CP foci and ECCAs.

Quantification of average total GFP signal confirmed a steady increase of PfCen1-GFP expressed from pFIO (Fig. 24A). It initially appeared linear until 6 h before S-phase onset, then rising exponentially before reaching a plateau at 6 h post S-phase onset with a slight decrease before egress. In total, the average PfCen1-GFP per cell increased 7.6-fold from the beginning in the trophozoite stage to its peak during schizogony. The average share of PfCen1-GFP within the foci fraction (ECCA and centrosomal) rises steadily from approximately the previously determined mean timepoint of foci formation (185 min prior to spindle collapse, Fig. 22A) until also reaching a plateau at 6 h post S-phase onset at a maximum of 9.2% of total cellular GFP signal (Fig. 24B). However, foci are then rapidly disassembled ~4 h later within ~2h prior to egress. As mitotic spindles were typically still present at this point this dissolution appears to occur prior to segmentation (Fig. 24C). A discrepancy of the time between S-phase (at ~30 hpi) and egress (here ~13 h later) with the theoretical 48 h length of the intraerythrocytic asexual cycle is reconciled by the consistent observation that Pf3D7 in culture is closer to a ~44 h cycle [50]. Meanwhile the average dilute concentration, also normalized to S-phase onset, showed a comparatively mild variation of 31% between 0.74 at the beginning to a peak of 1.05 at ~6 h. However, no noticeable change occurs in the inclination around the time where most foci arise, only a ~10% decrease at the time where the foci fraction reaches its plateau. Although the considerable variation between cells introduces some uncertainty into any such evaluation. I could not determine the PfCen1-GFP concentration within foci as the volume of these small, often sub-diffraction, foci could not be accurately measured due to insufficient resolution.

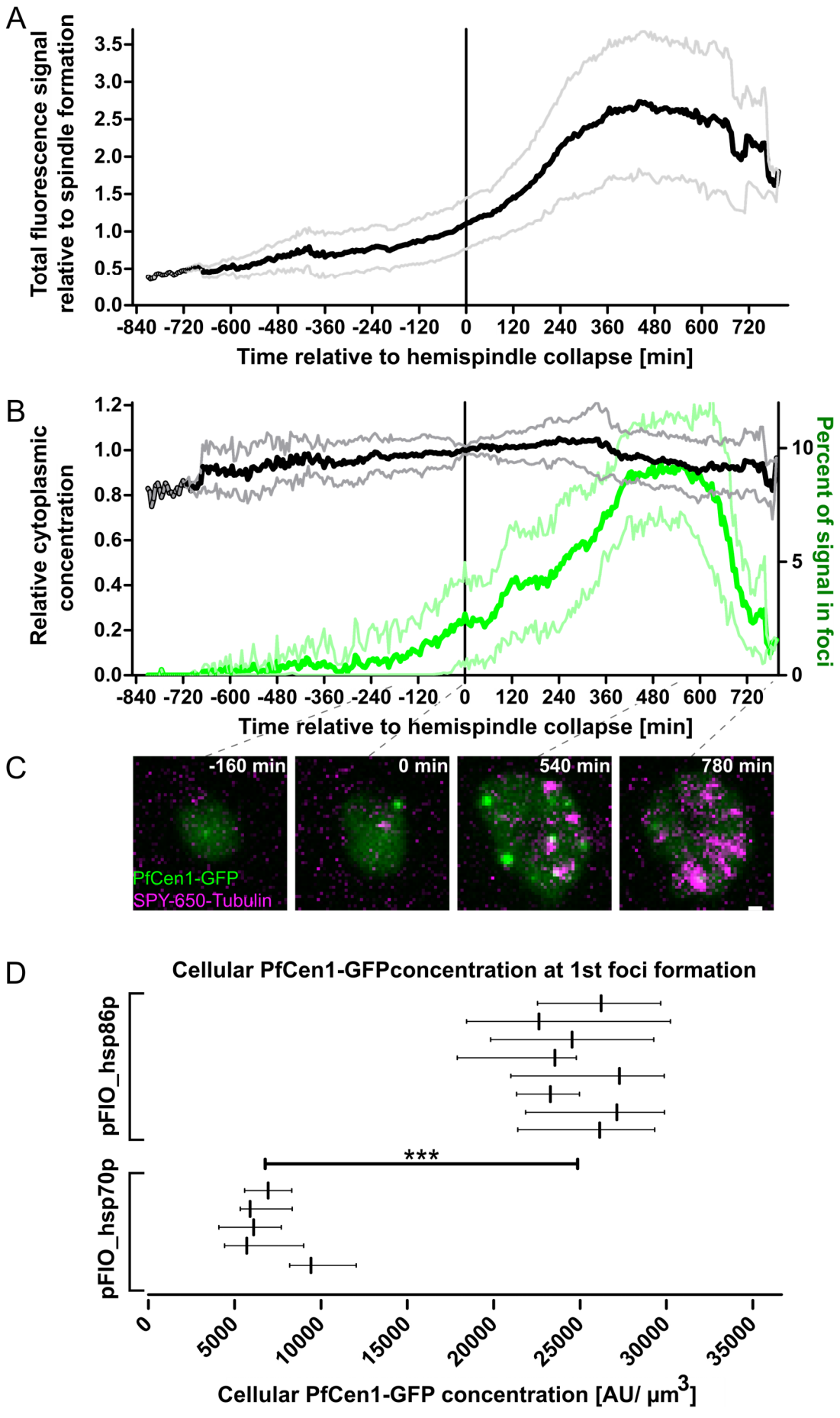

A
Total fluorescence signal relative to spindle formation
3.5
3.0
2.5
2.0
1.5
1.0
0.5
0.0
-840 -720 -600 -480 -360 -240 -120 0 120 240 360 480 600 720
Time relative to hemispindle collapse [min]
B
Relative cytoplasmic concentration
1.2
1.0
0.8
0.6
0.4
0.2
0.0
Percent of signal in foci
10
5
0
-840 -720 -600 -480 -360 -240 -120 0 120 240 360 480 600 720
Time relative to hemispindle collapse [min]
C
-160 min
0 min
540 min
780 min
PfCen1-GFP
SPY-650-Tubulin
D
Cellular PfCen1-GFPconcentration at 1st foci formation
pFIO_hsp86p
pFIO_hsp70p
***
0
5000
10000
15000
20000
25000
30000
35000
Cellular PfCen1-GFP concentration [AU/ µm3]

Figure 24 PfCen1-GFP dilute and foci fraction over time. 3D7-DiCre_pFIO_hsp86p_PfCen1-GFP cells were acquired via live-cell confocal imaging from before the appearance of their first PfCen1-GFP focus until egress. An ILASTIK based pipeline was used to determine signal and volume of the foci and dilute fraction to measure the total fluorescence signal over time **(A)**. These measurements were then used to derive the PfCen1-GFP signal density/concentration within the dilute fraction and the share of PfCen1-GFP bound within foci **(B)**. Values were normalized to the collapse of the hemispindle into the first mitotic spindle as visualized using SPY650-Tubulin and averaged. Timepoint 0 thus approximates the onset of schizogony, with the graph continuing until egress. $n \leq 33$. **(C)** Time-lapse confocal imaging of a representative 3D7-DiCre_pFIO_hsp86p_PfCen1-GFP schizont illustrating status of PfCen1-GFP (green) and spindles stained with SPY-650-tubulin (magenta, deconvolved) at different timepoints in the graphs. Maximum intensity projection. Scale bar 1 µm. Standard deviation is shown. **(D)** The cellular concentration in arbitrary units (AU) at the time of first foci formation (perpendicular lines) in 8 3D7-DiCre_pFIO_hsp86p_PfCen1-GFP and 5 3D7-DiCre_pFIO_hsp70p_PfCen1-GFP cells acquired in parallel as in (A-C). Thin horizontal lines mark the range of cellular concentration observed in each cell over the course of imaging. ***, $P<0.001$. Two-tailed t-test indicates statistical significance between both cell lines. (B) modified from Voß *et al.* (2023) [79]. Analysis performed jointly with Dr. Severina Klaus.

While I attempted to perform the same analysis on the 3D7-DiCre_pFIO_hsp70p_PfCen1-GFP cell line, no ILASTIK classifier with satisfactory accuracy could be generated due to the lower overall signal intensity and resulting inferior contrast. However, it did serve in testing another implication drawn from the hypothesis that rising PfCen1-GFP concentration acts as the trigger for assembly. If this is the case, then foci formation should commence at consistent intracellular PfCen1-GFP concentrations within each and between both cell lines (assuming consistent levels of endogenous PfCen1 and PfCen3). I plotted the manually determined appearance of the first focus against the total cellular PfCen1-GFP concentration at that time in cells from both pFIO_hsp70p and pFIO_hsp86p cell lines (Fig. 24D). To ensure that measurements were comparable I limited the analysis limited to cells that I had acquired in parallel under identical conditions. The sample size was therefore limited as only ~24 cells can be acquired simultaneously, of which a sizeable number die prematurely. Nonetheless, between both cell lines the first foci formed at significantly different concentrations, 6815 AU/µm^3 for pFIO_hsp70p and 24129 AU/µm^3 for pFIO_hsp86p. In addition, in each cell line, values varied over a range of 3731 AU/µm^3 and 7851 AU/µm^3 respectively. This indicates that foci formation does not occur at a consistent cellular PfCen1-GFP concentration between cell lines or within each independently.

In conclusion, the dilute PfCen1-GFP concentration does not indicate a clear critical threshold as the trigger for foci formation and dissolution. This indicates that other factors are involved in the regulation of this process. I further identified one or more yet unknown events at ~6 h post S-phase onset that stop further increase in centrin concentration and disassemble existing foci before egress in a coordinated manner.

[For the automated quantification of cellular GFP signal fractions I collaborated with Dr. Severina Klaus who provided instruction for the training of ILASTIK and programmed the ImageJ macros for subsequent data analysis and extraction.]

2.4 Determinants of centrin accumulation

My previous *in vitro* experiments highlighted which conditions and protein structures influence LLPS of PfCen1. As an extension, I sought to determine to which degree these findings are reflected by foci formation *in vivo*. Consistency or inconsistency between the two settings could help establish to which degree *in vitro* LLPS is relevant for understanding of *in vivo* accumulation.

2.4.1 Structural mutations abrogating LLPS *in vitro* impact *in vivo* foci formation

I previously showed the dependence of PfCen1 LLPS *in vitro* on specific structural elements, namely the Ca^{2+}-binding capability of the EFh-domains and the N-terminus (Fig. 11D, 15A). According to the hypothesis that PfCen1 foci *in vivo* are formed through LLPS, the previously studied Δ19-PfCen1 and EFh-dead-PfCen1 mutants would be expected to show an impairment in foci formation.

Towards this aim I employed the pFIO system to generate to cell lines, 3D7-DiCre_pFIO86p_EFh-dead-PfCen1-GFP and -Δ19-PfCen1-GFP, for the inducible over-expression of these mutants with a GFP tag to study their behaviour *in vivo*. A standard IFA against DNA and tubulin showed that Δ19-PfCen1-GFP continued to form foci at CPs, as well as ECCAs (Fig. 25A). Quantification of the ECCAs in early schizonts (1-5 nuclei, at least one spindle) did, however, show a lower ECCA frequency of 31% and ECCA to CP foci ratio of 0.16:1 (Fig. 25B). To put these numbers into context, I assessed expression intensity of Δ19-PfCen1-GFP via flow cytometry (Fig. 25C). The normalized median expression intensity of 9.7x fell in between the previously measured 3D7-DiCre_pFIO70p_PfCen1-GFP with 4.2x, and 3D7-DiCre_pFIO86p_PfCen1-GFP with 14.7x (Fig. 20D). The ECCA frequency and ECCA to CP foci ratio of Δ19-PfCen1-GFP was therefore even below that achieved by the far weaker expressing 3D7_hsp70p_PfCen1-GFP with 48% and 0.24:1. EFh-dead-PfCen1-GFP on the other hand had lost the ability to localize to the CP and form ECCAs, as I observed no GFP signal foci at the poles of mitotic spindles or in the cytoplasm (Fig. 25E). Instead, GFP signal was uniformly distributed across karyo- and cytoplasm.

Curiously, I also rarely (<3% of cells) observed atypical, extra-nuclear microtubules arising directly from Δ19-PfCen1-GFP foci at the outer CP core or ECCAs (Fig. 25D). I had not previously observed this for WT PfCen1-GFP foci.

In a contrasting approach, I sought to investigate how a phase separating centrin with N-terminal IDR and intact Ca^{2+}-binding from an evolutionary distant organism behaves in *Plasmodium*. While it is difficult to separate the influence of LLPS on PfCen1 foci formation from other potential interactions, a non-native centrin is less likely to engage with the native interaction partners due to limited homology. Towards this end I generated a 3D7-DiCre_pFIO_hsp86p_HsCen2-GFP cell line overexpressing the phase separating human centrin (see 2.2.1). As visualized using an IFA, HsCen2-GFP largely localized

diffusely across the cell, but also formed foci at CPs (Fig. 25F). These foci were less pronounced than those resulting from PfCen1-4-GFP but nonetheless consistent. However, I did not observe ECCAs.

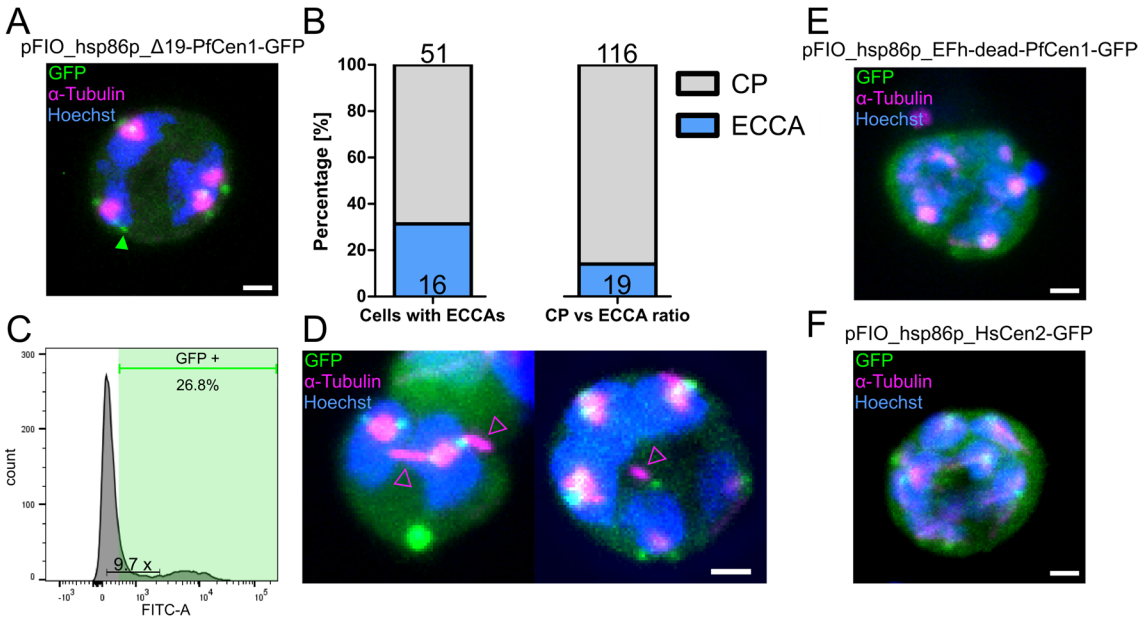


Figure 25 Influence of N-terminus and Ca^{2+}-binding on centrin foci formation. (A) Confocal IFA image of a 3D7-DiCre_pFIO_ hsp86p_Δ19-PfCen1-GFP schizont stained against tubulin (magenta) and DNA (Hoechst, blue), with PfCen1-GFP left unstained (green). Cell is a representative example of the cell population quantified in (B). Image is a maximum intensity projection. Scale bar 1 µm. **(B)** Quantification of the share of ECCA positive cells and ratio of ECCAs to CP foci in GFP positive induced 3D7_DiCre_ pFIO_hsp86p_Δ19-PfCen1-GFP cells. All cells were GFP positive schizonts with 1-5 nuclei and at least 1 intranuclear spindle. Inlays show number of events in the respective sub-population. **(C)** Flow cytometry analysis of 3D7_DiCre_ pFIO_hsp86p_Δ19-PfCen1-GFP cell line for frequency and intensity of Δ19-PfCen1-GFP expression 48 h post induction with RAP. Cells were gated for multinucleated parasites as determined using the DNA stain SYTO61. Share of the GFP positive (GFP +) population and ratio between median intensity of GFP positive to GFP negative population shown. **(D)** As in (A) but depicting rare events where unusual extranuclear microtubules arose from Δ19-PfCen1-GFP foci (magenta arrows) upon overexpression. **(E)** As in (A) but showing a representative induced schizont of the 3D7-DiCre_pFIO_ hsp86p_EFh-dead-PfCen1-GFP cell line. No foci were detected and thus not quantified. **(F)** As in (A) but showing a representative induced schizont of the 3D7-DiCre_pFIO_ hsp86p_HsCen2-GFP cell line. (A, E) modified from Voß *et al.* (2023) [79].

Taken together, these results show that mutations preventing LLPS *in vitro* affect foci formation *in vivo*, but to varying degrees. While the inability to bind Ca^{2+} completely prevents any foci formation, the deletion of the N-terminus does not affect CP localization and only decreases the frequency of ECCAs. Meanwhile the ability to localize to the CP is conserved in the evolutionary distant HsCen2.

2.4.2 PfCen1-GFP does not respond to intracellular Ca^{2+}-level modulation

As a central aspect of centrin biology, I demonstrated that Ca^{2+}-binding is integral for both LLPS *in vitro* and foci formation of PfCen1 *in vivo*. The cytoplasmic Ca^{2+} level changes over the course of the asexual cycle, starting at 373 nM during the ring stage (perhaps a remnant of 949 nM observed in merozoites), decreasing to 30 nM during the trophozoite stage, before rising again to 310 nM during the schizont stage [171]. I therefore hypothesized that a rise in Ca^{2+} levels could act as a trigger for foci formation, as the addition of Ca^{2+} does *in vitro*. If PfCen1-GFP responds to changes in cytoplasmic Ca^{2+} levels it is of further interest to determine how applicable findings from *in vitro* LLPS are to the *in vivo* setting.

Modulation of intracellular Ca^{2+} levels in *P. falciparum* has previously been achieved in various ways [171]. A particularly effective method was treatment with 10 µM of the calcium ionophore A23187, which increased cytoplasmic Ca^{2+} levels within 1 minute of addition by enabling the traversal of Ca^{2+} ions from internal storages and surrounding medium through membranes (Fig. 26A). Based on this principle, I further devised a variation of the experiment where the medium was saturated with EGTA, to instead attempt to deplete Ca^{2+} from the cell upon ionophore addition (Fig. 26B).

To study the effect of A23186 based Ca^{2+} increase and depletion on foci and their formation, I subjected induced 3D7-DiCre_pFIO_hsp86p_PfCen1-GFP to these methods of Ca^{2+} modulation during live-cell imaging. To observe whether Ca^{2+} acts as the trigger for foci formation at the onset of schizogony, I treated GFP-positive trophozoites with 10 µM A23187 (in DMSO) in cRMPI enriched with $CaCl_2$ to 0.75 mM to maximize the effect of the ionophore. While the physiological concentration of free Ca^{2+} ions in the serum is ~1.13 mM [172], increasing the concentration further leads to the precipitation of highly insoluble calcium phosphate, as RPMI uses a phosphate-based buffer system. 0.75 mM still exceeds the maximum concentration measured in schizont stages, which I thus considered sufficient. I could not observe clear formation of foci in the 25 minutes following exposure to the ionophore + Ca^{2+} across 10 cells (Fig. 26C). The only minor change was that after treatment, the PfCen1-GFP signal seemed to frequently increase within an unspecified subregion of the cell in proximity to the DNA. This accumulation, however, was much weaker and larger than foci, which I therefore considered an unrelated effect of the ionophore + Ca^{2+} treatment. No accumulation occurred in the control where I substituted the ionophore with DMSO.

In vitro chelation of Ca^{2+} by the addition of EDTA rapidly disassembles PfCen1 condensates. To study whether depletion of Ca^{2+} similarly leads to the disassembly of foci *in vivo*, I treated schizonts with established PfCen1-GFP foci with 10 µM A23187 in cRPMI containing 2 mM EGTA. EGTA is a metal chelator similar to EDTA with a higher specificity for Ca^{2+} over Mg^{2+}, which is also present in the cRMPI medium. Compared to the pre-treatment condition, I could not observe a clear change in the number or signal intensity of foci, both centrosomal and ECCAs, across 15 cells (Fig. 26D). Also, this time the treatment did not lead to an increase of GFP signal within a subset of the cell.

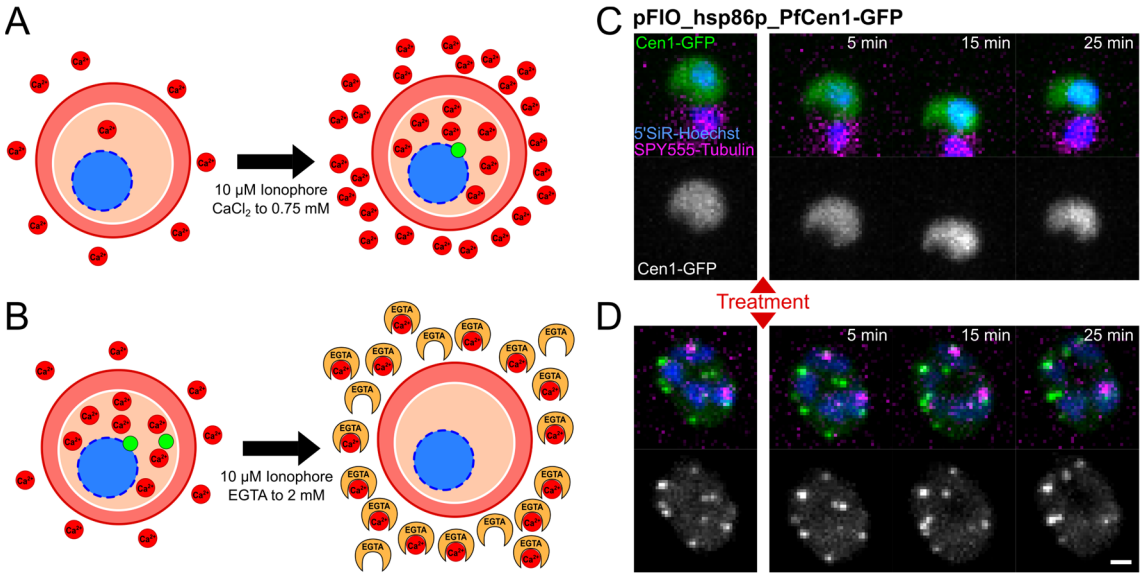


Figure 26 Effect of Ca^{2+} level on PfCen1-GFP foci formation and disassembly. Graphics illustrating the experimental principle behind the increase **(A)** or depletion **(B)** of intracellular Ca^{2+} via the calcium Ionophore A23187 in conjunction with increased Ca^{2+} concentration in the medium, or via chelation with EGTA. Hypothesized effect on PfCen1-GFP CP foci and ECCAs (green dots) is shown. Red circle, Erythrocyte; beige circle, parasite; blue circle, nucleus; red dots, Ca^{2+}; orange pincers, EGTA. **(C)** Representative confocal time-lapse images of induced 3D7-DiCre_pFIO_hsp86p_PfCen1-GFP parasites stained with SPY650-Tubulin (magenta) and 5'SiR-Hoechst (blue) before and after treatment. For increase of intracellular Ca^{2+} parasites without pre-formed foci were treated Ca^{2+} 10 µM Ionophore and $CaCl_2$ to 0.75 mM to observe potential foci formation. **(D)** As in C but schizonts with pre-formed foci were treated with 10 µM Ionophore and 2 mM EGTA for intracellular Ca^{2+} depletion to observe potential foci disassembly. Timepoints indicate time after treatment. Images are maximum intensity projections. Scale bar 1 µm.

In conclusion, modulation of cytoplasmic Ca^{2+}-levels using a previously reported method did not affect PfCen1-GFP foci assembly or disassembly to a measurable degree.

2.5 Investigating the material state of centrin foci

Thus far, I investigated whether the accumulation of PfCen1 could be driven by LLPS and observed the premature formation of both centrosomal foci and ECCAs under overexpression conditions. However, I did not yet assess material state of the resulting foci directly. While I previously observed dynamic rearrangement of PfCen1-Halo at the CP (Fig. 7C), the study of liquid behaviour on a sub-resolution limit scale via microscopy is challenging and often inconclusive. I therefore sought to determine whether these *in vivo* foci are liquid in nature by instead assessing their physical properties and comparing their characteristics to the PfCen1 liquids readily observable *in vitro*.

2.5.1 FRAP shows no exchange of PfCen1-GFP between foci and dilute fraction

While the liquid state of centrin assemblies can be easily assessed *in vitro* through characteristic behaviours such as droplet fusion or wetting, observation of these phenomena for PfCen1-GFP foci *in vivo* is more challenging. While deformation or wetting has been observed in live cells for certain biomolecular condensates like P-

granules [126], this was only possible due to their much larger size compared to the near-diffraction-limit centrin foci. Similarly, fusion of foci is difficult to differentiate from reciprocal attachment, which is further complicated by the rarity with which the sparse ECCAs come in close proximity within the cell. Another frequently used method employs fluorescence recovery after photobleaching (FRAP), wherein a subset of a presumed condensate is bleached to test for rapid recovery through the internal mixing expected in liquids. While this is approach is also not possible for the small centrin foci, liquid condensates typically show an exchange of protein between dilute and condensate phase [123], which can be assessed for the focus as a whole. While a typical feature, rapid recovery it is not exclusive to liquid but can also be observed in dynamic protein assemblies with high turnover [125], [153], [173].

The FRAP experiment was performed on PfCen1-GFP foci expressed by the 3D7-DiCre_pFIO_hsp86p_Cen1-GFP strain by Nicolas Lichti. The aim was to determine the percentage of PfCen1-GFP which can be freely exchanged with the dilute pool in the surrounding cytoplasm, called the mobile fraction (M_f). Towards this end live-cell imaging was performed on cells with established foci in 300 ms intervals, during which GFP within one CP or ECCA focus was bleached via strong 488 nm laser pulses, after which its recovery was observed for 60 s. To enable proper tracking the foci were only partially bleached as ECCAs especially are highly mobile. The intensity of the recovery plateau (I_p) relative to the initial pre-bleach intensity (I_i) and post-bleach intensity (I_o) determined the M_F (see 4.4.3 for details), with $M_f = 1$ indicating complete recovery[174]. Data points were compensated for gradual photobleaching resulting from imaging itself based on the decrease in GFP signal in an adjacent cell. To differentiate ECCAs and CPs cells were stained with SPY555-tubulin and SPY650-DNA so the proximity of the foci to spindles and nuclei could be assessed.
On average, neither CP foci nor ECCAs showed noticeable recovery up to 60 s post bleaching (Fig. 27A, B). This was reflected in an average M_F of 0.16 ± 0.21 for CPs and 0.05 ± 0.13 for ECCAs (Fig. 27C). Longer observation post bleaching did not lead to increased recovery. While the M_F of ECCAs was consistently low, the CPs showed a broader spectrum with an M_F up to 0.54. Nonetheless, there was no significant difference between CPs and ECCAs.

Importantly, these dynamics reflect the behaviour of PfCen1-GFP, not the WT protein. Given the relatively large size of the GFP-tag (27 kDa) compared to the small PfCen1 (19.6 kDa), concerns arose how it could influence the material properties of centrin assemblies. Indeed, PfCen1 does not tolerate endogenous tagging and I previously showed that PfCen1-GFP displays different LLPS dynamics than PfCen1 *in vitro* (Fig. 18A).

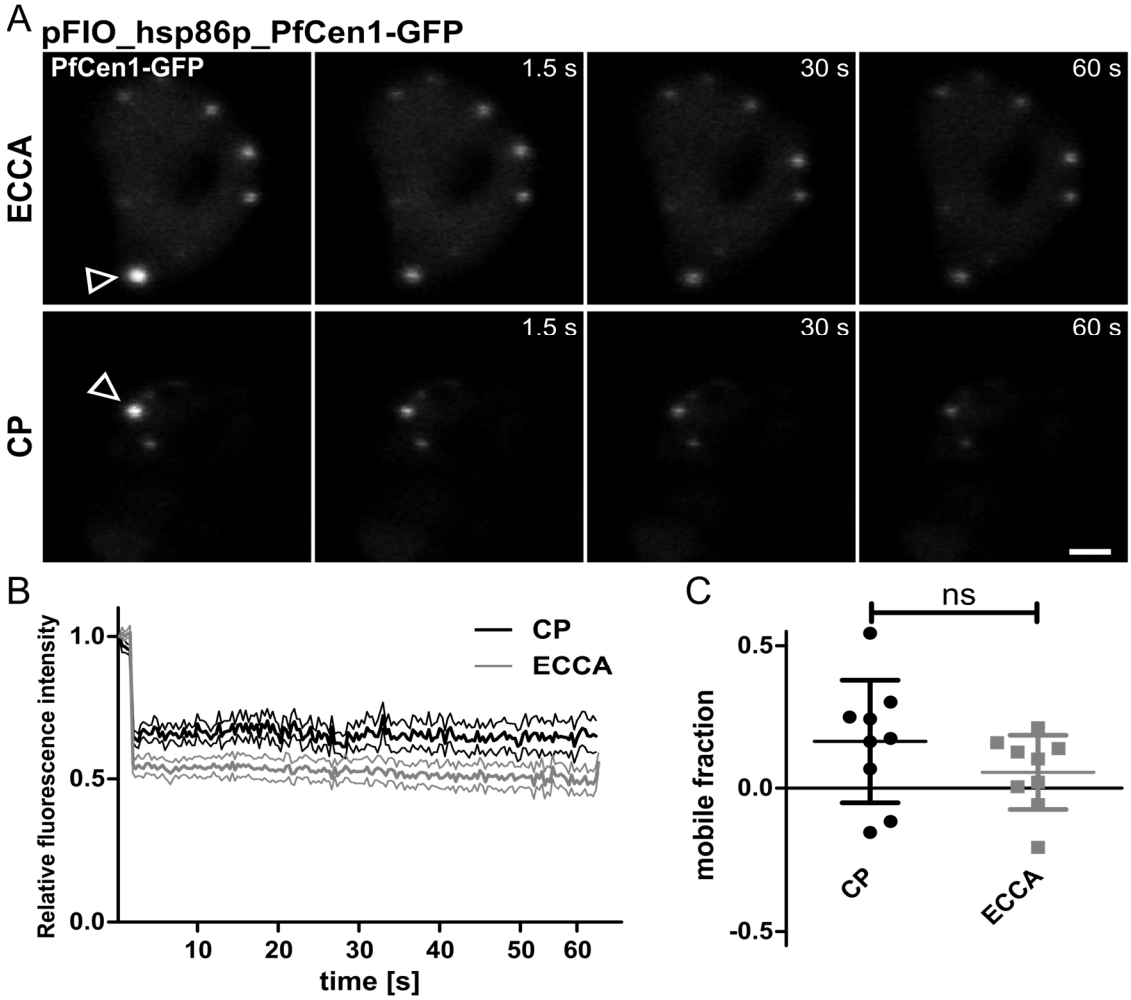


Figure 27 FRAP of PfCen1-GFP CP foci and ECCAs (A) Time-lapse confocal imaging of 3D7-DiCre_pFIO_hsp86p_PfCen1-GFP schizonts before and after bleaching of the indicated (white arrow) PfCen1-GFP focus. Scale bar 1 µm. **(B)** Average bleaching curves of CP (n = 9) and ECCA (n = 9) foci after bleaching. Standard deviation is shown. **(C)** M_F determined from individual bleaching curves for CP and ECCA foci. Significance analysed via t-test. Experiments and analysis performed by Nicolas Lichti. Modified from Lichti (2023) [175].

While PfCen1-GFP-6His also forms (at least initially) liquid droplets after Ca^{2+} addition and shows full EDTA reversibility, it had not yet been tested whether the tag could potentially influence the properties of the PfCen1 liquid such as internal fluidity and protein exchange rate as measured by FRAP. Towards this end, Nicolas Lichti performed FRAP on recombinant PfCen1-GFP-6His droplets *in vitro* formed after Ca^{2+} addition.

Here the size of the droplets allowed for partial bleaching to assess the internal mixing rate. Interestingly, droplets composed purely of PfCen1-GFP-6His only showed a very slow recovery and an M_F of 0.27 ± 0.06 in the bleached area, with the bleach spot remaining intact for over 2 min (Fig. 28). While no direct comparison with pure PfCen1-6His droplets was possible as FRAP requires a fluorescent tag, I devised a strategy where a difference to PfCen1-GFP-6His could be assessed by mixing them in different ratios. This approach revealed that the higher the ratio of PfCen1-6His. the higher the recovery and vice versa. As such, when PfCen1-GFP-6His content was reduced to a share of 10%, the M_F increased to 0.62 ± 0.1 after 2 min and the bleach spot would disappear completely, showing internal equilibration within the droplet. A 50% solution showed an

intermediary M_F of 37 ± 0.05. Of note, neither condition achieved an M_F approaching 1 after 2 min, which is reliant on protein exchange with the dilute fraction, as a major share of PfCen1-GFP within the droplet had been bleached. Importantly, it is this exchange which was measured by bleaching of the complete focus in *vivo*. This indicates that even under idealized *in vitro* conditions where centrin droplets are demonstrably liquid, only minor slow exchange with the dilute fraction is observed.

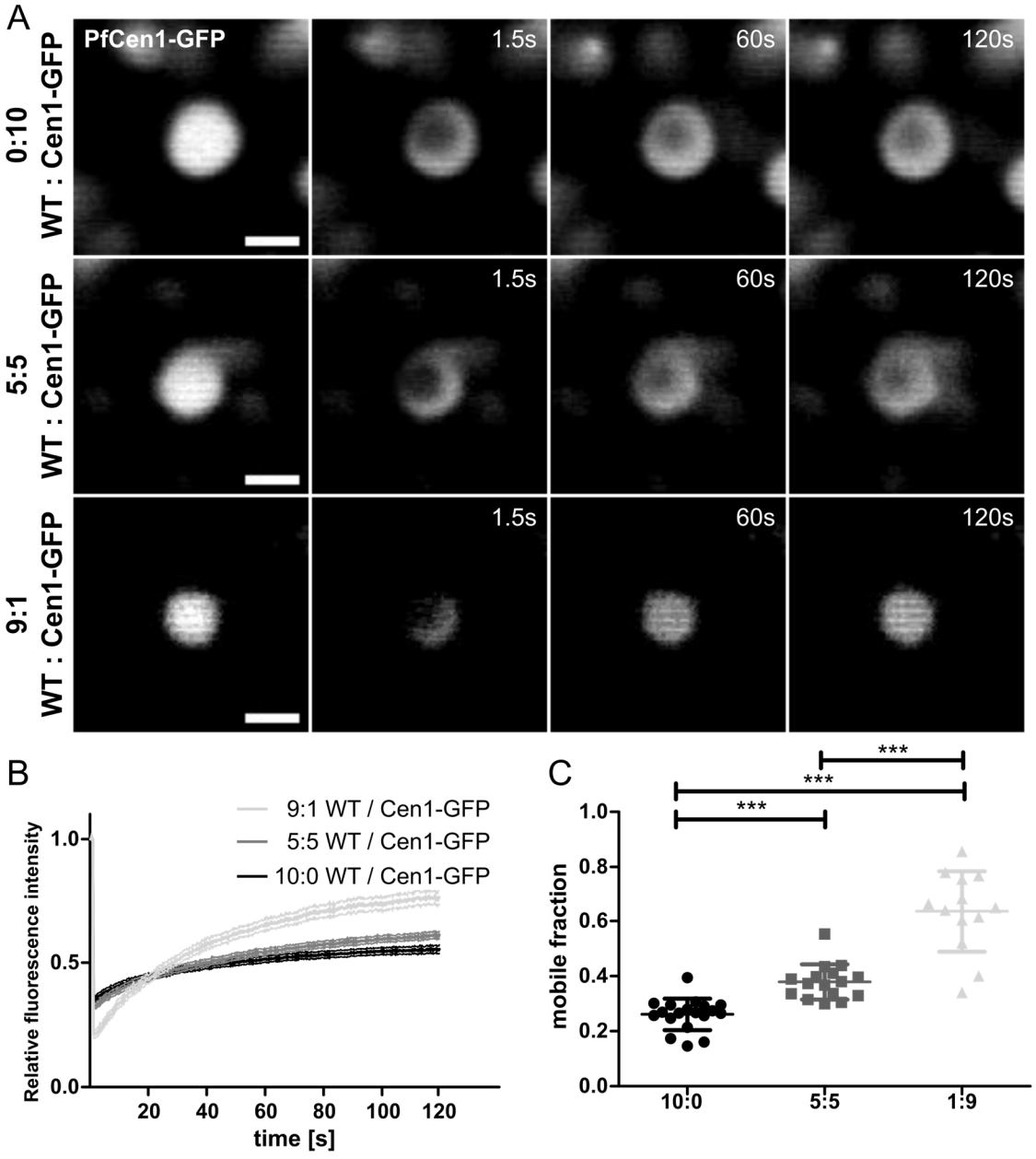


Figure 28 Influence of GFP tag on PfCen1 FRAP recovery. (A) FRAP of droplets consisting of recombinant PfCen1-6His (WT) and PfCen1-GFP-6His (Cen1-GFP) at different molar ratios at a combined concentration of 30 µM in 50 mM BisTris (pH 7.1), 2 mM Ca^{2+}, at 37°C. Timestamps indicate time post bleaching **(B)** Average bleaching curves of droplets after bleaching. Standard deviation is shown. $n_{0:10}$ = 20, $n_{5:5}$ = 16, $n_{9:1}$ = 21 **(C)** M_F determined from individual droplet bleaching curves. PfCen1-GFP-6His to PfCen1-6His is indicated below. Standard deviation is shown. Significance analysed via t-test. Experiments and analysis performed by Nicolas Lichti. Modified from Lichti (2023) [175]

In conclusion, neither CP nor ECCA foci showed significant recovery after FRAP, suggesting a more solid rather than liquid state. However, *in vitro* analysis casts doubt whether the experimental parameters could accurately assess a liquid state of native PfCen1 foci due to the strong influence of the GFP-tag on the properties of PfCen1 condensates, potentially introducing gel-like characteristics.

[All FRAP experiments and analysis were performed by Nicolas Lichti during his Master Thesis in 2022, which I supervised.]

2.5.2 Centrin foci are not stained by a protein aggregation dye

In previous experiments, PfCen1-GFP foci have exhibited behaviour partially in line with a gel-like or solid state (see 2.4.4). While gels and solid protein structures can arise in a controlled manner through coordinated assembly or maturation of condensates, uncontrolled aggregation is another theoretical possibility. To determine whether ECCAs arise through aggregation as an overexpression artifact I tested whether they can be recognized by the proprietary protein aggregate dye Proteostat.

Proteostat turns fluorescent if bound within the cross-β sheet structure formed by protein aggregates. To determine their presence in PfCen1 aggregates, which in its native conformation exclusively consists of loops and α-helices, I denatured recombinant PfCen1-6His by heating to 95°C and subsequent cooling. Investigation via confocal microscopy revealed successful staining of the resulting aggregates at a comparable intensity (above background) as aggregated lysozyme, a positive control provided by the manufacturer (Fig. 29A). In comparison, staining native PfCen1-6His as liquid droplets was barely visible (Fig. 29B).

With the ability of Proteostat to bind PfCen1 aggregates confirmed, I went on to investigate PfCen1-GFP foci *in vivo*. The dye had previously been employed as a dye in live *P. falciparum*, demonstrating the ability to stain intracellular aggregates [176]. 3D7-I induced DiCre_pFIO_hsp86p_PfCen1-GFP cells and stained them live with Hoechst and Proteostat. I employed live-cell imaging instead of IFAs of fixed cells to avoid potential aggregation induced by the fixation agent and staining process. The fluorescent spectra of Hoechst, GFP, and Proteostat did not allow for an additional tubulin staining (like SPY555-tubulin) to definitively distinguish whether PfCen1-GFP foci were centrosomal or ECCAs. Especially as I adjusted detector ranges to minimize bleed-through of GFP signal into the Proteostat channel to avoid a false-positive staining (see 4.4.3 for details). However, proximity to the nuclei provided a sufficient substitute.

Proteostat showed a successful staining of the parasite, with an inhomogeneous but ubiquitous distribution throughout the cell (Fig. 29C). PfCen1-GFP ECCAs did not show a Proteostat signal, which notably appeared to be excluded from the volume occupied by the GFP signal compared to the surrounding area.

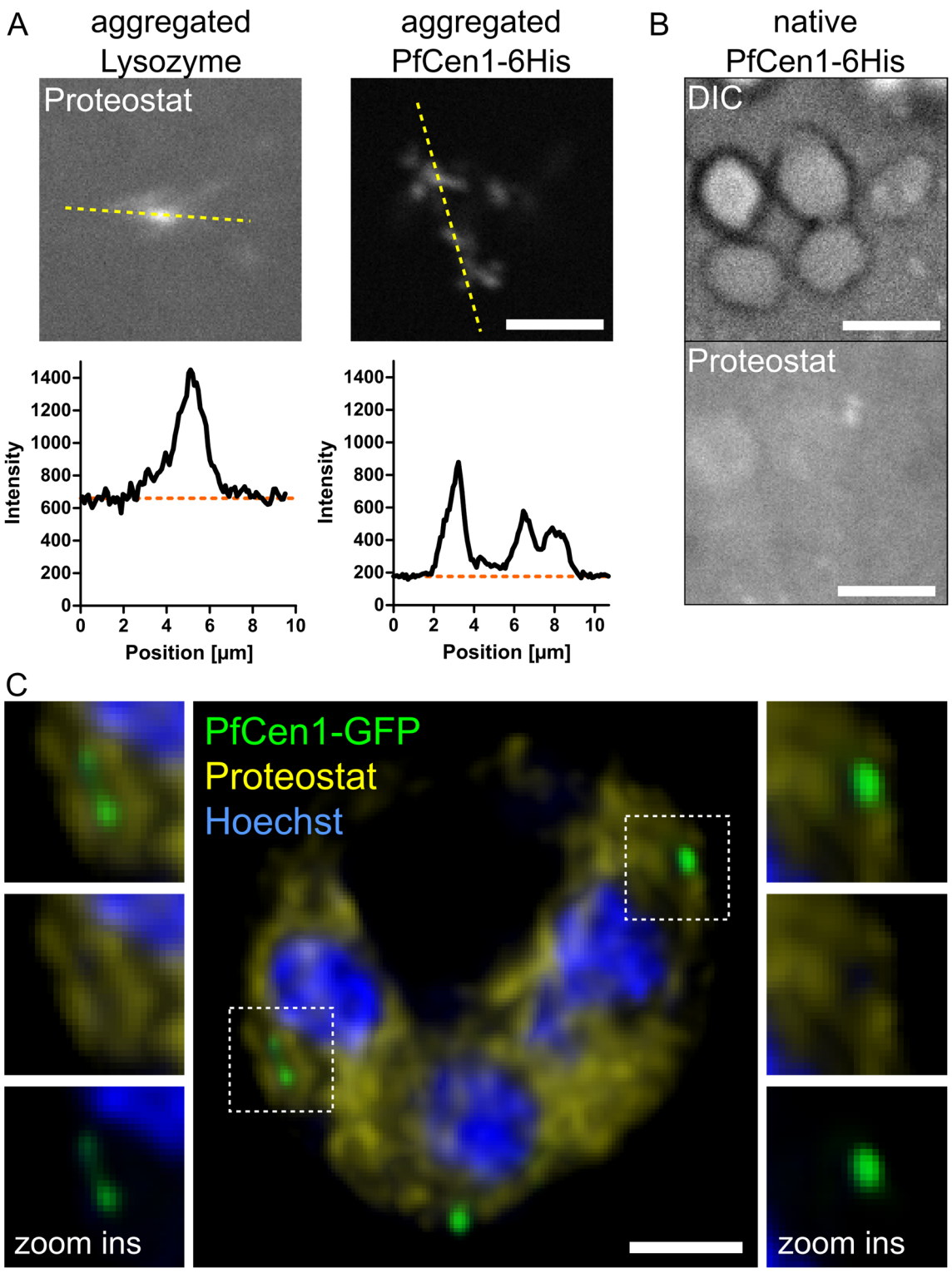


Figure 29 Testing of ECCAs for aggregation. (A) Confocal microscopy of 600 µg/ml aggregated lysozyme and 600 µg/ml heat-denatured PfCen1-6His (~30 µM) stained with Proteostat. 2 mM Ca^{2+} in 50 mM BisTris (pH 7.1) at 37°C. Graphs show intensity plot along the dashed yellow line (approximation). Orange dashed line indicates background signal outside aggregate. **(B)** PfCen1-6His droplets at 200 µM showing the DIC channel and Proteostat signal under the same conditions as in (B). Scale bars 5 µm. **(C)** Confocal imaging of a live 3D7-DiCre_pFIO_hsp86p_PfCen1-GFP schizont stained with Hoechst (blue) and Proteostat (yellow). Dashed squares show ECCAs enhanced for clarity. SP8 Lightning deconvolved. Scale bar 1 µm. (C) from Voß *et al.* (2023) [79].

In conclusion, Proteostat staining does not provide evidence supporting an aggregate nature of PfCen1-GFP ECCAs.

2.5.3 1,6-Hexanediole dissolves PfCen1 foci

My previous attempts at disrupting LLPS were specific for centrins (see 2.4). A frequently employed, non-specific method to dissolve condensates *in vivo* (and *vitro*) is the compound 1,6-hexanediole. The alkanediol interferes with non-polar interactions that often drive LLPS, typically leading to a near complete dissolution [177], [178]. It was further interesting to see how the CP, as a hypothesized liquid condensate, would be affected.

As PfCen1 would be used as marker for the CP, I first tested the effect of 5% (v/v) 1,6-hexanediole on PfCen1 LLPS *in vitro* via turbidity assay. As 1,6-hexanediole has a melting point of 45°C, addition to the reaction was only possible as a dilution (in H_2O). As this in turn necessitated the addition of a larger volume, which itself would dilute the turbidity and lower the protein concentration, potentially leading to a further decrease of LLPS, I performed a control experiment with the same volume of water (Fig. 30A). The volume addition itself led to a mild decrease in turbidity by 9.7%. In comparison the addition of 1,6-hexanediole only showed a minor additional effect with a decrease of 20.3%, far from complete dissolution. I nonetheless investigated the *in vivo* effect on PfCen1 foci at the CP. I treated non-overexpressing cells with 5% 1,6-hexanediole for 5 min at 37°C before paraformaldehyde (PFA) fixation, followed by an IFA against DNA, tubulin, and PfCen1 (Fig. 30B). Initial analysis showed the majority of mitotic spindles without adjacent foci. I confirmed this by quantification of 36 treated cells where 74.5% were without focus, whereas only 2.4% of spindles in 33 untreated cells lacked foci (Fig. 30C). I only counted early schizonts before the segmenter stage and past the onset of S-phase (based on nuclei number and intranuclear spindle stage). I chose this range as centrin foci disappear during segmentation and may not be present at hemispindle poles prior to onset of the S-phase. During this experiment I additionally observed atypical, elongated morphologies of the nuclear microtubules.

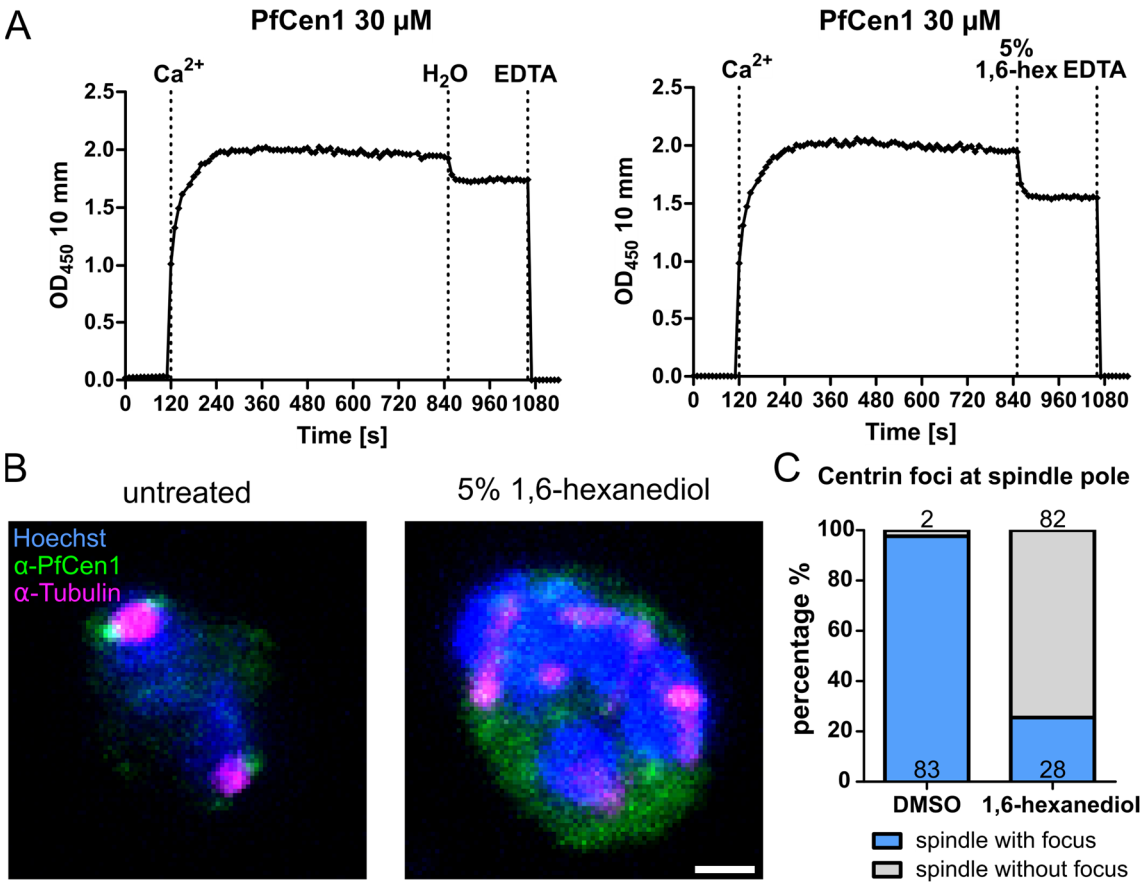


Figure 30 Effect of 1, 6-hexanediol on PfCen1-GFP foci. (A) Turbidity assays of recombinant PfCen1 at 37°C in 50 mM BisTris (pH 7.1). 50% 1,6-hexanediole (Hex) in H_2O was added to 5% (v/v). The same volume of ddH_2O was added as a control (H_2O). Turbidity was quantified as light adsorption at 450 nm. Ca^{2+}, $CaCl_2$ addition to 2 mM; EDTA, EDTA addition to 10 mM. **(B)** Confocal IFA image of uninduced 3D7-DiCre_pFIO_ hsp86p_GFP-T2A-PfCen1 schizonts stained against tubulin (magenta) and DNA (Hoechst, blue), and PfCen1-GFP (green). Cells were either treated for 5 min with 5% (v/v) 1,6-hexanediole in cRPMI or left untreated. Cells are representative example of the cell population quantified in C. Images are maximum intensity projections. Scale bar 1 µm. **(C)** Quantification of the share of spindles with at least one PfCen1 focus in cells treated with 1,6-hexanediole (36 cells) or left untreated (33 cells). All cells were schizonts with at least 1 intranuclear spindle. Inlays show number of events in the respective sub-population. Modified from Voß *et al.* (2023) [79].

In conclusion, the condensate dissolution compound 1,6-hexanediole removes PfCen1 foci from the CP and leads to aberrant spindle morphology. However, it has only a minor effect on PfCen1 condensates *in vitro*, which in turn raises the question whether the *in vivo* effect was caused by a disruption of centrin foci specifically or the CP in general.

3 Discussion

Since their first description almost 40 years ago, centrins have been established as a universal centrosome component across all branches of eukaryotes [76], [77]. Strongly conserved not only throughout evolution, but also in structure, and their consistent recruitment to a diverse range of centrosomal structures. Meanwhile, their function within this context remains poorly understood in most cases. In this work, I aimed to study centrins within the context of the atypical centriolar plaque of the malaria parasite *Plasmodium falciparum*. I therein uncovered a previously unknown aspect of centrin biology, the evolutionarily conserved ability to undergo liquid-liquid phase separation *in vitro*. This led to the first study of LLPS in *P. falciparum* with the aim to understand the role of this process in centrin recruitment to centrosomes. In the following I will discuss the implications and limitations of my findings for centrin biology within the context of malaria parasite schizogony and other eukaryotes. I will further suggest future experimental avenues where open questions remain.

3.1 Methodological advancements

Investigation of LLPS in living cells remains challenging even in model organisms [125], [173]. In addition, studies on divergent organisms such as *P. falciparum* are often complicated by smaller research communities as well as inherent biological obstacles such the parasite's asexual schizont stage's small size decreasing accessibility. As a result, many advanced or even basic research tools have not been adapted. As this work presents the first study of LLPS in *Plasmodium* parasites it therefore required the development and implementation of new tools as a pre-requisite for further research.

3.1.1 pFIO – An inducible overexpression system for *P. falciparum*

Overexpression has long since been established as a fundamental method in cell biology and genetics, with a broad range of applications [179]. It is frequently employed as an alternative to loss of function approaches, e.g. when gene knockouts or knockdowns prove impossible. While these methods rely on a depletion of the protein, overexpression can instead disturb the protein equilibrium in the opposite direction to evoke a phenotype. In addition, where loss-of-function mutations of endogenous genes are challenging, overexpression of mutants can evoke a dominant-negative phenotype by outcompeting the WT protein. Furthermore, many other fundamental methodologies like recombinant protein production or ectopic expression of tagged proteins for microscopy, rely on overexpression. More recently overexpression has also been routinely used for *in vivo* studies on LLPS due to the dependency of the phenomenon on protein concentration [153], [173].

Overexpression plasmids using strong promoters of housekeeping genes such as hsp70 have long been established in *Plasmodium* [164]. However, regardless of promoter strength, expression is very heterogenous as I observed for PfCen1-GFP using the pARL

system (Fig. 20F). This was also the case for other essential genes, that in my experience, could not be tagged endogenously, such as PfαTubulin-GFP, amongst others. On the other hand, expression of PfPCNA1-GFP from the same plasmid achieved almost universally high levels [50]. While circumstantial, the evidence points towards a negative selection by the parasite against fitness cost incurred through overexpression, such disturbances of sensitive equilibria or dominant-negative effects of altered and/or tagged proteins. While plasmids carry a resistance gene for drug selection, even parasites without measurable expression maintained drug resistance. Therefore, negative selection appears to occur by silencing, mutation, or recombination of the POI expression cassette and not loss of plasmid. As the low transfection efficiency of *P. falciparum* (~10^{-8} [180]) results in a lengthy recovery process of the population before a transgenic parasite can be analysed, the population has ample time to select against overexpression.

Inducible overexpression systems are thus attractive to minimize the exposure of the parasite to overexpression related fitness costs prior to analysis to prevent counterselection and preserve cells with strong expression. They can further offer the option to turn on expression at specific developmental stages for time-resolved phenotype analysis, with uninduced parasites additionally providing an excellent internal control. However, such systems are limited in *P. falciparum* and typically rely on reversal of an otherwise constant knockdown. One such example was introduced to inducibly express the sexual commitment factor GDV1, which was tagged with the FKBP destabilization domain to degrade the protein after translation [181]. While expressed from a constitutive promoter, the protein is constantly degraded until the stabilization ligand Shield-1 is supplied. Addition of Shield-1 achieved sexual conversion of 75% of the population, compared to a default of 3-5%. Another example is the TetR-DOZI system, which has, found much broader application as an inducible knockdown system [182]. Herein a parasite constitutively expressing the TetR-DOZI fusion protein silences an expression cassette by exploiting an mRNA sequestration mechanism of *Plasmodium*. This is accomplished by aptamer repeats in the 5' and 3'UTR of an mRNA, which are bound by the TetR domain, with the DOZI domain then targeting the mRNA to native quiescent complexes leading to translational repression [45]. Addition of anhydrotetracycline (aTc) releases TetR-Dozi from the mRNA effectively activating the expression cassette, thereby increasing mean normalized YFP intensity ~10-fold in flow cytometric analysis. A previous version similar to the Tet-ON system with a single aptamer in the 5-UTR and TetR alone was much less efficient [183].

These systems have disadvantages. To achieve leak-free repression for prevention of fitness costs and counterselection by the parasite the maximum, expression strength of the cassette is effectively limited by the knockdown efficiency. Introduction of the aptamers into the 3'UTR alone was noted to decrease maximum expression 2-3 fold [182]. In case of the FKBP system, the POI can only be expressed as a fusion protein with the degron, not in its tag-free form. In comparison pFIO employs a DiCre/loxP approach, wherein a single strong promotor is followed by a floxed 1st ORF, which mediates WR resistance and is removed upon DiCre activation, and a 2nd ORF encoding the POI. As the two are separated by a stop codon and 3'UTR the 2nd ORF is not transcribed in the

uninduced state, I observed no visible leakiness during imaging of uninduced populations or WB (Fig. 23C, D). The promoter strength is therefore not limited as no knockdown is necessary, thus allowing for the use of stronger promoters. As such, pFIO_hsp86p_PfCen1-GFP achieved a normalized expression of up to 14.7x compared to ~10x achieved by the TetR-DOZI system [182]. Although direct comparison is perhaps complicated by the expression of different proteins. Additionally, the POI can be expressed without tag.

However, the pFIO system also has its limitations. Most importantly, I only achieved successful expression in a subset of cells, ranging from 25-55% of the population depending on the POI (Fig. 20D, 23D, 25C). Surprisingly, this was even true for expression of GFP alone (data not shown), which should not incur a fitness cost. Other proteins such as PfαTubulin-GFP could not be expressed at all. The GFP-positive population could additionally be prone to overestimation as SYTO61-based flow cytometric analysis cannot differentiate between multi-nucleated cells and multiple infection of erythrocytes, which have a higher chance to contain a GFP-positive cell. In contrast, the FKBP system achieved expression in ~70% of the population (based on sexual conversion rate), while the TetR-DOZI system led to expression in the entire population ([181], [personal communication with Dr. Jacquin Niles, 2023]). Incomplete expression limits the applicability for bulk population analysis, but is fully compatible with single-cell based assays, such as microscopy. And while a tag-free expression is possible in principle, additional expression of a fluorescent tag is necessary to distinguish induced and uninduced cells. However, the T2A version of pFIO remedies this by efficiently separating the tag from the POI (Fig. 23). The pFIO system was vital for the high overexpression of PfCen1-GFP beyond what regular systems could achieve. As a result it has found routine application for the expression of proteins unrelated to this work due to its superior expression levels, even when using the lower expressing pFIO_hsp70p. It could therefore prove a valuable asset for the expression of challenging proteins for localization studies or investigation of dominant-negative effects using microscopy.

It should be mentioned that the principle pFIO architecture of two ORFs with the first being removed via DiCre is not entirely novel, but was inspired by similar designs employed in model organisms and previously in *P. berghei* [163]. Although in this case, the plasmid wasn't used for overexpression but merely as a qPCR reporter template to measure DiCre efficiency. My primary independent contribution to the design is the integration of the resistance gene into the 1st ORF, which not only reduces plasmid size, but in theory, also prevents silencing of the expression cassette prior to induction. Indeed, increased WR selection pressure prior to induction did select for increased POI expression. I also generated a follow-up design incorporating the T2A skip peptide (Fig. 23A), which in addition to offering an independent expression marker has potential use for multiplexed gene expression.

Beyond its practical benefits, the often unexpected behaviour of the system has revealed some potential knowledge gaps about gene silencing and plasmid biology in *P. falciparum*. As the 1st ORF mediates WR resistance, the plasmid must be present, and the

expression cassette actively expressed in 100% of the population. Yet after induction the 2nd ORF is only active in ~50% of the population. Potential underlying causes of this phenomenon are discussed below:

The first option is incomplete recombination (Fig. 31A). However, this is unlikely to be the cause, as a near 100% recombination efficiency of DiCre in *Plasmodium* has been repeatedly demonstrated by qPCR, Southern blot, or lethal knockouts, both for endogenous loci and episomal plasmids [161]–[163]. Two clonal lines I generated, with an endogenous pFIO_hsp86p_PfCen1-GFP cassette integrated into the silent *p230p* locus, also showed a very similar performance to the episomal version (data not shown). Liang *et al.* recently published a similar system for expression of dCas9 from an endogenous locus, with the difference that the first ORF only encoded GFP and no resistance gene [184]. Their system corroborates absence of leak expression, and a lethal knockdown can prevent growth across a culture. However, PCR and WB analysis suggest the presence of loci with the 1st ORF intact, suggesting a minor degree of incomplete recombination. However, these relatively rare events are likely insufficient to explain the degree of unsuccessful induction observed for pFIO, although efficiency could be confirmed via qPCR analysis.

A frequent observation were erythrocytes infected by multiple parasites in the same stage, of which some expressed PfCen1-GFP and others did not. These parasites likely originate from the same mother cell due to the spatial proximity required to infect the same host cell in a static blood culture system within a similar timeframe. This could be caused by an uneven distribution of plasmids to daughter cells (Fig. 31B), which has been documented in *Plasmodium* by DNA-FISH [185]. However, this does not explain the uneven expression by the endogenous version of pFIO, which should be present in every genome.

It is therefore more probable that recombination and plasmid distribution are mostly successful, but that the 2nd ORF fails to express. This could arise either from random nonsense-mutagenesis or epigenetic silencing prior to induction (Fig. 31C, D). In mammalian cells silencing of episomal plasmids was associated with the presence of bacterial sequences (e.g. origin or replication, bacterial drug resistance genes, etc.), which was speculated to be the result of heterochromatin formation and subsequent spreading from these transcriptionally inactive regions [186]. Further studies suggested that silencing is indeed associated with heterochromatin histone markers, but not caused by CpG methylation [187], [188]. The uneven expression in daughter cells arising from the same progenitor would argue against silencing being a trait inherited through parasite lineages, but also against the inheritance through mutated/silenced plasmid lineages. Instead, this would require mutation or silencing events to occur anew in each generation after induction. Especially considering that the promoter must have been active in the previous cycle due to being resistant to the then still applied drug pressure.

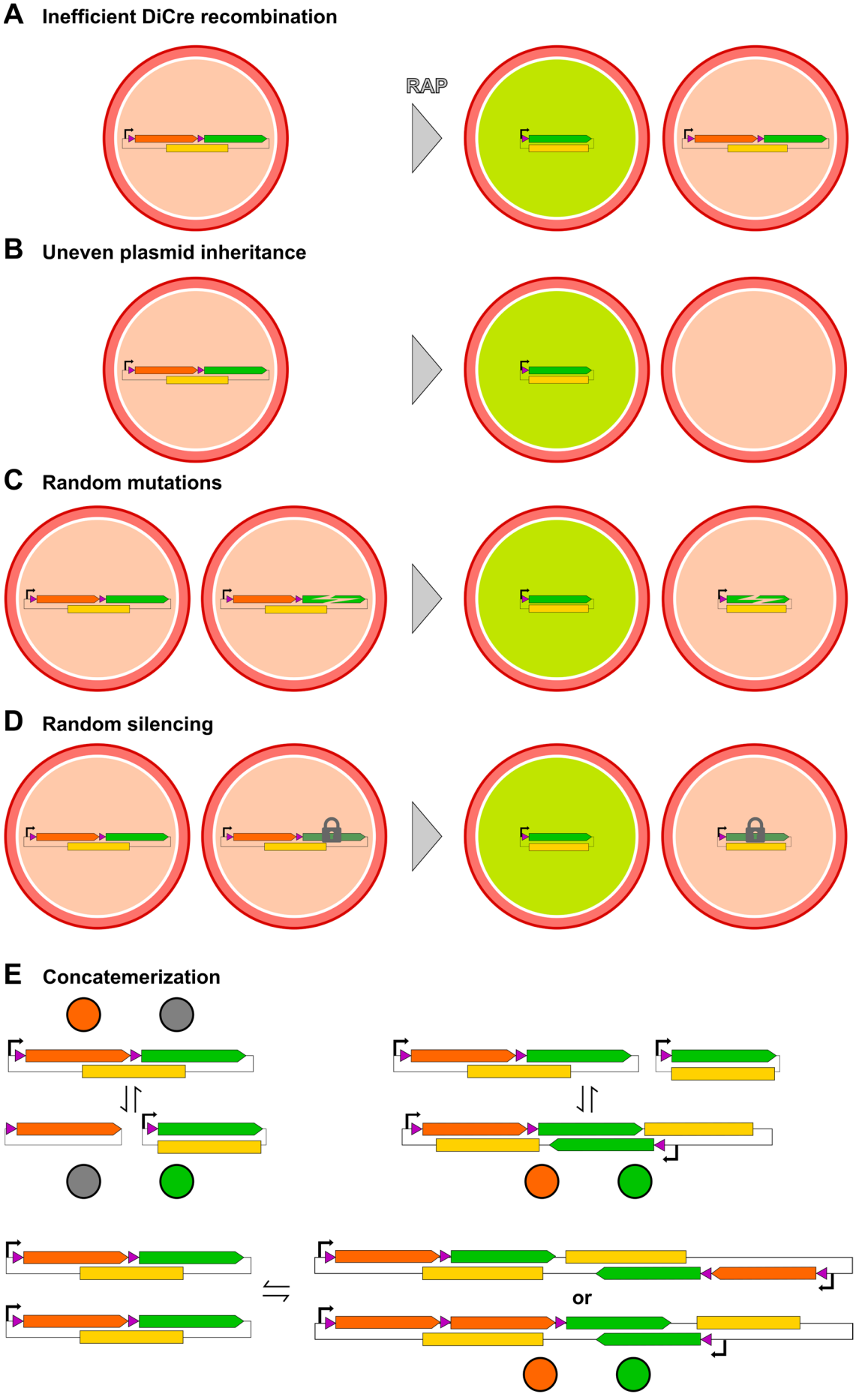

A Inefficient DiCre recombination
RAP
B Uneven plasmid inheritance
C Random mutations
D Random silencing
E Concatemerization
or

Figure 31 Potential causes underlying inconsistent pFIO expression. Graphics illustrating pFIO plasmids in parental parasites prior to induction and daughter cells in the generation post induction in different potential scenarios explaining inconsistent pFIO expression. Orange bar represents the 1st expression cassette (ORF + 3'UTR) with resistance gene, green bar represents 2nd expression cassette with GFP tagged gene, yellow bar represents other plasmid sequences, i.e. origin of replication, AmpR, etc. Arrow represents promoter, purple triangles loxP sites. **(A-E)** Green parasite represents detectable GFP-expression. **(C)** Crack in green bar represents nonsense-mutation. **(D)** Lock in green bar represents silencing. **(E)** Primary and alternative DiCre/loxP recombination events leading to concatemerization. Orange and green circles represent expression of resistance gene and GFP-tagged gene respectively.

Finally, persisting drug resistance after induction, including parasites expressing the 2nd ORF, suggests that recombination of pFIO is, at least partially, not functioning as intended. While this could be explained by the presence of multiple plasmid copies per parasite, one induced and one not, the high efficiency of DiCre would argue against a high prevalence of uninduced plasmids. However, multiple plasmid copies open the possibility for loxP recombination in *trans* between plasmids, leading to the formation of concatemers (Fig. 31E). While recombination in *trans* should be less likely than in *cis* due to the decreasing efficiency of DiCre/loxP with distance between loxP sites [189], it could create a stochastic distribution of plasmids expressing both ORFs after induction. Integrating the pFIO cassette into the genome as a single copy did not alleviate this problem, although additional non-integrated copies of the cassette as episomal plasmids cannot be ruled out. Also, the DiCre reaction itself is reversible, as long as the "looped-out" resistance gene is in physical proximity.

All these different explanations need to be further contextualized by the curious observation that the degree of expression appears to be affected by which POI is expressed. This is despite the absence of leak-expression theoretically precluding counterselection against potentially detrimental proteins prior to induction. Indeed, the induction efficiency remained fairly consistent over extended culturing period, while expression from pARL_PfCen1-GFP decreased noticeably after a few weeks in culture. Additionally, there was also little opportunity for counterselection post induction, as expression was typically induced only 48 h prior to analysis at the very end of the previous cycle. As this marks the minimum of hsp86p and hsp70p transcriptional activity and the delay from transcription to translated protein, the POI expression should not yet affect the production or viability of progeny. Additionally, induction during the ring stage of the same cycle as analysis showed worse performance (data not shown). This variation in induction and expression efficiency between proteins can therefore not be explained by the previously mentioned incomplete recombination, uneven plasmid distribution, concatemers, or random mutation/silencing prior to induction, as these would all be expected to occur randomly, thus leading to similar induction (in)efficiencies. In the case of epigenetic silencing, this mechanism would instead have to occur in a targeted sequence specific manner. Most likely after induction, given that parental parasites can give rise to both expressing and non-expressing daughter cells. This would happen in spite of, or perhaps especially because of, the genetic sequences matching the endogenous gene (minus introns). This theory would be contradicted by the fact that GFP, a non-native sequence, was also targeted by this hypothesized silencing. However, this could be tested by replacing the PfCen1 encoding sequence with a codon-optimized version.

Retrieval of the plasmid before and after recombination from transfected *P. falciparum* strains via PCR and subsequent analysis could provide further hints if recombination occured as intended. This would help elucidate if any of the mechanisms proposed above, or perhaps a combination thereof, is at the root of the issue. For the moment, however, the cause of pFIO's inconsistent expression remains a mystery.

3.1.2 Establishing live-cell STED in *P. falciparum*

As light-microscopy is constrained to a maximal resolution of ~200-250 nm due to the Abbe limit [190], microscopic analysis of *Plasmodium* has long been hampered by the small size of the parasite. The asexual blood stages range from 1 µm merozoites to 5 µm schizonts, with nuclei of only 1 µm diameter, and a CP of ~400 nm [52]. Recent established super-resolution methods like STED and Ultrastructure Expansion microscopy (U-ExM) have therefore greatly benefitted the structural resolution of small organelles [68], [191], [192]. However, super-resolution microscopy of live-cell processes in *Plasmodium* has thus far been limited to Airyscan-detector based and Structured Illumination (SIM) microscopy [53], [71], [193], which offer a limited lateral resolution improvement of up to 120 nm and 100 nm respectively [194], [195]. Meanwhile, STED microscopy on fixed *P. falciparum* schizonts can achieve up to 40 nm lateral resolution [personal communication with Dr. Julien Guizetti, 2023]. To study the processes within the CP I, therefore adapted live-cell STED microscopy to *Plasmodium* for the first time.

As available fluorescent protein tags are not suited for STED microscopy due to insufficient photostability, I employed the self-labelling enzyme tag Halo to label PfCen1 with STED-capable synthetic fluorophores. This tag is well established for live-cell STED in other organisms and did not affect the localization of PfCen1-Halo to the CP (Fig. 7B) [196]. A critical step in the adaptation to *P. falciparum* was the choice of dye, as PfCen1-Halo in the parasite cytoplasm is separated from the medium by 3 membranes (erythrocyte, PV, and parasite membrane). As such membrane-permeability was an important criterion. Two rhodamine based dyes developed by the Johnson lab, MaP618-Halo and MaP-SiR-Halo, achieved good results using a 640 nm excitation laser [144], [197]. MaP-SiR-Halo especially demonstrated excellent fluorogenic properties with the fluorescent zwitterion form being stabilized after binding to the Halo tag (Fig. 7A). This allows for continuous labelling of newly expressed protein, as it eliminates the need for a dye washout prior to imaging. While STED of red dyes generally yields higher resolution, using far-red dyes reduces phototoxicity due to lower-energy excitation [198]. In practicality, the limiting factor for performance was the expression level of PfCen1-Halo, as lower expression leads to quicker bleaching. This not only reduces the number of timepoints but also resolution, as this is determined by the intensity of the depletion laser, which is the primary cause of bleaching. As PfCen1-Halo expression from pARL was similarly inefficient as that of PfCen1-GFP, the resolution was therefore typically limited to ~90-100 nm. Bleaching further necessitated a trade-off between 3D information or imaging of a single focal plane over longer periods. Using stronger expression systems like pFIO or tagging proteins with better expression properties would likely improve

resolution, temporal sampling density, and allow for acquisition of 3D information. Implementation of adaptive illumination and recently improved Halo tag variants, which increase the brightness and fluorescence lifetime of rhodamine dyes could offer further improvements [199].

3.2 Implications for *Plasmodium* and centrin biology

The evolutionary distance between *Plasmodium* and established model organisms gave rise to a highly divergent replication biology [50], [68]. Amongst its many divergent aspects, the centriolar plaque is one of the most unique features. While important advancements regarding its structure were recently made, its organization and composition remain mostly unknown, with centrins being amongst the very few identified components [52], [71]. Members of this family of universal centrosomal proteins from different species have been researched for decades producing detailed studies on their biochemistry [117]–[120]. These studies consistently reached the conclusion that centrins can self-assemble, but the nature of the resulting structures and the implications for their cellular biology remained unknown. My discovery of their ability to undergo LLPS within this study could have important implications for understanding the interactions underlying the centrins' different ascribed cellular functions, as well as their mode of localization, not only to the centriolar plaque, but to the broad range of diverse eukaryotic centrosomes.

3.2.1 Centrosomal localization of PfCen1-4

Centrins were first described as a centrosomal component in *Chlamydomonas reinhardtii* and have since been consistently found at centrosomes of other eukaryotes as well, including those of humans and yeast [77], [97], [200]. However, other localizations have been documented, e.g. the striated flagellar root in *Tetraselmis striata* or as part of the basal complex, apical preconoidal ring, and peripheral annuli in *Toxoplasma gondii* [76], [105]. In this work, my observation of PfCen1-4-GFP in asexual stages showed a localization as an evenly distributed diffuse cellular background, which accumulates into foci exclusively at the outer CP core at the onset of schizogony (Fig. 6B). This is in line with antibody stainings against endogenous centrins also showing CP foci with no other prominent localizations [52], [68]. The presence of dispersed WT centrin can, however, not be easily confirmed as it cannot be clearly distinguished from unspecific antibody background staining. U-ExM studies suggest that centrins only occupy a subset of the protein-dense outer core [52], [68]. In case of NF54_pARL_PfCen1-GFP, accumulation was determined in a parallel study to commence very shortly before the collapse of the first hemispindle into the mitotic spindle [52]. Interestingly, this draws parallels to recruitment of HsCen2 during centriole duplication and during S-phase [98]. The diffuse background persists throughout schizogony, even after onset of foci formation (Fig. 6A, 21A, 24B, C). No GFP cleavage from PfCen1 was detected in these strains via WB analysis in a parallel study [71], meaning the diffuse signal reflects the actual localization of PfCen1-GFP. While the timing of localization was thereby measured under mild

overexpression conditions, which I showed have an impact on foci formation, the effect was only pronounced under strong overexpression with pFIO_hsp86p (Fig. 22A). The data of pFIO_hsp70_PfCen1-GFP and pARL_PfCen1-GFP are largely in agreement, suggesting that overexpression below a certain threshold does not significantly alter CP recruitment timing. On the other end, I now showed that PfCen1-GFP foci are disassembled ~10 h after S-phase onset, approximately at the transition point from active nuclear division to segmentation (further discussed in 3.2.5). The inconsistent observation of non-centrosomal foci in the pARL_PfCen1-4-GFP strains (Fig. 6B) without a clear localization pattern was likely an overexpression artifact, supported by the link of overexpression to ECCA formation (Fig. 21C).

The centrins' centrosomal localization and behaviour was corroborated in a recent study using PfCen1-mCherry and in line with the previously published localization of *P. berghei* Cen4-GFP [122], [201]. These studies also showed that these centrins form CP foci in activated male gametocytes. Co-localization of *Plasmodium* centrins was further supported by pulldowns of PbCen4-GFP indicating an interaction with PbCen1-3, which suggests cellular proximity. The strong evolutionary conservation of PbCen1-3 and PfCen1-3 (>95% identity) supports a similar biology, partially confirmed by the interaction of PfCen1 and PfCen3 in a pulldown study employing my NF54_pARL_PfCen1-GFP strain [71]. The same pulldown also identified an Sfi1-like PfSlp containing several centrin binding sites at the centrosome, further supporting a centrosomal localization of these proteins. An earlier study, which aimed to localize PfCen1-4 via polyclonal antibodies raised against the individual recombinantly produced centrins, only reported a clear centrosomal localization for PfCen3, while the other centrins showed a ubiquitous cellular staining [70]. However, due to the varying quality of antibodies and their inherent unspecificity, I consider the localization determined by myself and other studies via fluorophore tags to be more reliable. While a localization artifact arising from the relatively large GFP tag (GFP 27 kDa, centrins ~20 kDa) is theoretically possible, a specific targeting to the CP is highly unlikely, as this is not the case for GFP expression alone. An influence on the ratio between diffuse background and foci fraction is possible.

The specific sub-localization of centrins within the CP's outer core was heterogenous (showing different shapes) for all four centrins when imaged via fixed-cell STED, with live-cell STED of PfCen1-Halo suggesting a dynamic rearrangement as the cause (Fig. 7C). As imaging was restricted to a single focal plane due to the limitations of live-cell STED, it is possible that the apparent changes in shape could be the result of rotation in 3D. However, this would still require a certain freedom of motion within the CP. While live-cell STED typically suggested a single cohesive mass of PfCen1 (Fig. 7C), fixed-cell STED often showed separate foci (Fig. 6B). It is unclear whether individual foci appear as a cohesive mass due to the resolution limitation of live-cell STED, or if individual foci could perhaps be a PFA fixation artifact, which is reminiscent of those reported for several other organelles [202]. On the other hand, U-ExM images generally show cohesive centrin morphologies (Fig. 3B, C) [52], [68]. Regardless, inconsistent and rapidly rearranging centrin structures within the CP have not been described in mammalian

centrosomes and the yeast SPB, where centrin's positions within the centriole and along the half-bridge respectively are well defined [97], [200]. Potential shape shifting of centrin assemblies within these locations would have to similarly be assessed via time-lapse super-resolution microscopy. In the light of emerging theories of centrosomes consisting of liquid condensates, the question of how the CP allows for constant centrin rearrangement while simultaneously restricting its movement to itself is highly intriguing [62], [140].

3.2.2 Independence of centriolar plaque duplication from spindle formation

Centrosome duplication and segregation are essential for a successful mitosis. In *P. falciparum* the CP appears to duplicate at the onset of S-phase, as marked by the duplication of centrin foci [32], [53]. It is not yet clear if the daughter CPs are formed via *de novo* assembly, as in yeast [55], or fission as it has been hypothesized in *Toxoplasma gondii* [203]. A U-ExM study on the CP recently postulated a similar mode of fission first duplicating the outer and later the inner core [68]. However, as these postulated duplication stages were acquired across multiple fixed cells, a temporal progression of the different morphologies is not yet conclusively demonstrated over inherent variability. A frequently observed uneven distribution of centrin between the daughter CPs, evidenced by one anaphase spindle pole often displaying no visible centrin (example in Fig. 6B PfCen3 and Fig. 16C), could also support the fission model. In either case, a force is needed for segregation of the CPs during formation of the mitotic spindle. It is plausible that this force is generated during the transition from a monopolar hemispindle to a bipolar mitotic spindle along the intersecting microtubules (Fig. 2A). This spindle arrangement is reminiscent of yeast, where SPB segregation is dependent on microtubules and kinesin-related motor proteins [147], [148]. SPB duplication itself, on the other hand, was not affected by loss of microtubules, as expected of *de novo* assembly.

In my experiments, disruption of microtubules in *P. falciparum* by oryzalin did not prevent segregation (Fig. 8A). PfCen1-GFP foci, as a marker for the CP outer core, continued to duplicate in absence of spindles. In addition, these foci were still principally able to segregate, although they often bundled up in close proximity. It is therefore unclear whether the observed segregation was an active process or merely the result of a passive drift of the duplicated CPs across the nuclear envelope, to which they are tethered by a hitherto unidentified trans-membrane structure (Fig. 3) [52]. Without visualizing the rest of the CP either via U-ExM paired with NHS-ester protein density staining or electron microscopy, it is not certain if the daughter CPs are structurally intact, as centrin is only a marker for the outer core. Viability of the inner core could potentially be assessed by an oryzalin washout experiment, to see if spindles can be formed by duplicated CPs after the drug has been removed.

While these results are in line with a *de novo* assembly model of CP duplication as they mirror the observations in yeast closely [148], a fission model can not be ruled out. Especially considering the caveat that I only observed the outer core, while spindles contact the inner core. It is possible that their fission is driven by different forces. Fission

of the outer core or the entire CP would require the assumption of an alternative force source other than microtubule motor proteins. It is possible that the observed stretching and contraction morphology of PfCen1-Halo along an axis tangential to the nucleus could be an indicator of such a force (Fig. 7C). Early EM-based models also claimed the formation of a bridge-like structure akin to the SPB (half-)bridge within the inner core during CP duplication [204]. However, new evidence for its existence has not emerged since 1977 despite improvements in imaging technology [205].

Expectedly, destabilization of microtubules also causes a strong impairment of nuclear division, producing a single large "super-nucleus" with significantly more than the typical maximum of two centrin foci (Fig. 8A). This was very likely a mechanical defect arising from the absence of an anaphase spindle apparatus important for chromosome segregation and nuclear division. During less severe disruptions in spindle organization caused by a knockout of the mini-chromosome maintenance complex, incompletely separated nuclei also underwent duplication of multiple CPs simultaneously [57]. Alongside outer CP core duplication, DNA replication rate was unaffected with only a slight onset delay (Fig. 8B). These observations have interesting implications for the regulation of mitosis in *P. falciparum*. In mammals or yeast, the cell cycle is tightly regulated via checkpoints, e.g. the spindle assembly checkpoint which ensures attachment of the mitotic spindle to the kinetochores [150]. These checkpoints can induce a controlled and reversible arrest until the problem is resolved to prevent erroneous mitosis and its harmful downstream effects. In contrast, little evidence exists for the existence of checkpoints in the *Plasmodium* asexual cycle, with my further supporting the absence of a spindle assembly checkpoint [32], [206]. As AKiT7, a kinetochore protein with partial homology to spindle assembly checkpoint regulator, Mad1 was recently identified, investigations into its function will further help clarify the existence of this checkpoint [207]. Irrespectively, a reversible arrest prior to S-phase in response to Isoleucine starvation and putrescine depletion, point towards the existence of a G1/S checkpoint. As demonstrated by my data, CP and DNA replication are not tied to a successful anaphase and karyofission, but instead continues in the super-nucleus. In light of the proposed nuclear autonomy in mitotic regulation, it would be of interest to investigate whether all centrin foci of the super-nucleus duplicate simultaneously. This could help elucidate whether regulation of CP duplication is controlled by each nucleus individually, or whether on the contrary nuclear division and DNA-replication are regulated by extranuclear or CP internal signals.

3.2.3 Centrin *in vitro* LLPS capability is evolutionarily conserved

In this work, I demonstrated the ability of the evolutionary distant PfCen1, PfCen3, HsCen2, CrCen, TbCen2, and to some extent ScCdc31 to undergo LLPS *in vitro* in response to Ca^{2+} (Fig. 10, 13). This was evident from the formed droplets showing hallmarks of liquids, namely fusion/coalescence and deformability such as wetting. On a macroscopic level, these droplets in solution appear as turbidity. While it could also arise from protein aggregation, turbidity resulting from LLPS is usually reversible. Importantly, reversible turbidity in presence of Ca^{2+} has also been observed for other centrins, including HsCen1, HsCen2, *Toxoplasma gondii* Cen1 (but not TgCen2), and

EoCen [117]–[121]. While these studies performed detailed analyses on the energetics of centrin self-interaction, they never investigated the underlying nature of turbidity via microscopy. However, their results suggest that these centrins may be capable of LLPS as well. Based on centrins being reported as a significant element of fibrous structures in *Tetraselmis striata* [76] the structures resulting from centrin self-assembly were often interpreted as polymers or filaments [117], [119]. Thus far, *in vitro* formation of filamentous structures was only observed for centrin from *Scherffelia dubia* at 1500 µM, far exceeding the physiological relevant range. The same study also investigated HsCen1, HsCen2, and ScCdc31 where no filamentous structures were reported [208]. Already in 2004, *Tourbez et al*. noted "more complex energetics" of turbid HsCen2 solutions in calorimetric assays [117]. They further remarked on "polymers" increasing in size over time, which was very likely the result of droplet coalescence or Ostwald ripening. Herein, droplet size increases steadily as a result of the lower surface tension favouring diffusion from small to large condensates due to a gradient in Laplace pressure [131], [209]. My findings now provide important context for these previous observations as well as future studies.

Evolutionarily PfCen1, HsCen2 and TgCen2 are orthologues belonging to the same clade, as are PfCen3 and ScCdc31. PfCen2 and PfCen4, on the other hand, are *Alveolata*-specific expansion [70]. This draws an interesting parallel between members of the centrin family which are broadly conserved, and those that can undergo LLPS. The reason for this expansion is unknown, as is the functional distinction between PfCen1-4. In light of their similar structures and localization, the different LLPS behaviours could provide a first hint at functional differences between these four proteins of which at least PfCen1-3 are essential with high sequence conservation (94-99%) between *P. falciparum, P. berghei, and P. knowlesi* [115], [122].

In line with centrins largely consisting of Ca^{2+}-binding EFh domains, LLPS was Ca^{2+}-specific and dependent. As evidenced by NMR and CD spectroscopy, centrins like HsCen2 and ScCdc31 can undergo conformational changes in response to Ca^{2+}, which is absent in mutants incapable of Ca^{2+}-binding [85], [156]. It is therefore plausible that LLPS is triggered through binding of Ca^{2+} via the induction of conformational changes that promote centrin interaction and thus lower the c_{sat} (Centrin interaction further discussed in 3.2.4). Canonical EFh domains favour binding of Ca^{2+} over Mg^{2+} via the differences in ionic radius and requirements for geometric arrangement of the coordinating negatively charged ligand-sidechains (pentagonal bipyramidal for Ca^{2+}, octagonal for Mg^{2+}) [84]. HsCen2, for example, exclusively binds Ca^{2+}, although exceptions like calmodulin, HsCen3 or EoCen, exist that can also bind Mg^{2+} [2], [210], [211]. Interestingly, it was reported for HsCen2 that beyond Ca^{2+} in an equimolar ratio to EFh-domains, turbidity also required the presence of additional bivalent cations (either Ca^{2+}, Mg^{2+}, Mn^{2+}) [117]. Divalent cations have been reported to promote LLPS of certain proteins [212], [213]. In any case, PfCen1-6His, PfCen3-6His, and HsCen2-6His either showed no or only a minor turbidity reaction to Mg^{2+} and the reaction to subsequent Ca^{2+} was not significantly diminished or enhanced by the presence of Mg^{2+} (Fig. 1C). TgCen1 also showed no response to Mg^{2+} [120]. Of note the mild response I observed for PfCen3-

6His and HsCen2-6His could be an artifact caused by the 6His-tag, as in the study by Tourbez *et al.*, untagged HsCen2 did not show a turbidity reaction to Mg^{2+} even at 170 µM [117]. This could be easily tested by performing the experiment on the untagged PfCen3, and additionally assessing the Ca^{2+} specificity of ScCen-6His, TbCen2-6His, and ScCdc31-6His. While the untagged centrins are as close to the native state as possible within my technical limitation, the remaining N-terminal glycine, might still have had a minor impact on their behaviour, given the significance of the N-terminus for LLPS shown within this work (Fig. 15).

PfCen3 showed a fraction of EDTA-irreversible condensates, which increased over time and maintained the shape of the previous liquid droplets (Fig. 10, 11A, S3). This feature was exclusively conferred by the EFh-containing portion of the protein (Fig. 19). I speculated that this phenomenon was due to maturation, a process wherein liquid condensates of (often) disordered proteins can mature into highly viscous gel-like or solid states, such as in the case of FUS [137], [139], [153]. Depending on the protein, this process can occur within timescales of minutes, hours, days, or even weeks [132], [137], [138]. Hardening of PfCen3 droplets was relatively fast and comparable to that observed for SPD-5 [140]. Across the other centrins forming liquid droplets I only observed an EDTA irreversible fraction for ScCdc31-6His, which however lacked the previous droplet shape (Fig. 13). Considering that the 6His-tag appeared to cause aggregation of PfCen2-6His in response to Ca^{2+}, the irreversible fraction of ScCdc31 might be a tagging artifact. This is supported by the previously reported lack of solid or semi-solid protein formations that could be recovered via centrifugation from a 1500 µM solution of ScCdc31 after Ca^{2+} addition [208]. In this line it, can also not be excluded that the presence of partially degraded PfCen3 (Fig. S1A, C) might have had a role in droplet hardening.

Interestingly, while LLPS of other proteins is typically favoured by low temperatures [154], [214], centrin LLPS appears to be favoured by higher temperatures in the physiological range. This was the case for HsCen2, where turbidity increased with rising temperature up to 35.4°C, as well as with PfCen1-6His, which in my experience and parameters did not phase separate at 4°C [117]. While my experiments did not address the cause of this phenomenon, one could speculate that LLPS is promoted through the positive relation between temperature and affinity of EFh-domains for Ca^{2+}. Per $\Delta G = \Delta H - T\Delta S$ (H = enthalpy, S= entropy) this relationship arises from a decrease in Gibbs free energy (ΔG) between the unbound and bound states with increasing Temperature (T), as Ca^{2+} binding to proteins is typically entropically driven ($\Delta S>0$) [84]. The temperature dependency of centrin LLPS is therefore consistent with its natural environment. However, the other experimental parameters of my standard turbidity assay are not physiological due to their minimalist nature, as accurately recreating the environment of the cell with all its nuances is challenging. However, the use of cytomimetic media or bacterial cytosol has been suggested [125]. To maintain relevancy of *in vitro* results for an *in vivo* setting, an adherence to physiological pH and salt concentration (typically 150 mM NaCl or KCl) is recommended, as solvent conditions modulate the critical concentration significantly [153]. Progressive weakening of the electrostatic attraction

partially driving interaction and phase separation of many proteins with increasing salt concentration is known to dissolve many condensates [154], [214], [215]. The approximate intracellular concentrations of Na^+ and K^+ in *P. falciparum* are 20 mM and 130 mM respectively [216], [217]. HsCen2 and TgCen1 turbidity and lower level self-interaction were previously noted to be adversely affected by the presence of KCl [117], [120]. This was considered to be due to an inhibitory effect on the electrostatic component of centrin interaction (further discussed in 3.2.4). Under my experimental parameters 30 µM PfCen1 also showed no LLPS in the presence of 50 mM KCl (data not shown). Similarly, pH can modulate phase separation extensively [218]. The c_{sat} of α-Synuclein changed from 5-10 µM to >200 µM between the pH of 5.4 and 7.4 [138]. An acidic pH favouring turbidity was also described for HsCen2 [117]. In *P. falciparum* the cytoplasmic pH has been measured as approximately 7.15 [219], close to the pH of 7.1 I across my turbidity assays, which I chose for consistency with the HsCen2 study inspiring the assay [117]. However, as I adjusted the pH of BisTris at 4°C, it was likely more acidic at the time of measurement at 37°C, in the range of pH 6.5 – 6.7. However, alternative temperature stable phosphate-based buffers are known to strongly influence LLPS in their own right [153].

The c_{sat} of PfCen1-6His and PfCen3-6His was in between 10-15 µM under the standard conditions of 37°C in 50 mM BisTris (pH 7.1). This is within range of critical concentrations observed for other phase separating proteins *in vitro* [220]. However, considering that transcript levels suggest relatively low expression levels of centrins, this concentration likely exceeds the physiological range within the cell, even under overexpression conditions [116], [165]. In principle, intracellular protein concentration of GFP-tagged centrin could be assessed by measuring the cellular GFP signal per volume and matching it to a defined concentration/intensity curve acquired with purified recombinant GFP [221]. However, this method could only assess the concentration of overexpressed centrins, as the endogenous gene loci are refractory to tagging. Under these conditions, centrin would therefore likely not reach sufficient concentrations for phase separation *in vivo*, especially in the presence of other compounding factors such as Na^+ or K^+. On the other hand, the c_{sat} of 10-15 µM also excluded many factors of the cellular environment promoting LLPS. Foremost among them is molecular crowding. The cytoplasmic protein concentration is estimated to be in between 100 mg/ml and 400 mg/ml for all macromolecules, which are estimated to occupy 20-30% of the volume giving it viscoelastic properties [222]–[224]. The direct cellular environment of centrins especially, the CP, is particularly protein-dense [52], [68]. Crowded environments promote LLPS and crowding agents such as dextran or PEG are frequently employed to trigger or enable phase separation in *in vitro* studies [153], [225]. I also observed this effect for PfCen3-6His, where 8% PEG lowered the critical concentration below 10 µM (Fig. 11B). While I did not determine the exact threshold, the PfCen3-6His solution at 10 µM reached a similar turbidity plateau as the one without PEG at 20 µM. Assuming similar kinetics, c_{sat} could therefore be estimated to be ~5 µM. I did not measure the effect of PEG on PfCen1. Additional contributing factors are the interaction between PfCen1 and PfCen3 contributing to a joint c_{sat} as well as other potential interaction partners. One such candidate is the centrosomal PfSlp with its centrin binding sites as further discussed

in 3.2.5 [71]. A last point to consider is that recombinant protein purified from *E. coli* does not necessarily fully reflect the state of the same proteins in eukaryotic cells. Various PTMs have been documented for PfCen1-4 (Fig. 4B), while the recombinant versions were not modified (Fig. S1B).

Overall, it is important to exercise caution when interpreting *in vitro* LLPS, as it can not be understood as proof of a protein's ability to phase separate *in vivo* or relevance of the phenomenon for its biology [125], [173]. While an *in vitro* setting can serve to assess the principal ability of a protein to phase separate, it primarily offers insight into which factors could influence potential LLPS behaviour *in vivo*. It is nonetheless interesting that only some centrins undergo LLPS despite their high structural similarity, which could argue for an evolutionary purpose rather than *in vitro* artifact associated with the general structure. This remains speculative, however, and would require a better understanding of the structural elements differentiating centrins that phase separate and those that do not.

3.2.4 Structures driving homotypic and heterotypic centrin interactions

Centrins are structural proteins without documented enzymatic function. Therefore, understanding their interaction partners and the structures mediating these interactions is critical to understanding their role. Centrins across different eukaryotes consistently form homotypic self-interactions, which have been studied in detail [117]–[120]. While itself a product of these interactions, the centrins' ability to undergo LLPS revealed within this study now adds an additional layer of complexity. In the following I will discuss which conclusions about the interaction of *P. falciparum* centrins can be drawn from my experiments in the context of previous studies and LLPS.

Centrins consist of a highly variable N-terminus followed by two pairs of EFh domains, of which a variable number can bind Ca^{2+} with physiological relevant affinities [70], [78], [84], [85]. In line with the high likelihood of IDRs within the N-terminus of many centrins, prior NMR spectroscopy or X-ray diffraction crystallography studies on HsCen2, ScCen, Cdc31, EoCen and *Mus musculus* centrin 1 were not able to resolve its structure [80]–[83]. The failure of both the Δ19-PfCen1 and EFh-dead-PfCen1 mutants to undergo LLPS shows that both N-terminus and C-terminal domains are involved in this process (Fig. 11D, 15). This is supported by other studies on HsCen2 and TgCen1 demonstrating the necessity of both elements for turbidity formation [117], [121]. However, despite multiple studies, no conclusive unifying model for the underlying interactions has emerged. In the following I will briefly review previously published self-interactions of centrins and interpret the results as coherent models of the underlying interactions, which aim to explain the respective observations:

The first stems from a biochemical analysis of HsCen2 self-assembly by Tourbez *et al.* published in 2004 [117] (Fig. 32). Their analysis revealed a Ca^{2+}-dependent and specific "multimerization" of the complete protein forming turbidity, which had both electrostatic as well as hydrophobic components, based on sensitivity to pH, NaCl/KCl, and

hydrophobic probe 8-anilino-naphthalene-1-sulfonic acid (ANS) respectively. Isothermal calorimetry of different truncation mutants revealed that, while only integral HsCen2 could form turbidity, lower-level interaction between domains still occurred in the presence of Ca^{2+}, which is bound by the C-terminal EFh domain IV. As such, the C-terminal half C-HsCen2 (94-172 AA) and N-terminal deletion mutant Δ25-HsCen2 still interacted with themselves. C-HsCen2 also interacted with the integral HsCen2. The majority of C-HsCen2 specifically oligomerized to complexes no larger than tetramers. N-HsCen2 (1-98 AA) on the other hand, neither interacted with itself nor C-HsCen2. It could, however, interact with pre-assembled Δ25-HsCen2 oligomers, with reaction stoichiometry suggesting a binding ratio of 3-4 Δ25-HsCen2 binding one N-HsCen2. Interestingly, lower-level interaction of HsCen2 as well as Δ25-HsCen2 was not inhibited by high NaCl concentration, indicating that only LLPS is dependent on electrostatic interactions. They concluded that Ca^{2+}-bound C-terminal domains form small oligomers, which evolve towards turbidity forming "polymers" through heterologous binding of the positively charged disordered N-terminus to a negatively charged area of the C-terminus. This was supported by a follow-up study showing an interaction of the disordered N-terminus with this time two (instead of 3-4) Δ25-HsCen2 or two C-HsCen2 [80]. Calorimetry showed no interaction of the N-terminus with itself. Ca^{2+}-binding by HsCen2 also exposes a hydrophobic pocket, which could decrease solubility in the surrounding solution to instead promote phase separation.

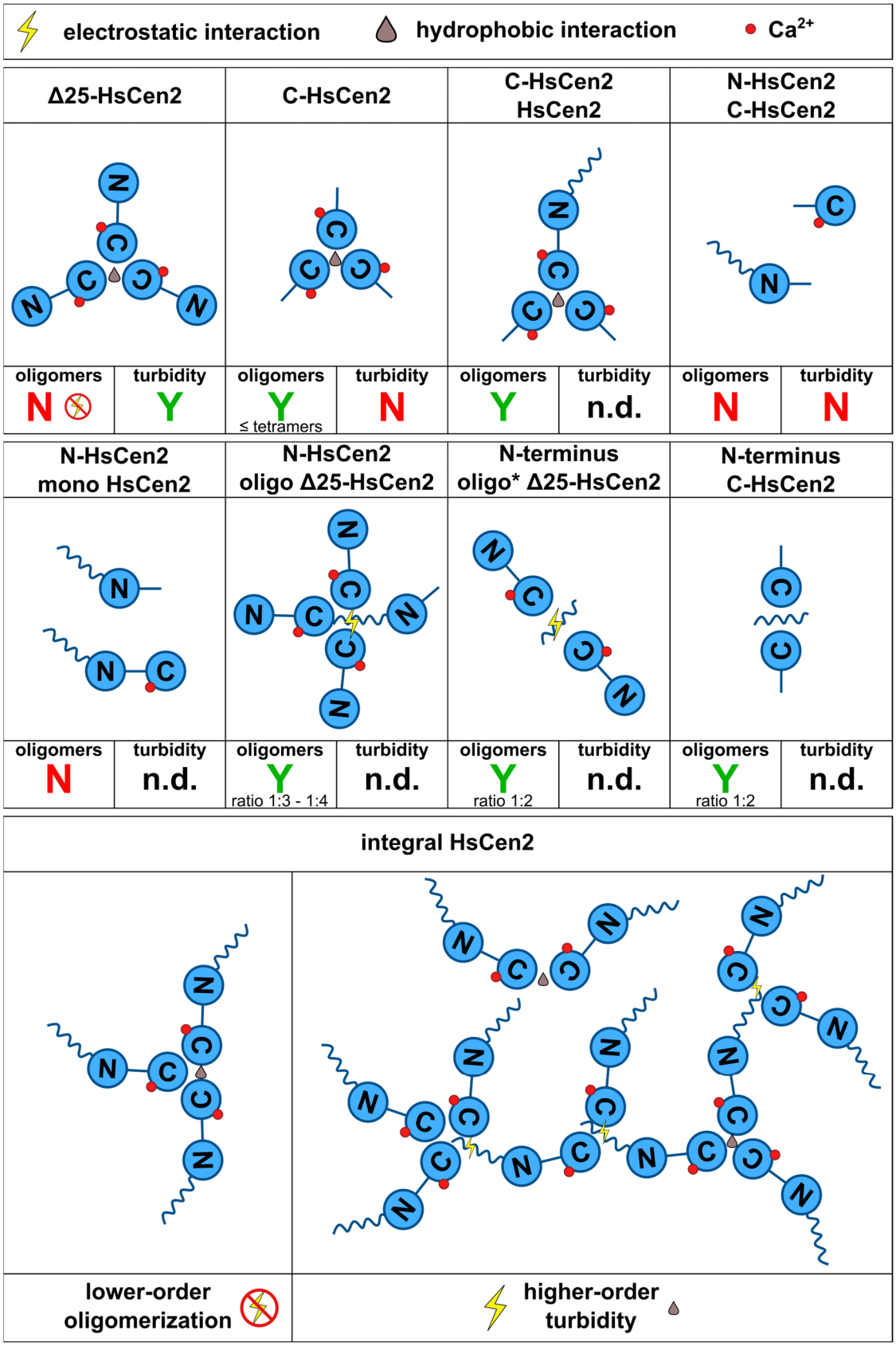


Figure 32 Result from previous HsCen2 interaction studies. Summary of previous isothermal calorimetry studies on HsCen2 interaction [80], [117]. Documented presence (Y) or absence (N) lower-order oligomerization and higher-order interactions indicated by turbidity, with details are indicated. Illustrations represent my interpretation of an interaction model explaining these observations. * not explicitly stated to be oligomeric, but probable due experimental parameters. n.d., not defined; red circle, Ca^{2+}; yellow bolt, electrostatic interaction; brown droplet, hydrophobic interaction. Relative size indicates which interaction type was dominant.

The second model was published by Conter *et al.* on TgCen1 self-assembly in 2021 [120] (Fig. 33). They too demonstrated Ca^{2+}-dependent turbidity of the complete protein with electrostatic and hydrophobic components, based on sensitivity to KCl and ANS. However, in their case the electrostatic component appeared more dominant. In dynamic light scattering and calorimetric studies they showed that C-TgCen1 (95-169 AA) could form larger particles as well, which they characterized as a Ca^{+2}-**in**depdenent, exclusively hydrophobic interaction. In contrast to HsCen2, N-TgCen1 (1-94 AA) could form larger particles as well, in a Ca^{2+}-dependent and exclusively electrostatic fashion. Of note, this N-fragment contains the only Ca^{2+}-binding domain of TgCen1. Curiously, the N-terminal truncation mutant Δ21-TgCen1 showed no particle formation despite the sequence C-TgCen1 being included in its structure. This calls into question whether the independent particle formation of C-TgCen1 might have been an artifact, possibly due to steric inhibition by the N-terminal domain, and not actually relevant in the integral protein. Especially considering the comparatively small (albeit not irrelevant) role hydrophobic interactions appear to play for particle formation and turbidity of the integral TgCen1. Surprisingly, addition of the negatively charged 21 AA N-terminus as a peptide not only led to particle formation of Δ21-TgCen1 but also turbidity, despite the peptide and protein not being covalently linked. They postulated a model wherein N-N and C-C interactions form small oligomers, with larger particles/turbidity forming through binding of the disordered N-terminus to a C-terminal domain. However, the relevance of the C-C interaction can be called into question (see above) and an interaction between the N-terminus and C-terminal domain is not formally shown, albeit not ruled out either. The turbidity promoting effect of the independent 21 AA N-terminus could suggest that its primary function is to mediate or stabilize heterologous interactions between domains through non-covalent interactions.

Lastly, a crystal structure showed the N-terminal Ca^{2+}-binding domain N-EoCen (1-101 AA) of *E. octocarinatus* centrin interacting in a trimeric arrangement. However, the position of disordered N-terminus (1-24 AA) could not be resolved [83].

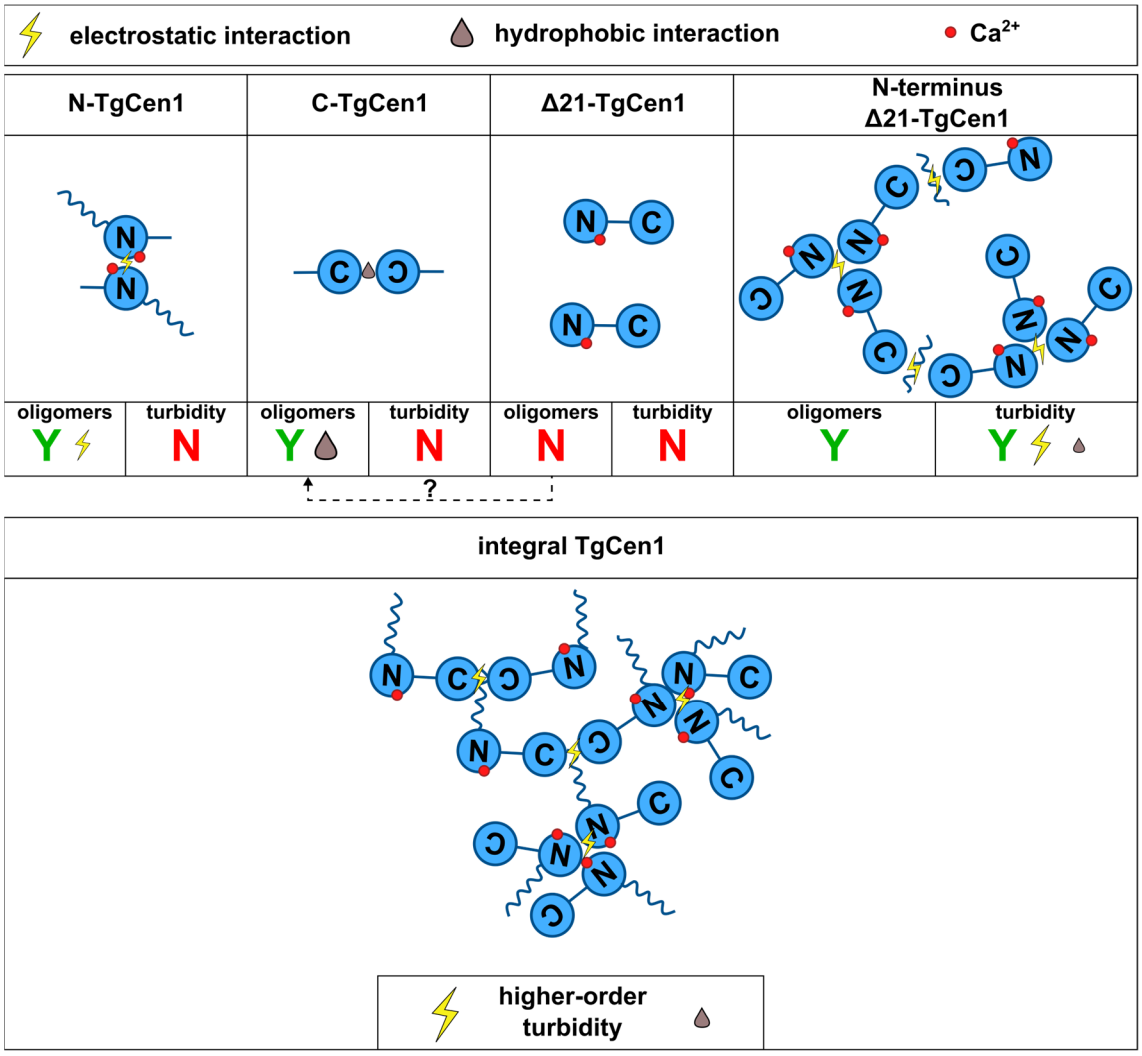


Figure 33 Results from previous TgCen1 interaction study. Summary of previous isothermal calorimetry studies on TgCen1 interaction [120]. Documented presence (Y) or absence (N) lower-order oligomerization and higher-order interactions meaning turbidity, with details are indicated. Illustrations represent my interpretation of an interaction model explaining these observations. Green Y, positive; Red N, negative; n.d., not defined; red circle, Ca^{2+}; yellow flash, electrostatic interaction; brown droplet, hydrophobic interaction. Relative size indicates which interaction was dominant. Dotted arrow with "?" indicating seemingly conflicting results.

While it is possible that centrins from different species evolved entirely different modes of interaction, certain consistent patterns emerge. In general, phase separating centrins below c_{sat} or in an impaired state (e.g. N-terminal deletion) form low-order oligomers via N-N or C-C interactions, potentially depending on the location of the Ca^{2+}-binding domains. This might also determine whether the oligomerization reaction is primarily driven by electrostatic or hydrophobic interactions, with the other type acting in a supporting role. While lower-order interactions are formed independently of condensates, they are in turn necessary for phase separation to occur. Higher-order interactions, i.e. LLPS, then occurs through mediation of dynamic heterologous interaction by charged N-terminus with other centrins, driven by electrostatic forces (Fig. 32, 33). Whether this pattern persists for phase separating centrins beyond the ones discussed or centrins that don't phase separate is not currently known. Importantly, evidence from the above mentioned centrins suggests that both N-N/C-C as well as N-terminus interactions enable the binding of multiple client proteins, making centrins multivalent in theory. Proteomic

analysis suggested multivalent proteins to be a hallmark component of membraneless organelles that are thought to be liquid condensates, such as stress granules or the nucleolus [133], [136], [226]. Mutagenesis studies since demonstrated a dependence, with the c_{sat} decreasing with increasing valency of the participating proteins [124], [129], [153], [227]. The calcium induced change in valency is therefore a likely trigger for LLPS [131]. While there is often a focus on condensates formed by unspecific multivalent interactions, site-specific multivalent interactions are also capable of driving LLPS [125]. In either case, multivalency is an important component for LLPS to occur, with the aforementioned models providing a potential explanation for how centrins can achieve both in a Ca^{2+}-regulatable manner.

Similarly IDR-containing proteins are frequent in membraneless organelles and a common feature of phase separating proteins [130], [131], [133], [214]. Herein they are thought to act as flexible linkers/spacers between acceptor domains, or as "stickers" mediating interaction themselves, for example through blocks of oppositely charged residues [128], [130], [153], [228], [229]. Some IDRs have also been shown to phase separate on their own [230]. It is therefore interesting that a high likelihood of an N-terminal IDR has proven a good predictor for the *in vitro* LLPs-capability of centrins (Fig. 14). Phylogenetic analysis of a broad range of eukaryotic species showed that each encoded at least one centrin with a (likely) N-terminal IDR [79]. However, as I only tested two non-phase separating centrins, PfCen2 and PfCen4, more datapoints are required to establish if a consistent correlation exists. While the inability of the IDR-free 4NCen1 chimera to phase separate does lend some support to the importance of an N-terminal IDR in this process, its impact is difficult to judge in isolation when deleting or substituting entire N-termini. For instance, the PfCen4 N-terminus has a slight negative charge at physiological pH, as opposed to the strong positive charge of the PfCen1 or PfCen3 N-terminus, which in itself could also be a factor. Ideally one could integrate specifically an isolated IDR into an existing centrin. The 1NCen4 chimeras were a first step in this direction, which showed that an N-terminal IDR alone is not sufficient, as the increased reaction to Ca^{2+} compared to PfCen4 was likely due to instability of the protein (Fig. 15). This experiment also gave no insight whether the IDR was essential. While exchanging the N-terminus of PfCen1 with the IDR containing N-terminus of PfCen3 allowed for LLPS of the resulting 3NCen1 chimera this is conflated by the heterotypic interaction of PfCen1 and PfCen3 (Fig. 18C, 19). It is therefore not clear whether 3NCen1 LLPS was enabled by the N-terminal IDR or the PfCen1 N-terminus in general. Additionally other structural factors besides the IDR should be considered. A previous analysis by Mahajan *et al.* (2008) based on primary sequence predicted that PfCen1 and PfCen3 contain 3 potentially active EFh domains, while PfCen2 and 4 only contain 1 [70]. They claimed that all four centrins could bind radioactive Ca^{2+} isotopes, implying that each has at least one active Ca^{2+}-binding site, although the data was not shown. As HsCen2 with also only one Ca^{2+}-binding site is capable of phase separation, the number of active EFh-hand domains alone does not appear to be a limiting factor.

While a number of homotypic centrin self-assemblies have been reported (HsCen2, TgCen1, EoCen, etc.) the ability of PfCen1 and PfCen3 to form co-condensates is the first reported heterotypic mode of assembly between centrins (Fig. 18C). While I did not directly assess if and how PfCen1 and PfCen3 can engage in lower-order interactions, the ability of the 1NCen3-6His and the 3NCen1-6His chimera to phase separate individually (at 60 µM) strongly implies that higher-order interactions are mediated by the ability of the PfCen1 N-terminus to interact with the PfCen3 N- or C-lobe (Fig. 19). The higher critical concentration threshold suggests that this heterotypic interaction has a lower affinity than the homotypic one. Interestingly, while the mixture at individually subcritical concentrations of the chimeras (Fig. 19C) showed an interaction between them, LLPS efficiency was not improved as might have been expected from re-enabling the more efficient interaction between the respective N-termini with their original EFh-domains (Fig. 34). While speculative, this could hint at an interference from lower-order interactions between PfCen3 and PfCen1 EFh-domains as well. Lastly, the EDTA-irreversible fraction of 1NCen3-6His showed that despite IDR sequences being responsible for increasing viscosity of certain condensates [228], the maturation of PfCen3 is mediated by its EFh domains. In any case, the discovery of co-condensation of PfCen1 and PfCen3 could help inform of the mode of the documented interaction *in vivo*, as well as that of PbCen1-4 [71], [122].

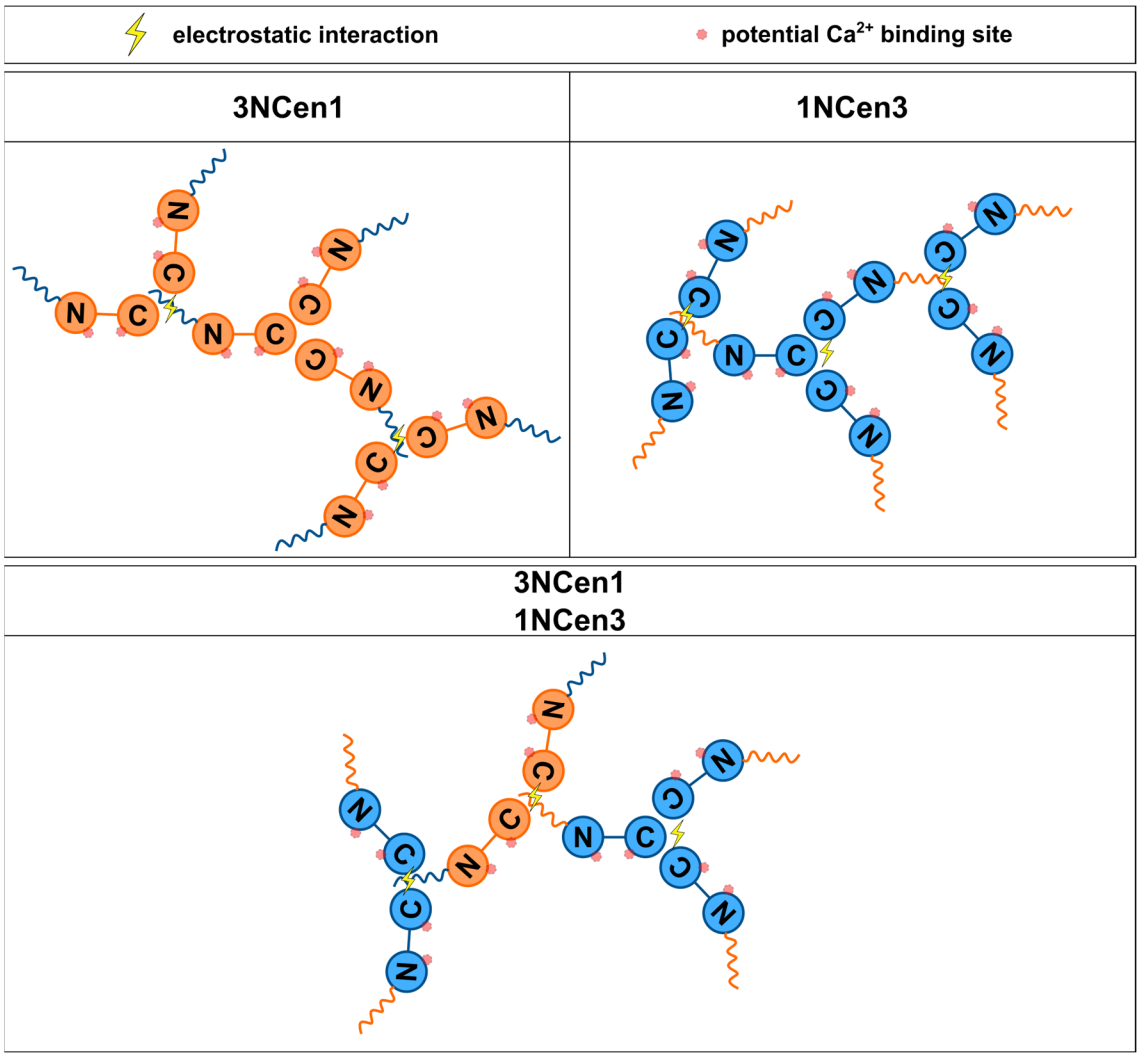


Figure 34 1NCen3 and 3NCen1 interaction models. Illustrations represent my interpretation of an interaction model explaining the observed 3NCen1-6His and 1NCen3-6His. Opaque red dot, potential Ca^{2+}-binding site; yellow bolt, electrostatic interaction.

While this work did not assess lower-order oligomerization of PfCen1-4, my assessment of compounds and mutations affecting higher-order LLPS can provide some information on the underlying interactions driving this process (Fig. 34). As described above, centrin LLPS is driven by both electrostatic and hydrophobic interactions. In case of PfCen1, strong sensitivity to KCl but low sensitivity to 1,6-hexanediole (Fig. 30A), which is a hydrophobic interaction disrupter [215], suggest that hydrophobic interactions are not the primary driver of the lower-order interactions that in turn enable higher-order LLPS. Instead, electrostatic interactions appear to be the dominant factor not only in the higher-order interactions mediated by the charged N-terminus, but also the lower-order oligomerization. While I did not assess the sensitivity of PfCen3 to monovalent cations or 1,6-hexanediole, the inhibitory effect of charge alteration of the N-terminus via phosphomimetic mutations on LLPS supports an electrostatic nature of the higher order N-terminus interactions (Fig. 16B). Investigations into which EFh-domains can bind Ca^{2+} could offer further insight into whether lower-order oligomerization is driven by the C- or N-terminal domains of PfCen1 and PfCen3.

In conclusion, my data is consistent with a model for centrin interaction wherein PfCen1 forms lower-order oligomers in a Ca^{2+}-dependent manner primarily driven by electrostatic heterologous interactions between the N- and/or C-lobe, with a small hydrophobic component. LLPS then occurs through the charged and disordered N-terminus mediating or stabilizing heterologous electrostatic interactions with the EFh-domains of other PfCen1 (or PfCen3) proteins. Whether binding of the N-terminus to other centrins is also dependent on Ca^{2+}-induced EFh-domain conformation changes or if turbidity is solely dependent on Ca^{2+} for the lower-order interactions is not known.

3.2.5 Assembly and disassembly of PfCen1 foci *in vivo*

LLPS has been proposed as the assembly mechanism for many membraneless organelles, including centrosomes [62], [140]. I therefore sought to investigate whether localization of centrins to their compartment in the outer CP core and foci formation in general could be driven by LLPS. While *in vitro* studies confirmed the principal capability of PfCen1 to phase separate, on their own they should not be considered predictive for *in vivo* as previously discussed (3.2.3). To assess whether PfCen1 could also undergo LLPS *in vivo* I exploited the strong concentration dependency of phase separation to investigate whether, akin to the *in vitro* experiments, increasing concentration via overexpression could force the formation of foci. Indeed, foci emerged from a dilute phase with premature foci formation and ECCA frequency being positively correlated with concentration (Fig. 20D, 21C, 22A). However, for single-component LLPS assembly is expected to be triggered at a consistent c_{sat} with the concentration of the dilute and dense fraction not increasing further afterwards [125], [170], [173]. This has been beautifully illustrated with the synthetic protein ArtiG [231]. In case of PfCen1-GFP I observed no

clear plateau in the average cytoplasmic concentration once the dense phase emerged (Fig. 24B). Graphs where the population was normalized to the timepoint of first focus formation also gave no evidence for a plateau, suggesting that the c_{sat} did not simply get masked by averaging cells where the dense fraction arose at different timepoints relative to S-phase onset (data not shown). I could not accurately determine the concentration of the dense phase due to the small size of foci (see 2.3.3). Riback *et al.* observed similar dynamics with nucleolar protein NPM1, where both the dense fraction (i.e. nucleolus) and dilute fraction increased with overexpression without a fixed c_{sat} [170]. They demonstrated that this behaviour can be explained by multi-component LLPS occurring through heterotypic interactions and was observed for components of many other membraneless organelles like P-bodies. As discussed before, PfCen1 is known to interact with PfCen3 and PfSlp, therefore adherence to multi-component instead of single-component LLPS dynamics would not seem surprising. However, in a recent comment, Dr. Andrea Musacchio argued that the supposed multi-component LLPS dynamics of NPM1 could be explained just as well by "traditional" site-specific interactions between proteins, wherein binding sites eventually become saturated [125]. Prior *in vitro* studies suggested that centrin interactions are driven by site-specific interactions rather than unspecific weak interactions (see 3.2.4). An interaction-site saturation of a hypothetical scaffold by PfCen1-GFP could be supported by centrosomal foci increasing in signal intensity (often leading to detachment and ECCA formation), but always maintaining a stable intensity eventually. However, this could also be the result of potential maturation (further discussed in 3.2.6). PfSlp knockdown leading to decrease of centrin in an approximately linear ratio at the CP could also support a site-specific interaction driven scaffold-client relationship [71]. The observed influence of concentration on assembly is also not unique to LLPS, but has been documented for aggregates or many biopolymers, such as microtubules, which are also dependent on critical concentrations for growth [232], [233]. Assembly kinetics consistent with nucleation driven polymerization, such as a lag and elongation phase, were previously observed for HsCen2, although these can likely be partially attributed to LLPS [117]. HsCen2 and TgCen1 studies also demonstrated that centrins can engage in (lower-order) interactions with themselves and other interaction partners without the need for LLPS [117], [120].

Potential triggers of foci assembly under the LLPS paradigm

Increase in cellular centrin concentration

I originally hypothesized that a steadily rising concentration of PfCen1(-GFP) alone could provide the trigger for CP foci assembly at the onset of S-phase once the c_{sat} is reached. This would require very precise control of centrin levels by the parasite to accurately time foci formation in a sensitive equilibrium. Unfortunately, the unavailability of endogenous tagging prevents assessment whether PfCen1 levels would rise significantly around entry into schizogony to trigger foci formation through a concentration threshold alone. As transcriptomic data suggests that centrins are expressed at relatively low levels [116], [165], it is likely that even milder pFIO_hsp70p overexpression increases cellular concentration by a considerable margin. However, even under these elevated centrin levels, the first foci formation occurred close to S-phase onset like in the WT [52], with

only strong overexpression shifting the timing significantly (Fig. 22A). The exact ratio between overexpressed PfCen1-GFP and endogenous PfCen1/PfCen3 could be quantified via WB of highly synchronized cultures for better judgement of the potential impact. Furthermore, high PfCen1-GFP concentrations in early trophozoites or ring-stages never produced foci, which only formed in relative proximity to schizogony. This strongly implies that native CP foci formation is triggered by other factors than a precisely timed crossing of a c_{sat}. Potential alternatives are discussed below:

Calcium signalling

The EFh-dead-PfCen1 mutant demonstrated that Ca^{2+}-binding is critical for *in vivo* foci formation (Fig. 25E), either due to its inability to undergo LLPS or site-specific interactions. Conveniently, cytoplasmic Ca^{2+} levels rise significantly during the transition from trophozoite to schizont stage [171]. In mammalian cells, a spatially restricted Ca^{2+} signal at the centrosome is essential for mitosis [234]. Although speculative a similar mechanism could be imagined as the cause for targeting of centrin assembly to the CP. However, artificial increase of Ca^{2+} levels via ionophore treatment of strongly PfCen1-GFP overexpressing trophozoites did not induce foci formation (Fig. 26C). While I did not measure the internal Ca^{2+} levels directly to confirm an effect of the ionophore, e.g. by the Ca^{2+}-sensitive dye Fura-Red used in *P. falciparum* before [235], the same treatment was shown to have a rapid effect by another study [171]. Furthermore, it evoked an unknown but specific cellular reaction that I observed as an apparent local increase in PfCen1-GFP signal intensity/concentration, which was not present in the control or ionophore + EGTA condition, suggesting that this reaction was the result of a Ca^{2+} influx. In case of HsCen2, an equimolar ratio of Ca^{2+} cations to the number of active EFh binding sites was observed as the minimal Ca^{2+} concentration needed for turbidity [117]. It is therefore possible that the lower concentration of 310 nM observed in trophozoites is already sufficient to activate enough centrins, with Ca^{2+} thereby not being a limiting factor.

Post translational modifications

PTMs can achieve rapid regulation of protein behaviour. For HsCen2, phosphorylation at T45, T47, and T118 by Mps1 are essential for recruitment to the centriole [100]. Furthermore, a phosphorylation of S170 by Aurora kinase A regulates HsCen2 stability [93]. However, across various proteomic studies, no evidence for the presence of homologous residues in PfCen1 exists (Fig. 4B) [51], [87]–[91]. While acetylation has also been documented in HsCen2, their importance has not been investigated thus far [236]. On the other hand, a striking accumulation of N-terminal phosphorylation has been reported for PfCen3 (Fig. 4B). Of note, a similar accumulation of 7 documented phosphosites within the first 27 AA has also been documented for TbCen2 [237], [238]. As discussed (see 2.2.4), these phosphorylation could negatively impact electrostatic interactions between centrins by inverting the charge of the N-terminus, explaining the inability to undergo LLPS (Fig. 16B). However, in case of PfCen3 no impact of phosphomimetic mutants on foci formation and localization was observed (Fig. 16C). While phosphomimetic mutations are an imperfect approximation, for instance carrying only a -1 instead of a -2 charge, this indicates that phosphorylation is not directly involved

in the regulation of PfCen3 CP localization. The role of posttranslational modification in the role of centrin foci formation therefore remain in the theoretical realm thus far.

Nucleation sites

Another option is the existence and activation of a nucleation site at the CP, which could either occur via LLPS by quickly creating a local c_{sat} minimum, e.g. through enzymatic activity as proposed for centrosome assembly at centrioles [141], or via the presence of specific interaction partners. Nucleation sites can offer a convenient way for cells to determine localization and number of condensates [123]. I noted preferential assembly at the CP even for foci that would later turn into ECCAs (Fig. 21E). This foci formation often occurred before the first evidence for CP presence in the form of hemi-spindle assembly and centrin localization, given the lack of alternative markers. However, clustering of the centromere histone CenH3 at the nuclear periphery in early trophozoites, consistent with its localization after hemi-spindle assembly, suggests the presence of at least a form of inner CP core prior to tubulin and centrin recruitment [52], [74]. U-ExM studies further suggest that an inner core exists prior to centrin recruitment, while the outer core shows no protein density (Fig. 3C) [68]. Since centrin only occupies a subset of the protein-dense region of the outer core, this implies the recruitment of other factors besides centrin as well, which make up the rest of the structure. In any case, as centrins must be targeted to the CP, it would seem plausible and efficient that an interaction partner could serve a dual function in acting both as the assembly trigger and special cue. One potential candidate is the Sf1-like protein PfSlp, which is also present in the outer CP core and was shown to interact with PfCen1 [71]. Knockdown of PfSlp decreases localization of centrins to the CP in equal proportions, suggesting a role in recruitment, hierarchy and potential other upstream factors are not established at this point. PfSlp has multiple predicted centrin binding sites along an elongated α-helical structure. Therefore, a mode of surface assisted pre-wetting, which is known to promote phase separation of transcription factors along DNA strands, could be speculated on for centrins [239]. Experiments investigating a supportive or antagonistic effect of PfSlp on centrin LLPS *in vitro* were not realized as fragments of the very large protein (407 kDa) could not be recombinantly expressed.

The impact of structural mutations on PfCen1 foci formation and CP localization revealed that Ca^{2+}-binding is critical for both (Fig. 11D, 25E). Although a previous study involving a non Ca^{2+}-binding mutant of ScCdc31 did not assess its localization directly, the mutation was lethal [156]. Its inability to bind the spindle-pole body protein Kar1 in a Ca^{2+}-dependent manner was implied as a reason. This shows that although certain isolated domains of TgCen1 and HsCen2 could engage in Ca^{2+}-independent interactions (Fig. 32, 33), such interactions (if present) are not sufficient for *in vivo* function of PfCen1 or ScCdc31. A deletion of the N-terminus on the other hand, only influenced ECCA frequency and did not affect CP localization (Fig. 25A, B). One caveat is the tendency of Δ19-PfCen1-6His to aggregate *in vitro* (Fig. 15), which could mean that its remaining ECCAs are the result of unspecific aggregation, although it is unclear if Δ19-PfCen1-GFP is similarly unstable. Another point to consider, is the remaining presence of WT PfCen1 and PfCen3 in the cell expressed from the endogenous locus, which could

potentially rescue Δ19-PfCen1-GFP localization via N-terminus independent interactions. Similar concession can be made for the continued localization of the phosphomimetic PfCen3-ST/SYT-GFP mutants to the CP (Fig. 16C). In either case, it can be concluded that foci assembly as ECCAs or at the CP is driven primarily by the PfCen1 EFh-domains in a Ca^{2+}-dependent manner. The original concept behind the experimental approach was to correlate *in vitro* LLPS behaviour with *in vivo* foci formation. As it stands, only one of the non-LLPS mutants, EFh-dead-PfCen1, strongly influenced foci formation. Keeping the aforementioned caveats in mind, this would argue against LLPS as a driver for foci formation (CP and ECCA) *in vivo*. And while the localization of HsCen2-GFP to the CP (Fig. 25E) is interesting given the structural divergence between the *Plasmodium* and human centrosome, this localization could be readily explained by partially conserved site-specific interactions, as HsCen2 retains a 72% identity to PfCen1. In fact, the lack of ECCAs could argue against the ability of centrins to undergo LLPS *in vivo*, despite being able to *in vitro*. In general, the study of these mutants has its limitations, as all investigated mutations also interfere with site-specific interactions. Ideally, one would devise a mutant where only solubility is affected to determine if site-specific interactions are insufficient to establish localization [125]. This would be highly challenging, not only because centrin LLPS appears to be at least partially dependent on site-specific interactions (see 3.2.4), but the proteome of its compartment and thus other interaction partners besides PfSlp remain largely unknown. With the current level of knowledge, the conclusions that can be drawn from my experiments were therefore inevitably limited.

Lately, the reliance on ectopic overexpression in the study of LLPS phenomena *in vivo* has come under scrutiny as it shifts the sensitive protein concentration equilibrium on which the regulation of condensate formation supposedly relies, with potentially drastic influence on the observed behaviour [125], [173]. While I employed overexpression merely to determine if verifiable LLPS of PfCen1-GFP could be induced *in vivo* at all, as a prerequisite for also occurring under native conditions, the impact on the physiological relevance of other observations must also be considered. For instance, the average share of PfCen1-GFP bound within foci peaked at ~9% (Fig. 24B). While non-centrosomal roles for centrins e.g. in nuclear mRNA, protein export, or DNA repair have been reported ([110], [113], [240]), I observed no particularly pronounced cellular localization outside the CP in *P. falciparum* (Fig. 6B). It would seem counter-intuitive and inefficient, that the cell would express a 90% surplus of PfCen1 only to drive 10% to the centrosome in an LLPS scenario. It therefore seems plausible that in accordance with a localization through site-specific interactions alone, the binding sites at the CP merely become supersaturated by PfCen1-GFP overexpression. Especially considering that transcript levels of PfCen1-4 suggest low expression levels under native conditions [116], [165]. While I observed an increase in the amount of centrin at the CP by overexpression, as evidenced by the ECCA-ripoff phenotype resulting from supersaturation, it is plausible that the large amount of dilute PfCen1-GFP is the result of the outer core lacking the binding capacity for an additional 10-fold amount of PfCen1-GFP on top of the endogenous WT PfCen1. However, it has also been noted in human lymphoblasts that the bulk of centrin is not located at the centrosome, as it likely performs other cellular

functions as well [78], [241]. The presence of dispersed WT centrin in non-overexpressing *Plasmodium* cells, on the other hand, has not been confirmed thus far due to the ambiguity between ubiquitous distribution and the unspecific background resulting from antibody staining (see 3.2.1). Assessing the ratio of dilute and dense fraction of endogenous PfCen1 could determine whether this is indeed a consequence of overexpression. Unfortunately, this is complicated by the unspecific binding of antibodies across the cytoplasm. While also suffering from antibody-specificity the pFIO_hsp86p_GFP-T2A-PfCen1 experiments, however, showed a strong increase in cytoplasmic background too, demonstrating that this phenomenon, in principle, is not caused by the GFP-tag alone (Fig. 23D).

Irrespective of how PfCen1 foci assembly is mediated, I observed that their disassembly is highly coordinated. Foci started to uniformly decrease in intensity approximately 10 h post S-phase onset (Fig. 24B). Disassembly of ECCAs further demonstrated that this process did not specifically target CPs but PfCen1 assemblies in general. Cellular PfCen1-GFP levels remaining mostly constant throughout the process (until right before egress) further suggests that it does not involve centrin degradation (Fig. 24A). While the absence of centrin foci in segmenter stages was known [52], [122], this is the first quantification of disassembly timing. The coordinated manner of disassembly strongly implies a cellular signalling event as the underlying cause. Based on timing, foci disassembly starts in proximity to the last rounds of DNA-replication, which was measured to occur at ~11 h post S-phase onset [50]. PfCen1 persisting at the CP until its final duplication, which roughly coincides with DNA-replication [32], [52], appears logical in light of a likely role in CP function or duplication. However, foci disassembly was not instantaneous and could feasibly start before the final CP duplication while retaining functionality. The precise regulator inducing disassembly is currently unknown, given the sparse knowledge about the regulatory processes governing asexual schizogony [206]. Segmentation is also a multilayered process, with first preparations occurring as early as the 3 nuclei stage in the form of rhoptry assembly and first IMC component recruitment [70], [79], [242]. Without correlation with other cellular markers, it is therefore not possible to determine whether foci disassemble in conjunction with another process or fully independently.

In conclusion, foci formation and dissolution are likely triggered by factors other than concentration, although it can exert an influence under extreme conditions. While an involvement of LLPS in centrosome recruitment of centrins and the physiochemical properties of the CP cannot be excluded, the localization of PfCen1 and regulation thereof can be readily explained by conventional site-specific interaction partners.

3.2.6 The material state of foci

Membraneless organelles have been characterized as a wide range of material states, including liquids, gels, and solids [133]. These can be distinguished by their different properties: Liquids have a consistent volume but no memory, meaning they can be deformed without returning to their prior shape afterwards [123], [133]. The resistance

therein is determined by the viscosity of the liquid. As a consequence, liquid droplets can drip and wet upon contact or fuse with other droplets. Otherwise, they typically assume a round shape due to surface tension. In contrast, solids display elasticity, deforming in response to force (until a breaking point) but return to their original shape afterwards. An intermediate phenomenon is viscoelasticity of complex fluids (e.g. shaving cream), wherein a material remains elastic up until a certain threshold (time, deformation) after which it flows without memory of the original form [123]. Furthermore liquids display a high internal mobility and turnover [123], [125]. To determine whether *in vivo* PfCen1-GFP foci constitute liquids in line with an assembly via LLPS, I attempted to assess these properties experimentally.

In regard to fusion of PfCen1-GFP foci, I never observed any such events between ECCAs or ECCAs with CPs. It is difficult to determine, however, whether this reflects on their material state rather than lack of opportunity, as the likelihood of two foci coming in proximity within the cell volume was slim given their small numbers and size (Fig. 21A). Deformability, such as wetting, could only be assessed via live-cell STED of PfCen1-Halo due to the near-diffraction limit size of the foci. While the “wobble” shape (Fig. 7C) would be in line with the spherical shape expected of droplets, the contracting “stretching” shape instead implies elasticity, which is a property of solids or viscoelastic fluids. As previously discussed (3.2.1), even at improved resolution it remained difficult to determine whether the observed shapes were cohesive and homogeneous or instead made up of smaller particles as they appeared with fixed cell STED (Fig. 6B), which in turn could suffer from fixation artifacts.

The internal mixing of the PfCen1-GFP assemblies and exchange with the surrounding dilute phase was assessed via FRAP. In case of *in vivo* foci, assessment was limited to exchange with the cellular PfCen1-GFP pool due to their small size, wherein partial bleaching was not technically possible. Both CP and ECCA PfCen1-GFP foci showed no or very little recovery after photobleaching indicating a small mobile fraction M_f, suggesting a very limited exchange of PfCen1-GFP between the dilute and dense fraction, (Fig. 27). The broader variation in the M_f of the CP could indicate speculative changes in material properties of the compartment during different stages of centrosomal duplication. However, this should not be overinterpreted without further investigation and correlation with spindle stages. Unfortunately, the relevance of the FRAP results has to be questioned due to the unexpected influence of the GFP tag on internal and external turnover of PfCen1 liquids as observed *in vitro* (Fig. 28). Herein, PfCen1-GFP-6His droplets showed very little recovery after photobleaching despite their liquid nature evident by their round shape and wetting. At high concentrations, GFP is known to dimerize via the residues A206, L221, and F223 [243]. Even though monomeric versions (mGFP) have been created by mutation of these residues, they have not been exchanged within the eGFP I employed within this work. While the interaction between GFP is too weak to drive foci formation on its own (K_d = 0.11 mM [243]), it could influence the material properties of the foci. Alternatively, the relatively large size of the tag of 25 kDa (PfCen1 19.6 kDa) could also exert an influence. Increasing the molecular volume (v_m) while maintaining the same concentration (c) results in it occupying a larger volume

fraction φ of the solution ($\varphi = c*v_m$), which is an important factor in determining the thermodynamic viability of LLPS and the underlying reason for its concentration dependency [123]. In this case, an effect of the Halo tag (33 kDa) could not be excluded either. The effect of an mGFP tag on the M_f of PfCen1 could be assessed *in vitro* to determine whether a repeat of the *in vivo* FRAP experiments and generation of the required cell lines would be warranted.

If the "hardening" was not a GFP induced artifact then the hypothesis of foci assembling via LLPS would need to assume a gelation or maturation process, transforming an initial PfCen1 liquid into a viscous gel-like or solid state. This is a documented phenomenon of membraneless organelles including the centrosome and intracellular condensates [62], [140], [228]. While PfCen1 (or PfCen1-GFP) did not show any maturation *in vitro*, its interaction partner PfCen3 did (Fig. 11A). A model wherein PfCen3 interaction drives maturation of PfCen1 foci *in vivo* could therefore be conceived on a speculative basis. However, PfCen1-GFP rapidly drained from PfCen1-GFP + PfCen3 co-condensates after Ca^{2+}-depletion, an effect I did not observe during (attempted) *in vivo* Ca^{2+}-depletion (Fig. 26D). Of course, it is not clear whether the ionophore-based Ca^{2+}-depletion was efficient as discussed previously for intracellular Ca^{2+}-increase (see 3.2.5). On the other hand, PfCen3 maturation might also be an *in vitro* artifact. Furthermore, overexpression could feasibly induce unspecific aggregation, which is an inherent danger of condensates due to their high protein density [123]. However, the previously discussed (3.2.5) coordinated dissolution of PfCen1-GFP foci prior to egress (Fig. 24B, C) does show that assembly of these foci is reversible, arguing against an aggregate nature. This is further supported by their non-reactivity to the aggregate dye Proteostat, which they, in fact, seemed to exclude (Fig. 29C). The proprietary dye binds to cross-β spine structure typical for amyloid aggregates [244]. However, these structures are also found in amorphous aggregates and can form from non β-sheet secondary structures such as helices [245], [246]. This was of concern as centrins do not contain β-sheets. The fact that the dye could bind heat-denatured PfCen1-6His (Fig. 29A) showed that centrins can at least theoretically form the required cross-β spines. Testing Proteostat's affinity to the aggregates formed by Δ19-PfCen1-6His (Fig. 15B) could've provided a more realistic assessment, as aggregates arising from heat-denaturing might not be representative of those that could potentially form within cells. While it is not entirely certain that Proteostat would've been able to recognize intracellular PfCen1-GFP aggregates, the staining at least provides no support for foci consisting of or containing aggregates.

Finally, disregarding their material state, it is likely that PfCen1-GFP foci contain other proteins as well. Besides the aforementioned PfCen3 or PfSlp, potential downstream PfCen1 interaction partners could be recruited to the foci as well. Furthermore, as ECCAs often rip off from the outer CP core (Fig. 21E), it is possible that other components of the compartment detach alongside them. Albeit a rare event, this was hinted at by the ability of some Δ19-PfCen1-GFP ECCAs to nucleate tubulin and produce spindles (Fig. 25D), which centrins alone are unlikely to be capable of. An ability of the outer core to nucleate subpellicular microtubules was recently described, although only at a much later cell stage than when I observed it in early schizonts (2-5 nuclei) [69]. Due to the rarity of this

observation, it is unclear if this was merely a curious property of the mutant. To gain insight into the composition of ECCAs a PfCen1-GFP pulldown could be performed under mild (pARL) and strong overexpression conditions. The presence of other components would be an important factor as it could realistically affect the material properties of foci and would require more complex studies than those of PfCen1 alone.

3.2.7 Implications for centrosomal structures

An important part of the discussion of centrin LLPS as an evolutionarily conserved feature driving localization to centrosomes, is the evaluation of this hypothesis in the context of centrosomal structures. What implications would liquid centrin assemblies have for our understanding of not only the centriolar plaque but eukaryotic centrosomes in general, and are they consistent with observations? In the following I will discuss these questions at the examples of PfCen1 for the CP, HsCen2 for human centrioles, and ScCdc31 for the yeast SPB.

If the CP houses centrin liquids, could it itself be a liquid condensate? This would offer a tempting explanation for its high protein density and amorphous structure without apparent solid elements [52], [68]. It would furthermore mechanically simplify the problem of the hypothesized CP duplication by fission (also see 3.2.2). Centrosomes incorporating LLPS is not a novel concept. Already in 2017, Woodruff *et al.* declared the centrosome of *C. elegans* to form as a liquid condensate, based on its spherical shape and their successful *in vitro* assembly of PCM from recombinant proteins via LLPS that could nucleate microtubules [62], [140]. While the DNA-free region formed by the CP's inner core also assumes a spherical shape, in line with surface tension of liquids, U-ExM protein density stainings of the outer core are less consistent, potentially changing throughout the nuclear cycle [43], [52], [68]. Some showed globule-like assemblies, while others suggested inverted cone shape or "split" elongated structures (Fig. 3B, C). All studies seemed to confirm that centrins only occupy a sub-compartment of the outer core. Regardless of the material state of centrins, I further observed their rapid reorganization at the CP (Fig. 7C, D). This not only demonstrated that the structure of the outer CP core allows for rearrangement of proteins contained within, it also means that it restricts the movement of centrins. One could imagine a liquid-in-liquid model wherein centrin condensates are a subphase of the CP condensate, as it has been suggested for the nucleolus [135], [247]. In this light it is interesting that the 1,6-hexanediole treatment efficiently removed centrin foci from CPs, despite the fact that it had little effect on PfCen1 condensates *in vitro* (Fig. 30). Instead, it could have dissolved the hypothesized CP condensate thus releasing centrin. A CP disruption would be supported by the simultaneous aberrant spindle morphologies (Fig. 30B), which have previously been observed when depleting PfSlp from the outer core [71]. Caution regarding the interpretation of this effect has to be exerted, however, as 1,6-hexanediole is known to have many side effects on kinase and phosphatase activity as well as exhibiting a general cytotoxicity [125], [177], [248]. While I kept the incubation time short (5 min) and the employed concentration of 5% v/v was well within the typically used range already, 1% can impair certain cellular functions [248]. Besides retention via solubility within a CP

condensate, centrin might alternatively be retained through interaction with other centrosomal protein like PfSlp. Either through site-specific interactions or by acting as a local condensate nucleation site, e.g. via pre-wetting as discussed earlier (3.2.3) [239].

The interaction between centrins and Sfi1-like proteins such as PfSlp is of particular interest when discussing centrin localization to centrioles or the SPB. In humans HsCen2 forms two complexes at the highly organized centriole, one at the distal tip where it colocalizes with human Sfi1 (HsSfi1), and another alongside the inner walls of the core region while absent from the center [97], [98]. HsSfi1 was shown to bind HsCen2 directly and accordingly depletion of HsSfi1 or HsCen2 prevented the recruitment of the other, showing an interdependence for localization [98]. Meanwhile HsCen2 localization along the inner scaffold persisted in the absence of HsSfi1, where its recruitment is instead dependent on POC5, another documented binding partner [97], [98], [249]. Viewed through the lens of LLPS, HsCen2's localization and retention at the inner walls could constitute a form of surface-assisted condensation with POC5 acting as a nucleation factor [239], [250]. However, its localization could easily be explained through classical site-specific interaction with centriolar binding partners HsSfi1 or POC5. Unlike the CP, the rigid centriole on its own provides a separation from the surrounding medium, without the additional need for segregation via phase separation.

In the well characterized yeast SPB, ScSfi1 is a prominent component of the (half-) bridge, which is attached to the central SPB plaque on one end, with the other serving as the site for *de novo* assembly of a new SPB for duplication [55]. ScSfi1 forms a parallel array with its elongated α-helix, along which ScCdc31 binds via repeated interaction sites, stabilizing the structure [82], [103], [104]. As the site-specific interactions driving ScCdc31 association with ScSfi1 are well defined [82], an additional need for LLPS to facilitate localization of centrin in this eukaryote is dubious. Theoretically, a scenario could be conceived wherein a liquid coat of ScCdc31 around the filament, akin to what has been observed for LEM2 along microtubules [251], could increase local concentration to enhance saturation of centrin binding sites along ScSfi1. However, this remains fully speculative while current non-LLPS based interaction models appear to sufficiently explain ScCdc31's localization. Considering that *in vitro* LLPS of ScCdc31 only occurred at a markedly higher concentration threshold than the other centrins (Fig. 13A), one could also think of the SPB and ScCdc31 as an exception from the (hypothesized) rule of LLPS driven centrosomal centrin localization.

Overall, while an involvement of LLPS in CP formation and structure is an enticing concept, localization of centrin to centrosomes of other eukaryotes can likely be sufficiently explained as a client recruited through site-specific interactions alone. An introduction of LLPS into models therefore appearing superfluous, at least for recruitment. To test or exclude an involvement experimentally, thorough investigations would have to show that these classical interactions alone are sufficient for localization through careful mutagenesis of interaction sites of known, and yet unknown, binding partner [125]. This research would be complicated and require extensive efforts, highlighting the challenge of conclusively determining the relevance of LLPS in cells.

3.3 Conclusion

In appreciation of its critical relevance to disease transmission and pathogenesis, the highly atypical proliferation of the *Plasmodium* parasite has recently received renewed attention [32]. Despite significant advances, many of the fundamental aspects of the underlying biology remain enigmatic. While a central regulatory and mechanical player in schizogony, the composition and structural organisation of the centriolar plaque remains poorly understood. In this work, I aimed to gain deeper insights into its makeup by studying the localization and interactions of *P. falciparum* centrins as a highly conserved component eukaryotic MTOCs. I herein uncovered a novel aspect of centrin biology with potential relevance throughout eukaryotes.

While the localization of PfCen3 had previously been described, I discovered that all four *P. falciparum* centrins localize as foci to the outer core of the CP at the onset of schizogony. I further provide evidence for a yet unknown coordinated disassembly event of at least PfCen1-GFP foci prior to segmentation. Employing PfCen1-GFP as a marker to study the dynamics of the outer CP core in the presence of oryzalin, further revealed that its duplication and segregation is microtubule independent, suggesting the presence of an alternate duplication mechanism. Importantly, my investigation of the documented *in vitro* self-assembly of centrins revealed their ability to undergo Ca^{2+}-dependent LLPS for the first time. I observed this phenomenon for PfCen1, PfCen3, HsCen2, CrCen, TgCen2, and ScCdc31, suggesting it to be an evolutionarily conserved feature, which provides important context for future studies on centrin interactions. I also reported the first case of heterotypic centrin assembly between PfCen1 and PfCen3, which can form joint condensates. This could provide insight into the mechanics underlying their documented interaction *in vivo*. My studies further showed a critical role of the N-terminus for phase separation, with the presence of an IDR within this highly variable domain correlating with the ability of centrins to phase separate. Likewise, Ca^{2+}-binding was also of critical importance and likely mediates conformational changes that increase the valency of centrins to promote LLPS. PfCen1/3 undergoing phase separation while PfCen2/4 do not also provides a first potential functional difference that explains their non-redundancy during the intraerythrocytic cycle.

Centrins as resident centrosomal proteins, also carries interesting implications for the material state of the membraneless centrosome. Interpretation of the CP as a proteinaceous liquid would provide an intriguing explanation for its amorphous protein-dense organisation in the absence of any underlying “solid” structures. I therefore sought to determine whether centrin can form condensates *in vivo* and whether LLPS plays a role in their recruitment to the CP. As this marked the first study of LLPS in *Plasmodium*, I first needed to establish some critical methodology. First, I adapted live-cell STED to *P. falciparum* and observed the rapid rearrangement of PfCen1-Halo at the CP, which would be in line with a fluid-like state. I further developed a new DiCre/loxP based inducible and leak-free overexpression system, pFIO, that can generate high intracellular concentrations of proteins, which are challenging to express with classical systems (e.g.

pARL). Although the system curiously only led to expression in a subset of an induced population, it was still a very useful tool for single-cell microscopy analysis. In line with the strong concentration dependency of LLPS I observed the formation of non-centrosomal PfCen1 foci (ECCAs) and a premature recruitment to the CP, both of which correlated with expression levels. A liquid state of centrin foci and perhaps the CP was further supported by their dissolution, either through the cellular disassembly event prior to egress or artificially via 1,6-hexanediole treatment.

However, several observations seemed to argue against a role of LLPS in centrin foci assembly. While concentration had a major effect on centrin foci localization and assembly timing, the concentration at which foci formed was highly variable. This demonstrated that assembly is not triggered by crossing a critical concentration threshold alone. Neither was foci assembly or disassembly affected by attempts to modulate intracellular calcium levels. However, the EFh-dead-PfCen1 mutant nonetheless proved that Ca^{2+}-binding is critical for assembly and CP localization. Other structural mutants, on the other hand, namely Δ19-PfCen1 and the phosphomimetic PfCen3 mutants, which had lost the ability to phase separate *in vitro*, still formed both centrosomal and non-centrosomal foci (Fig. 16C, 25A). Together with PfCen2 and PfCen4 also localizing to the CP despite absence of *in vitro* LLPS, this would instead suggest a more conventional localization mechanism via site-specific interactions. Lack of exchange between the dense and dilute fraction shown by FRAP furthermore implies a more solid state of PfCen1-GFP foci, although the validity of this data is questioned by the effect of the GFP-tag on the material properties *in vitro* condensates. In any case, absence of Proteostat staining suggests that the solid state of the foci is not the result of aggregate formation.

While the observation of centrin LLPS could be an *in vitro* artifact, the stark contrast between different centrins in their phase separation capability despite their similar structure and simultaneous evolutionary conservation still argues for a biological function. For example, the above-mentioned observations could be reconciled in the following LLPS based model for PfCen1 recruitment to the CP (Fig. 35):

Just prior to the onset of S-phase recruitment or activation of a centrin binding partner at the outer CP core locally decreases the critical concentration, creating a nucleation site triggering PfCen1 LLPS. This interaction partner could potentially be PfSlp, with its centrin binding sites offering potential for surface assisted wetting [239]. Here, PfCen1 further interacts with PfCen3 forming a joint condensate within the compartment of the outer CP core, which could be imagined as a liquid-in-liquid arrangement confining the centrins while allowing some fluid rearrangement. During CP duplication the centrin condensate is then gradually stretched alongside PfSlp, before the outer core is split. Based on the observed hardening of PfCen3, it could furthermore undergo cycles of hardening, as observed for the PCM of other eukaryotes [62], [140], to comply with the alternating need for fission or mechanical stability.

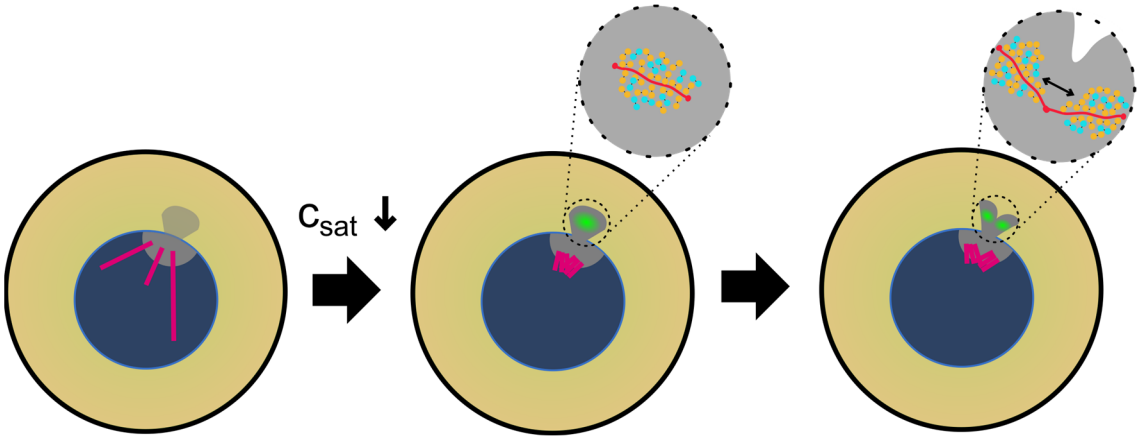


Figure 35 A model for centrin CP recruitment via LLPS. The illustration represents the speculative recruitment and arrangement of PfCen1 and PfCen3 (green dots and diffuse background; orange and cyan dots in zoom ins) to the CP (grey) from hemispindle collapse at the onset of S-phase to the initial stage of CP duplication. Herein interaction with PfSlp (red line) acts as the nucleation site triggering recruitment by locally decreasing the critical concentration threshold for LLPS (c_{sat}). During duplication, the centrin condensate is then split along an axis provided by the elongated α-helical structure of PfSlp molecules. Modified from Voß *et al.* (2023) [79].

Of course, this model remains speculative, while centrin recruitment could also be explained via conventional site-specific interactions outside the LLPS paradigm. Indeed, as the LLPS field evolved, initial enthusiasm about a role of LLPS in a broad range of cellular structures has grown into caution. While extensive evidence has been gathered in support of phase separation as a cellular phenomenon, recently more critical voices emerged, voicing concerns about commonly applied experimental approaches while questioning the conclusions postulated by previous studies [125], [153], [173]. As a result, the standard of proof has increased drastically over recent years. Therefore, demonstration of LLPS over mere site-specific interactions, let alone a functional role of LLPS, has become very challenging even in model organisms. While this experimental rigor will benefit the quality of future research, it exacerbates the limitations which divergent organism like *Plasmodium* impose upon LLPS studies. While this study may have taken some initial steps in this direction, proper investigation of LLPS to the current standards is not currently feasible for centrins in *Plasmodium*. My results therefore do not allow for a final determination about the role of phase separation in the biology of *Plasmodium* centrins and the centriolar plaque. However, the findings of my work and tools developed therein can inform future centrin interaction studies, motivate more advanced investigations into their phase separation, and support *Plasmodium* research in many other contexts.

4 Methods

4.1 Cloning of plasmids

4.1.1 Cloning strategy

Unless stated otherwise all plasmids were assembled via Gibson assembly (see 4.1.4). Primers used for sequence amplification and their templates are listed in Table 15 and sequences of synthetic oligos in Table 16. A list of final plasmids is provided in Table 17.

pARL plasmids

pARL-PfCen1-GFP, -PfCen2-GFP, and -PfCen4_GFP were generated by Nicolas Lichti under my supervision from pARL-PfCen3-GFP by removing the PfCen3 sequence via KpnI-HF + AvrII restriction digest and replacing it with PfCen1, PfCen2, or PfCen4 sequences that were PCR amplified via the primer pairs P1+2, P3+4, or P5+6, respectively.

pARL-PfCen3-ST-GFP and pARL-PfCen3-SYT-GFP were generated by Marina Iocca under my supervision from pARL-PfCen3-GFP by removing the PfCen3 sequence as well as the CRT promoter via NotI-HF and AvrII restriction digest and replacing it with CRTp-PfCen3-ST and PfCen3-SYT. Sequences were amplified using two fragments each generated via the primer pairs P7+8 and P10+11 or P7+P9 and P10+11 respectively. The introduced point mutations spanned a large area, which necessitated that the PfCen3 mutant sequence was split across two fragments, one of which included the CRT promoter, to reach an adequate fragment size. As the PCR likely introduced errors in the promoter sequence the now assembled mutant PfCen3 ORFs were cut out via KpnI-HF and AvrII digest and ligated back into the original pARL-PfCen3-GFP (digested via the same enzymes) using T4 ligase (see 4.1.4).

pARL-PfCen1-Halo was generated by Johanna Bauer under the supervision of Dr. Caroline Simon from pARL-PfCen1-GFP by removing the GFP sequence via AvrII + PstI-HF restriction digest and replacing it with the Halo sequence PCR amplified via the primer pair P12+P13.

pFIO plasmids

I generated pFIO from pARL-PfCen3-GFP in a first step by NotI-HF + HindIII-HF restriction digest leaving only the hrp2 3'UTR of the hDHFR resistance cassette and integrating the Pfhsp70 5'UTR and hDHFR sequences that were PCR amplified via the primer pairs P14+P15 and P16+P17 respectively. This intermediate plasmid was digested with BamHI-HF to insert an mCherry and GFP sequence that was PCR amplified via the primer pairs P19+P20 and P21+P22 respectively.

I then generated pFIO_hsp70p_GFP by SalI-HF restriction digest to insert a PbDHFR 3'UTR sequence PCR amplified via primer pair P18+P19.

I then generated pFIO_hsp86p_GFP by removal of the Pfhsp70 promoter by NotI-HF + BamHI-HF restriction digest (which also removed the hDHFR sequence) and replacing it with the Pfhsp86 5'UTR and hDHFR sequences that were PCR amplified using primer pairs P25+26 and P16+P18 respectively.

I generated pFIO_hsp70p/hsp86p_Cen1-GFP and pFIO_hsp86p_ Δ19-PfCen1-GFP from pFIO_hsp70p_GFP and pFIO_hsp86p_GFP by removing the GFP sequence via MluI-HF + XhoI restriction digest and replacing it with PfCen1-GFP or Δ19-PfCen1-GFP sequences that were PCR amplified via the primer pairs P27+P22 or P28+P22 respectively.

I generated pFIO_hsp86p_ EFh-dead-Cen1-GFP, and _HsCen2-GFP from pFIO_hsp86p_Cen1-GFP by removing the Cen1 sequence via MluI-HF + AvrII restriction digest and replacing it with the synthesized genestring dsDNA sequences codon optimized for *P. falciparum* encoding EFh-dead-PfCen1 and HsCen2 of oligo 1 and 2.

I generated pFIO_hsp86p_~~mCherry~~_GFP-T2A-PfCen1 by first removing mCherry sequence from pFIO_hsp86p_PfCen1-GFP via BamHI-HF + SalI-HF restriction digest and replacing it with ssDNA oligo 3, introducing a stop codon after the hDHFR sequence. The PfCen1-GFP sequence was then removed via MluI-HF + XhoI restriction digest and replaced with GFP-T2A and PfCen1 (without start codon) sequences PCR amplified using primer pairs P29+P30 and P31+P32 respectively and into the same backbone.

<u>pET-28 constructs</u>

To generate the pET-28 constructs pET-28a(+) was digested with NcoI-HF + XhoI and HsCen2 as well as codon optimized PfCen1, Δ19-PfCen1, or PfCen2 sequences were inserted. Sequences were PCR amplified using primer pairs P33+P34, P35+P36, P37+P35 and P39+P40 respectively. To generate pET-28_PfCen1-GFP PfCen1 and GFP sequences were PCR amplified via the primer pairs P35+P38 and P41+P42 respectively and integrated into the same backbone. pET-28_EFh-dead-PfCen1, -ScCdc31, -TbCen2, and -CrCen were generated by inserting dsDNA oligo 8, oligo 9, oligo 10, and oligo 11 respectively. Since a residual guanine from the pET-28 backbone located before the 6His tag could not be removed, two additional guanines were integrated to encode a minimal glycine linker in all cases via the respective reverse primers. pET28_PfCen1 and pET28_PfCen2 were generated by Nicolas Lichti under my supervision, while the remaining constructs were generated by myself (see table 17).

pET-28_1NCen4 and _4NCen1 were generated by Marina Iocca under my supervision by digesting pET-28 with NcoI-HF and XhoI to insert the 1NCen4 or 4NCen1 sequences. They were PCR amplified via primer pair P47+P50 and P48+P50 respectively.

pZE13d plasmids

First, a new version of the bacterial expression vector pZE13d, encoding a C-terminal instead of N-terminal 6-His, called pZE13d-C was generated. Towards this end, pZE13d was digested with BamHI-HF and PstI-HF to remove the previous N-terminal 6His sequence and multiple cloning site (MCS). A *de novo* sequence containing a new MCS, including a BamHI and SalI site and C-terminal 6His tag was then created by annealing ssDNA oligo 12 and 13 (see 4.1.2). The sequence was then integrated through T4 ligation (see 4.1.4).

pZE13d-C_PfCen3 and _PfCen4 were generated via restriction digest of pZE13d-C with BamHI-HF and SalI-HF and integrating the PfCen3 and PfCen4 encoding sequences amplified via the primer pairs P43+P44 and P45+P46 respectively.

To generate pZE13d- PfCen3_ST and -PfCen3_SYT, pZE13d-C was digested with AatII and SalI-HF. PfCen3_ST and PfCen3_SYT were then inserted in two fragments that were PCR amplified with P53+P44 and either P50+P51 or P50+P52. The introduced point mutations spanned a large area, which necessitated that the PfCen3 mutant sequence was split across two fragments, one of which included part of the plasmid's promoter region to reach an adequate fragment size.

pZE13d-C_1NCen3 was generated from pZE13d-C via digestion with BamHI-HF and SalI-HF to insert the 1NCen3 sequence that was PCR amplified via the primer pair P54+P44. pZE13d-C_3NCen1 was generated from pZE13d-C via digestion with AatII and SalI-HF to insert the 1NCen3 sequence in two parts that were PCR amplified via the primer pairs P50+P55 and P56+P57.

Another version of the pZE13d vector encoding an N-terminal 6His tag followed by a TEV (Tobacco Etch Virus) protease cleavage site to allow for the removal of the 6His tag via TEV protease, called pZE13d-TEV, was generated. Towards this end pZE13d was digested with EcoRV-HF and PstI-HF to insert a 6His-Linker-TEV sequence (followed by an SfoI site) via ssDNA oligo 14. pZE13d-TEV_PfCen1-4 were then generated from this plasmid by restriction digest with SfoI to integrate the PfCen1-4 sequences that were PCR amplified via the primer pairs P58+P62, P59+P62, P60+P62, and P61+P62 respectively.

4.1.2 Generation of dsDNA fragments

Restriction digest

To generate linearized dsDNA inserts or plasmid backbone required for plasmid assembly (see 4.1.4) 2 µg of plasmid was digested in a 50 µl volume with 5 µl 10x Cutsmart buffer and 1 µl of each restriction enzyme for 1-2 h at 37°C.

PCR

PCRs with the purpose of generating linear dsDNA fragments for cloning or for genotyping were typically performed using Phusion High-Fidelity DNA polymerase using the following reaction mix composition:

Table 1 Phusion polymerase PCR reaction mix

Reagent	Final concentration
5X Phusion HF buffer	1 x
dNTPs	200 µM
Forward Primer	500 nM
Reverse primer	500 nM
Phusion HF DNA polymerase	1 unit/50 µl

In cases where this approach failed to generate sufficient amounts of specific product, Q5 High-Fidelity DNA polymerase was employed instead using the following reaction mix composition:

Table 2 Q5 polymerase PCR reaction mix

Reagent	Final concentration
5X Q5 Reaction Buffer	1 x
dNTPs	200 µM
Forward Primer	500 nM
Reverse primer	500 nM
Q5 High-Fidelity DNA polymerase	1 unit/50 µl

For amplification of insert fragments, reactions were performed in a total volume of 50 µl, using ~5 ng of plasmid as the template. Primers were ordered in desalted lyophilized form and resuspended in ddH_2O to a final stock concentration of 100 µM. Reaction mixes were prepared on ice and briefly mixed before transfer to the thermocycler.

Both polymerases used the following standard PCR cycle parameters:

Table 3 PCR thermocycler settings

Step	Temperature	Time
Initial Denaturation	98°C	30 s
Denaturation	98°C	10 s
Annealing	X	30 s
Extension	62/68/72°C	Y
Final Extension	62/68/72°C	5 min
Cooling	4°C	Hold

The standard Extension temperature of 72°C was decreased to 68°C when *P. falciparum* or *P. berghei* genetic sequences were amplified due to the high AT content of the template. The temperature was further decreased to 62°C for UTRs as this decreased the

error-rate during amplification of these highly repetitive sequences. Human and bacterial sequences were amplified at 72°C. The annealing temperature X varied between primers and was calculated using the NEB TM calculator webtool. Extension time Y was based on amplicon length and set according to the manufacturer's recommendation, but extended for 68°C and 62°C elongation assuming a 50% decrease in efficiency per 10°C difference from 72°C.

Refer to 4.1.1 for cloning strategies and Table 15 for primer sequences.

ssDNA Oligo annealing

To generate short *de novo* dsDNA sequences for integration into a linearized plasmid backbone via ligation, two mostly complementary ssDNA oligos/primers were annealed. The short non-complimentary overhangs served to generate sticky ends for ligation. As subsequent T4 ligation requires a 5' phosphate group not included in the ssDNA oligos, they were also phosphorylated using a polynucleotide kinase. The following reaction mix was used:

Table 4 ssDNA oligo annealing reaction mix

Reagent	Volume
Oligo 1 (100 µM)	1 µl
Oligo 2 (100 µM)	1 µl
10x ligation buffer	1 µl
T4 Polynucleotide Kinase	0.5 µl
H_2O	6.5 µl

Phosphorylation reaction and annealing of the oligos via a temperature gradient was subsequently performed using a thermocycler with the following parameters:

Table 5 ssDNA oligo annealing thermocycler settings

Step	Temperature	Time
Phosphorylation	37°C	30 min
Denaturation	94°C	5 min
Annealing	94°C -> 25°C	690 s
Cooling	4°C	Hold

4.1.3 Purification of dsDNA fragments

Gel electrophoresis

To visualize and separate DNA fragments generated via digest or PCR (see 4.1.2) by size, gel electrophoresis was performed using 0.8% (w/v) agarose gels. Short dsDNA oligos resulting from annealing (4.1.2) were not purified further. Samples were mixed with Gel Loading Dye Purple (6x) that had been supplemented 1:500 with Midori Green Advance

DNA Stain and loaded onto the hardened gel. 1 kb DNA ladder was employed as reference to determine the size of DNA fragments. Electrophoresis was performed at 135 V, 130 W, and 1000 mA for 15-25 min. DNA bands were visualized and recorded in the dark using the UVT-28 L UV table and an E.A.S.Y 440 K camera.

DNA purification from agarose gels

DNA fragments separated via gel electrophoresis were excised using a scalpel and purified from the agarose gel using the High Pure PCR Product Purification kit. Per 100 mg weight the excised agarose was dissolved in 300 µl supplied dissolution buffer at 56°C for 10-15 min and subsequently vortexed with 150 µl isopropanol per 100 mg. The suspension was transferred to a High Pure Filter tube, centrifuged at 12000g for 1 min, then washed twice with 500 µl and 200 µl supplied washing buffer. DNA was eluted in 20 µl H_2O.

4.1.4 Plasmid assembly

T4 ligation

To ligate linear dsDNA fragments that resulted from annealing two oligos (see 4.1.2) into a linearized plasmid backbone, the following reaction mix was used:

Table 6 T4 ligation reaction mix for dsDNA inserts generated by ssDNA oligo annealing

Reagent	Volume/mass
Annealed oligos (1:200)	1 µl
Plasmid backbone	50 ng
T4 ligase buffer	1 µl
T4 ligate	1 µl
H_2O	to 10 µl

If two linear dsDNA fragments, i.e. a backbone and an insert, resulted from restriction digest they were ligated using the following reaction mix:

Table 7 T4 ligation reaction mix for dsDNA inserts generated by restriction digest

Reagent	Volume/mass
Insert	*
Plasmid backbone	50 ng
T4 ligase buffer	2 µl
T4 ligate	1 µl
H_2O	to 20 µl

*1:3 backbone to insert molar ratio

Ligation was performed for 20 min at RT and the product was transformed into chemically competent Dh5α *E. coli* cells (see 4.1.5).

Gibson Assembly

For assembling thelinear backbone and inserts into new plasmids via Gibson assembly, the molar ratio depended on the number of total fragments, including the backbone. If possible, 50 µg of backbone was mixed in a 1:2 molar ratio with the insert in cases of 2-3 fragment assembly (including the backbone), and 1:1 molar ratio if ≥ 4 fragments were assembled. DNA concentrations were previously measured via 260 nm photometric absorption using the NP80 NanoPhotometer. The resulting volume was supplemented with ddH_2O to 5 µl where necessary, and then mixed with the same volume 2X Gibson Assembly Master Mix in 200 µl PCR tubes. These were incubated on a thermocycler at 50°C for 15 min or 60 min depending on whether 2-3 or ≥ 4 fragments were assembled. Products were transformed into chemically competent Dh5α *E. coli* cells (see 4.1.5).

4.1.5 Plasmid selection and purification

Transformation

Afterwards the newly assembled plasmids were transformed into chemically competent Dh5α *E. coli* cells. 20 µl of cells were incubated with 2 µl of the reaction mix for 20 min on ice before a heat shock at 42°C for 30 s, followed by recovery on ice for 2 min. After resuspension in RT SOC medium and a recovery period of 1 h at 37°C shaking at 130 rpm, the cells were plated to prewarmed LB-Kan or LB-Amp plates and incubated overnight (o/n) at 37°C until visible colonies emerged.

Miniprep & Glycerol stocks

For small scale amplification and purification of cloned or pre-existing plasmids minipreps were performed using the GenElute HP Plasmid Miniprep Kit. A 3 ml LB-Amp/Kan o/n culture was inoculated with a single colony picked from an agar plate or from a glycerol cryo stock and then incubated o/n at 37°C shaking at 130 rpm. The next day, 2 ml of o/n culture was centrifuged in a 2 ml tube at 14000g for 1 min, supplemented with 200 µl chilled resuspension buffer and resuspended by running (“ratcheting”) the tube over an Eppendorf tube rack. Bacteria were then lysed by adding 200 µl basic lysis buffer, with which it was mixed by inverting the tube six times, followed by a 4 min incubation at RT and subsequent neutralization with 350 µl acidic neutralization buffer, equally mixed in through inversion. The cell debris was then spun down at 14000g for 10 min. The supernatant was then transferred to a provided column, which was pre-equilibrated with 500 µl equilibration buffer. After centrifugation at 14000g for 1 min each, column-bound DNA was washed first with 500 µl Wash buffer I followed by 700 µl Wash buffer II. Residual ethanol contained within the washing buffers was removed from the column by centrifugation at 21000 g for 3 min. DNA was then eluted in 35 µl elution buffer after 1 min of incubation followed by 14000g centrifugation for 1 min.

For new plasmids, the remaining o/n culture that had not been processed was supplemented in a 1:1 (volume) ratio with a 50% glycerol solution in H_2O to a final concentration of 25% glycerol, mixed via pipetting, before being transferred to a cryo tube and frozen for storage at -80°C.

Sequencing
Correct plasmid sequences were confirmed via Sanger-sequencing. 20 µl of each 80 ng/µl plasmid and 10 µM primer solution were sent to the Eurofinsgenomic Supremerun overnight service.

4.2 *P. falciparum* strain culturing and generation

4.2.1 *P. falciparum* blood culturing and synchronization

P. falciparum strains were maintained within human O+ erythrocyte cultures in cRPMI (supplemented with selection drugs where relevant) at a haematocrit of 2.5%. Cultures were incubated at 37°C in flasks equipped with filter caps for gas exchange in a 3% CO_2, 5% O_2, and 90% humidity atmosphere. The parasitemia and distribution of asexual stages were regularly assessed via thin blood smears that were fixed with methanol and stained with Hemacolor before observation through the Nikon E100 microscope 100x oil objective. Parasitemia was typically maintained below 5% through splitting. If required for an experiment, parasites were synchronised to the ring stage via incubation of iRBCs in a 25x volume of 5% sorbitol solution at 37°C for 10-15 min. iRBCs were then centrifuged at 800g for 2 min, washed once with prewarmed cRPMI, and returned to culture.

4.2.2 Freezing & thawing of *P. falciparum* cell lines

For the purpose of long term-storage parasite strains were frozen in cryostocks and thawed on demand. Prior to freezing, cultures were expanded to 1 ml iRBCs in 35 ml medium with a ring-stage parasitemia above 1.5%, as later stages would not survive the freezing process. iRBCs were pelleted at 800 g for 3 min and mixed slowly with 400 µl pre-warmed freezing solution by dropwise addition under constant agitation. After 5 min of rest at RT, the procedure was repeated with 1.2 ml and finally 2.4 ml of freezing solution. 1 ml aliquots were then transferred to cryotubes and stored at either -80°C or in liquid nitrogen.

For thawing, the cryostock was retrieved and thawed in the palm of a (gloved) hand. Once liquid, it was transferred to a 50 ml tube and mixed slowly with 400 µl pre-warmed 12% (w/v) NaCl (in H_2O) solution by dropwise addition under constant agitation. After 5 min of rest at RT, the procedure was repeated with pre-warmed 9 ml 1.6% (w/v) NaCl (in H_2O) solution. The remaining erythrocytes were pelleted at 800 g for 2 min and resuspended in 8 ml pre-warmed cRMPI and supplemented to 200 µl erythrocytes. The culture was then placed into the standard blood-culture incubation conditions (see 4.2.1). Parasitemia of the culture was assessed the next day and split if necessary.

4.2.3 pFIO DiCre induction

The expression of the 2nd ORF in 3D7-DiCre_pFIO parasite lines was induced approximately 48 h prior to experiments during the schizont stage of synchronized cultures. iRBCs were diluted to a parasitemia of 0.5% in 25 µl RBC volume, which was incubated in 400 µl cRPMI supplemented with 100 nM RAP or 1% DMSO as a control

for 4 h at 37°C. Afterward the cells were pelleted at 800 g for 30 s and washed 4 x with 1 ml cRPMI and finally cultured in 1 ml cRPMI (without WR) until further processing for flow cytometric analysis or imaging.

4.2.4 *P. falciparum* transfection

Preparation of DNA for transfection

Transgenic parasite strains were generated via electroporation using *P. falciparum* NF54 WT as the acceptor strain for pARl plasmids and 3D7-DiCre for pFIO plasmids. To generate the required amount, plasmids were amplified and purified from 200 ml transformed *E. coli* o/n culture via the NucleoBond Xtra Midi Kit. 100 µg of total plasmid was precipitated by supplementing 0.1 x volume 3 M sodium acetate and 2x volume -20°C ethanol under gentle agitation followed by o/n incubation at -20°C. After precipitation the DNA was pelleted at 17000 g for 30 min at 4°C, washed with 70% ethanol to wash and sterilize the interior of the tube. After another centrifugation step at 17000 g 4°C for 15 min all liquid was removed and the pellet airdried in the sterile environment of a cell culture hood. The DNA was resuspended via vigorous pipetting in 30 µl TE buffer and stored at -20°C until transfection.

Electroporation of parasites

Once a pre-synchronized acceptor strain had reached a ring stage parasitaemia of ≥ 4% 150 µl iRBCs were centrifuged at 800 g for 3 min, washed with prewarmed CytoMix and then thoroughly mixed with the DNA solution followed by 350µl prewarmed CytoMix. This mixture was transferred into a chilled (4°C) Gene Pulser Electroporation cuvette and electroporated with the Gene Pulser II system at 310 kV, 950 µF in exponential mode. The transfected iRBC solution was then quickly transferred to 5 ml prewarmed cRPMI for 30 min recovery at 37°C. iRBCs were then pelleted at 800 g for 2 min and transferred to regular culture (5 ml).

Selection

Drug selection with 2.5 nM WR99210 was started 6 h post transfection and maintained indefinitely. Efficacy of the drugs, as evidenced by the visible absence of intact parasites, was confirmed 2 days post transfection via blood smear. Medium was exchanged daily for 2 days post transfection, followed by a 1:5 split on day 3. From then on, medium was exchanged on Mondays, Wednesdays, and Fridays with a 2:3 culture split being performed once per week to supply fresh erythrocytes. This regimen was maintained until resistant parasites could be detected via blood smear, from which point on the parasite line was cultured as normal (see 4.2.1).

4.3 *P. falciparum* population analysis

4.3.1 Western Blot

P. falciparum protein extraction

For the analysis of GFP-T2A-PfCen1 expression and skipping efficiency, proteins were first extracted from 3D7-DiCre_pFIO_hsp86p_~~mCherry~~_GFP-T2A-PfCen1 parasites treated with RAP or DMSO 5 days prior (see 4.2.3). For the evaluation of the generated anti PfCen1-6His antibody, I used WT NF54 parasites. Parasitemia of the culture was assessed via blood smear. iRBCs were then pelleted at 800 g for 2 min and washed once with a 1 ml prewarmed phosphate buffered saline (PBS). Parasites were then isolated via erythrocyte lysis by resuspension in 1 ml 0.15% Saponin/PBS. Once visually completed erythrocyte lysis was achieved after a few seconds the isolated parasites were pelleted at 3250 g for 5 min followed by 3 PBS wash steps. The cells were then lysed by boiling them at 95°C in 1x Laemmli/PBS buffer, the volume of which was adjusted to a final concentration of 10^7 parasites per 10 µl lysate using the following formula:

$$Buffer\ volume\ [\mu l] = \frac{10^{10} \times volume\ iRBCs\ [ml] \times Parasitemia\ [\frac{\%}{100}]}{10^6}$$

(assuming 10^{10} erythrocytes per 1 ml blood pellet)

The sample was then boiled at 95°C for 10 min and afterwards stored at -20°C.

Western Blot

Prior to use for WB analysis the lysate samples were thawed and boiled again at 95°C for 5 min and centrifuged at 21000 g for 1 min to remove hemozoin, which can negatively affect the WB quality. 10 µl lysate or 20 ng recombinant protein were loaded onto a precast 12 well 12% Mini-PROTEAN TGX precast gel and an SDS-PAGE was performed as described in 4.5.2. Afterwards the gel was placed onto the nitrocellulose membrane of the Trans-Blot Turbo Transfer Pack and covered with the provided wet tissues. Air bubbles were removed via a roller and proteins blotted onto the membrane using the Trans-Blot Turbo Transfer system at 1.3 A, 25 V for 10 min. Then gel was then discarded and the membrane blocked in filtered 5% milk/0.5% Tween-20/PBS blocking buffer for 15 min shaking. The membrane was transferred to a 15 ml tube for primary antibody staining, which was performed under rotation in 3 ml blocking buffer at 4°C o/n. The next day the membrane was washed 3x 10 min with blocking buffer under shaking before secondary antibody staining was performed in a 15 or 50 ml tube for 1 h at RT under rotation. After 3x 10 min washing steps with blocking buffer and a final wash with PBS, the membrane was analysed using the Li-COR Odyssey CLx.

4.3.2 GFP quantification via flow cytometry

To determine the share of GFP positive cells of transgenic parasite strains 2.5 µl iRBCs (induced in case of pFIO, see 4.2.3) were pelleted at 800 g for 30 s, washed once in 0.9% NaCl solution, and stained with 5 µM SYTO 61 for 1 h at 37°C in 0.9% NaCl. Afterwards the cells were pelleted at 800 g for 30 s, washed with 0.9% NaCl, and resuspended in an appropriate volume of 0.9% NaCl. Flow cytometric analysis was performed at RT using the FACSCanto II. First erythrocytes were gated in the forward and side scatter (FSC-A, SSC-A), followed by gating for single cells in the FSC-H/FSC-A scatter, and finally for multinucleated iRBCs via the SYTO 61 staining acquired using a 640 nm laser and 660/20 emission filter (Fig. 36). The share of GFP positive cells was determined via a 488 nm laser and 530/30 nm emission filter.

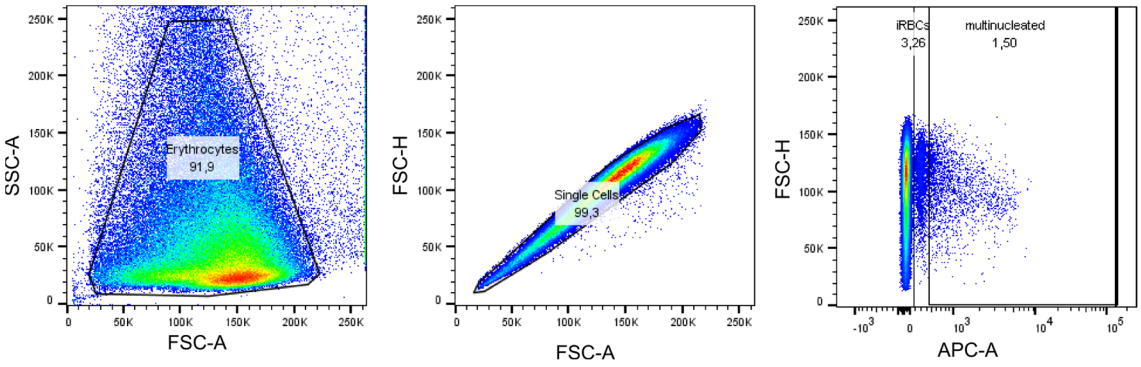


Figure 36 Flow cytometry gating strategy for iRBCs with SYTO61. Gating strategy selecting for intact erythrocytes in SSC-A and FSC-A, then for single cells in FSC-A and FSC-H, and finally for multinucleated infected erythrocytes (e.g. schizonts) via SYTO61 DNA staining via APC-A.

DNA replication time course

To study the impact of oryzalin treatment on DNA replication 3D7-DiCre_pFIO_hsp70_Cen1-GFP, cells (uninduced) were synchronized via MACS purification. Herein 8 ml of culture (200 µl RBCs) was loaded onto an LS column that had been pre-equilibrated with 3 ml cRPMI and placed within the magnetic field of a QuadroMACS Separator to enrich trophozoites and schizonts via their magnetic hemozoin. Gravity flow was throttled through a 0.6 mm syringe needle. The column was washed twice with prewarmed 3 ml cRPMI before the magnet and syringe were removed and the purified late stages eluted in prewarmed 5 ml cRPMI facilitated via a plunger. Cells were subsequently incubated at 37°C for 3 h with 50 nM ML10 to prevent egress of daughter cells and thus enrich the culture for late schizonts (segmenters). Egress was initiated via removal of ML10 via two washes in 5 ml cRPMI. The culture was supplemented with fresh uRBCs and incubated at 37°C for a 1.5 h invasion window while shaking at 80 rpm to minimize double-infections. Further invasion was prevented via the addition of heparin to 50 U, and by removing remaining schizonts or trophozoites via sorbitol treatment (see 4.2.1), thus only leaving rings that had invaded within the previous 1.5 h. The culture was split and treatment with 0.02% DMSO or 20 µM Oryzalin started at 14 hpi. To track the DNA content over time, samples were taken at 1 hpi and from 14 hpi onward in 4 h intervals up until 46 hpi. 50 µl of resuspended culture was taken from the culture in triplicates, transferred to a 96-well U-bottom plate, centrifuged at 1500 rpm

for 2 min, washed once with 100 µl PBS, and subsequently fixed with 4% PFA and 0.0075% glutaraldehyde in PBS for 1 h at RT. The cells were washed once with 100 µl PBS and stored at 4°C. Once all timepoints had been acquired the cells were first permeabilized with 100 µl 0.1% Triton X-100 in PBS for 10 min at RT, washed with 200 µl PBS, and then treated with 100 µl 0.3 mg/ml RNase A for 30 min at 37°C to reduce the RNA background, as described by Ganter *et al.* [51] . After a wash in 2x 200 µl PBS, cells were then stained with 1:2000 SYBR Green I in PBS for 20 min RT in the dark, washed a final time with 200 µl PBS, and finally resuspended in PBS. DNA content was then assessed using flow cytometry at the FACSCanto II via the SYBR Green I signal. First erythrocytes were gated in the FSC-A/SSC scatter, followed by gating for single cells in the FSC-H/FSC-A scatter. The share of SYBR Green positive cells and their average signal was determined via a 488 nm laser and 530/30 nm emission filter (Fig. 37).

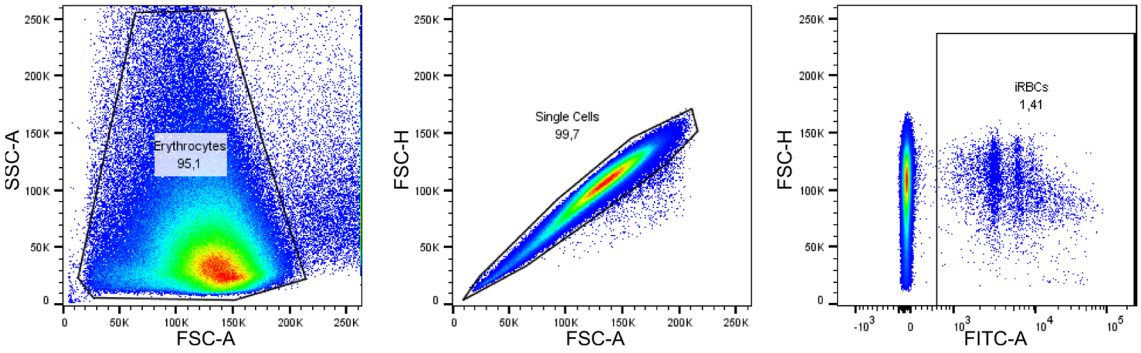


Figure 37 Flow cytometry gating strategy for iRBCs with SYBR Green. Gating strategy selecting for intact erythrocytes in SSC-A and FSC-A, then for single cells in FSC-A and FSC-H, and finally for multinucleated infected erythrocytes (schizonts) via SYBR Green DNA staining via APC-A.

4.4 Microscopy

4.4.1 Seeding of iRBCs on imaging dishes

For the purpose of IFAs or live-cell imaging, iRBCs were first seeded onto the glass bottom of a 8-well chambered slides in a monolayer. For this purpose, the bottom of each well was coated with 70 µl of a 5 mg/ml Concanavalin A solution for 25 min at 37°C. The solution was then aspirated and washed once with either iRPMI or PBS. Concanavalin A coating was unnecessary and thus skipped if IbidiTreat 8-well slides were employed. The IbidiTreat 8-well slides were never employed for STED microscopy due to the superior optical properties of glass bottom slides. During the coating process 100 µl of parasite culture for each well had previously been pelleted at 800 g for 30 s and washed in prewarmed iRPMI 3x to remove lipids and proteins from cRPMI. Washed iRBCs were then transferred to the coated well to settle for 10 min at 37°C. Afterwards unbound cells were washed away through gentle pressure from pipetting up and down of the solution and were subsequently aspirated. Cells were then either incubated with 400 µl prewarmed cRPMI or immediately fixed (see 4.4.2).

4.4.2 Confocal microscopy for IFAs

Cells previously seeded to 8-well dishes (see 4.4.1) were quickly washed with prewarmed PBS and subsequently chemically fixed with 200 µl prewarmed 4% PFA/PBS for 20 min at 37°C. Cells were then washed twice with PBS and either stored at 4°C in PBS or processed immediately according to a previously published protocol by Mehnert, Simon *et al*. [191]. Therein cells were permeabilized 0.1% TritonX-100/PBS for 15 min, washed three times with PBS before quenching remaining free aldehyde groups with ~0.1 mg/ml $NaBH_4$ in PBS, followed by three more PBS washes. Blocking of unspecific binding sites was performed via incubation with a 3% (w/v) Albumin Faction V in PBS (BSA/PBS) for 1 h at RT. The cells were stained with primary antibodies (Table 9) diluted in 3% (w/v) BSA/PBS under gentle shaking and afterwards washed three times with 0.5% Tween-20/PBS shaking for 5-10 min. Secondary antibody and Hoechst staining was performed for 60 min at RT in 3% (w/v) BSA/PBS in the dark under gentle shaking. Cells were washed twice with 0.5% Tween-20/PBS and once with PBS shaking for 5-10 min. Cells were stored at 4°C in the dark before and in between imaging sessions.

Routine confocal microscopy was performed with the SP8 point laser scanning confocal microscope using the HC PL APO CS2 63x/1.4 N.A. oil immersion objective. 405 nm, 488 nm, 561 nm, and 633nm lasers were used for excitation and emission detected via two HyD detectors placed after a spectral emission filter. 128x128 pixel multichannel images with a pixel size of 72.6 nm and a z-interval of 300 nm were acquired sequentially to avoid bleed-through. Care was taken to not overexpose the sensors to avoid introducing errors into quantifications. Where quantification and comparison between different experimental conditions was required acquisition settings were kept consistent unless stated otherwise.

ECCA frequency quantification

Confocal microscopy for the quantification of ECCA frequency in the various 3D7-DiCre_pFIO_Cen1-GFP and _ΔPfCen1-GFP cell lines was performed using induced cells fixed approximately 48 h post induction and immuno-stained against DNA and tubulin. GFP was stained using an Alexa 488 labelled primary antibody "GFP booster" to preserve GFP signal with minimal off-target staining in case samples had to be imaged over multiple microscopy sessions. In the case of cells overexpressing untagged PfCen1 from pFIO_hsp86_~~mCherry~~_GFP-T2A-Cen1, a staining against PfCen1 was performed. Cells were acquired using the Leica Sp8. For 3D7-DiCre_pFIO_hsp70p_Cen1-GFP, -_pFIO_hsp86p_Cen1-GFP, and -_pFIO_hsp86p_Δ19-PfCen1-GFP 54, 60, and 51 GFP positive early schizonts, defined as parasites with at least one intranuclear spindle and 1-5 nuclei, were acquired in separate session. Foci located outside direct proximity to the spindle poles, as determined via the tubulin staining, were classified as ECCAs. No such quantification was performed for induced (see 4.2.3) 3D7-DiCre_pFIO_hsp86p_EFh-dead-Cen1-GFP as no cells with any GFP foci could be found. For induced and DMSO treated 3D7-DiCre_pFIO+_GFP-T2A-Cen1 53 and 49 early schizonts were acquired. These were all GFP positive in case of the induced population, but negative in the uninduced. Due to the anti-PfCen1 antibody inevitably introducing unspecific signals, an

additional cutoff for the classification as ECCA was applied. Only foci located outside direct proximity of the spindle poles that had an identical to or higher than the weakest centrosomal signal were counted as ECCAs. Analysis was performed using Fiji software. To quantify the GFP signal density a (1 to 255) threshold was applied to isolate cell from background signal. The multimeasure tool was then used to read out the area and raw integrated density of each Z-slice, which were added up and used to calculate the signal density.

Quantifying impact of 1,6-hexanediole on centrin foci

3D7-DiCre_pFIO_hsp86p_GFP-T2A-Cen1 cells were induced with RAP or treated with DMSO (see 4.2.3), seeded to 8-well dishes one day after (see 4.41), and left to incubate in cRPMI o/n at 37°C under normal atmospheric culture conditions (see 4.2.1). They were then either left untreated or cRPMI was replaced with pre-warmed cRPMI supplemented to 5% (v/v) 1,6-hexanediole. After 5 min cells were briefly washed with pre-warmed PBS and fixed with PFA for an IFA staining against DNA, tubulin, and PfCentrin1. Seeded wells of treated and untreated cells were spaced out to rule out any potential spillover of 1,6-hexanediole. Cells were imaged at the Leica SP8 as described above. Of the DMSO-treated population ,36 1,6-hexanediole treated and 33 untreated early schizonts (1-5 nuclei with one or more intranuclear spindle) were analysed. The RAP treated population was not analysed further due to the strong cytoplasmic staining resulting from the PfCen1 overexpression potentially obfuscated centrosomal foci. Spindles without centrin foci adjacent to their 1-2 spindle poles (depending on spindle stage) were counted as spindles without centrosome. Mitotic spindles with only one pole lacking a centrin foci were not counted as such, as drastically uneven distribution of centrin during prior CP duplication is a documented naturally occurring phenomenon [52], [252]. Early hemispindles at the trophozoite to schizont transition, where a centrin assembly might not have yet occurred, were excluded by only including mononucleated cells with a mitotic spindle or later.

4.4.3 Confocal time-lapse microscopy

Effect of Oryzalin on PfCen1-GFP dynamics

For long term live-cell imaging studying the dynamics of PfCen1-GFP foci under the influence of Oryzalin 3D7-DiCre_pFIO_hsp70_Cen1-GFP cells were induced (see 4.2.3) approximate 48 h before imaging and seeded the previous day to two adjacent wells of an 8-well chamber (see 4.4.1). 3 h before imaging, cells were pre-incubated in sealed wells at 37°C in pre-equilibrated imaging medium supplemented with 1:8000 5-Sir-Hoechst, 1:2000 SPY555-Tubulin, and either 20 µM Oryzalin or 0.02% DMSO. Here the wells were not filled completely to rule out any cross-contamination between the different treatment solutions. Cells were imaged using the PerkinElmer UltraVIEW VoX microscope as described above with the addition of acquiring an additional red channel using a 561 nm laser and corresponding filters. This time, 8 µm stacks of 10 cells were imaged per condition in 5 min 30 s intervals.

Effect of calcium modulation on PfCen1-GFP dynamics

To study the effect of altered cytoplasmic Ca^{2+} concentrations on Cen1-GFP foci, 3D7-DiCre_pFIO_hsp86_Cen1-GFP parasites were induced (see 4.2.3) approximate 48 h

before imaging and seeded the previous day an 8-well chamber (see 4.4.1). Cells were pre-incubated for 2 h in 1:2000 Spy555-tubulin and 1:8000 5-SiR-hoechst in 200 µl imaging medium. Cells were then imaged at the PerkinElmer UltraVIEW VoX microscope as described above at 37°C in a 5% CO_2 environment with an open lid. One well at a time, 5 min image series were started and after 2-3 timepoints 200 µl of a 2x concentrated treatment solutions (in imaging medium) was added directly to the well to the following final concentrations:
-10 µM A23187 ionophore (1% DMSO), 0.25 mM CaCl2 (concentration which in combination with the phosphate buffer present in RPMI 1640 does not precipitate calcium phosphate)
-0.5% DMSO (control)
-10 µM A23187 ionophore (1% DMSO), 2 mM EGTA

Reactivity of Proteostat with PfCen1-GFP foci

To assess if ECCAs interact with amyloid aggregate dyes, induced (see 4.2.3) and seeded (see 4.4.1) live 3D7-DiCre_pFIO_hsp86p_Cen1-GFP parasites were stained with 1:1000 Hoechst3342 and 1:3000 Proteostat in imaging medium for 30 min at 37°C prior to imaging in a sealed 8-well chamber. Life cells were imaged at 37°C using the Lightning module of the LeicaSp8 microscope with a L HC PL APO CS2 63x/1.4 numerical aperture (NA). oil immersion objective. 264x264 pixel images were acquired with a pixel size of 35.1 nm and 130 nm z-intervals, and a pinhole of 0.6 airy units. Both Cen1-GFP and Proteostat were excited with the 488 nm laser. GFP emission was detected with GaAsP detectors at 490 to 550 nm range while Proteostat emission was imaged at 600 to 700 nm, leading to a negligible bleed-through of GFP into the Proteostat channel.

Analysis of PfCen1-GFP dilute and foci fraction during schizogony

For long term live-cell imaging of Cen1-GFP, dynamics 3D7-DiCre_pFIO_hsp70/86p_Cen1-GFP cells were induced (see 4.2.3) approximately 48 h before and seeded the previous day (see 4.4.1) to an 8-well chamber. 2 h before imaging cells were pre-incubated at 37°C with the sealed wells filled completely (no air bubbles) with 0.5 µM SPY650-Tubulin in imaging medium that had been pre-equilibrated in 3% CO_2, 5% O_2 o/n. Time-lapse image-series were acquired in 5 min intervals at 37°C using the Apo 60x/1.49 NA oil immersion objective of the PerkinElmer UltraVIEW VoX microscope equipped with Yokogawa CSU-X1 spinning disk head and Nikon TiE microscope body. 8 µm stacks of 12 pFIO_hsp70p_Cen1-GFP and pFIO_hsp86p_Cen1-GFP cells each were imaged simultaneously in neighbouring wells using the automated stage and Perfect Focus System. Multichannel images were acquired sequentially with 3% power 488 nm and 6% power 640 nm excitation lasers as well as DIC using the Hamamatsu C9100-23B electron-multiplying charge-coupled device (EM-CCD) camera with a pixel size of 59.8 nm and z-intervals of 500 nm. The timepoint of hemispindle collapse into the first mitotic spindle was marked by a strong increase of microtubule signal intensity and decrease in mobility coinciding with the collapse of the hemispindle at the transition to the mitotic spindle. To ease detection, the SPY650-tubulin signal was deconvolved using the Fiji Decolvolutionlab2 with 10 iterations of the Richardson Lucy. The point spread function was generated using the PSF Generator plugin.

Dr. Severina Klaus was consulted for semi-automated quantification of the area and signal of the PfCen1-GFP dilute and foci fraction across a large dataset of time-lapse movies acquired of 3D7-DiCre_pFIO_hsp86p_Cen1-GFP cells. The following workflow was published in a joint paper:

"For quantification of GFP signal within the cytoplasmic and foci fraction images were processed and analysed in a semi-automated workflow using ImageJ macros in the 64-bit 2.3.0 Fiji distribution of ImageJ 50. Image segmentation was carried out in 3D using version 1.3.2 of the Windows distribution of the image classification software ilastik 51. All macros are available on request. 3D time-lapse GFP images were cropped to 80x80 pixel images containing individual iRBCs. Only iRBCs containing a single parasite were examined. To facilitate improved segmentation, image size was increased four times to 320x320 pixel using the adjust size function of ImageJ without interpolation. Segmentation of GFP foci was carried out on enlarged images using a pixel classification workflow in ilastik. With ilastik, a Random forest classifier utilizing all features up to and including a sigma of 3.5 in 3D was trained on two reference GFP time-lapses via manual annotation. Subsequently, all 3D GFP time-lapse images were batch processed using the same classifier. Segmentation files were exported as multipage tiff and reconstructed into 4D image sets matching the original 80x80 files by reordering stacks and decreasing the image size via the size adjust function of ImageJ without interpolation. Reconstructed segmentation images were then converted into binary masks containing only 0 (background) and 1 (object, here GFP foci) pixel values using the ImageJ math functions. Subsequently, signal intensities for GFP were measured in the following compartments over time: the foci, the whole parasite excluding the foci and the whole parasite including the foci. In parallel, the total area occupied by each compartment at a given time was also quantified. Results were collected as comma separated value (.csv) files and imported into Microsoft excel for analysis using an excel macro. To create masks for the whole parasite, images were segmented on background GFP values. Briefly, a median filter with a radius of 1 and a default threshold of 2200 (2200, 65535) were applied. To create binary parasite masks containing only 0 (background) and 1 (parasite) pixel values the thresholded image was divided by 255 using the ImageJ math functions. To create a mask of the whole parasite excluding the foci, the binary foci mask was inverted using the ImageJ math functions and the inverted foci mask multiplied with the parasite mask using the ImageJ image calculator function. The resulting binary mask contains only 0 (background and foci) and 1 (remaining parasite) pixel values. Areas were measured from binary segmentation masks by applying the multimeasure function on thresholded (1, 255) masks. To measure GFP signal intensities in different compartments, first background subtraction of 2000 was performed on the original 80x80 GFP images. The background subtracted image was then multiplied with one of the binary masks via the ImageJ calculator function, effectively removing any signal outside the compartment of interest. From the 4D image containing only the signal in the areas of interest, a summed z-projection was then created, from which signal intensity was measured as the raw integrated density using the ImageJ multimeasure function. Where indicated data of individual cells was normalized to the average value at the timepoints ranging from 10 min before and after mitotic spindle formation of that cell."

Voß, Klaus *et al*., bioRxiv, 2022.07.26.501452 v2 (2023) [79]

Imaging of LLPS droplets

Imaging of recombinant protein solutions was performed at the PerkinElmer UltraVIEW VoX microscope (see above). To facilitate detection of potential droplet fusion events, higher protein concentrations were used than in the photometric measurements (see 4.5.6), namely 200 µM for PfCen1-6his, 100 µM PfCen1, 120 µM for PfCen2-6his, 193 µM for PfCen3-6his, 70 µM PfCen3, 120 µM for PfCen4-6his, 200 µM for HsCen2-6his, 100 µM CrCen-6His, 200 µM ScCdc31-6His, and 100 µM TbCen2-6His in 50 mM BisTris (pH 7.1). For fluorescent imaging, 30 µM protein samples were supplemented with 300 nM (100:1 molar ratio) NTA-Atto 550. 20 µl of each sample was imaged in non-binding PS µCLEAR 384 well plates at 37°C. Movies were acquired in 1 s intervals with the Apo 60x/1.49 NA oil immersion objective and Hamamatsu sCMOS OrCA Flash 4.0 camera with a pixel size of 89.7 nm in the DIC channel. If NTA-Atto 550 was present a 561 nm later was used for excitation. For addition of 0.2 µl 200 mM $CaCl_2$ solution or 0.4 µl 500 mM EDTA solution, the sample was briefly removed from the microscope stand for better access and mixing. Co-condensation of PfCen1 and PfCen3 was imaged in an untreated µSlide 8-Well glass bottom dish under the same conditions and settings. 150 µl 30 µM PfCen3-6His in 50 mM BisTris (pH 7.1) was mixed with 1.5 µl 200 mM $CaCl_2$ solution to induce droplet formation. 20 µl 255 µM uninduced PfCen1-GFP-6His solution was carefully added to the well to a final equimolar concentration of 30 µM. GFP was excited with a 488 nm laser.

FRAP of PfCen1-GFP foci

Frap experiments were performed by Nicolas Lichti during his master thesis in 2023, which I supervised. First PfCen1-GFP foci 3D7_DiCre_pFIO_hsp86p_PfCen1-GFP parasites were induced 48 h prior and stained with 1:8000 SPY-650 DNA and 1:1000 SPY555-tubulin 1 h prior to imaging. Cells were acquired at 37°C using the Zeiss LSM900 Plan-Apochromat 63x/1,4 oil immersion objective and Airyscan detector. Multichannel images were acquired sequentially in line scanning mode using a 488 nm, 561 nm, and 640 nm diode laser using dichroic mirrors to measure emission of GFP at 500-550 nm. Focus stabilization was achieved using the Definite Focus module. FRAP was performed using the FastAiryScanSheppardSum SR-4Y mode to minimize frame time to 30 ms, which was acquired every 300-350 ms. After five frames an area overlapping a focus was bleached twice with the 488 nm laser at 100% power for a total of 70 ms. Bleaching intensity was adjusted so foci were not completely bleached for continued tracking. ECCAs and CP foci were differentiated by proximity to the DNA-free area of the nuclei and tubulin signal.

Analysis of FRAP time-lapse microscopy was performed using Fiji. Therein three different measurements were performed: The PfCen1-GFP signal within the bleached area over time, the signal over time within an unbleached area of the cell or within a separate unbleached droplet within the same field of view, and the background signal outside the cell or dilute fraction. The signal within the bleaching area was thereby corrected for background signal and gradual bleaching over time arising from the imaging laser. Intensity over time was blotted and the pre-bleaching intensity I_i, the minimum intensity right after bleaching I_0, and the intensity of the plateau I_p were determined. The

mobile fraction M_f of PfCen1-GFP droplets and foci was calculated using the following equation [174]:

$$M_f = \frac{I_p - I_0}{I_i - I_0}$$

4.4.4 STED microscopy

Immunofluorescence assay (IFA)
STED microscopy of fixed NF54-pARL_Cen1-4 -GFP cells (see 4.4.2) was performed using the STED/RESOLFT single-point scanning supper resolution microscope using a 100x oil immersion objective/1.4 NA. Confocal images were acquired with a pixel size of 70 nm and 300 nm z-intervals. 405 nm, 488 nm, 590 nm, and 640 nm lasers were used for excitation with respective 525/50, 615/20, and 685/70 emission filters placed in front of three avalanche photodiodes for detection. Super resolution images were acquired using 590 and 640 nm excitation lasers and a 775 nm STED laser employed at 10-15% intensity (maximum 3 mW). RescueSTED adaptive illumination was used to turn off the STED laser for pixels below a signal intensity threshold to prevent destructive heating of the dark hemozoin crystals. Deconvolution was performed using Imspector Software based on the Richardson-Lucy algorithm with default settings.

Time-lapse imaging
Prior to live-cell STED time-lapse imaging, NF54_pARL_Cen1-Halo cells were seeded to an 8-well chamber the day before (see 4.4.1) and pre-treated with 1 µM SPY505-DNA as a proxy for the nuclei and 1 µM MaP-SiR-Halo [144] to stain Cen1-Halo with a STED-capable flurorophore for 3 h at 37°C in imaging medium. Imaging was performed at the STED/RESOLFT at 37°C. Image series were acquired from a single Z-level in 1-30 seconds intervals, using the same hardware and laser setup as described above. Deconvolution was performed using the Huygens Professional software Express deconvolution based on the optical acquisition parameters with the standard algorithm settings.

4.5 Recombinant protein biochemistry

4.5.1 Recombinant Protein expression and purification

Expression
Bacterial strains for the expression of all PfCen1-6His variants, PfCen1-GFP-6His, PfCen2-6His, and HsCen2-6His were generated by transforming BL21-CodonPlus (De3) cells with the respective pET-28 vector. In detail, 20 µl chemically competent cells were incubated with ~50 ng plasmid purified via miniprep for 20 min on ice, heat shocked at 42°C for 30 s, and transferred back to ice for 2 min. After resuspension in RT SOC medium and a recovery period of 1 h at 37°C shaking at 130 rpm, the cells were plated to prewarmed LB-Kan plates and incubated o/n at 37°C. In the evening of the next day, LB-Kan (50 mg/l) pre-culture was inoculated with a single colony and incubated o/n at 37°C

130 rpm. The next morning 400 to 800 ml of expression culture was created from a 1:50 dilution of the pre-culture into pre-warmed LB-Kan. Bacterial strains for the expression of all PfCen3-6His variants, PfCen4-6His, and 6His-TEV tagged centrins were generated by transforming chemically competent W3110-Z1 cells with the respective pZE13d-C/-TEV vector via 42°C heat shock as described above. Here, inoculation of 800 ml pre-warmed LB-Amp (50 mg/l) expression culture with colonies scraped directly from the LB-Amp plate to an OD_{600} of 0.06 was possible due to higher transformation efficiency of this strain. These expression cultures were incubated shaking with 130 rpm at 37°C until reaching an OD_{600} of 0.5 for W3110-Z1 or 0.7 for BL21 cells, upon which IPTG was added to a final concentration of 1 mM to induce expression. After continued incubation for 3 h and 5 h respectively. bacteria were pelleted with 4000 g for 25 min at 4°C, which was maintained for all further steps.

Protein extraction & Ni-NTA purification

Bacteria were resuspended in 8 ml bacterial lysis buffer and lysed via sonication on ice via 9x 30 s cycles of ~0.5 s pulses at 50% power at the Branson Sonifier 250. The Lysate was cleared from inclusion bodies and cell debris via centrifugation at 17000 g for 20 min. The soluble fraction was supplemented with imidazole to 10 mM, mixed with 1 ml pre-equilibrated Ni-NTA agarose beads in a 15 ml tube, and incubated under rotation for 1 h. The beads were then filtered from the suspension via gravity flow through a Pierce centrifuge column, washed with a 12x volume of Ni-NTA wash buffer (20 mM imidazole), before the protein was eluted in 2 ml Ni-NTA elution buffer (250 mM imidazole). Buffer was exchanged via dialysis using 6-8 kDA cutoff dialysis tubes in two consecutive steps with first 2 h and then o/n in a 300x volume of chilled 50 mM BisTris (pH 7.1 at 4°C). In the case of 6His-TEV-PfCen1-4, an additional step was performed before. Ni-NTA eluate was supplemented with 6His-TEV protease in an estimated 1:100 mass ratio relative to the purified protein and the buffer was exchanged to 3 mM β-Mercaptoethanol in PBS using the same dialysis protocol to remove imidazole. This enabled removal of 6His-TEV via (reverse) Ni-NTA purification as described above, where the flowthrough was collected instead, with the protease remaining attached to the beads. Buffer was then exchanged to 50 mM BisTris (pH 7.1) as with the other proteins before. Due to yielding a low concentration, 2 ml PfCen3 (no 6His tag) solution was additionally concentrated via 3000g centrifugation through Vivaspin 6 columns at 4°C for 7 min. Final protein solutions were aliquoted and snap frozen in liquid nitrogen for storage at -80°C.

Determination of protein concentration

Protein concentration was determined primarily via the Pierce 660 nm protein assay using a BSA dilution series from 2 mg/ml to 50 µg/ml diluted in 50 mM BisTris (pH 7.1), as well as a buffer only sample. 10 µl of each sample (protein solutions in multiple dilution) were supplemented with 150 µl Pierce 660 nm solution in a 96 well plate, shaken for 1 min, incubated at RT for 5 min in the dark, and then measured at 660 nm using the Tecan M200 Pro plate photometer. The buffer-only absorption was subtracted and a BSA standard curve generated. Only dilutions within the linear concentration range (2000-50 mg/ml) were assessed.

Additionally, protein concentration was checked by measuring the OD_{280} using the NP80 nanophotometer. Extinction coefficients were estimated using the ExPASy ProtParam tool [253].

All proteins expressions and purifications were performed by myself with the exception of 1NCen4-6His and 4NCen1-6His, which were performed by Marina Iocca under my supervision.

Recombinant proteins are summarized in table 18.

4.5.2 Coomassie SDS-PAGE

To assess the purity, protein samples were boiled for 95°C in 1x Laemmli buffer and an SDS-PAGE was performed by loading 1.125 µl of protein alongside Precision Plus protein marker on a 12 well 12% Mini-PROTEAN TGX precast gels at 140 V for ~45 min in SDS running buffer. Afterwards gels were washed briefly in ddH_2O, fixed for 10 min with Coomassie Fixation Solution, and stained with Coomassie Staining Solution for 10 min after briefly microwaving. Gels were then de-stained in Coomassie Fixation Solution o/n after briefly microwaving again, and subsequently documented with the Li-COR Odyssey CLx using the 700 nm laser.

4.5.3 Mass spectrometry analysis

To confirm proteins were fully intact and possessed the correct mass, LC-MS was performed by the CFMP facility at the ZMBH Heidelberg using a maXis UHR-TOF (Bruker Daltonics) coupled with nanoUPLC Acquity (Waters).

4.5.4 Circular dichroism spectroscopy

The following protocol was performed and provided by the EMBL Heidelberg Protein Expression and Purification Core Facility. A modified version was previously published in *Voß et al.* (2023) [79]:

Recombinant wild type Cen1-6His or mutant EFh-dead PfCen1-6His was diluted with size-exclusion chromatography (SEC) buffer at 4°C, to 0.4 ml. The samples were injected onto a Superdex S200 10/300 column (equilibrated in SEC buffer) running at a flow rate of 0.75 ml/min in the SEC buffer. Samples from the different fractions were loaded on 4-20 % Mini-PROTEAN TGX Precast Gels and run under denatured and reduced conditions using Tris/glycine/SDS running buffer. The gel was run for 15-17 min at 300 V and stained with Coomassie Blue. Fractions with highly purified protein were diluted into the SEC buffer to a final concentration of 0.5 mg/ml and centrifuged for 10 min at maximal speed prior to the CD measurements. CD spectra were recorded using a Jasco J-815 CD spectrophotometer using a 0.2 mm path length CD Quartz cuvette, at 20°C, between 260 nm to 190 nm, with 50 nm/min scan speed, digital integration time of 1 sec, a bandwidth of 1 nm, a data-pitch of 0.1 nm and 10 accumulations were averaged. A

buffer spectrum was first recorded as baseline and subtracted from the sample spectrum. The spectra were analysed with the Contin-LL50 method with the protein reference data 751 using the Dichroweb server52.

4.5.5 Generation of Antibodies

To raise polyclonal antibodies against PfCen1-6His, the protein was additionally purified via SEC due to its relatively small size. Freshly produced protein was expressed, purified as described in 4.5.1 but dialysed with a 300x volume of PBS at 4°C once for 2 h and then o/n. Dialysed protein was then loaded in 2x 0.5 ml fractions at a flowrate of 800 µl/min with PBS onto a Superdex 75 10/300 column attached to the ÄKTA Pure at 4°C. Protein concentration was determined via Pierce 660 nm assay as described in 4.5.1. Immunization was performed by Davids Biotechnology using 250 µg PfCen1-6His for a 63 day, 5 immunization regimen.

4.5.6 Quantification of Centrin LLPS dynamics via turbidity assay

To study the LLPS dynamics of recombinant centrins in response to Ca^{2+}, Mg^{2+}, and EDTA over time, 350 µl of a protein sample solution in 50 mM BisTris (pH 7.1 at 4°C) was prepared in a 1.5 ml polystyrene cuvette on ice. The cuvette was placed into the NP80 nanophotometer, which had been pre-heated to 37°C and blanked with either buffer or in case of PfCen1-GFP, with the protein solution itself (prior to Ca^{2+} addition), as the fluorophore-tag affected the base absorption significantly. The $OD_{200-900}$ 10 mm path length was then measured in 10 s intervals for 25 min for standard assays, or in 1 min intervals for up to 3 h during long-term measurements to assess maturation. The first 330 s were used to equilibrate the sample to 37°C and are not shown due to frequent air humidity condensation on the initially cold cuvette interfering with the measurement. At 450 s, 3.5 µl 200 mM $CaCl_2$ or $MgCl_2$ solution was added to 2 mM final concentration, and at 1160 s, 7 µl 500 mM EDTA solution to 10 mM final concentration. Rapid mixing of the solutions within the cuvette was facilitated by pre-loading the salt solution into a 200 µl pipette tip (using a 10 µl pipette for accuracy), with which the sample was pipetted up and down three times during addition in between two measurements. In a modified version of the assay, a PfCen1 protein solution was supplemented with 39 µl of a 50% (v/v) 1,6-hexanediol solution in ddH_2O (final concentration 5% v/v) or ddH_2O (control) was added to the cuvette at 1170 s after the cuvette was placed into the photometer. $CaCl_2$ had already been added at 450 s and EDTA was added at 1400 s as described above.

4.5.7 IDR likelihood analysis via IUPRED

To determine the likelihood of IDRs within the N-termini of various centrins, their amino acid sequences (including tags) were analysed using the online IUPred3 long disorder algorithm with Medium smoothing [158]. IDR score for individual positions were retrieved as a .txt file.

4.6 List of materials

Table 8 List of chemicals

Type	Name	Supplier
Chemicals	1,6-Hexanediol	Sigma-Aldrich
	2-Mercaptoethanol	Carl Roth GmbH
	2-Popanol	Zentralbereich Neuenheimer Feld
	A23187 Calcium Ionophore (C7522)	Sigma-Aldrich
	Acetic acid	Honeywell
	Agarose NEEO ultra-quality EEO = 0,05-0,13	Carl Roth GmbH
	L-Arginine	Carl Roth GmbH
	BisTris	Carl Roth GmbH
	CaCl2	Merck
	Coomassie brilliant blue R 250	Merck
	Dimethyl Sulfoxide, 276855	Sigma-Aldrich
	dNTP mix (10 mM), N0447L	New England Biolabs
	EDTA Na_2 $2H_2O$	Sigma-Aldrich
	EGTA	Sigma-Aldrich
	Ethanol absolute	VWR Chemicals
	Ethanol (96%, 99.9%)	Zentralbereich Neuenheimer Feld
	Glutaraldehyde 25% (6257)	Sigma-Aldrich
	Glycerol (anhydrous)	AppliChem
	Glycine	Labochem international
	H_4BNa	Sigma-Aldrich
	HEPES (H4034)	Sigma-Aldrich
	Imidazole	Carl Roth GmbH
	IPTG	Thermo Fisher Scientific
	K_2HPO_4	Merck
	KCl	Merck
	KH_2PO_4	Sigma-Aldrich
	Methanol	VWR Chemicals
	MgCl2	Fluka
	Milk powder	Carl Roth GmbH
	$Na_2H_2PO_4$ $2H_20$	AppliChem
	NaCl	Sigma-Aldrich
	NaH_2PO_4 H_20	Thermo Fisher Scientific
	Nycodenz	Alere Technologies
	Paraformaldehyde, EM-grade	Electron Microscopy Sciences
	Saponin quillaae sp.	Sigma-Aldrich
	Sodium Acetate	MERCK
	Sodium borohydrate (NaBH4)	Sigma-Aldrich
	Sodium dodecylsulfate	Serva
	D-Sorbitol (S1876-500G)	Sigma-Aldrich
	TRIS	Carl Roth GmbH
	Triton X-100	Sigma-Aldrich
	Tween-20	Carl Roth GmbH
Buffer	4x Laemmli Sample Buffer	Bio-Rad
	5x Phusion HF Reaction Buffer	New England Biolabs
	10x ligation buffer	New England Biolabs
	CutSmart™	New England Biolabs
	DPBS	Thermo Fisher Scientific
	Gel Loading Dye Purple (6x)	New England Biolabs
	Q5 Reaction Buffer (B9027)	New England Biolabs
	T4 DNA ligase buffer	New England Biolabs
Media Components	AlbuMAX II Lipid-Rich BSA	Thermo Fisher Scientific
	Bacto Agar	Becton, Dickinson and Company

	Bacto Trypton	Becton, Dickinson and Company
	BactoYeast Extract	Becton, Dickinson and Company
	Concentrated erythrocytes (O+)	Blutbank Mannheim
	Hypoxanthine (Z-41-M)	c.c.pro
	RPMI 1640 GlutaMAX, phenol red (61870010)	Thermo Fisher Scientific
	RPMI 1640, stable Glutamine, w/o phenol-red, 2 g/l NaHCO3 (P04-16520)	PAN Biotech
	SOC Outgrowth Medium	New England Biolabs
Drugs	Ampicillin	Carl Roth GmbH
	Gentamycin sulphate solution (HN09.1)	Carl Roth GmbH
	Heparin sodium salt from porcine intestinal mucosa (9041-08-1)	Sigma-Aldrich
	ML10	Prof. Dr. David A. Baker [254]
	Oryzalin (36182)	Riedel-de Haën
	Rapamycin (R0395)	Sigma-Aldrich
	WR99210	Jacobus chemicals
Proteins	6His-TEV protease	EMBL Protein Expression and Purification Core Facility
	Albumin (BSA)	Carl Roth GmbH
	BSA Standard Ampules, 2mg/mL (23209)	Thermo Fisher Scientific
	Concanavalin A C2010	Sigma-Aldrich
	DNase I	Thermo Fisher Scientific
	Gibson Assembly Master Mix	New England Biolabs
	HiFi DNA Assembly Master Mix (E2621)	New England Biolabs
	Lysozyme	Carl Roth GmbH
	Phusion High-Fidelity DNA polymerase (M0530)	New England Biolabs
	Proteinase K	Roche
	Restriction Enzymes	New England Biolabs
	Q5 High-Fidelity DNA polymerase (M04911)	New England Biolabs
	Ribonuclease A	Sigma-Aldrich
	T4 ligase (M0202)	New England Biolabs
	T4 PNK (M0201)	New England Biolabs
Stains	Hemacolor® Rapid staining of blood smear Solution 2 (1.11956.2500)	VWR
	Hemacolor® Rapid staining of blood smear Solution 3 (1.11957.2500)	VWR
	Midori Green Advance DNA Stain	Nippon Genetics Europe
	Pierce 660 nm Protein Assay Reagent (22660)	Thermo Fisher Scientific
Other	1 kb DNA ladder	New England Biolabs
	C0mplete Mini, EDTA-free (11836170001)	Roche
	Ni-NTA Agarose	QIAGEN
	Precision Plus Protein™ Dual Color Standard	Bio-Rad

Table 9 List of antibodies

Antibody	Species	Concentration	Source
anti-α-tubulin B-5-1-2, monoclonal	mouse	1:500	Sigma-Aldrich (T5168)
anti-GFP, monoclonal	rabbit	1:50	Thermo Fisher Scientific (G10362)
anti-GFP, monoclonal	mouse	WB 1:1000	Roche (11814460001)
anti-PfAldolase	rabbit	WB 1:1000	Abcam (ab207494)
anti-PfCen1, polyclonal	rat	1:500, WB 1:1000	This study
anti-PfCen3, polyclonal	rabbit	1:500	Simon *et al.* 2021 [52]
anti-mouse-Atto 594	goat	1:1000, STED 1:200	Sigma-Aldrich (76085)
anti-mouse-Atto 647	goat	1:1000, STED 1:200	Sigma-Aldrich (50185)
anti-mouse-800	donkey	1:10000, WB	Rockland (610-745-002)
anti-rabbit-Atto 594	goat	1:1000, STED 1:200	Sigma-Aldrich (77671)
anti-rabbit-Atto 647	goat	1:1000, STED 1:200	Sigma-Aldrich (40839)

anti-rabbit-680	donkey	1:10000, WB	Rockland (610-744-002)
anti-rat-Atto 594	goat	1:1000, STED 1:200	Rockland (612-155-120)
anti-rat-800	donkey	1:10000, WB	Rockland (612-145-002)
GFP-Booster Alexa Fluor® 488	alpaca	1:500	ChromoTek (gb2AF)

Table 10 List of fluorescent dyes

Dye	Concentration	Source
5-SiR-Hoechst	1:5000	Bucevičius *et al.*,2019
Hoechst 33342	1:1000	Thermo Fisher Scientific
NTA-Atto 550 (94159)	300 nM	Sigma-Aldrich
Proteostat protein aggregation assay	1:3000	Enzo Life Sciences
SPY505-DNA (SC101)	1 µM	Spirochrome
SPY555-Tubulin (SC203)	1:2000	Spirochrome
SPY650-Tubulin (SC503)	0.5 µM	Spirochrome
SPY650-DNA (SC501)	0.5 µM	Spirochrome
SYBR™ Green I Nucleic Acid Gel Stain	1:2000 (flow cytometry)	Invitrogen
SYTO61 (S11343)	1:1000/ 5 µM	Thermo Fisher Scientific

Table 11 Non-commercial buffer compositions

Name	Composition
Bacteria Lysis Buffer	20 U/ml DNaseI
	10 µg/ml lysozyme
	3 mM β-Mercaptoethanol
	1 protease inhibitor tablet
	C0mplete protease inhibitor tablet
	In PBS, pH 7.4
Complete RPMI (cRPMI)	0.2 mM Hypoxanthin
	12.4 µg/ml Gentamycin
	0.5% AlbuMAX II Lipid-Rich BSA
	25 mM HEPES [pH 7.4]
	in RPMI 1640 GlutaMAX, phenol red
Coomassie Fixation Solution	50% (v/v) H_2O
	40% (v/v) methanol
	10% (v/v) acetic acid
Coomassie Staining Solution	40% (v/v) H_2O
	50% (v/v) methanol
	10% (v/v) acetic acid
	0.25% (w/v) Coomassie blue
Cytomix	120 mM KCl
	0.15 mM $CaCl_2$
	2 mM EGTA
	5 mM $MgCl_2$
	10 mM K_2HPO_4/ $KHPO_4$
	25 mM HEPES
	pH 7.6
Dialysis Buffer	50 mM BisTris
	pH 7.1 (adjusted with sodium hydroxide at 4°C)
EMSA Buffer	50 mM NaH_2PO_4 H_20
	300 mM NaCl
	10 mM EDTA/ 1 mM $CaCl_2$/ 10 µM $CaCl_2$/ 1µM $CaCl_2$/ -
	pH 7.1
Freezing Solution	28% (w/v) glycerol
	0.65% (w/v) NaCl
	3% (w/v) sorbitol

Imaging Medium	0.2 mM Hypoxanthin
	12.4 µg/ml Gentamycin
	0.5% AlbuMAX II Lipid-Rich BSA
	25 mM HEPES [pH 7.4]
	in RPMI 1640, w/o phenol-red
Incomplete RPMI (iRPMI)	25 mM HEPES [pH 7.4]
	in RPMI 1640 GlutaMAX, phenol red
Ni-NTA Elution Buffer	50 mM NaH_2PO_4 H_20
	300 mM NaCl
	250 mM imidazole
	pH [8]
Ni-NTA Wash Buffer	50 mM NaH_2PO_4 H_20
	300 mM NaCl
	20 mM imidazole
	pH [8]
Nycodenz stock solution	27.6% (w/v)
	10 mM Tris
	pH 7.0
SDS Running Buffer	25 mM TRIS
	192 mM glycine
	0.1% SDS (w/v), 3.5 mM
	pH 8.3
SEC Buffer	50 mM Tris-HCl
	pH 7.1
TAE Buffer	20 mM Acetic acid
	1 mM EDTA
	40 mM Tris
	pH 8.3
TE Buffer	10 mM Tris-HCl
	1 mM EDTA
	pH 7.5
WB Blocking Solution	5% milk powder
	0.05% Tween-20
	in PBS, pH 7.4
WB Washing Solution	0.05% Tween-20
	in PBS, pH 7.4

Table 12 List of consumables

Type	Name	Supplier
Kits	12% Mini-PROTEAN TGX™ Gels	Bio-Rad
	20% Mini-PROTEAN TGX™ Gels	Bio-Rad
	DNeasy Blood & Tissue Kit	QIAGEN
	High Pure PCR Product Purification Kit	Roche
	GenElute™ HP Plasmid Miniprep Kit	Sigma-Aldrich
	NucleoBond Xtra Midi Plus	Macherey-Nagel
	Trans-Blot Turbo™ Transfer Pack	Bio-Rad
Glassware	Erlenmeyer Flask	DWK Life sciences
	Microscope slides	Epredia
	Test tube	DWK Life sciences
Plastics	Inoculation loops (10 µl)	Sarstedt
	Autoclavable bags	Sarstedt
	Cellstar cell culture dishes	Greiner bio-one
	Cellstar Cell culture flasks (T25, T75)	Greiner bio-one

	Cellstar Cell culture plates, PS, (6/12/96 well), flat bottom	Greiner bio-one
	Cellstar Cell culture plate, PS, 96 well, U-bottom	Greiner bio-one
	Cellstar Serological pipettes (5, 10, 25 ml)	Greiner bio-one
	Cellstar tubes (15, 50 ml)	Greiner bio-one
	Costar Stripette 50 ml	Sigma-Aldrich
	Cryo.S tubes, 2 ml (122263)	Greiner bio-one
	Gene Pulser Cuvette	Bio-Rad
	Low-Binding Barrier Tips (20 µl)	AvantGuard
	Micro tube (1.5, 2 ml)	Sarstedt
	OneTouch barrier sterile (10 µl, 200 µl, 1 ml)	Sorenson BioScience
	Parafilm Laboratory Film	Bemis
	Polystyrene Semi-micro cuvette (67.746)	Sarstedt
	PCR SingleCap 8er-SoftStrips 0.2ml	Biozym Scientific
	Pierce Centrifuge columns 5 ml	Thermo Fisher Scientific
	µ-dish 35 mm	Ibidi
	µ-slide 8 Well IbidiTreat	Ibidi
	µ-slide 8 Well Glass Bottom	Ibidi
	TouchNTuff	Ansell
	µClear 384 microplate, non-binding (781906)	Greiner bio-one
	Vivaspin 6 10,000 MWCO	Sartorius
Other	Facial tissues – Virgin Pulp	Sofidel
	Fp 30/02 CA-S Filter uni	GE Healthcare
	Dialysis membrane tubing Spectra/Por 1 RC 6-8 kDA MWCO (132650)	Thermo Fisher Scientific

Table 13 List of devices

Application	Device	Supplier
Agarose gel imaging	E.A.S.Y 440 K	Herolab
	UVT-28 L	Herolab
CD spectroscopy	J-815 CD spectrophotometer	JASCO
Cell culture	BVC professional	Vacuubrand
	Envair eco safe Basic Plus	ENVAIR Deutschland
	Stretching table OTS 40	Medite
	Cell culture shaker DOS-20S	neoLab Migge
Centrifugation	Avanti J-26S XR centrifuge	Beckman Coulter
	Heraeus Fresco 21 centrifuge	Thermo Fisher Scientific
	Heraeus Pico 21 centrifuge	Thermo Fisher Scientific
	Multifuge 1 S-R	Thermo Fisher Scientific
	Rotor JA-10	Beckman Coulter
	Rotor JA-10	Beckman Coulter
	Su1550	Sunlab
Chromatography	ÄKTA Pure	Cytiva/GE Healthcare
	Superdex 75 10/300 column	Cytiva
	Superdex S200 10/300 column	Cytiva
Electroporation	Gene Pulser II	Bio-Rad
Flow cytometry	FACSCantoII	BD Biosciences
Gel electrophoresis	EV231	Consort
	Gel Chamber	Consort
	Mini-PROTEAN Tetra Cell	Bio-Rad

	PowerPac Basic	Bio-Rad
Incubators	CH-4103	Infors
	IN75	Memmert
	Isotemp 210	Marshall Scientific
	Labo C201	Labotect
MACS purification	QuadroMACS™ Separator	Miltenyi Biotec
Microscopy	Axiostar plus	Carl ZEISS AG
	Eclipse E100	Nikon
	Leica TCS SP8 DLS	Leica Microsystems
	STED/RESOLFT	Abberior Instruments
	UltaVIEW VoX with TiE body	PerkinElmer, Nikon
	Airyscan 2 LSM900	Zeiss
PCR	FlexCycler^2	Analytik Jena
PH-meter	FiveEasy	Toledo-Mettler
Photometer	Infinite M200 Pro	Tecan
	NanoPhotometer NP80	Implen
Scale	Kern EW600–2M	Kern & Sohn GmbH
	TE124S-0CE	Sartorius
Sonication	Branson Sonifier 250	Thermo Fisher Scientific
Storage	Innova U725 (-80°C)	New Brunswick Scientific
	MediLine Freezer (−20°C)	Liebherr
	MediLine Fridge (4°C)	Liebherr
	Liquid nitrogen container LS6000	Worthington Industries
Western Blot	Li-COR Odysseay CLx	LI-COR Biotechnology
	Trans-Blot Turbo™ Transfer System	Bio-Rad
Workbench	Butane burner	CampingGaz
	Discovery Comfort pipet	Kinesis GmbH
	Dry bath dual block	Labnet
	Ice dispenser AF 80	Scotsman Ice Systems
	Microwave 900 & Grill	Severin
	neoBlock 1 (Heatblock)	neoLab Migge
	Pipetman	Gilson Inc.
	Shaker HS250 basic	Ika labortechnik
	Su1400	Sunlab shaker
	ThermoProtect 2100W	Philips GmbH
	Vortexer 7-2020	neoLab Migge

Table 14 List of software tools

Application	Sofware	Source
Amino acid sequence alignment	Clustal Omega	https://www.ebi.ac.uk/Tools/msa/clustalo/ [255]
DNA Sequence analysis	ApE	biologylabs.utah.edu/jorgensen/wayned/ape
	SnapGene	snapgene.com
Figure Design	GIMP2	gimp.org/downloads/
	Inkscape	inkscape.org
	Jalview	https://www.jalview.org [256]
Flow cytometry analysis	FlowJo	Tree Star
Gel pictures	E.A.S.Y Win32	Herolab
	Image Studio Lite	licor.com/bio/image-studio-lite/
Graphs, statistics	GraphPad prism	graphpad.com/scientific-software/prism/
IDR prediction	IUPred3	https://iupred3.elte.hu [158]
Image Analysis	Fiji (ImageJ)	fiji.sc [257]
	Ilastik	Ilastik.orgs
	Imspector	Abberior Instruments
Image Deconvolution	Huygens professional	Scientific Volume Imaging

Information resource (protein & DNA sequences, Transcriptomics, etc.)	PlasmoDB	https://plasmodb.org [258]
Primer TM calculation	NEB Tm Calculator	tmcalculator.neb.com
Protein parameter calculation	Protein Molecular weight calculator	sciencegateway.org
	ProtParam	web.expasy.org/protparam/ [253]
	Prot PI	www.protpi.ch
Protein structure prediction	AlphaFold	https://alphafold.ebi.ac.uk [159]

Table 15 List of primers

#	Amplicon	Template	Fwd /Rev	Sequence (5' → 3')
P1	PfCen1	NF54 cDNA	F	cgacccgggatggtaccATGAGCAGAAAAAATCAAACTATG
P2	PfCen1	NF54 cDNA	R	ttcttctcctttactcctaggAAATAAGTTGGTCTTTTTCATAATTC
P3	PfCen2	NF54 cDNA	F	cgacccgggatggtaccATGACCGATAACACAGCTG
P4	PfCen2	NF54 cDNA	R	ttcttctcctttactcctaggTAAGAAGCTTTTTTTGGTCATTATTG
P5	PfCen4	NF54 cDNA	F	cgacccgggatggtaccATGAACACAATGTTAATTAAGG
P6	PfCen4	NF54 cDNA	R	ttcttctcctttactcctaggTGAATCTGAATCAACATCAC
P7	CRTp + PfCen3 ST	pARL-Cen3-GFP	F	TGACACTATAGAATACTCGC
P8	CRTp + PfCen3 ST	pARL-Cen3-GFP	R	ATCAATTGCTCTAGGATCATAATCCACATCTTCATCTTTT CTATTTATCATGGTACC
P9	CRTp + PfCen3 SYT	pARL-Cen3-GFP	R	ATCAATTGCTCTAGGATCATAATCCACATCTTCATCTTTT CTATTTATCATGGTACC
P10	PfCen3 ST/SYT	pARL-Cen3-GFP	F	GATCCTAGAGCAATTGATAATAGACCAATCGATGATAATCGAAGAAGGGGACGTAAC
P11	PfCen3 ST/SYT	pARL-Cen3-GFP	R	AGTTCTTCTCCTTTACTCCTAGG
P12	Halo+Linker	p238-actin-chromobody-Halo	F	gaaaaagaccaacttatttcctaggCCAACCACTGAGGATCTGT
P13	Halo+Linker	p238-actin-chromobody-Halo	R	ccctcgaggaattcctgcaggtctggacatTTAACCGGAAATCTCCAGAGTAGAC
P14	PfHsp70 5' UTR	NF54 gDNA	F	cactatagaatactcgcggccgcCGCATAAATATCTGGTGAAATACAAAC
P15	PfHsp70 5' UTR	NF54 gDNA	R	atgtatgctatacgaagttatgaaCCTTTTGCACTAGCCAATTTTTC
P16	hDHFR+GGGS linker	pARL-Cen3-GFP	F	cttcgtatagcatacattatacgaagttatATGCATGGTTCGCTAAAC
P17	hDHFR+GGGS linker	pARL-Cen3-GFP	R	aatctattattaaataaatggatccacctccaccATCATTCTTCTCATATACTTC
P18	hDHFR+GGGS linker	pARL-Cen3-GFP	R	TCTTCTCCCTTAGATACGG
P19	mCherry	p3xNLS-mCherry-hsp86-BSD	F	gaatgatggtggaggtggatccGTATCTAAGGGAGAAGAG
P20	mCherry	p3xNLS-mCherry-hsp86-BSD	R	gtataatgtatgctatacgaagttatgtcgacttaTGTAGAGTGTCTACCTTC

P21	GFP	pARL-Cen3-GFP	F	gtatagcatacattatacgaagttatacgcgtATGGTTAGTAAAGGAGAAGAACTTTTC
P22	GFP	pARL-Cen3-GFP	R	ctattattaaataaatgctcgagTTATTTGTATAGTTCATCCATG
P23	PbDHFR 3'UTR	PbANKA gDNA	F	gtagacactctacataagtcgacGATATGGCAGCTTAATGTTC
P24	PbDHFR 3'UTR	PbANKA gDNA	R	atgctatacgaagttat G ATATCGAAATTGAAGG
P25	PfHsp86 5'UTR	NF54 gDNA	F	cactatagaatactcgcggccgcGGGAATTTCCTTATAAGATCTTTC
P26	PfHsp86 5'UTR	NF54 gDNA	R	atgtatgctatacgaagttATTTTATTCGAAATGTGGGAAG
P27	Cen1	pARL-Cen1-GFP	F	acattatacgaagttatacgcgtATGAGCAGAAAAAATCAAAC
P28	Δ19-PfCen1	pARL-Cen1-GFP	F	acattatacgaagttatacgcgtATGGAATTAAATGAAGAACAAAAATTAG
P29	GFP-T2A	pSLI_TGD_SAS6-GFP	F	acattatacgaagttatacgcgtATGAGTAAAGGAGAAGAACTTTTC
P30	GFP-T2A	pSLI_TGD_SAS6-GFP	R	agtttgatttttctgctTGGTCCTGGATTTTCTTCTAC
P31	Cen1 -ATG +TAA	pARL-Cen1-GFP	F	AGCAGAAAAAATCAAACTATG
P32	Cen1 -ATG +TAA	pARL-Cen1-GFP		Ctattattaaataaatgctcgag tta AAATAAGTTGGTCTTTTTCATAATTC
P33	HsCen2	human cDNA	F	actttaagaaggagatataccATGGCCTCCAACTTTAAGAAGG
P34	HsCen2	human cDNA	R	agtggtggtggtggtggtgcccATAGAGGCTGGTCTTTTTCATG
P35	PfCen1 (*E. coli*)	oligo 4	F	actttaagaaggagatataccATGTCTCGTAAAAACCAAACC
P36	PfCen1 (*E. coli*)	oligo 4	R	agtggtggtggtggtggtgcccGAATAAGTTAGTTTTTTTCATAATGCG
P37	Δ19-PfCen1 *(E. coli*)	oligo 4	F	tttaagaaggagatataccatgGAGCTGAATGAGGAACAAAAG
P38	PfCen1 (*E. coli*)	oligo 4	R	ttctcctttactcctaggGAATAAGTTAGTTTTTTTCATAATGCG
P39	PfCen2 (*E. coli*)	oligo 5	F	actttaagaaggagatataccATGACAGATAACACTGCC
P40	PfCen2 (*E. coli*)	oligo 5	R	agtggtggtggtggtggtgcccCAGGAAACTTTTCTTGGTC
P41	GFP	pARL-Cen3-GFP	F	CCTAGGAGTAAAGGAGAAGAAC
P42	GFP	pARL-Cen3-GFP	R	agtggtggtggtggtggtgcccTTTGTATAGTTCATCCATGCC
P43	PfCen3 (*E. coli*)	oligo 6	F	ttaaagaggagaaaggatccATGATTAACCGTAAGAGC
P44	PfCen3 (*E. coli*)	oligo 6	R	gtggtgatgatggtgATATAAGGATGTCTGCTTC
P45	PfCen4 (*E. coli*)	oligo 7	F	ttaaagaggagaaaggatccATGAATACTATGCTGATCAAAG
P46	PfCen4 (*E. coli*)	oligo 7	R	gtggtgatgatggtgAGAGTCGCTGTCAACGTC
P47	N1-PfCen4 (*E. coli*)	pET-28_PfCen4	F	Tttaagaaggagatataccatgtctcgtaaaaaccaaaccatgattcgtaatccgaatccgcgtagcaaacgcaa CTCAATTAACGAGGATGTAG
P48	N4-PfCen1 (*E. coli*)	pET-28_PfCen1	F	tttaagaaggagatatacc atgaatactatgctgatcaaagataacattaacatc GAGCTGAATGAGGAACAAAAG
P49	PfCen1/4 (*E. coli*)	pET-28	R	ATCTCAGTGGTGGTGGTG

P50	PfCen3 ST/SYT (*E. coli*)	pZE13d-C_PfCen3	F	GAAAAGTGCCACCTGACG
P51	PfCen3_ST (*E. coli*)	pZE13d-C_PfCen3	R	GTCGATTGCACGAGGGTCGTAATCGACGTCTTCAT CCTTACGGTTAATCATGGATCC
P52	PfCen3_SYT (*E. coli*)	pZE13d-C_PfCen3	R	GTCGATTGCACGAGGGTCTTCATCGACGTCTTCAT CCTTACGGTTAATCATGGATCC
P53	PfCen3_ST/SYT (*E. coli*)	pZE13d-C_PfCen3	F	GACCCTCGTGCAATCGACAACCGCCCTATTGATGA CAATCGCCGTCGCGGGCGC
P54	1NCen3	pZE13d-C_PfCen3	F	ttaaagaggagaaaggatccatgtctcgtaaaaaccaaaccatgattcgtaatccg aatccgcgtagcaaacg AACGAAATTACAGACGAGCAG
P55	PfCen3 N-terminus	pZE13d-C_PfCen3	R	ttgttcctcattcagc TCGTTGCGCCCGCGACG
P56	PfCen1 Δ19	pET-28_PfCen1	F	GAGCTGAATGAGGAACAAAAG
P57	PfCen1 Δ19	pET-28_PfCen1	R	gtggtgatgatggtgGAATAAGTTAGTTTTTTTCATAATGC GC
P58	PfCen1 (*E. coli*)	oligo 4	F	aacctgtattttcagggcATGTCTCGTAAAAACCAAACC
P59	PfCen2 (*E. coli*)	oligo 5	F	aacctgtattttcagggcATGACAGATAACACTGCC
P60	PfCen3 (*E. coli*)	oligo 6	F	aacctgtattttcagggcATGATTAACCGTAAGAGCG
P61	PfCen4 (*E. coli*)	oligo 7	F	aacctgtattttcagggcATGAATACTATGCTGATCAAAG
P62	pZE13d ORF	pZE13d	R	CAGCTAATTAAGCTTGGCTGCAG

Uppercase letters indicate binding sequence.

Table 16 List of DNA oligos

#	Encodes	Sequence (5' → 3')
1	EFh-dead PfCen1 aspartate 37, 73, 110, 146 mutated to alanine, dsDNA	acattatacgaagttatacgcgtATGAGCAGAAAAAATCAAACTATGATAAGGAACCCTAATCC TCGAAGTAAAAGAAACGAATTAAATGAAGAACAAAAATTAGAAATTAAGGAAG CTTTTGATTTATTTGCTACAAACGGCACTGGAAGAATTGATGCAAAAGAATTAAA AGTTGCAATGAGAGCTTTAGGATTCGAACCAAAAAAAGAAGATATAAGGAAAAT AATATCTGATGTTGCTAAAGATGGATCTGGTACAATTGACTTTAATGACTTTTTAG ACATTATGACAATAAAAATGAGTGAAAGAGATCCTAAGGAGGAAATACTAAAAG CTTTCCGATTATTTGCTGATGATGAGACTGGAAAAATCTCCTTCAAAAATTTAAA ACGTGTAGCAAAAGAACTTGGAGAGAATATTACTGATGAGGAAATTCAAGAAAT GATAGACGAAGCAGCCAGAGATGGAGACGGAGAAATTAATGAAGAAGAATTTAT GAGAATTATGAAAAAGACCAACTTATTTcctaggagtaaaggagaagaa
2	HsCen2 codon optimized for *P. falciparum,* dsDNA	acattatacgaagttatacgcgtATGGCAAGTAATTTTAAAAAAGCAAATATGGCAAGTTCAAG TCAAAGAAAAAGAATGAGTCCAAAACCAGAATTAACAGAAGAACAAAAACAAG AAATTAGAGAAgcaTTTGATTTAttcGATGCAGATGGAACTGGAACAATAGATGTAA AAGAATTAAAAGTAGCAATGAGAGCATTAGGATTTGAACCTAAAAAAGAAGAAA TTAAAAAAATGATAAGTGAAATAGATAAAGAAGGAACTGGAAAAATGAATTTTG GAGATTTTcttACAGTAATGACACAAAAAATGAGTGAAAAAGATACAAAAGAAGA AATATTAAAAGCTTTTAAACTTTTTGATGATGATGAAACTGGAAAAATTtccTTTAA AAATTTAAAAAGAGTAGCTAAAGAActtGGAGAAAATTTAACAGATGAAGAATTA CAAGAAATGATAGATGAAGCAGATAGAGATGGAGATGGAGAAGTATCAGAACA AGAATTTTTAAGAATTATGAAAAAAACATCATTATATcctaggagtaaaggagaagaa
3	pFIO mCherry removal, ssDNA	gaagaatgatggtggaggtggatcctaagtcgacgatatggcagcttaatgtt
4	PfCen1	catcaccaccacatcgatATGTCTCGTAAAAACCAAACCATGATTCGTAATCCGAATCCGCG TAGCAAACGCAACGAGCTGAATGAGGAACAAAAGCTTGAAATTAAAGAAGCGTT CGATCTTTTTGACACAAATGGTACAGGGCGTATCGACGCAAAAGAGCTTAAAGTG

	codon optimized for *E. coli,* dsDNA	GCAATGCGCGCATTGGGGTTTGAACCAAAAAAGGAGGACATCCGTAAAATTATT TCAGATGTCGATAAAGACGGCTCTGGGACGATTGATTTCAATGACTTTTTAGACA TTATGACCATTAAAATGTCGGAACGCGATCCCAAAGAGGAAATTCTTAAAGCGTT TCGTTTATTCGACGACGACGAAACCGGAAAAATTTCCTTCAAAAACCTGAAGCGC GTAGCAAAAGAGCTTGGAGAAAATATCACGGACGAGGAAATTCAAGAGATGATT GATGAAGCGGACCGCGATGGAGATGGAGAAATTAACGAGGAAGAGTTCATGCGC ATTATGAAAAAAACTAACTTATTCTAActgcagccaagcttaatt
5	PfCen2 codon optimized for *E. coli,* dsDNA	catcaccaccacatcgatATGACAGATAACACTGCCGTGCGCCGCCGTTATGAAAAATCTTT CACGGAACGTCCGGGTTTTACGGAGGATGAGATTGAGGAAATTCGTGAAGCCTTT AACCTTTTGGACACCGACGGGACGGGGACCATCGATCCTAAGGAAATTAAATGT GCCATGCAATCGCTTGGCTTAGATGCAAAGAATCCCATGATTTTCCGCATGATCG CGGACCTGGAAAAAGACGGCTATTCCTCCATCGATTTTGAAGAATTCATGGAGGT GATTACAAGTAAGTTGGGCAACAAGGACACGCGTGAGGGCATTCAGCGCATCTT CAACTTATTTGATGACGATAAAACAGGTTCGATCTCTCTTAAAAACTTAAAACGT GTTGCTAAAGAGTTAGGCGAAACATTAACGGACGAAGAATTGCGTGATATGATT GATCGTGCCGATTCGAAGGGGGAGGGCGAAATCAGCTTCGAGGACTTTTACACT ATTATGACCAAGAAAAGTTTCCTGTAActgcagccaagcttaatt
6	PfCen3 codon optimized for *E. coli,* dsDNA	catcaccaccacatcgatATGATTAACCGTAAGAGCGAATCTGTCAGCTACACGCCTCGTGC AATCACTAACCGCCCTATTAGTAGCAATCGCCGTCGCGGGCGCAACGAAATTACA GACGAGCAGAAAAATGAAATTAAGGAAGCGTTTGATCTTTTCGATACAGAGAAA ACCGGCAAAATCGACTATCATGAGCTGAAGGTTGCCATCCGTGCATTAGGATTCG ATATTAAGAAAGCGGACGTTTTAGACTTGATGCGCGAATACGACAAGACCAACA GTGGGCATATCGATTATAACGATTTTCTTGACATTATGACTCAAAAGATTTCTGA GCGTGACCCAACGGAAGAAATTATTAAGGCTTTTAAGCTTTTCGATGACGACGAT ACTGGGAAAATCTCCTTGAAGAATTTGCGTCGTGTTTCGCGTGAGCTGGGTGAAA ATTTAAGCGATGACGAGTTACAAGCTATGATCGACGAATTCGACAAAGACATGG ATGGGGAAATCTCTCAAGAGGAATTCTTGTCAATCATGAAGCAGACATCCTTATA TTAActgcagccaagcttaatt
7	PfCen4 codon optimized for *E. coli,* dsDNA	catcaccaccacatcgatATGAATACTATGCTGATCAAAGATAACATTAACATCTCAATTAA CGAGGATGTAGAAAAAGAACTGTACGAATGCTTTTCACTGTTTGACACGAACAA GTGCGGCTACATTGATATTCGTGAGTTTTACTTTGCCTTGAAATCCTTGGGCCTGA ACTTCAAGAAGGAGCAGGTTAAAAATATTTTTTTGGACATCAAGAAAGATATTGA CGAGAAATTGAATTTTGACGAATTTTTTGATATCGCAACGAAATATCTGCATACC CGCTATAATGACGACGAAATGGACCAAATGTTCTCATTGTTTGACCCCAACGATA CTGGTAAAATTACACTTCAGGCTCTGCGTAAGGTTTGCACTGACATCGGGGAGAA TATCTCGGATACCGAGCTGAATAACATGATCCACTTCGCAGACAAAAACAATGAT AAAGTCATCGATAAAAACGAGTTCAAAAAGGTGCTTCTTTGCTCCTGGAAGAATG ATCCGTTATCGGACGTTGACAGCGACTCTTAActgcagccaagcttaatt
8	EFh-dead PfCen1 aspartate 37, 73, 110, 146 mutated to alanine, E. coli codon, dsDNA	actttaagaaggagatataccATGTCTCGTAAAAACCAAACCATGATTCGTAATCCGAATCCG CGTAGCAAACGCAACGAGCTGAATGAGGAACAAAAGCTTGAAATTAAAGAAGCG TTCGATCTTTTTGCCACAAATGGTACAGGGCGTATCGACGCAAAAGAGCTTAAAG TGGCAATGCGCGCATTGGGGTTTGAACCAAAAAAGGAGGACATCCGTAAAATTA TTTCAGATGTCGCGAAAGACGGCTCTGGGACGATTGATTTCAATGACTTTTTAGA CATTATGACCATTAAAATGTCGGAACGCGATCCCAAAGAGGAAATTCTTAAAGC GTTTCGTTTATTCGCCGACGACGAAACCGGAAAAATTTCCTTCAAAAACCTGAAG CGCGTAGCAAAAGAGCTTGGAGAAAATATCACGGACGAGGAAATTCAAGAGATG ATTGATGAAGCGGCCCGCGATGGAGATGGAGAAATTAACGAGGAAGAGTTCATG CGCATTATGAAAAAAACTAACTTATTCgggcaccaccaccaccaccact
9	ScCdc31 codon optimized for *E. coli,* dsDNA	actttaagaaggagatataccATG TCC AAA AAT CGC TCC AGT TTG CAG TCA GGA CCG TTG AAC TCG GAG TTG TTG GAG GAA CAA AAG CAG GAG ATT TAC GAG GCA TTT TCA CTG TTT GAT ATG AAT AAT GAC GGT TTT TTA GAC TAC CAT GAG TTA AAA GTC GCT ATG AAA GCA CTG GGA TTC GAA TTA CCC AAA CGT GAA ATT CTT GAT TTG ATT GAC GAG TAT GAC TCG GAG GGT CGC CAT TTA ATG AAA TAT GAT GAT TTT TAC ATC GTA ATG GGC GAA AAA ATT CTG AAA CGT GAC CCG CTG GAC GAG ATC AAG CGT GCG TTC CAG TTG TTT GAT GAC GAT CAT ACA GGC AAG ATC AGC ATT AAA AAC TTA CGT CGC GTG GCA AAG GAA CTG GGT GAG ACC CTG ACG GAT GAG GAG TTG CGC GCA ATG ATC GAG GAG TTT GAC CTT GAT GGC GAT GGG GAG ATC AAT GAG AAC GAG TTC ATC GCA ATC TGT ACT GAT AGT TTCgggcaccaccaccaccaccact

10	TbCen2 codon optimized for *E. coli,* dsDNA	actttaagaaggagatataccATG TCT ACT ACC AAC CGT GGA GGT AAT TCG CCA GTG GCC CAG AGT GTG AAC CGT AGC ATC GCT CCG GGC ATG TCA CTT AGT GGC TCC GCC CTG GCG GTA CTT ACT GAG GAA CAA CGT CAG GAA ATC AAA GAA GCA TTT GAC CTT TTT GAT ACA GAT GGA TCT GGG ACC ATC GAT GTC AAA GAA TTG AAA GTT GCG ATG CGC GCC TTG GGG TTC GAG CCC CGT AAG GAC GAG GTA CGT CGT CTG ATC GCT TCC ACG ATG GAG GAA CGC GGA GAT CCC GCT CCA GTG AAA CCT GGC ACC GCG CCG GGA GCC GAC AAC CAT GTC ATC GGG TTC GCC GAG TTC GTC GAT TTG ATG GCC CGT AAA ATG AAC GAA CGT GAT TCC CGT GAA GAG ATG TTG AAA GCT TTC CAC TTA TTT GAT GAC GAT AAA ACA GGT AAA ATT ACT TTT AAA AAC TTA AAG CGT GTG GCT CAG GAA TTA GGT GAA AAC ATG ACC GAT AGT GAA ATT CAA GAG ATG ATC GAT GAA GCA GAC CGC GAC GGA GAT GGA GAG GTC AGT GAG GAA GAG TTC CTG CGT ATT ATG AAG AAG ACG AGT CTT TAT TTCgggcaccaccaccaccaccact
11	CrCen codon optimized for *E. coli,* dsDNA	actttaagaaggagatatacc ATG TCA TAC AAG GCA AAA ACC GTA GTT TCG GCC CGC CGC GAC CAA AAG AAA GGA CGC GTC GGT CTT ACC GAG GAG CAG AAA CAA GAA ATC CGC GAA GCG TTT GAT TTA TTC GAC ACT GAT GGA AGT GGG ACC ATC GAC GCC AAG GAA TTA AAG GTG GCG ATG CGC GCT TTA GGA TTC GAA CCC AAG AAG GAA GAG ATC AAA AAA ATG ATT TCG GAA ATT GAT AAG GAC GGC TCC GGC ACA ATC GAC TTT GAG GAA TTT TTA ACG ATG ATG ACA GCG AAG ATG GGT GAA CGT GAT AGC CGT GAG GAA ATT CTT AAA GCA TTC CGT CTG TTC GAC GAT GAC AAC AGT GGC ACC ATT ACG ATC AAG GAC TTA CGC CGT GTG GCA AAG GAG TTG GGG GAG AAT TTA ACC GAA GAG GAG TTG CAA GAA ATG ATT GCC GAA GCC GAT CGT AAT GAT GAT AAT GAA ATT GAT GAG GAC GAA TTT ATT CGT ATT ATG AAA AAG ACG AGT CTG TTCgggcaccaccaccaccaccact
12	6His, ssDNA	gatcCATACGCGTCGACACCATCATCACCACCACTAACtgca
13	6His, ssDNA	GTTAGTGGTGGTGATGATGGTGTCGACGCGTATG
14	6His-Linker-TEV, ssDNA	atcatcaccaccacatcgatTACGATATCCCAACGACCGAAAACCTGTATTTTCAGGGCGCCA CGCGTctgcagccaagcttaattagctgat

Table 17 List of plasmids

Previously existing plasmids	
Name	**Source**
pARL_PfCen3-GFP	Prof. Dr. Tim Gilberger, BNITM Hamburg
pARL_PfCen1-Halo	Johanna Bauer
pZE13d	Lutz and Bujard (1996) [151]
pET-28a(+)	Merck
p238-actin-chromobody-Halo	Prof. Dr. Friedrich Frischknecht lab, CIID Heidelberg
pSLI_TGD_SAS6-GFP	Dr. Caroline Simon based on [142]
Derived plasmids created within the scope of this thesis	
Name	**Creators**
pARL_PfCen1-GFP	Nicolas Lichti, Yannik Voß
pARL_PfCen2-GFP	Nicolas Lichti, Yannik Voß
pARL_PfCen4-GFP	Nicolas Lichti, Yannik Voß
pARL_PfCen3_ST_GFP	Marina Iocca, Yannik Voß
pARL_PfCen3_SYT_GFP	Marina Iocca, Yannik Voß
pET-28_1NCen4	Marina Iocca, Yannik Voß
pET-28_4NCen1	Marina Iocca, Yannik Voß
pET-28_CrCen	Yannik Voß
pET-28_ Δ19-PfCen1-GFP	Marina Iocca, Yannik Voß
pET-28_ EFh_dead-PfCen1	Yannik Voß
pET-28_HsCen2	Nicolas Lichti, Yannik Voß

pET-28_PfCen1	Nicolas Lichti, Yannik Voß
pET-28_PfCen1-GFP	Yannik Voß
pET-28_PfCen2	Nicolas Lichti, Yannik Voß
pET-28_ScCdc31	Yannik Voß
pET-28_TbCen2	Yannik Voß
pFIO_hsp70p_Cen1-GFP	Yannik Voß
pFIO_hsp70p_GFP	Yannik Voß
pFIO_hsp86p_Cen1-GFP	Yannik Voß
pFIO_hsp86p_ Δ19-Cen1-GFP	Yannik Voß
pFIO_hsp86p_ EFh_dead-Cen1-GFP	Yannik Voß
pFIO_hsp86p_ HsCen2-GFP	Yannik Voß
pFIO_hsp86p_ ~~mCherry~~_GFP-T2A-Cen1	Yannik Voß
pFIO_hsp86p_ ~~mCherry~~_PfCen1-Halo	Nicolas Lichti, Yannik Voß
pZE13d-C	Yannik Voß
pZE13d-C_1NCen3	Yannik Voß
pZE13d-C_3NCen1	Yannik Voß
pZE13d-C_PfCen3	Yannik Voß
pZE13d-C_PfCen3_ST	Yannik Voß
pZE13d-C_PfCen3_SYT	Yannik Voß
pZE13d-C_PfCen4	Yannik Voß
pZE13d-TEV	Yannik Voß
pZE13d-TEV_PfCen1	Yannik Voß
pZE13d-TEV_PfCen2	Yannik Voß
pZE13d-TEV_PfCen3	Yannik Voß
pZE13d-TEV_PfCen4	Yannik Voß

Table 18 List of recombinant proteins

Protein	Additions	Expression system	Creators
1NCen3-6His	C-terminal: 6His	pZE13d-C, W3110-Z1	Yannik Voß
1NCen4-6His	C-terminal: G + 6His	pET-28, Bl21 (De3)	Marina Iocca, Yannik Voß
3NCen1-6His	C-terminal: 6His	pZE13d-C, W3110-Z1	Yannik Voß
4NCen1-6His	C-terminal: G + 6His	pET-28, Bl21 (De3)	Marina Iocca, Yannik Voß
CrCen-6His	C-terminal: G + 6His	pET-28, Bl21 (De3)	Yannik Voß
Δ19-PfCen1-6His	C-terminal: G + 6His	pET-28, Bl21 (De3)	Marina Iocca, Yannik Voß
EFh_dead-PfCen1-6His	C-terminal: G + 6His	pET-28, Bl21 (De3)	Yannik Voß
HsCen2-6His	C-terminal: G + 6His	pET-28, Bl21 (De3)	Yannik Voß
PfCen1	N-terminal: G	pZE13d-TEV, W3110-Z1	Yannik Voß
PfCen1-6His	C-terminal: G + 6His	pET-28, Bl21 (De3)	Yannik Voß
PfCen1-GFP	C-terminal: G + 6His	pET-28, Bl21 (De3)	Yannik Voß
PfCen2	N-terminal: G	pZE13d-TEV, W3110-Z1	Yannik Voß
PfCen2-6His	C-terminal: G + 6His	pET-28, Bl21 (De3)	Yannik Voß
PfCen3	N-terminal: G	pZE13d-TEV, W3110-Z1	Yannik Voß
PfCen3-6His	C-terminal: 6His	pZE13d-C, W3110-Z1	Yannik Voß
PfCen3-ST-6His	C-terminal: 6His	pZE13d-C, W3110-Z1	Yannik Voß
PfCen3-SYT-6His	C-terminal: 6His	pZE13d-C, W3110-Z1	Yannik Voß
PfCen4	N-terminal: G	pZE13d-TEV, W3110-Z1	Yannik Voß
PfCen4-6His	C-terminal: 6His	pZE13d-C, W3110-Z1	Yannik Voß
ScCdc31-6His	C-terminal: G + 6His	pET-28, Bl21 (De3)	Yannik Voß
TbCen2-6His	C-terminal: G + 6His	pET-28, Bl21 (De3)	Yannik Voß

Table 19 List of bacterial strains

Strains	Purpose	Source
E. coli BL21-CodonPlus (De3)	Recombinant protein expression	Studier and Moffatt (1986) [259]
E. coli DH5α F'Iq	Plasmid amplification	New England Biolabs (C2992H)
E. coli W3110-Z1	Recombinant protein expression	Lutz and Bujard (1996) [151]

Table 20 List of P. falciparum strains

Parental Strain	Plasmid	Expressed transgenes	Source
NF54	Wild type	-	Ponnudurai *et al.*(1981)
	pARL_PfCen1-GFP	hDHFR, PfCen1-GFP	This thesis, Nicolas Lichti
	pARL_PfCen2-GFP	hDHFR, PfCen2-GFP	This thesis, Nicolas Lichti
	pARL_PfCen3-GFP	hDHFR, PfCen3-GFP	Dr. Caroline Simon
	pARL_PfCen4-GFP	hDHFR, PfCen4-GFP	This thesis, Nicolas Lichti
	pARL_PfCen3_ST_GFP	hDHFR, PfCen3_ST-GFP	This thesis, Marina Iocca
	pARL_PfCen3_SYT_GFP	hDHFR, PfCen3_SYT-GFP	This thesis, Marina Iocca
	pARL_PfCen1-Halo	hDHFR, PfCen1-Halo	Johanna Bauer
3D7-DiCre	Wild type	-	Dr. Moritz Treeck [260]
	pFIO_hsp70p_GFP	hDHFR-mCherry/ GFP	This thesis
	pFIO_hsp70p_Cen1-GFP	hDHFR-mCherry/ PfCen1-GFP	This thesis
	pFIO_hsp86p_Cen1-GFP	hDHFR-mCherry/ PfCen1-GFP	This thesis
	pFIO_hsp86p_ Δ19-Cen1-GFP	hDHFR-mCherry/ Δ19-PfCen1-GFP	This thesis
	pFIO_hsp86p_ EFh_dead-Cen1-GFP	hDHFR-mCherry/ EFh_dead-PfCen1-GFP	This thesis
	pFIO_hsp86p_ HsCen2-GFP	hDHFR-mCherry/ HsCen2-GFP	This thesis
	pFIO_hsp86p_~~mCherry~~_GFP-T2A-Cen1	hDHFR/ GFP-T2A-PfCen1	This thesis

5 List of References

[1] R. Carter and K. N. Mendis, 'Evolutionary and Historical Aspects of the Burden of Malaria', *Clin. Microbiol. Rev.*, vol. 15, no. 4, pp. 564–594, Oct. 2002, doi: 10.1128/CMR.15.4.564-594.2002.

[2] J. A. Cox *et al.*, 'Calcium and magnesium binding to human centrin 3 and interaction with target peptides', *Biochemistry*, vol. 44, no. 3, pp. 840–850, Jan. 2005, doi: 10.1021/bi048294e.

[3] S. A. Sundararaman *et al.*, 'Genomes of cryptic chimpanzee Plasmodium species reveal key evolutionary events leading to human malaria', *Nat. Commun.*, vol. 7, p. 11078, Mar. 2016, doi: 10.1038/ncomms11078.

[4] D. E. Loy *et al.*, 'Out of Africa: origins and evolution of the human malaria parasites Plasmodium falciparum and Plasmodium vivax', *Int. J. Parasitol.*, vol. 47, no. 2–3, pp. 87–97, Feb. 2017, doi: 10.1016/j.ijpara.2016.05.008.

[5] World Health Oganisation, 'World malaria report 2022'. Accessed: Oct. 03, 2023. [Online]. Available: https://www.who.int/teams/global-malaria-programme/reports/world-malaria-report-2022

[6] J. L. Gallup and J. D. Sachs, 'The economic burden of malaria', *Am. J. Trop. Med. Hyg.*, vol. 64, no. 1-2 Suppl, pp. 85–96, 2001, doi: 10.4269/ajtmh.2001.64.85.

[7] N. Sarma, E. Patouillard, R. E. Cibulskis, and J.-L. Arcand, 'The Economic Burden of Malaria: Revisiting the Evidence', *Am. J. Trop. Med. Hyg.*, vol. 101, no. 6, pp. 1405–1415, Dec. 2019, doi: 10.4269/ajtmh.19-0386.

[8] D. Gollin and C. Zimmermann, 'Malaria: Disease Impacts and Long-Run Income Differences'. Rochester, NY, Aug. 01, 2007. doi: 10.2139/ssrn.1012564.

[9] D. P. Kwiatkowski, 'How Malaria Has Affected the Human Genome and What Human Genetics Can Teach Us about Malaria', *Am. J. Hum. Genet.*, vol. 77, no. 2, pp. 171–192, Aug. 2005.

[10] A. Laveran, *Un nouveau parasite trouvé dans le sang des malades atteints de fièvre palustre: origine parasitaire des accidents de l'impaludisme*. 1881.

[11] S. Sato, 'Plasmodium—a brief introduction to the parasites causing human malaria and their basic biology', *J. Physiol. Anthropol.*, vol. 40, p. 1, Jan. 2021, doi: 10.1186/s40101-020-00251-9.

[12] M. A. Ahmed and J. Cox-Singh, 'Plasmodium knowlesi – an emerging pathogen', *Isbt Sci. Ser.*, vol. 10, no. Suppl 1, pp. 134–140, Apr. 2015, doi: 10.1111/voxs.12115.

[13] F. Ariey *et al.*, 'A molecular marker of artemisinin-resistant Plasmodium falciparum malaria', *Nature*, vol. 505, no. 7481, pp. 50–55, Jan. 2014, doi: 10.1038/nature12876.

[14] N. Arora, L. C Anbalagan, and A. K. Pannu, 'Towards Eradication of Malaria: Is the WHO's RTS,S/AS01 Vaccination Effective Enough?', *Risk Manag. Healthc. Policy*, vol. 14, pp. 1033–1039, Mar. 2021, doi: 10.2147/RMHP.S219294.

[15] M. S. Datoo *et al.*, 'A Phase III Randomised Controlled Trial Evaluating the Malaria Vaccine Candidate R21/Matrix-M^{TM} in African Children'. Rochester, NY, Sep. 26, 2023. doi: 10.2139/ssrn.4584076.

[16] A. F. Cowman, J. Healer, D. Marapana, and K. Marsh, 'Malaria: Biology and Disease', *Cell*, vol. 167, no. 3, pp. 610–624, Oct. 2016, doi: 10.1016/j.cell.2016.07.055.

[17] D. F. Wirth, 'Biological revelations', *Nature*, vol. 419, no. 6906, pp. 495–496, Oct. 2002, doi: 10.1038/419495a.

[18] F. Frischknecht and K. Matuschewski, 'Plasmodium Sporozoite Biology', *Cold Spring Harb. Perspect. Med.*, vol. 7, no. 5, p. a025478, May 2017, doi: 10.1101/cshperspect.a025478.

[19] F. Frischknecht *et al.*, 'Imaging movement of malaria parasites during transmission by Anopheles mosquitoes', *Cell. Microbiol.*, vol. 6, no. 7, pp. 687–694, 2004, doi: 10.1111/j.1462-5822.2004.00395.x.

[20] V. Risco-Castillo *et al.*, 'Malaria Sporozoites Traverse Host Cells within Transient Vacuoles', *Cell Host Microbe*, vol. 18, no. 5, pp. 593–603, Nov. 2015, doi: 10.1016/j.chom.2015.10.006.

[21] A. M. Vaughan *et al.*, 'Complete *Plasmodium falciparum* liver-stage development in liver-chimeric mice', *J. Clin. Invest.*, vol. 122, no. 10, pp. 3618–3628, Oct. 2012, doi: 10.1172/JCI62684.

[22] A. M. Vaughan and S. H. I. Kappe, 'Malaria Parasite Liver Infection and Exoerythrocytic Biology', *Cold Spring Harb. Perspect. Med.*, vol. 7, no. 6, p. a025486, Jun. 2017, doi: 10.1101/cshperspect.a025486.

[23] C. S. Simon, V. S. Stürmer, and J. Guizetti, 'How Many Is Enough? - Challenges of Multinucleated Cell Division in Malaria Parasites', *Front. Cell. Infect. Microbiol.*, vol. 11, 2021, Accessed: Oct. 03, 2023. [Online]. Available: https://www.frontiersin.org/articles/10.3389/fcimb.2021.658616

[24] V. S. Stürmer, S. Stopper, P. Binder, A. Klemmer, N. B. Becker, and J. Guizetti, 'Progeny counter mechanism in malaria parasites is linked to extracellular resources'. bioRxiv, p. 2023.01.20.524890, Feb. 24, 2023. doi: 10.1101/2023.01.20.524890.

[25] H. B. Reilly, H. Wang, J. A. Steuter, A. M. Marx, and M. T. Ferdig, 'Quantitative dissection of clone-specific growth rates in cultured malaria parasites', *Int. J. Parasitol.*, vol. 37, no. 14, pp. 1599–1607, Dec. 2007, doi: 10.1016/j.ijpara.2007.05.003.
[26] L. B. Stewart *et al.*, 'Intrinsic multiplication rate variation and plasticity of human blood stage malaria parasites', *Commun. Biol.*, vol. 3, p. 624, Oct. 2020, doi: 10.1038/s42003-020-01349-7.
[27] M. Koch and J. Baum, 'The mechanics of malaria parasite invasion of the human erythrocyte – towards a reassessment of the host cell contribution', *Cell. Microbiol.*, vol. 18, no. 3, pp. 319–329, Mar. 2016, doi: 10.1111/cmi.12557.
[28] A. G. Maier, B. M. Cooke, A. F. Cowman, and L. Tilley, 'Malaria parasite proteins that remodel the host erythrocyte', *Nat. Rev. Microbiol.*, vol. 7, no. 5, Art. no. 5, May 2009, doi: 10.1038/nrmicro2110.
[29] C. Grüring, A. Heiber, F. Kruse, J. Ungefehr, T.-W. Gilberger, and T. Spielmann, 'Development and host cell modifications of Plasmodium falciparum blood stages in four dimensions', *Nat. Commun.*, vol. 2, no. 1, Art. no. 1, Jan. 2011, doi: 10.1038/ncomms1169.
[30] S. A. Desai, S. M. Bezrukov, and J. Zimmerberg, 'A voltage-dependent channel involved in nutrient uptake by red blood cells infected with the malaria parasite', *Nature*, vol. 406, no. 6799, pp. 1001–1005, Aug. 2000, doi: 10.1038/35023000.
[31] G. Pishchany and E. P. Skaar, 'Taste for Blood: Hemoglobin as a Nutrient Source for Pathogens', *PLoS Pathog.*, vol. 8, no. 3, p. e1002535, Mar. 2012, doi: 10.1371/journal.ppat.1002535.
[32] Y. Voß, S. Klaus, J. Guizetti, and M. Ganter, 'Plasmodium schizogony, a chronology of the parasite's cell cycle in the blood stage', *PLoS Pathog.*, vol. 19, no. 3, p. e1011157, Mar. 2023, doi: 10.1371/journal.ppat.1011157.
[33] W. Trager and J. B. Jensen, 'Human malaria parasites in continuous culture', *Science*, vol. 193, no. 4254, pp. 673–675, Aug. 1976, doi: 10.1126/science.781840.
[34] P. Dasari *et al.*, 'Digestive vacuole of Plasmodium falciparum released during erythrocyte rupture dually activates complement and coagulation', *Blood*, vol. 119, no. 18, pp. 4301–4310, May 2012, doi: 10.1182/blood-2011-11-392134.
[35] C. A. Moxon, M. P. Gibbins, D. McGuinness, D. A. Milner, and M. Marti, 'New Insights into Malaria Pathogenesis', *Annu. Rev. Pathol. Mech. Dis.*, vol. 15, no. 1, pp. 315–343, 2020, doi: 10.1146/annurev-pathmechdis-012419-032640.
[36] S. C. Wassmer *et al.*, 'Investigating the Pathogenesis of Severe Malaria: A Multidisciplinary and Cross-Geographical Approach', *Am. J. Trop. Med. Hyg.*, vol. 93, no. 3 Suppl, pp. 42–56, Sep. 2015, doi: 10.4269/ajtmh.14-0841.
[37] K. B. Seydel *et al.*, 'Brain Swelling and Death in Children with Cerebral Malaria', *N. Engl. J. Med.*, vol. 372, no. 12, pp. 1126–1137, Mar. 2015, doi: 10.1056/NEJMoa1400116.
[38] M. Bernabeu *et al.*, 'Severe adult malaria is associated with specific PfEMP1 adhesion types and high parasite biomass', *Proc. Natl. Acad. Sci.*, vol. 113, no. 23, pp. E3270–E3279, Jun. 2016, doi: 10.1073/pnas.1524294113.
[39] P. Cao *et al.*, 'Modeling the dynamics of Plasmodium falciparum gametocytes in humans during malaria infection', *eLife*, vol. 8, p. e49058, doi: 10.7554/eLife.49058.
[40] N. M. B. Brancucci *et al.*, 'Lysophosphatidylcholine Regulates Sexual Stage Differentiation in the Human Malaria Parasite Plasmodium falciparum', *Cell*, vol. 171, no. 7, pp. 1532-1544.e15, Dec. 2017, doi: 10.1016/j.cell.2017.10.020.
[41] K. Venugopal, F. Hentzschel, G. Valkiūnas, and M. Marti, 'Plasmodium asexual growth and sexual development in the haematopoietic niche of the host', *Nat. Rev. Microbiol.*, vol. 18, no. 3, Art. no. 3, Mar. 2020, doi: 10.1038/s41579-019-0306-2.
[42] M. Singh, Suryanshu, Kanika, G. Singh, A. Dubey, and R. K. Chaitanya, 'Plasmodium's journey through the Anopheles mosquito: A comprehensive review', *Biochimie*, vol. 181, pp. 176–190, Feb. 2021, doi: 10.1016/j.biochi.2020.12.009.
[43] R. Rashpa and M. Brochet, 'Expansion microscopy of Plasmodium gametocytes reveals the molecular architecture of a bipartite microtubule organisation centre coordinating mitosis with axoneme assembly', *PLOS Pathog.*, vol. 18, no. 1, p. e1010223, Jan. 2022, doi: 10.1371/journal.ppat.1010223.
[44] M. Zeeshan *et al.*, 'Plasmodium ARK2 and EB1 drive unconventional spindle dynamics, during chromosome segregation in sexual transmission stages', *Nat. Commun.*, vol. 14, no. 1, Art. no. 1, Sep. 2023, doi: 10.1038/s41467-023-41395-3.
[45] G. R. Mair *et al.*, 'Translational Repression is essential for Plasmodium sexual development and mediated by a DDX6-type RNA helicase', *Science*, vol. 313, no. 5787, pp. 667–669, Aug. 2006, doi: 10.1126/science.1125129.
[46] D. S. Guttery, M. Zeeshan, A. A. Holder, E. C. Tromer, and R. Tewari, 'Meiosis in Plasmodium: how does it work?', *Trends Parasitol.*, vol. 39, no. 10, pp. 812–821, Oct. 2023, doi: 10.1016/j.pt.2023.07.002.

[47] F. Hentzschel and F. Frischknecht, ‘Still enigmatic: Plasmodium oocysts 125 years after their discovery’, *Trends Parasitol.*, vol. 38, no. 8, pp. 610–613, Aug. 2022, doi: 10.1016/j.pt.2022.05.013.
[48] K. Matuschewski, ‘Getting infectious: formation and maturation of Plasmodium sporozoites in the Anopheles vector’, *Cell. Microbiol.*, vol. 8, no. 10, pp. 1547–1556, 2006, doi: 10.1111/j.1462-5822.2006.00778.x.
[49] M. E. Francia and B. Striepen, ‘Cell division in apicomplexan parasites’, *Nat. Rev. Microbiol.*, vol. 12, no. 2, pp. 125–136, Feb. 2014, doi: 10.1038/nrmicro3184.
[50] S. Klaus *et al.*, ‘Asynchronous nuclear cycles in multinucleated Plasmodium falciparum facilitate rapid proliferation’, *Sci. Adv.*, vol. 8, no. 13, p. eabj5362, Mar. 2022, doi: 10.1126/sciadv.abj5362.
[51] M. Ganter *et al.*, ‘Plasmodium falciparum CRK4 directs continuous rounds of DNA replication during schizogony’, *Nat. Microbiol.*, vol. 2, p. 17017, Feb. 2017, doi: 10.1038/nmicrobiol.2017.17.
[52] C. S. Simon *et al.*, ‘An extended DNA-free intranuclear compartment organizes centrosome microtubules in malaria parasites’, *Life Sci. Alliance*, vol. 4, no. 11, p. e202101199, Sep. 2021, doi: 10.26508/lsa.202101199.
[53] M. Machado, S. Klaus, D. Klaschka, J. Guizetti, and M. Ganter, ‘Plasmodium falciparum CRK4 links early mitotic events to the onset of S-phase during schizogony’, *mBio*, vol. 14, no. 4, p. e0077923, Aug. 2023, doi: 10.1128/mbio.00779-23.
[54] P. T. Conduit, A. Wainman, and J. W. Raff, ‘Centrosome function and assembly in animal cells’, *Nat. Rev. Mol. Cell Biol.*, vol. 16, no. 10, pp. 611–624, Oct. 2015, doi: 10.1038/nrm4062.
[55] D. Rüthnick and E. Schiebel, ‘Duplication of the Yeast Spindle Pole Body Once per Cell Cycle’, *Mol. Cell. Biol.*, vol. 36, no. 9, p. 1324, May 2016, doi: 10.1128/MCB.00048-16.
[56] M. Aikawa and R. L. Beaudoin, ‘Studies on nuclear division of a malarial parasite under pyrimethamine treatment’, *J. Cell Biol.*, vol. 39, no. 3, pp. 749–754, Dec. 1968, doi: 10.1083/jcb.39.3.749.
[57] B. Liffner and S. Absalon, ‘Expansion Microscopy Reveals Plasmodium falciparum Blood-Stage Parasites Undergo Anaphase with A Chromatin Bridge in the Absence of Mini-Chromosome Maintenance Complex Binding Protein’, *Microorganisms*, vol. 9, no. 11, p. 2306, Nov. 2021, doi: 10.3390/microorganisms9112306.
[58] R. M. Rudlaff, S. Kraemer, J. Marshman, and J. D. Dvorin, ‘Three-dimensional ultrastructure of Plasmodium falciparum throughout cytokinesis’, *PLoS Pathog.*, vol. 16, no. 6, p. e1008587, Jun. 2020, doi: 10.1371/journal.ppat.1008587.
[59] C. Arquint, A.-M. Gabryjonczyk, and E. A. Nigg, ‘Centrosomes as signalling centres’, *Philos. Trans. R. Soc. B Biol. Sci.*, vol. 369, no. 1650, p. 20130464, Sep. 2014, doi: 10.1098/rstb.2013.0464.
[60] E. H. Hinchcliffe, F. J. Miller, M. Cham, A. Khodjakov, and G. Sluder, ‘Requirement of a Centrosomal Activity for Cell Cycle Progression Through G $_1$ into S Phase’, *Science*, vol. 291, no. 5508, pp. 1547–1550, Feb. 2001, doi: 10.1126/science.1056866.
[61] D. Kitagawa *et al.*, ‘Structural Basis of the 9-Fold Symmetry of Centrioles’, *Cell*, vol. 144, no. 3, pp. 364–375, Feb. 2011, doi: 10.1016/j.cell.2011.01.008.
[62] J. B. Woodruff, ‘The material state of centrosomes: lattice, liquid, or gel?’, *Curr. Opin. Struct. Biol.*, vol. 66, pp. 139–147, Feb. 2021, doi: 10.1016/j.sbi.2020.10.001.
[63] J. B. Woodruff, O. Wueseke, and A. A. Hyman, ‘Pericentriolar material structure and dynamics’, *Philos. Trans. R. Soc. B Biol. Sci.*, vol. 369, no. 1650, p. 20130459, Sep. 2014, doi: 10.1098/rstb.2013.0459.
[64] J. V. Kilmartin, ‘Lessons from yeast: the spindle pole body and the centrosome’, *Philos. Trans. R. Soc. B Biol. Sci.*, vol. 369, no. 1650, p. 20130456, Sep. 2014, doi: 10.1098/rstb.2013.0456.
[65] A. M. Cavanaugh and S. L. Jaspersen, ‘Big Lessons from Little Yeast: Budding and Fission Yeast Centrosome Structure, Duplication, and Function’, *Annu. Rev. Genet.*, vol. 51, no. 1, pp. 361–383, Nov. 2017, doi: 10.1146/annurev-genet-120116-024733.
[66] C. Funaya *et al.*, ‘Transient Structure Associated with the Spindle Pole Body Directs Meiotic Microtubule Reorganization in S. pombe’, *Curr. Biol.*, vol. 22, no. 7, pp. 562–574, Apr. 2012, doi: 10.1016/j.cub.2012.02.042.
[67] D. Rüthnick, J. Vitale, A. Neuner, and E. Schiebel, ‘The N-terminus of Sfi1 and yeast centrin Cdc31 provide the assembly site for a new spindle pole body’, *J. Cell Biol.*, vol. 220, no. 3, p. e202004196, Feb. 2021, doi: 10.1083/jcb.202004196.
[68] L. Benjamin *et al.*, ‘Atlas of Plasmodium falciparum intraerythrocytic development using expansion microscopy’, *eLife*, vol. 12, May 2023, doi: 10.7554/eLife.88088.
[69] L. Tilley *et al.*, *Plasmodium falciparum kinetochore proteins stabilise a nexus between the mitotic apparatus and the apical complex*. 2023. doi: 10.21203/rs.3.rs-3404985/v1.
[70] B. Mahajan *et al.*, ‘Centrins, cell cycle regulation proteins in human malaria parasite Plasmodium falciparum’, *J. Biol. Chem.*, vol. 283, no. 46, pp. 31871–31883, Nov. 2008, doi: 10.1074/jbc.M800028200.

[71] C. Wenz *et al.*, 'An Sfi1-like centrin-interacting centriolar plaque protein affects nuclear microtubule homeostasis', *PLOS Pathog.*, vol. 19, no. 5, p. e1011325, May 2023, doi: 10.1371/journal.ppat.1011325.
[72] L. Reininger, J. M. Wilkes, H. Bourgade, D. Miranda-Saavedra, and C. Doerig, 'An essential Aurora-related kinase transiently associates with spindle pole bodies during Plasmodium falciparum erythrocytic schizogony', *Mol. Microbiol.*, vol. 79, no. 1, pp. 205–221, Jan. 2011, doi: 10.1111/j.1365-2958.2010.07442.x.
[73] B. J. Morahan *et al.*, 'Human Aurora kinase inhibitor Hesperadin reveals epistatic interaction between Plasmodium falciparum PfArk1 and PfNek1 kinases', *Commun. Biol.*, vol. 3, p. 701, Nov. 2020, doi: 10.1038/s42003-020-01424-z.
[74] W. A. M. Hoeijmakers *et al.*, 'Plasmodium falciparum centromeres display a unique epigenetic makeup and cluster prior to and during schizogony', *Cell. Microbiol.*, vol. 14, no. 9, pp. 1391–1401, 2012, doi: 10.1111/j.1462-5822.2012.01803.x.
[75] J. Kimmel *et al.*, 'Gene-by-gene screen of the unknown proteins encoded on Plasmodium falciparum chromosome 3', *Cell Syst.*, vol. 14, no. 1, pp. 9-23.e7, Jan. 2023, doi: 10.1016/j.cels.2022.12.001.
[76] J. L. Salisbury, A. Baron, B. Surek, and M. Melkonian, 'Striated flagellar roots: isolation and partial characterization of a calcium-modulated contractile organelle', *J. Cell Biol.*, vol. 99, no. 3, pp. 962–970, Sep. 1984, doi: 10.1083/jcb.99.3.962.
[77] R. L. Wright, J. Salisbury, and J. W. Jarvik, 'A nucleus-basal body connector in Chlamydomonas reinhardtii that may function in basal body localization or segregation', *J. Cell Biol.*, vol. 101, no. 5 Pt 1, pp. 1903–1912, Nov. 1985, doi: 10.1083/jcb.101.5.1903.
[78] T. J. Dantas, O. M. Daly, and C. G. Morrison, 'Such small hands: the roles of centrins/caltractins in the centriole and in genome maintenance', *Cell. Mol. Life Sci. CMLS*, vol. 69, no. 18, pp. 2979–2997, Sep. 2012, doi: 10.1007/s00018-012-0961-1.
[79] Y. Voß, S. Klaus, N. P. Lichti, M. Ganter, and J. Guizetti, 'Malaria parasite centrins assemble by Ca2+-inducible condensation'. bioRxiv, p. 2022.07.26.501452, Apr. 17, 2023. doi: 10.1101/2022.07.26.501452.
[80] A. Yang, S. Miron, P. Duchambon, L. Assairi, Y. Blouquit, and C. T. Craescu, 'The N-terminal domain of human centrin 2 has a closed structure, binds calcium with a very low affinity, and plays a role in the protein self-assembly', *Biochemistry*, vol. 45, no. 3, pp. 880–889, Jan. 2006, doi: 10.1021/bi051397s.
[81] L. D. V. Sosa *et al.*, 'The structure, molecular dynamics, and energetics of centrin-melittin complex', *Proteins*, vol. 79, no. 11, pp. 3132–3143, Nov. 2011, doi: 10.1002/prot.23142.
[82] S. Li, A. M. Sandercock, P. Conduit, C. V. Robinson, R. L. Williams, and J. V. Kilmartin, 'Structural role of Sfi1p-centrin filaments in budding yeast spindle pole body duplication', *J. Cell Biol.*, vol. 173, no. 6, pp. 867–877, Jun. 2006, doi: 10.1083/jcb.200603153.
[83] W. Wang, Y. Zhao, H. Wang, and B. Yang, 'Crystal structure of the trimeric N-terminal domain of ciliate Euplotes octocarinatus centrin binding with calcium ions', *Protein Sci. Publ. Protein Soc.*, vol. 27, no. 6, pp. 1102–1108, Jun. 2018, doi: 10.1002/pro.3418.
[84] J. L. Gifford, M. P. Walsh, and H. J. Vogel, 'Structures and metal-ion-binding properties of the Ca2+-binding helix–loop–helix EF-hand motifs', *Biochem. J.*, vol. 405, no. 2, pp. 199–221, Jul. 2007, doi: 10.1042/BJ20070255.
[85] E. Matei *et al.*, 'C-Terminal Half of Human Centrin 2 Behaves like a Regulatory EF-Hand Domain', *Biochemistry*, vol. 42, no. 6, pp. 1439–1450, Feb. 2003, doi: 10.1021/bi0269714.
[86] J. R. Thompson, Z. C. Ryan, J. L. Salisbury, and R. Kumar, 'The structure of the human centrin 2-xeroderma pigmentosum group C protein complex', *J. Biol. Chem.*, vol. 281, no. 27, pp. 18746–18752, Jul. 2006, doi: 10.1074/jbc.M513667200.
[87] M. Treeck, J. L. Sanders, J. E. Elias, and J. C. Boothroyd, 'The phosphoproteomes of Plasmodium falciparum and Toxoplasma gondii reveal unusual adaptations within and beyond the parasites' boundaries', *Cell Host Microbe*, vol. 10, no. 4, pp. 410–419, Oct. 2011, doi: 10.1016/j.chom.2011.09.004.
[88] S. A. Cobbold, J. M. Santos, A. Ochoa, D. H. Perlman, and M. Llinás, 'Proteome-wide analysis reveals widespread lysine acetylation of major protein complexes in the malaria parasite', *Sci. Rep.*, vol. 6, no. 1, Art. no. 1, Jan. 2016, doi: 10.1038/srep19722.
[89] B. N. Pease *et al.*, 'Global analysis of protein expression and phosphorylation of three stages of Plasmodium falciparum intraerythrocytic development', *J. Proteome Res.*, vol. 12, no. 9, pp. 4028–4045, Sep. 2013, doi: 10.1021/pr400394g.
[90] B. N. Pease *et al.*, 'Characterization of Plasmodium falciparum Atypical Kinase PfPK7– Dependent Phosphoproteome', *J. Proteome Res.*, vol. 17, no. 6, pp. 2112–2123, Jun. 2018, doi: 10.1021/acs.jproteome.8b00062.

[91] E. Lasonder *et al.*, 'The Plasmodium falciparum Schizont Phosphoproteome Reveals Extensive Phosphatidylinositol and cAMP-Protein Kinase A Signaling', *J. Proteome Res.*, vol. 11, no. 11, pp. 5323–5337, Nov. 2012, doi: 10.1021/pr300557m.
[92] D. Grecu and L. Assairi, 'CK2 phosphorylation of human centrins 1 and 2 regulates their binding to the DNA repair protein XPC, the centrosomal protein Sfi1 and the phototransduction protein transducin β', *FEBS Open Bio*, vol. 4, pp. 407–419, 2014, doi: 10.1016/j.fob.2014.04.002.
[93] K. B. Lukasiewicz, T. M. Greenwood, V. C. Negron, A. K. Bruzek, J. L. Salisbury, and W. L. Lingle, 'Control of Centrin Stability by Aurora A', *PLOS ONE*, vol. 6, no. 6, p. e21291, Jun. 2011, doi: 10.1371/journal.pone.0021291.
[94] K. T. G. Rigbolt *et al.*, 'System-wide temporal characterization of the proteome and phosphoproteome of human embryonic stem cell differentiation', *Sci. Signal.*, vol. 4, no. 164, p. rs3, Mar. 2011, doi: 10.1126/scisignal.2001570.
[95] J. V. Olsen *et al.*, 'Global, in vivo, and site-specific phosphorylation dynamics in signaling networks', *Cell*, vol. 127, no. 3, pp. 635–648, Nov. 2006, doi: 10.1016/j.cell.2006.09.026.
[96] N. Dephoure *et al.*, 'A quantitative atlas of mitotic phosphorylation', *Proc. Natl. Acad. Sci. U. S. A.*, vol. 105, no. 31, pp. 10762–10767, Aug. 2008, doi: 10.1073/pnas.0805139105.
[97] M. Le Guennec *et al.*, 'A helical inner scaffold provides a structural basis for centriole cohesion', *Sci. Adv.*, vol. 6, no. 7, p. eaaz4137, Feb. 2020, doi: 10.1126/sciadv.aaz4137.
[98] M. H. Laporte *et al.*, 'Human SFI1 and Centrin form a complex critical for centriole architecture and ciliogenesis', *EMBO J.*, vol. 41, no. 21, p. e112107, Sep. 2022, doi: 10.15252/embj.2022112107.
[99] J. L. Salisbury, K. M. Suino, R. Busby, and M. Springett, 'Centrin-2 is required for centriole duplication in mammalian cells', *Curr. Biol. CB*, vol. 12, no. 15, pp. 1287–1292, Aug. 2002, doi: 10.1016/s0960-9822(02)01019-9.
[100] D. B. Sawant, S. Majumder, J. L. Perkins, C.-H. Yang, P. A. Eyers, and H. A. Fisk, 'Centrin 3 is an inhibitor of centrosomal Mps1 and antagonizes centrin 2 function', *Mol. Biol. Cell*, vol. 26, no. 21, pp. 3741–3753, Nov. 2015, doi: 10.1091/mbc.E14-07-1248.
[101] C.-H. Yang, C. Kasbek, S. Majumder, A. M. Yusof, and H. A. Fisk, 'Mps1 Phosphorylation Sites Regulate the Function of Centrin 2 in Centriole Assembly', *Mol. Biol. Cell*, vol. 21, no. 24, pp. 4361–4372, Dec. 2010, doi: 10.1091/mbc.E10-04-0298.
[102] P. Baum, C. Furlong, and B. Byers, 'Yeast gene required for spindle pole body duplication: homology of its product with Ca2+-binding proteins', *Proc. Natl. Acad. Sci. U. S. A.*, vol. 83, no. 15, pp. 5512–5516, Aug. 1986, doi: 10.1073/pnas.83.15.5512.
[103] J. V. Kilmartin, 'Sfi1p has conserved centrin-binding sites and an essential function in budding yeast spindle pole body duplication', *J. Cell Biol.*, vol. 162, no. 7, pp. 1211–1221, Sep. 2003, doi: 10.1083/jcb.200307064.
[104] C. Seybold *et al.*, 'Kar1 binding to Sfi1 C-terminal regions anchors the SPB bridge to the nuclear envelope', *J. Cell Biol.*, vol. 209, no. 6, pp. 843–861, Jun. 2015, doi: 10.1083/jcb.201412050.
[105] J. M. Leung, J. Liu, L. A. Wetzel, and K. Hu, 'Centrin2 from the human parasite Toxoplasma gondii is required for its invasion and intracellular replication', *J. Cell Sci.*, vol. 132, no. 13, p. jcs228791, Jul. 2019, doi: 10.1242/jcs.228791.
[106] K. Hu *et al.*, 'Cytoskeletal Components of an Invasion Machine—The Apical Complex of Toxoplasma gondii', *PLOS Pathog.*, vol. 2, no. 2, p. e13, Feb. 2006, doi: 10.1371/journal.ppat.0020013.
[107] C. Y. He, M. Pypaert, and G. Warren, 'Golgi duplication in Trypanosoma brucei requires Centrin2', *Science*, vol. 310, no. 5751, pp. 1196–1198, Nov. 2005, doi: 10.1126/science.1119969.
[108] A. Selvapandiyan, P. Kumar, J. L. Salisbury, C. C. Wang, and H. L. Nakhasi, 'Role of Centrins 2 and 3 in Organelle Segregation and Cytokinesis in Trypanosoma brucei', *PLoS ONE*, vol. 7, no. 9, p. e45288, Sep. 2012, doi: 10.1371/journal.pone.0045288.
[109] T. J. Dantas, Y. Wang, P. Lalor, P. Dockery, and C. G. Morrison, 'Defective nucleotide excision repair with normal centrosome structures and functions in the absence of all vertebrate centrins', *J. Cell Biol.*, vol. 193, no. 2, pp. 307–318, Apr. 2011, doi: 10.1083/jcb.201012093.
[110] R. Nishi *et al.*, 'Centrin 2 Stimulates Nucleotide Excision Repair by Interacting with Xeroderma Pigmentosum Group C Protein', *Mol. Cell. Biol.*, vol. 25, no. 13, pp. 5664–5674, Jul. 2005, doi: 10.1128/MCB.25.13.5664-5674.2005.
[111] I. D. Acu *et al.*, 'Coordination of Centrosome Homeostasis and DNA Repair Is Intact in MCF-7 and Disrupted in MDA-MB 231 Breast Cancer Cells', *Cancer Res.*, vol. 70, no. 8, p. 10.1158/0008-5472.CAN-09–3800, Apr. 2010, doi: 10.1158/0008-5472.CAN-09-3800.
[112] L. Chen and K. Madura, 'Centrin/Cdc31 Is a Novel Regulator of Protein Degradation', *Mol. Cell. Biol.*, vol. 28, no. 5, pp. 1829–1840, Mar. 2008, doi: 10.1128/MCB.01256-07.
[113] T. Fischer, S. Rodríguez-Navarro, G. Pereira, A. Rácz, E. Schiebel, and E. Hurt, 'Yeast centrin Cdc31 is linked to the nuclear mRNA export machinery', *Nat. Cell Biol.*, vol. 6, no. 9, pp. 840–848, Sep. 2004, doi: 10.1038/ncb1163.

[114] D. Jani *et al.*, 'Sus1, Cdc31, and the Sac3 CID region form a conserved interaction platform that promotes nuclear pore association and mRNA export', *Mol. Cell*, vol. 33, no. 6, pp. 727–737, Mar. 2009, doi: 10.1016/j.molcel.2009.01.033.
[115] M. Zhang *et al.*, 'Uncovering the essential genome of the human malaria parasite Plasmodium falciparum by saturation mutagenesis', *Science*, vol. 360, no. 6388, p. eaap7847, May 2018, doi: 10.1126/science.aap7847.
[116] V. M. Howick *et al.*, 'The Malaria Cell Atlas: Single parasite transcriptomes across the complete Plasmodium life cycle', *Science*, vol. 365, no. 6455, p. eaaw2619, Aug. 2019, doi: 10.1126/science.aaw2619.
[117] M. Tourbez *et al.*, 'Calcium-dependent self-assembly of human centrin 2', *J. Biol. Chem.*, vol. 279, no. 46, pp. 47672–47680, Nov. 2004, doi: 10.1074/jbc.M404996200.
[118] Y. Zhao, X. Guo, and B. Yang, 'Calcium-induced human centrin 1 self-assembly and double-regulating the binding with peptide R18-Sfi1p', *Int. J. Biol. Macromol.*, vol. 128, pp. 314–323, May 2019, doi: 10.1016/j.ijbiomac.2019.01.096.
[119] Y. Zhao, L. Song, A. Liang, and B. Yang, 'Characterization of self-assembly of Euplotes octocarinatus centrin', *J. Photochem. Photobiol. B*, vol. 95, no. 1, pp. 26–32, Apr. 2009, doi: 10.1016/j.jphotobiol.2008.12.006.
[120] C. Conter *et al.*, 'The interplay of self-assembly and target binding in centrin 1 from Toxoplasma gondii', *Biochem. J.*, vol. 478, no. 13, pp. 2571–2587, Jul. 2021, doi: 10.1042/BCJ20210295.
[121] L. Bombardi, M. Pedretti, C. Conter, P. Dominici, and A. Astegno, 'Distinct Calcium Binding and Structural Properties of Two Centrin Isoforms from Toxoplasma gondii', *Biomolecules*, vol. 10, no. 8, p. 1142, Aug. 2020, doi: 10.3390/biom10081142.
[122] M. Roques *et al.*, 'Plasmodium centrin PbCEN-4 localizes to the putative MTOC and is dispensable for malaria parasite proliferation', *Biol. Open*, vol. 8, no. 1, p. bio036822, Jan. 2019, doi: 10.1242/bio.036822.
[123] A. A. Hyman, C. A. Weber, and F. Jülicher, 'Liquid-Liquid Phase Separation in Biology', *Annu. Rev. Cell Dev. Biol.*, vol. 30, no. 1, pp. 39–58, 2014, doi: 10.1146/annurev-cellbio-100913-013325.
[124] S. F. Banani *et al.*, 'Compositional Control of Phase-Separated Cellular Bodies', *Cell*, vol. 166, no. 3, pp. 651–663, Jul. 2016, doi: 10.1016/j.cell.2016.06.010.
[125] A. Musacchio, 'On the role of phase separation in the biogenesis of membraneless compartments', *EMBO J.*, vol. 41, no. 5, p. e109952, Mar. 2022, doi: 10.15252/embj.2021109952.
[126] C. P. Brangwynne *et al.*, 'Germline P granules are liquid droplets that localize by controlled dissolution/condensation', *Science*, vol. 324, no. 5935, pp. 1729–1732, Jun. 2009, doi: 10.1126/science.1172046.
[127] A. C. Dumetz, A. M. Chockla, E. W. Kaler, and A. M. Lenhoff, 'Protein Phase Behavior in Aqueous Solutions: Crystallization, Liquid-Liquid Phase Separation, Gels, and Aggregates', *Biophys. J.*, vol. 94, no. 2, pp. 570–583, Jan. 2008, doi: 10.1529/biophysj.107.116152.
[128] S. F. Banani, H. O. Lee, A. A. Hyman, and M. K. Rosen, 'Biomolecular condensates: organizers of cellular biochemistry', *Nat. Rev. Mol. Cell Biol.*, vol. 18, no. 5, Art. no. 5, May 2017, doi: 10.1038/nrm.2017.7.
[129] P. Li *et al.*, 'Phase Transitions in the Assembly of Multi-Valent Signaling Proteins', *Nature*, vol. 483, no. 7389, pp. 336–340, Mar. 2012, doi: 10.1038/nature10879.
[130] V. N. Uversky, 'Intrinsically disordered proteins in overcrowded milieu: Membrane-less organelles, phase separation, and intrinsic disorder', *Curr. Opin. Struct. Biol.*, vol. 44, pp. 18–30, Jun. 2017, doi: 10.1016/j.sbi.2016.10.015.
[131] S. Alberti, 'Phase separation in biology', *Curr. Biol.*, vol. 27, no. 20, pp. R1097–R1102, Oct. 2017, doi: 10.1016/j.cub.2017.08.069.
[132] Y. Lin, D. S. W. Protter, M. K. Rosen, and R. Parker, 'Formation and Maturation of Phase-Separated Liquid Droplets by RNA-Binding Proteins', *Mol. Cell*, vol. 60, no. 2, pp. 208–219, Oct. 2015, doi: 10.1016/j.molcel.2015.08.018.
[133] S. Boeynaems *et al.*, 'Protein Phase Separation: A New Phase in Cell Biology', *Trends Cell Biol.*, vol. 28, no. 6, pp. 420–435, Jun. 2018, doi: 10.1016/j.tcb.2018.02.004.
[134] S. Ranganathan and E. I. Shakhnovich, 'Dynamic metastable long-living droplets formed by sticker-spacer proteins', *eLife*, vol. 9, p. e56159, Jun. 2020, doi: 10.7554/eLife.56159.
[135] M. Feric *et al.*, 'Coexisting Liquid Phases Underlie Nucleolar Subcompartments', *Cell*, vol. 165, no. 7, pp. 1686–1697, Jun. 2016, doi: 10.1016/j.cell.2016.04.047.
[136] S. Jain, J. R. Wheeler, R. W. Walters, A. Agrawal, A. Barsic, and R. Parker, 'ATPase modulated stress granules contain a diverse proteome and substructure', *Cell*, vol. 164, no. 3, pp. 487–498, Jan. 2016, doi: 10.1016/j.cell.2015.12.038.
[137] A. Patel *et al.*, 'A Liquid-to-Solid Phase Transition of the ALS Protein FUS Accelerated by Disease Mutation', *Cell*, vol. 162, no. 5, pp. 1066–1077, Aug. 2015, doi: 10.1016/j.cell.2015.07.047.

[138] S. Ray *et al.*, 'α-Synuclein aggregation nucleates through liquid–liquid phase separation', *Nat. Chem.*, vol. 12, no. 8, pp. 705–716, Aug. 2020, doi: 10.1038/s41557-020-0465-9.
[139] L. Jawerth *et al.*, 'Protein condensates as aging Maxwell fluids', *Science*, vol. 370, no. 6522, pp. 1317–1323, Dec. 2020, doi: 10.1126/science.aaw4951.
[140] J. B. Woodruff, B. Ferreira Gomes, P. O. Widlund, J. Mahamid, A. Honigmann, and A. A. Hyman, 'The Centrosome Is a Selective Condensate that Nucleates Microtubules by Concentrating Tubulin', *Cell*, vol. 169, no. 6, pp. 1066-1077.e10, Jun. 2017, doi: 10.1016/j.cell.2017.05.028.
[141] D. Zwicker, M. Decker, S. Jaensch, A. A. Hyman, and F. Jülicher, 'Centrosomes are autocatalytic droplets of pericentriolar material organized by centrioles', *Proc. Natl. Acad. Sci.*, vol. 111, no. 26, pp. E2636–E2645, Jul. 2014, doi: 10.1073/pnas.1404855111.
[142] J. Birnbaum *et al.*, 'A genetic system to study Plasmodium falciparum protein function', *Nat. Methods*, vol. 14, no. 4, pp. 450–456, Apr. 2017, doi: 10.1038/nmeth.4223.
[143] G. V. Los *et al.*, 'HaloTag: a novel protein labeling technology for cell imaging and protein analysis', *ACS Chem. Biol.*, vol. 3, no. 6, pp. 373–382, Jun. 2008, doi: 10.1021/cb800025k.
[144] N. Lardon *et al.*, 'Systematic Tuning of Rhodamine Spirocyclization for Super-resolution Microscopy', *J. Am. Chem. Soc.*, vol. 143, no. 36, pp. 14592–14600, Sep. 2021, doi: 10.1021/jacs.1c05004.
[145] B. R. Mardin and E. Schiebel, 'Breaking the ties that bind: New advances in centrosome biology', *J. Cell Biol.*, vol. 197, no. 1, pp. 11–18, Apr. 2012, doi: 10.1083/jcb.201108006.
[146] A. Toso, J. R. Winter, A. J. Garrod, A. C. Amaro, P. Meraldi, and A. D. McAinsh, 'Kinetochore-generated pushing forces separate centrosomes during bipolar spindle assembly', *J. Cell Biol.*, vol. 184, no. 3, pp. 365–372, Feb. 2009, doi: 10.1083/jcb.200809055.
[147] 'Kinesin-related proteins required for assembly of the mitotic spindle', *J. Cell Biol.*, vol. 118, no. 1, pp. 95–108, Jul. 1992.
[148] C. W. Jacobs, A. E. Adams, P. J. Szaniszlo, and J. R. Pringle, 'Functions of microtubules in the Saccharomyces cerevisiae cell cycle', *J. Cell Biol.*, vol. 107, no. 4, pp. 1409–1426, Oct. 1988, doi: 10.1083/jcb.107.4.1409.
[149] B. J. Fennell, J. A. Naughton, E. Dempsey, and A. Bell, 'Cellular and molecular actions of dinitroaniline and phosphorothioamidate herbicides on Plasmodium falciparum: Tubulin as a specific antimalarial target', *Mol. Biochem. Parasitol.*, vol. 145, no. 2, pp. 226–238, Feb. 2006, doi: 10.1016/j.molbiopara.2005.08.020.
[150] A. Musacchio, 'The Molecular Biology of Spindle Assembly Checkpoint Signaling Dynamics', *Curr. Biol.*, vol. 25, no. 20, pp. R1002–R1018, Oct. 2015, doi: 10.1016/j.cub.2015.08.051.
[151] R. Lutz and H. Bujard, 'Independent and Tight Regulation of Transcriptional Units in Escherichia Coli Via the LacR/O, the TetR/O and AraC/I1-I2 Regulatory Elements', *Nucleic Acids Res.*, vol. 25, no. 6, pp. 1203–1210, Mar. 1997, doi: 10.1093/nar/25.6.1203.
[152] P. Wingfield, 'N-Terminal Methionine Processing', *Curr. Protoc. Protein Sci.*, vol. 88, p. 6.14.1-6.14.3, Apr. 2017, doi: 10.1002/cpps.29.
[153] S. Alberti, A. Gladfelter, and T. Mittag, 'Considerations and challenges in studying liquid-liquid phase separation and biomolecular condensates', *Cell*, vol. 176, no. 3, pp. 419–434, Jan. 2019, doi: 10.1016/j.cell.2018.12.035.
[154] S. Alberti, S. Saha, J. B. Woodruff, T. M. Franzmann, J. Wang, and A. A. Hyman, 'A User's Guide for Phase Separation Assays with Purified Proteins', *J. Mol. Biol.*, vol. 430, no. 23, pp. 4806–4820, Nov. 2018, doi: 10.1016/j.jmb.2018.06.038.
[155] J. R. Geiser, D. van Tuinen, S. E. Brockerhoff, M. M. Neff, and T. N. Davis, 'Can calmodulin function without binding calcium?', *Cell*, vol. 65, no. 6, pp. 949–959, Jun. 1991, doi: 10.1016/0092-8674(91)90547-c.
[156] B. M. Geier, H. Wiech, and E. Schiebel, 'Binding of Centrins and Yeast Calmodulin to Synthetic Peptides Corresponding to Binding Sites in the Spindle Pole Body Components Kar1p and Spc110p *', *J. Biol. Chem.*, vol. 271, no. 45, pp. 28366–28374, Nov. 1996, doi: 10.1074/jbc.271.45.28366.
[157] F. Burki, 'The eukaryotic tree of life from a global phylogenomic perspective', *Cold Spring Harb. Perspect. Biol.*, vol. 6, no. 5, p. a016147, May 2014, doi: 10.1101/cshperspect.a016147.
[158] G. Erdős, M. Pajkos, and Z. Dosztányi, 'IUPred3: prediction of protein disorder enhanced with unambiguous experimental annotation and visualization of evolutionary conservation', *Nucleic Acids Res.*, vol. 49, no. W1, pp. W297–W303, May 2021, doi: 10.1093/nar/gkab408.
[159] J. Jumper *et al.*, 'Highly accurate protein structure prediction with AlphaFold', *Nature*, vol. 596, no. 7873, Art. no. 7873, Aug. 2021, doi: 10.1038/s41586-021-03819-2.
[160] P. Prommana *et al.*, 'Inducible Knockdown of Plasmodium Gene Expression Using the glmS Ribozyme', *PLOS ONE*, vol. 8, no. 8, p. e73783, Aug. 2013, doi: 10.1371/journal.pone.0073783.
[161] M. Tibúrcio *et al.*, 'A Novel Tool for the Generation of Conditional Knockouts To Study Gene Function across the Plasmodium falciparum Life Cycle', *mBio*, vol. 10, no. 5, pp. e01170-19, Sep. 2019, doi: 10.1128/mBio.01170-19.

[162] C. R. Collins *et al.*, 'Robust inducible Cre recombinase activity in the human malaria parasite Plasmodium falciparum enables efficient gene deletion within a single asexual erythrocytic growth cycle', *Mol. Microbiol.*, vol. 88, no. 4, pp. 687–701, May 2013, doi: 10.1111/mmi.12206.
[163] R. S. Kent, K. K. Modrzynska, R. Cameron, N. Philip, O. Billker, and A. P. Waters, 'Inducible developmental reprogramming redefines commitment to sexual development in the malaria parasite Plasmodium berghei', *Nat. Microbiol.*, vol. 3, no. 11, pp. 1206–1213, Nov. 2018, doi: 10.1038/s41564-018-0223-6.
[164] C. M. Mogollon *et al.*, 'Rapid Generation of Marker-Free P. falciparum Fluorescent Reporter Lines Using Modified CRISPR/Cas9 Constructs and Selection Protocol', *PLoS ONE*, vol. 11, no. 12, p. e0168362, Dec. 2016, doi: 10.1371/journal.pone.0168362.
[165] T. D. Otto *et al.*, 'New insights into the blood-stage transcriptome of Plasmodium falciparum using RNA-Seq', *Mol. Microbiol.*, vol. 76, no. 1, pp. 12–24, Apr. 2010, doi: 10.1111/j.1365-2958.2009.07026.x.
[166] S. H. Adjalley, C. D. Chabbert, B. Klaus, V. Pelechano, and L. M. Steinmetz, 'Landscape and dynamics of transcription initiation in the malaria parasite Plasmodium falciparum', *Cell Rep.*, vol. 14, no. 10, pp. 2463–2475, Mar. 2016, doi: 10.1016/j.celrep.2016.02.025.
[167] L. Chappell *et al.*, 'Refining the transcriptome of the human malaria parasite Plasmodium falciparum using amplification-free RNA-seq', *BMC Genomics*, vol. 21, no. 1, p. 395, Jun. 2020, doi: 10.1186/s12864-020-06787-5.
[168] J. H. Kim *et al.*, 'High Cleavage Efficiency of a 2A Peptide Derived from Porcine Teschovirus-1 in Human Cell Lines, Zebrafish and Mice', *PLoS ONE*, vol. 6, no. 4, p. e18556, Apr. 2011, doi: 10.1371/journal.pone.0018556.
[169] J. Straimer *et al.*, 'Site-Specific Editing of the Plasmodium falciparum Genome Using Engineered Zinc-Finger Nucleases', *Nat. Methods*, vol. 9, no. 10, pp. 993–998, Oct. 2012, doi: 10.1038/nmeth.2143.
[170] J. A. Riback *et al.*, 'Composition-dependent thermodynamics of intracellular phase separation', *Nature*, vol. 581, no. 7807, Art. no. 7807, May 2020, doi: 10.1038/s41586-020-2256-2.
[171] K. Pandey, P. E. Ferreira, T. Ishikawa, T. Nagai, O. Kaneko, and K. Yahata, 'Ca2+ monitoring in Plasmodium falciparum using the yellow cameleon-Nano biosensor', *Sci. Rep.*, vol. 6, p. 23454, Mar. 2016, doi: 10.1038/srep23454.
[172] D. A. Goldstein, 'Serum Calcium', in *Clinical Methods: The History, Physical, and Laboratory Examinations*, 3rd ed., H. K. Walker, W. D. Hall, and J. W. Hurst, Eds., Boston: Butterworths, 1990. Accessed: Oct. 02, 2023. [Online]. Available: http://www.ncbi.nlm.nih.gov/books/NBK250/
[173] D. T. McSwiggen, M. Mir, X. Darzacq, and R. Tjian, 'Evaluating phase separation in live cells: diagnosis, caveats, and functional consequences', *Genes Dev.*, vol. 33, no. 23–24, pp. 1619–1634, Jan. 2019, doi: 10.1101/gad.331520.119.
[174] H. C. Ishikawa-Ankerhold, R. Ankerhold, and G. P. C. Drummen, 'Advanced fluorescence microscopy techniques--FRAP, FLIP, FLAP, FRET and FLIM', *Mol. Basel Switz.*, vol. 17, no. 4, pp. 4047–4132, Apr. 2012, doi: 10.3390/molecules17044047.
[175] N. Lichti, 'Investigation of phase separation mechanism of centrosomal proteins in Plasmodium falciparum', Master Thesis, Ruprecht-Karls-Universität Heidelberg, 2023.
[176] A. Biosca *et al.*, 'Detection of Protein Aggregation in Live Plasmodium Parasites', *Antimicrob. Agents Chemother.*, vol. 64, no. 6, pp. e02135-19, May 2020, doi: 10.1128/AAC.02135-19.
[177] S. Kroschwald, S. Maharana, and A. Simon, 'Hexanediol: a chemical probe to investigate the material properties of membrane-less compartments', *Matters*, May 2017, doi: 10.19185/matters.201702000010.
[178] B. R. Sabari *et al.*, 'Coactivator condensation at super-enhancers links phase separation and gene control', *Science*, vol. 361, no. 6400, p. eaar3958, Jul. 2018, doi: 10.1126/science.aar3958.
[179] G. Prelich, 'Gene Overexpression: Uses, Mechanisms, and Interpretation', *Genetics*, vol. 190, no. 3, pp. 841–854, Mar. 2012, doi: 10.1534/genetics.111.136911.
[180] S. Hasenkamp, K. T. Russell, and P. Horrocks, 'Comparison of the absolute and relative efficiencies of electroporation-based transfection protocols for Plasmodium falciparum', *Malar. J.*, vol. 11, no. 1, p. 210, Jun. 2012, doi: 10.1186/1475-2875-11-210.
[181] S. D. Boltryk *et al.*, 'CRISPR/Cas9-engineered inducible gametocyte producer lines as a valuable tool for Plasmodium falciparum malaria transmission research', *Nat. Commun.*, vol. 12, no. 1, Art. no. 1, Aug. 2021, doi: 10.1038/s41467-021-24954-4.
[182] S. M. Ganesan, A. Falla, S. J. Goldfless, A. S. Nasamu, and J. C. Niles, 'Synthetic RNA–protein modules integrated with native translation mechanisms to control gene expression in malaria parasites', *Nat. Commun.*, vol. 7, p. 10727, Mar. 2016, doi: 10.1038/ncomms10727.
[183] S. J. Goldfless, J. C. Wagner, and J. C. Niles, 'Versatile control of Plasmodium falciparum gene expression with an inducible protein-RNA interaction', *Nat. Commun.*, vol. 5, p. 5329, Nov. 2014, doi: 10.1038/ncomms6329.

[184] X. Liang *et al.*, 'A Leak-Free Inducible CRISPRi/a System for Gene Functional Studies in Plasmodium falciparum', *Microbiol. Spectr.*, vol. 10, no. 3, pp. e02782-21, May 2022, doi: 10.1128/spectrum.02782-21.
[185] R. A. O'Donnell *et al.*, 'A genetic screen for improved plasmid segregation reveals a role for Rep20 in the interaction of Plasmodium falciparum chromosomes', *EMBO J.*, vol. 21, no. 5, pp. 1231–1239, Mar. 2002, doi: 10.1093/emboj/21.5.1231.
[186] Z. Y. Chen, C. Y. He, L. Meuse, and M. A. Kay, 'Silencing of episomal transgene expression by plasmid bacterial DNA elements in vivo', *Gene Ther.*, vol. 11, no. 10, pp. 856–864, May 2004, doi: 10.1038/sj.gt.3302231.
[187] E. Riu, Z.-Y. Chen, H. Xu, C.-Y. He, and M. A. Kay, 'Histone Modifications are Associated with the Persistence or Silencing of Vector-mediated Transgene Expression In Vivo', *Mol. Ther.*, vol. 15, no. 7, pp. 1348–1355, Jul. 2007, doi: 10.1038/sj.mt.6300177.
[188] L. Zang, M. Nishikawa, M. Ando, Y. Takahashi, and Y. Takakura, 'Contribution of Epigenetic Modifications to the Decline in Transgene Expression from Plasmid DNA in Mouse Liver', *Pharmaceutics*, vol. 7, no. 3, pp. 199–212, Aug. 2015, doi: 10.3390/pharmaceutics7030199.
[189] B. Zheng, M. Sage, E. A. Sheppeard, V. Jurecic, and A. Bradley, 'Engineering Mouse Chromosomes with Cre-loxP: Range, Efficiency, and Somatic Applications', *Mol. Cell. Biol.*, vol. 20, no. 2, pp. 648–655, Jan. 2000.
[190] B. Hein, K. I. Willig, and S. W. Hell, 'Stimulated emission depletion (STED) nanoscopy of a fluorescent protein-labeled organelle inside a living cell', *Proc. Natl. Acad. Sci.*, vol. 105, no. 38, pp. 14271–14276, Sep. 2008, doi: 10.1073/pnas.0807705105.
[191] A.-K. Mehnert, C. S. Simon, and J. Guizetti, 'Immunofluorescence staining protocol for STED nanoscopy of Plasmodium-infected red blood cells', *Mol. Biochem. Parasitol.*, vol. 229, pp. 47–52, Apr. 2019, doi: 10.1016/j.molbiopara.2019.02.007.
[192] J.-G. Schloetel, J. Heine, A. F. Cowman, and M. Pasternak, 'Guided STED nanoscopy enables super-resolution imaging of blood stage malaria parasites', *Sci. Rep.*, vol. 9, p. 4674, Mar. 2019, doi: 10.1038/s41598-019-40718-z.
[193] N. D. Geoghegan *et al.*, '4D analysis of malaria parasite invasion offers insights into erythrocyte membrane remodeling and parasitophorous vacuole formation', *Nat. Commun.*, vol. 12, no. 1, Art. no. 1, Jun. 2021, doi: 10.1038/s41467-021-23626-7.
[194] J. Huff, A. Bergter, J. Birkenbeil, I. Kleppe, R. Engelmann, and U. Krzic, 'The new 2D Superresolution mode for ZEISS Airyscan', *Nat. Methods*, vol. 14, no. 12, Art. no. 12, Dec. 2017, doi: 10.1038/nmeth.f.404.
[195] X. Chen *et al.*, 'Superresolution structured illumination microscopy reconstruction algorithms: a review', *Light Sci. Appl.*, vol. 12, no. 1, Art. no. 1, Jul. 2023, doi: 10.1038/s41377-023-01204-4.
[196] R. S. Erdmann *et al.*, 'Labeling Strategies Matter for Super-Resolution Microscopy: A Comparison between HaloTags and SNAP-tags', *Cell Chem. Biol.*, vol. 26, no. 4, pp. 584-592.e6, Apr. 2019, doi: 10.1016/j.chembiol.2019.01.003.
[197] L. Wang *et al.*, 'A general strategy to develop cell permeable and fluorogenic probes for multicolour nanoscopy', *Nat. Chem.*, vol. 12, no. 2, pp. 165–172, Feb. 2020, doi: 10.1038/s41557-019-0371-1.
[198] N. Kilian *et al.*, 'Assessing photodamage in live-cell STED microscopy', *Nat. Methods*, vol. 15, no. 10, pp. 755–756, Oct. 2018, doi: 10.1038/s41592-018-0145-5.
[199] M. S. Frei, M. Tarnawski, M. J. Roberti, B. Koch, J. Hiblot, and K. Johnsson, 'Engineered HaloTag variants for fluorescence lifetime multiplexing', *Nat. Methods*, vol. 19, no. 1, Art. no. 1, Jan. 2022, doi: 10.1038/s41592-021-01341-x.
[200] A. Spang, I. Courtney, U. Fackler, M. Matzner, and E. Schiebel, 'The calcium-binding protein cell division cycle 31 of Saccharomyces cerevisiae is a component of the half bridge of the spindle pole body.', *J. Cell Biol.*, vol. 123, no. 2, pp. 405–416, Oct. 1993, doi: 10.1083/jcb.123.2.405.
[201] J. Li *et al.*, 'Repurposing the mitotic machinery to drive cellular elongation and chromatin reorganisation in Plasmodium falciparum gametocytes', *Nat. Commun.*, vol. 13, no. 1, Art. no. 1, Aug. 2022, doi: 10.1038/s41467-022-32579-4.
[202] M. H. Laporte, N. Klena, V. Hamel, and P. Guichard, 'Visualizing the native cellular organization by coupling cryofixation with expansion microscopy (Cryo-ExM)', *Nat. Methods*, vol. 19, no. 2, Art. no. 2, Feb. 2022, doi: 10.1038/s41592-021-01356-4.
[203] E. S. Suvorova, M. Francia, B. Striepen, and M. W. White, 'A Novel Bipartite Centrosome Coordinates the Apicomplexan Cell Cycle', *PLoS Biol.*, vol. 13, no. 3, p. e1002093, Mar. 2015, doi: 10.1371/journal.pbio.1002093.
[204] N. Gerald, B. Mahajan, and S. Kumar, 'Mitosis in the Human Malaria Parasite Plasmodium falciparum', *Eukaryot. Cell*, vol. 10, no. 4, pp. 474–482, Apr. 2011, doi: 10.1128/EC.00314-10.

[205] J. Schrével, G. Asfaux-Foucher, and J. M. Bafort, '[Ultrastructural study of multiple mitoses during sporogony of Plasmodium b. berghei]', *J. Ultrastruct. Res.*, vol. 59, no. 3, pp. 332–350, Jun. 1977, doi: 10.1016/s0022-5320(77)90043-0.

[206] H. Matthews, C. W. Duffy, and C. J. Merrick, 'Checks and balances? DNA replication and the cell cycle in Plasmodium', *Parasit. Vectors*, vol. 11, p. 216, Mar. 2018, doi: 10.1186/s13071-018-2800-1.

[207] L. Brusini, N. Dos Santos Pacheco, E. C. Tromer, D. Soldati-Favre, and M. Brochet, 'Composition and organization of kinetochores show plasticity in apicomplexan chromosome segregation', *J. Cell Biol.*, vol. 221, no. 9, p. e202111084, Aug. 2022, doi: 10.1083/jcb.202111084.

[208] H. Wiech *et al.*, 'Characterization of Green Alga, Yeast, and Human Centrins: SPECIFIC SUBDOMAIN FEATURES DETERMINE FUNCTIONAL DIVERSITY *', *J. Biol. Chem.*, vol. 271, no. 37, pp. 22453–22461, Sep. 1996, doi: 10.1074/jbc.271.37.22453.

[209] K. A. Rosowski, T. Sai, E. Vidal-Henriquez, D. Zwicker, R. W. Style, and E. R. Dufresne, 'Elastic ripening and inhibition of liquid–liquid phase separation', *Nat. Phys.*, vol. 16, no. 4, pp. 422–425, Apr. 2020, doi: 10.1038/s41567-019-0767-2.

[210] A. Malmendal, J. Evenäs, E. Thulin, G. P. Gippert, T. Drakenberg, and S. Forsén, 'When Size Is Important: ACCOMMODATION OF MAGNESIUM IN A CALCIUM BINDING REGULATORY DOMAIN *', *J. Biol. Chem.*, vol. 273, no. 44, pp. 28994–29001, Nov. 1998, doi: 10.1074/jbc.273.44.28994.

[211] Y. Zhao, J. Yan, Y. Feng, A. Liang, and B. Yang, 'Analysis of the role of Mg2+ on conformational change and target recognition by Ciliate Euplotes octocarinatus centrin', *J. Photochem. Photobiol. B*, vol. 105, no. 1, pp. 60–68, Oct. 2011, doi: 10.1016/j.jphotobiol.2011.06.010.

[212] V. Singh, L. Xu, S. Boyko, K. Surewicz, and W. K. Surewicz, 'Zinc promotes liquid-liquid phase separation of tau protein', *J. Biol. Chem.*, vol. 295, no. 18, pp. 5850–5856, May 2020, doi: 10.1074/jbc.AC120.013166.

[213] P. L. Onuchic, A. N. Milin, I. Alshareedah, A. A. Deniz, and P. R. Banerjee, 'Divalent cations can control a switch-like behavior in heterotypic and homotypic RNA coacervates', *Sci. Rep.*, vol. 9, no. 1, Art. no. 1, Aug. 2019, doi: 10.1038/s41598-019-48457-x.

[214] T. J. Nott *et al.*, 'Phase Transition of a Disordered Nuage Protein Generates Environmentally Responsive Membraneless Organelles', *Mol. Cell*, vol. 57, no. 5, pp. 936–947, Mar. 2015, doi: 10.1016/j.molcel.2015.01.013.

[215] G. Krainer *et al.*, 'Reentrant liquid condensate phase of proteins is stabilized by hydrophobic and non-ionic interactions', *Nat. Commun.*, vol. 12, no. 1, Art. no. 1, Feb. 2021, doi: 10.1038/s41467-021-21181-9.

[216] S. Wünsch, C. P. Sanchez, M. Gekle, L. Große-Wortmann, J. Wiesner, and M. Lanzer, 'Differential Stimulation of the Na+/H+ Exchanger Determines Chloroquine Uptake in Plasmodium falciparum', *J. Cell Biol.*, vol. 140, no. 2, pp. 335–345, Jan. 1998.

[217] J. M. A. Mauritz *et al.*, 'X-Ray Microanalysis Investigation of the Changes in Na, K, and Hemoglobin Concentration in Plasmodium falciparum-Infected Red Blood Cells', *Biophys. J.*, vol. 100, no. 6, pp. 1438–1445, Mar. 2011, doi: 10.1016/j.bpj.2011.02.007.

[218] O. Adame-Arana, C. A. Weber, V. Zaburdaev, J. Prost, and F. Jülicher, 'Liquid Phase Separation Controlled by pH', *Biophys. J.*, vol. 119, no. 8, pp. 1590–1605, Oct. 2020, doi: 10.1016/j.bpj.2020.07.044.

[219] Y. Kuhn, P. Rohrbach, and M. Lanzer, 'Quantitative pH measurements in Plasmodium falciparum-infected erythrocytes using pHluorin', *Cell. Microbiol.*, vol. 9, no. 4, pp. 1004–1013, Apr. 2007, doi: 10.1111/j.1462-5822.2006.00847.x.

[220] Q. Li *et al.*, 'LLPSDB: a database of proteins undergoing liquid–liquid phase separation in vitro', *Nucleic Acids Res.*, vol. 48, no. D1, pp. D320–D327, Jan. 2020, doi: 10.1093/nar/gkz778.

[221] C.-A. Lo, I. Kays, F. Emran, T.-J. Lin, V. Cvetkovska, and B. E. Chen, 'Quantification of Protein Levels in Single Living Cells', *Cell Rep.*, vol. 13, no. 11, pp. 2634–2644, Dec. 2015, doi: 10.1016/j.celrep.2015.11.048.

[222] B. J. Zeskind *et al.*, 'Nucleic acid and protein mass mapping by live-cell deep-ultraviolet microscopy', *Nat. Methods*, vol. 4, no. 7, pp. 567–569, Jul. 2007, doi: 10.1038/nmeth1053.

[223] G. Guigas, C. Kalla, and M. Weiss, 'Probing the nanoscale viscoelasticity of intracellular fluids in living cells', *Biophys. J.*, vol. 93, no. 1, pp. 316–323, Jul. 2007, doi: 10.1529/biophysj.106.099267.

[224] R. J. Ellis, 'Macromolecular crowding: an important but neglected aspect of the intracellular environment', *Curr. Opin. Struct. Biol.*, vol. 11, no. 1, pp. 114–119, Feb. 2001, doi: 10.1016/S0959-440X(00)00172-X.

[225] A. A. M. André and E. Spruijt, 'Liquid–Liquid Phase Separation in Crowded Environments', *Int. J. Mol. Sci.*, vol. 21, no. 16, p. 5908, Aug. 2020, doi: 10.3390/ijms21165908.

[226] J. S. Andersen *et al.*, 'Nucleolar proteome dynamics', *Nature*, vol. 433, no. 7021, pp. 77–83, Jan. 2005, doi: 10.1038/nature03207.
[227] Y. Shin, J. Berry, N. Pannucci, M. P. Haataja, J. E. Toettcher, and C. P. Brangwynne, 'Spatiotemporal control of intracellular phase transitions using light-activated optoDroplets', *Cell*, vol. 168, no. 1–2, pp. 159-171.e14, Jan. 2017, doi: 10.1016/j.cell.2016.11.054.
[228] T. S. Harmon, A. S. Holehouse, M. K. Rosen, and R. V. Pappu, 'Intrinsically disordered linkers determine the interplay between phase separation and gelation in multivalent proteins', *eLife*, vol. 6, p. e30294, doi: 10.7554/eLife.30294.
[229] J. Wang *et al.*, 'A molecular grammar governing the driving forces for phase separation of prion-like RNA binding proteins', *Cell*, vol. 174, no. 3, pp. 688-699.e16, Jul. 2018, doi: 10.1016/j.cell.2018.06.006.
[230] D. T. Murray *et al.*, 'Structure of FUS Protein Fibrils and Its Relevance to Self-Assembly and Phase Separation of Low-Complexity Domains', *Cell*, vol. 171, no. 3, pp. 615-627.e16, Oct. 2017, doi: 10.1016/j.cell.2017.08.048.
[231] M. Garcia-Jove Navarro *et al.*, 'RNA is a critical element for the sizing and the composition of phase-separated RNA–protein condensates', *Nat. Commun.*, vol. 10, no. 1, Art. no. 1, Jul. 2019, doi: 10.1038/s41467-019-11241-6.
[232] E. M. Jonasson *et al.*, 'Behaviors of individual microtubules and microtubule populations relative to critical concentrations: dynamic instability occurs when critical concentrations are driven apart by nucleotide hydrolysis', *Mol. Biol. Cell*, vol. 31, no. 7, pp. 589–618, Mar. 2020, doi: 10.1091/mbc.E19-02-0101.
[233] M. J. Treuheit, A. A. Kosky, and D. N. Brems, 'Inverse relationship of protein concentration and aggregation', *Pharm. Res.*, vol. 19, no. 4, pp. 511–516, Apr. 2002, doi: 10.1023/a:1015108115452.
[234] N. Helassa, C. Nugues, D. Rajamanoharan, R. D. Burgoyne, and L. P. Haynes, 'A centrosome-localized calcium signal is essential for mammalian cell mitosis', *FASEB J. Off. Publ. Fed. Am. Soc. Exp. Biol.*, vol. 33, no. 12, pp. 14602–14610, Dec. 2019, doi: 10.1096/fj.201901662R.
[235] P. Rohrbach, O. Friedrich, J. Hentschel, H. Plattner, R. H. A. Fink, and M. Lanzer, 'Quantitative Calcium Measurements in Subcellular Compartments of Plasmodium falciparum-infected Erythrocytes *', *J. Biol. Chem.*, vol. 280, no. 30, pp. 27960–27969, Jul. 2005, doi: 10.1074/jbc.M500777200.
[236] P. Van Damme *et al.*, 'N-terminal acetylome analyses and functional insights of the N-terminal acetyltransferase NatB', *Proc. Natl. Acad. Sci. U. S. A.*, vol. 109, no. 31, pp. 12449–12454, Jul. 2012, doi: 10.1073/pnas.1210303109.
[237] I. R. E. Nett *et al.*, 'The phosphoproteome of bloodstream form Trypanosoma brucei, causative agent of African sleeping sickness', *Mol. Cell. Proteomics MCP*, vol. 8, no. 7, pp. 1527–1538, Jul. 2009, doi: 10.1074/mcp.M800556-MCP200.
[238] M. D. Urbaniak, D. M. A. Martin, and M. A. J. Ferguson, 'Global quantitative SILAC phosphoproteomics reveals differential phosphorylation is widespread between the procyclic and bloodstream form lifecycle stages of Trypanosoma brucei', *J. Proteome Res.*, vol. 12, no. 5, pp. 2233–2244, May 2013, doi: 10.1021/pr400086y.
[239] J. A. Morin *et al.*, 'Sequence-dependent surface condensation of a pioneer transcription factor on DNA', *Nat. Phys.*, vol. 18, no. 3, Art. no. 3, Mar. 2022, doi: 10.1038/s41567-021-01462-2.
[240] K. K. Resendes, B. A. Rasala, and D. J. Forbes, 'Centrin 2 localizes to the vertebrate nuclear pore and plays a role in mRNA and protein export', *Mol. Cell. Biol.*, vol. 28, no. 5, pp. 1755–1769, Mar. 2008, doi: 10.1128/MCB.01697-07.
[241] A. Paoletti, M. Moudjou, M. Paintrand, J. L. Salisbury, and M. Bornens, 'Most of centrin in animal cells is not centrosome-associated and centrosomal centrin is confined to the distal lumen of centrioles', *J. Cell Sci.*, vol. 109 (Pt 13), pp. 3089–3102, Dec. 1996, doi: 10.1242/jcs.109.13.3089.
[242] S. Absalon, J. A. Robbins, and J. D. Dvorin, 'An essential malaria protein defines the architecture of blood-stage and transmission-stage parasites', *Nat. Commun.*, vol. 7, p. 11449, Apr. 2016, doi: 10.1038/ncomms11449.
[243] D. A. Zacharias, J. D. Violin, A. C. Newton, and R. Y. Tsien, 'Partitioning of Lipid-Modified Monomeric GFPs into Membrane Microdomains of Live Cells', *Science*, vol. 296, no. 5569, pp. 913–916, May 2002, doi: 10.1126/science.1068539.
[244] R. Nelson *et al.*, 'Structure of the cross-β spine of amyloid-like fibrils', *Nature*, vol. 435, no. 7043, pp. 773–778, Jun. 2005, doi: 10.1038/nature03680.
[245] M. R. H. Krebs, K. R. Domike, and A. M. Donald, 'Protein aggregation: more than just fibrils', *Biochem. Soc. Trans.*, vol. 37, no. Pt 4, pp. 682–686, Aug. 2009, doi: 10.1042/BST0370682.
[246] B. Shivu, S. Seshadri, J. Li, K. A. Oberg, V. N. Uversky, and A. L. Fink, 'Distinct β-sheet structure in protein aggregates determined by ATR-FTIR spectroscopy', *Biochemistry*, vol. 52, no. 31, pp. 5176–5183, Aug. 2013, doi: 10.1021/bi400625v.

[247] A. R. Strom and C. P. Brangwynne, ‘The liquid nucleome – phase transitions in the nucleus at a glance’, *J. Cell Sci.*, vol. 132, no. 22, p. jcs235093, Nov. 2019, doi: 10.1242/jcs.235093.
[248] R. Düster, I. H. Kaltheuner, M. Schmitz, and M. Geyer, ‘1,6-Hexanediol, commonly used to dissolve liquid–liquid phase separated condensates, directly impairs kinase and phosphatase activities’, *J. Biol. Chem.*, vol. 296, Jan. 2021, doi: 10.1016/j.jbc.2021.100260.
[249] J. Azimzadeh *et al.*, ‘hPOC5 is a centrin-binding protein required for assembly of full-length centrioles’, *J. Cell Biol.*, vol. 185, no. 1, pp. 101–114, Apr. 2009, doi: 10.1083/jcb.200808082.
[250] T. Wiegand and A. A. Hyman, ‘Drops and fibers — how biomolecular condensates and cytoskeletal filaments influence each other’, *Emerg. Top. Life Sci.*, vol. 4, no. 3, pp. 247–261, Dec. 2020, doi: 10.1042/ETLS20190174.
[251] A. von Appen *et al.*, ‘LEM2 phase separation governs ESCRT-mediated nuclear envelope reformation’, *Nature*, vol. 582, no. 7810, pp. 115–118, Jun. 2020, doi: 10.1038/s41586-020-2232-x.
[252] D. E. Arnot, E. Ronander, and D. C. Bengtsson, ‘The progression of the intra-erythrocytic cell cycle of Plasmodium falciparum and the role of the centriolar plaques in asynchronous mitotic division during schizogony’, *Int. J. Parasitol.*, vol. 41, no. 1, pp. 71–80, Jan. 2011, doi: 10.1016/j.ijpara.2010.07.012.
[253] E. Gasteiger *et al.*, ‘Protein Identification and Analysis Tools on the ExPASy Server’, in *The Proteomics Protocols Handbook*, J. M. Walker, Ed., in Springer Protocols Handbooks. , Totowa, NJ: Humana Press, 2005, pp. 571–607. doi: 10.1385/1-59259-890-0:571.
[254] D. A. Baker *et al.*, ‘A potent series targeting the malarial cGMP-dependent protein kinase clears infection and blocks transmission’, *Nat. Commun.*, vol. 8, no. 1, Art. no. 1, Sep. 2017, doi: 10.1038/s41467-017-00572-x.
[255] H. McWilliam *et al.*, ‘Analysis Tool Web Services from the EMBL-EBI’, *Nucleic Acids Res.*, vol. 41, no. W1, pp. W597–W600, Jul. 2013, doi: 10.1093/nar/gkt376.
[256] A. M. Waterhouse, J. B. Procter, D. M. A. Martin, M. Clamp, and G. J. Barton, ‘Jalview Version 2—a multiple sequence alignment editor and analysis workbench’, *Bioinformatics*, vol. 25, no. 9, pp. 1189–1191, May 2009, doi: 10.1093/bioinformatics/btp033.
[257] J. Schindelin *et al.*, ‘Fiji: an open-source platform for biological-image analysis’, *Nat. Methods*, vol. 9, no. 7, Art. no. 7, Jul. 2012, doi: 10.1038/nmeth.2019.
[258] B. Amos *et al.*, ‘VEuPathDB: the eukaryotic pathogen, vector and host bioinformatics resource center’, *Nucleic Acids Res.*, vol. 50, no. D1, pp. D898–D911, Jan. 2022, doi: 10.1093/nar/gkab929.
[259] F. W. Studier and B. A. Moffatt, ‘Use of bacteriophage T7 RNA polymerase to direct selective high-level expression of cloned genes’, *J. Mol. Biol.*, vol. 189, no. 1, pp. 113–130, May 1986, doi: 10.1016/0022-2836(86)90385-2.
[260] E. Knuepfer, M. Napiorkowska, C. van Ooij, and A. A. Holder, ‘Generating conditional gene knockouts in Plasmodium - a toolkit to produce stable DiCre recombinase-expressing parasite lines using CRISPR/Cas9’, *Sci. Rep.*, vol. 7, no. 1, p. 3881, Jun. 2017, doi: 10.1038/s41598-017-03984-3.

6 Acknowledgements

Many a tale has been told of the PhD experience. Of a formative time in one's life that fosters critical thinking, scientific acumen, and maturity. Of a path that tests just as much as it grows one's passion for science through many highs and as many lows. Much of that I have found to be true. However, the fact that I can't seem to recall those infamous lows when thinking back on these past five years is testament to a wonderful environment and the people that have created it.

The man to blame most for my fantastic experience is of course Dr. Julien Guizetti. I am deeply grateful for the opportunities and trust you have offered me over these years. Your ever-open ear, mindfulness in everything, and strive to foster improvement in those around you as well as in yourself have created an environment where curiosity can thrive without any undue pressure. Thank you for giving me the confidence and freedom to pursue my own ideas while being willing to listen to all the thoughts that came with them. In the often harsh and competitive world of science you are one of a kind and I am very lucky to have had you as my supervisor.

I furthermore would like to express my gratitude to Dr. Markus Ganter, not only for first igniting my excitement for *Plasmodium* cell division, but also for consistently offering his vast knowledge, advice in all things science or life, and the rare kind of wonderfully constructive criticism that makes one happy to have received it. In the same vein, I want to thank Prof. Dr. Friedrich Frischknecht for his insightful scientific life-lessons as well as his truly generous and manifold support throughout my thesis. I am very privileged to have had mentors whose passion for science is more infectious than any *Plasmodium* strain.

Special thanks to Prof. Michael Lanzer, Prof. Dr. Gislene Pereira, Dr. Niccolò Banterle, and Prof. Dr. Friedrich Frischknecht for generously offering their time to evaluate my thesis. In case of Prof. Dr. Lanzer, Prof. Dr. Perreira, and Prof. Dr. Frischknecht I owe an additional thank you for the scientific discussions and guidance throughout our previous TAC meetings.

This work was further supported by Dr. Severina Klaus who contributed her reign over Fiji and general advice on live-cell imaging. Much of the microscopy would also not have been possible without the dedicated work and support by Dr. Vibor Laketa and Dr. Sylvia Olberg of the Infectious Disease Imaging Platform (IDIP). Live-cell STED microscopy further benefitted greatly by the generous contribution of the fantastic Halo dyes by Dr. Nicolas Lardon and Prof. Dr. Kai Johnsson. In regard to protein purification, I would like to thank Dr. Renè Sahm for his initial guidance, as well as Karine Lapouge and Dr. Kim Remans at the EMBL Heidelberg Protein Expression and Purification Core Facility for performing the CD spectroscopy. Additional thanks to Prof. Dr. Christian Doerig for discussions on protein kinases and phosphorylation, as well as Prof. Dr. Paul Guichard, Dr. Virginie Hamel, and Dr. Sónia Gomes Pereira for discussions on human centrin and

Sfi1 biology. Of course, nothing would have ever worked without Sandra Niebel and Miriam Griesheimer making everything run smoothly on the administrative side, for which I cannot thank them enough.

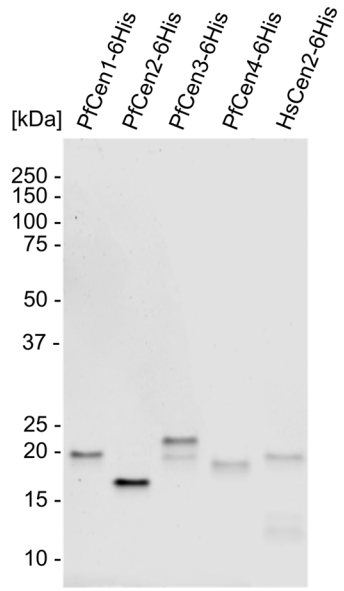
The best part about walking down the academic track are the people who travel down the road alongside you. I was exceedingly fortunate to be part of the incredibly passionate, wholesome, and just-the-right-amount-of-crazy, group of people that is the “Ganzetti” lab! No matter how many hours we spent in the lab together I would never get tired of it, nor forget the many special moments we shared. And not just because Aiste keeps documenting them in picture and writing. Therefore, all the appreciation to both the old guard, Caro, Anja, Marta, Severina; and to the next generation, Vanessa, Chris, Aiste and all the other students that joined us temporarily and often repeatedly. Speaking of which, a special thank you to Nicolas Lichti and Marina Iocca who joined me for part of this project and probably taught me just as much as I hopefully taught them. And of course, much appreciation goes out to our next-door neighbours from the Frischknecht lab for their years of advice, supplies, and close ties.

I furthermore want to express my gratitude to Desirée Evjen and Dr. Gabrielle Anicker-Evjen for proofreading this thesis and therein enlightening me on the hitherto unrealized potential of commas. A very special thank you to Desirée for listening to me ramble about my strange little parasites for the past few years while blessing me with your kindness and many warm smiles along the way.

Zu sehr guter Letzt ein herzliches Dankeschön an meine Eltern für ihre jahrelange Unterstützung während meines Studiums, Doktors, und alledem was davor kam. Ihr habt nie versucht mir einen Weg vorzugeben und es mir durch eure Großzügigkeit ermöglicht meine Leidenschaft zu finden und ihr nachzugehen. Es ist schön jemanden zu haben der manchmal mehr an einen geglaubt hat als man es selbst. Auf eure offenen Ohren und Herzen konnte ich mich immer verlassen.

7 Supplements

A



B

	Expected size [kDa]	Major peak size [kDa]	Minor peaks size [kDa]
PfCen1-6His	20.422	20.291 Met1 absent	
PfCen2-6His	20.134	20.003 Met1 absent	
PfCen3-6His	21.736	21.736	21.605 Met1 absent 20.085 Δ14 AA N-terminus
PfCen4-6His	20.926	20.926	
HsCen2-6His	20.561	20.430 Met1 absent	12.545 11.255 alternate start codons M72 & M84

C

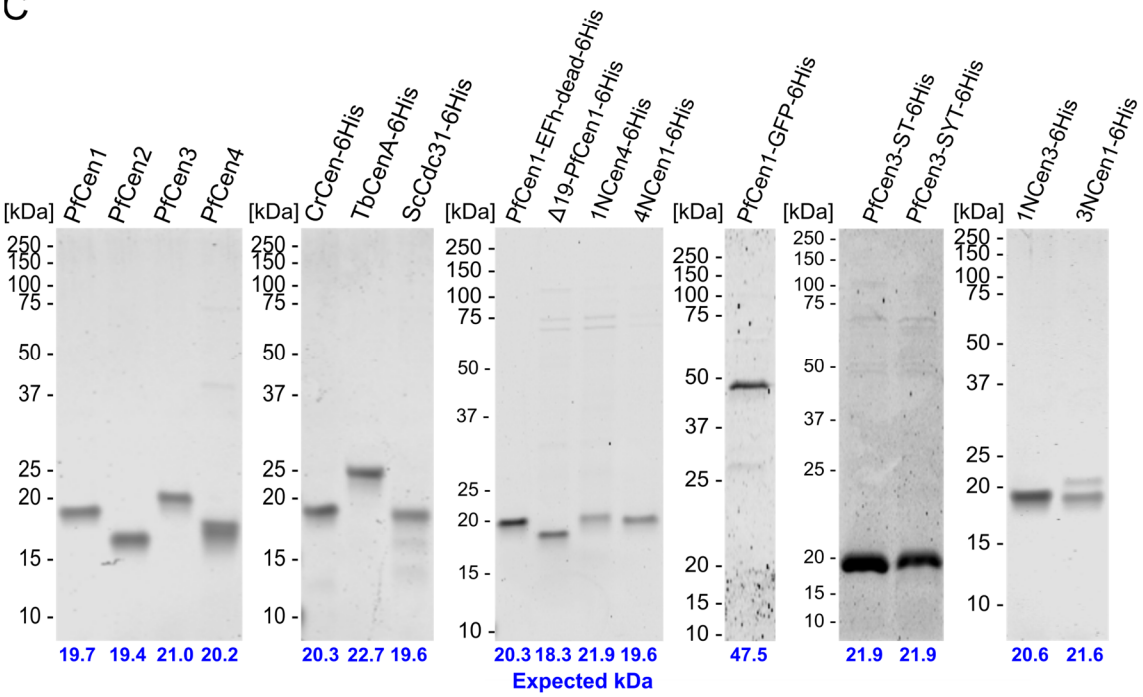


Figure S1 Size and purity of recombinant centrins. (A, C) Coomassie stained gels after SDS-PAGE of various recombinantly produced, Ni-NTA purified, and dialysed centrins. 1.125 µg protein loaded per lane. Expected molecular weights shown underneath in blue. **(B)** Molecular weights of major and minor peaks as determined via mass spectrometry on native protein solutions. Missing amino acids were determined by referencing the measured molecular weight against the known amino acid sequences, assuming that the C-terminus was intact as proteins were purified via C-terminal 6His tags. Modified from Voß *et al.* (2023) [79].

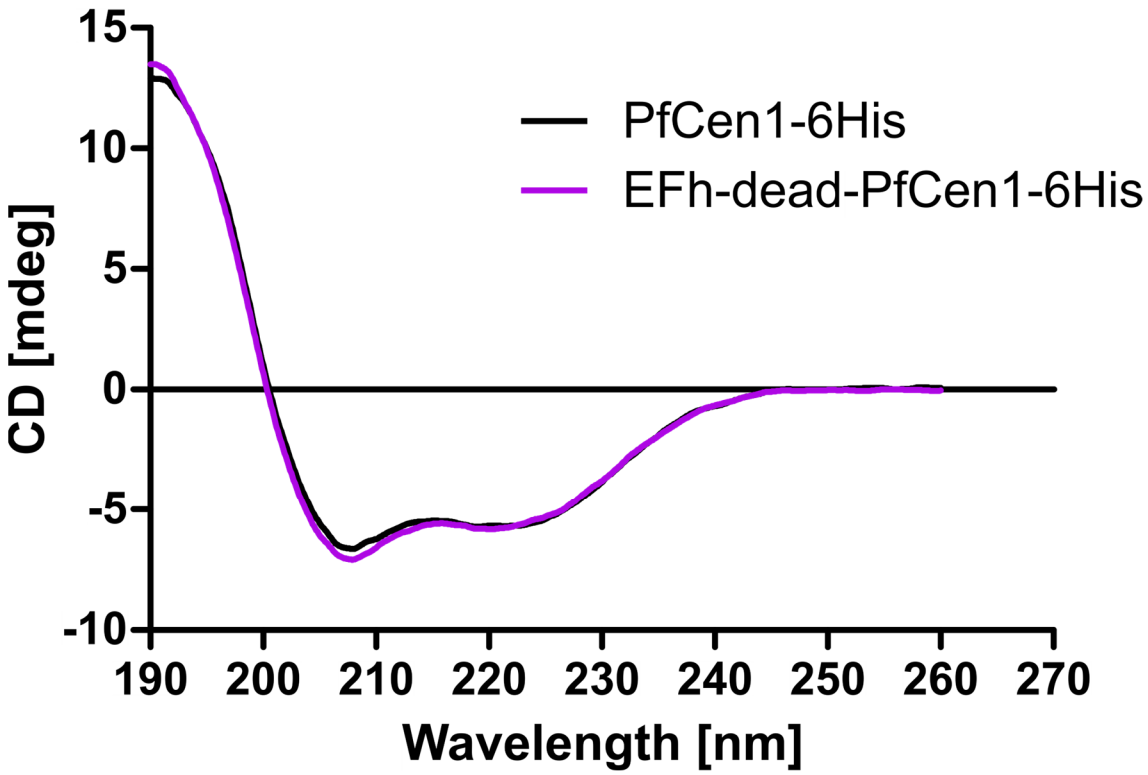


Figure S2 Effect of EFh-dead mutation on PfCen1 conformation. CD spectra of recombinant PfCen1-6His and EFh-dead-PfCen1-6His mutant. CONTIN-LL analysis of WT vs mutant in the respective following secondary structure composition: 24.7% vs 24.6% helices, 23% vs 22.9% strands, 15.8% vs 15.9% turns, 36.5% vs 36-6% disordered regions. From Voß *et al.* (2023) [79]. Experiment and analysis performed by Karine Lapouge from the Protein Expression and Purification Core Facility at EMBL Heidelberg.

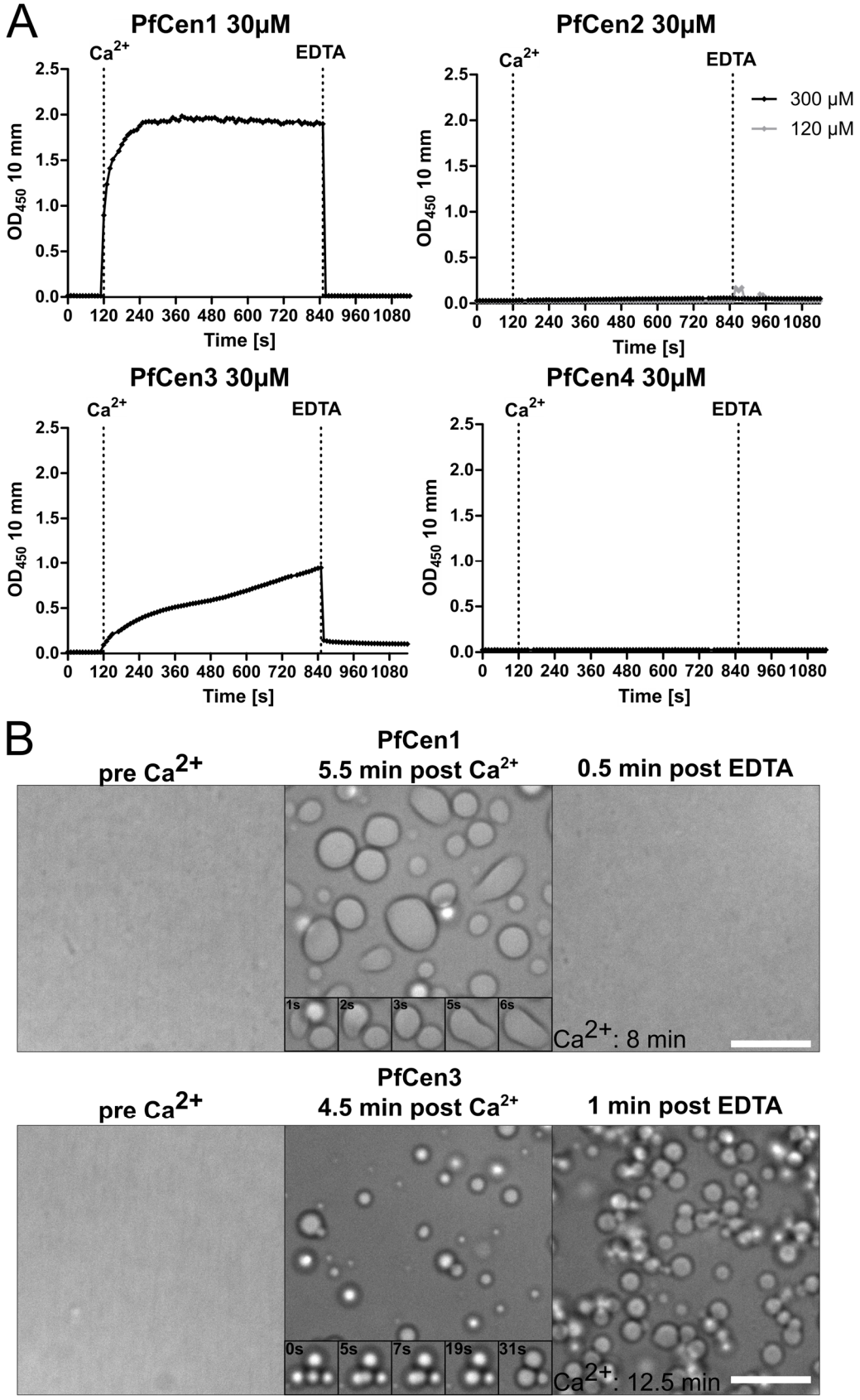


Figure S3 Recombinant PfCen1-4 without 6His-tag. (A) Turbidity assays of tag-free recombinant centrins at indicated concentrations at 37°C in 50 mM BisTris (pH 7.1). Turbidity was quantified as light adsorption at 450 nm. Ca^{2+}, $CaCl_2$ addition to 2 mM; Mg^{2+}, $MgCl_2$ addition to 2 mM, EDTA, EDTA addition to 10 mM. **(B)** The three stages of the turbidity assay as in A observed by bright-field microscopy for 100 µM PfCen1 and 70 µM PfCen3. Inlays show droplet fusion or wetting events. Approximate elapsed time after Ca^{2+} and EDTA addition is indicated. Higher protein concentrations were used to increase droplet density. Scalebars 10 µm**. (**A) from Voß *et al.* (2023) [79].

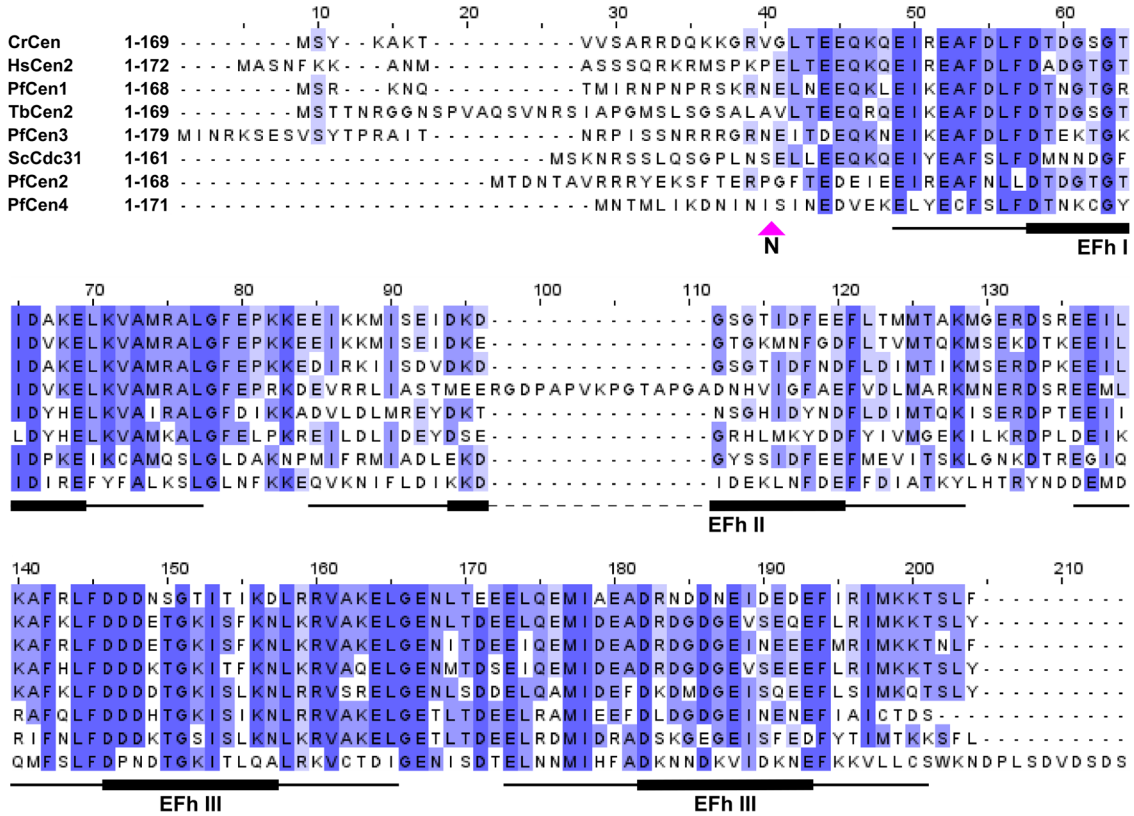


Figure S4 Amino acid sequence alignment of different centrin. Clustal Omega alignment of the centrins studied within this work. Blue shading indicates residue similarity ≥50%. Lines mark positions of predicted EFh domains based on Mahajan *et al.* [70] (interrupted in case of TbCen2) with thick lines further marking the inner Ca^{2+}-binding loop. Purple arrow indicates the end of the N-terminus according to the definition applied within this work for PfCen1-4.

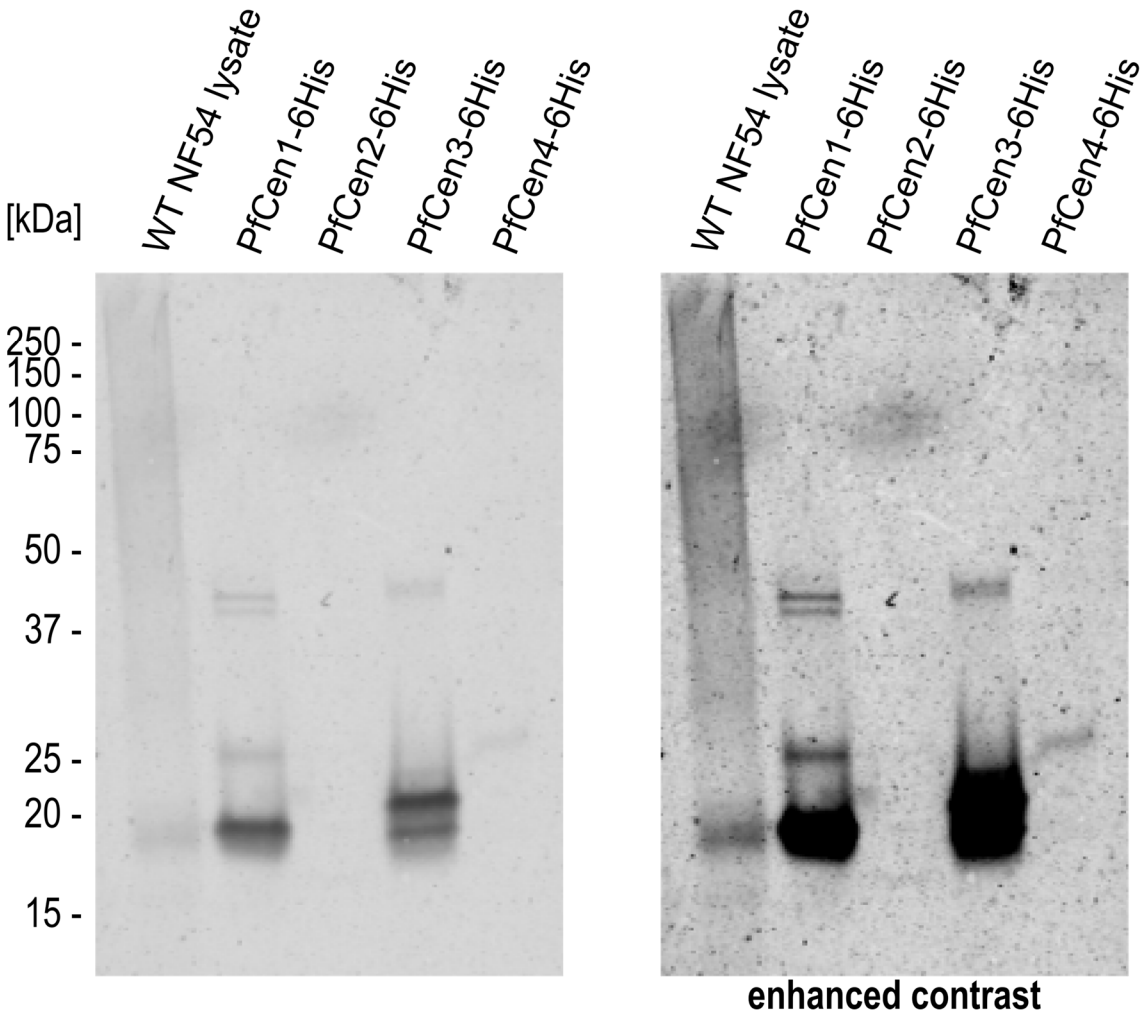


Figure S5 Specificity of the rat αPfCen1-6His antibody WB evaluating the αPfCen1-6His rat antiserum newly generated by me against *P. falciparum* lysate and recombinant PfCen1-4-6His. The same blot is shown in two contrast settings for better visibility. Modified from Voß *et al.* (2023) [79]. Antibodies commissioned from Davids Biotechnology GmbH.